UNIVERSITÀ DEGLI STUDI DI PALERMO
Energia e Tecnologie dell'Informazione
Dipartimento di Ingegneria
ING-IND/32

Enhanced mathematical modelling of interior permanent magnet synchronous machines for loss minimization control

IL DOTTORE
Ing. Claudio Nevoloso

IL COORDINATORE
Prof. Maurizio Cellura

IL TUTOR
Prof. Rosario Miceli

CO TUTOR
Prof. Antonino O. Di Tommaso

CICLO XXXII.
2020

Preface

The activity of PhD was carried out at the Department of Energy, Information Engineering and Mathematics Model (DEIM) of the University of Palermo (Italy) from November 2016 to October 2019.

The theoretical development, simulation analysis, implementation and experimental tests has been performed in Sustainable Development and Energy Saving Laboratory (SDESLAB) of the University of Palermo.

Part of the activity was developed during the visiting period in Nuremberg (Germany) at the Institute of Power Electronics System (ELSYS) of the "Technische Hochschule Nürnberg Georg-Simon Ohm" from 5 November 2019 to 5 May 2019.

Index

Introduction

Energy management is a fundamental facility for humanity. At present, the awareness that renewable energy cannot satisfy the entire energy needs of the community and that traditional energy sources have a limited duration makes it imperative to address the problem of their careful and responsible use. Therefore, the need for an intelligent and functional use of energy has led the technical-scientific community to concentrate its efforts on the issues of sustainable development and energy savings. The electric drives industrial sector has suffered this influence in a visceral way. This sector plays a leading role in the industrial frame as it is one of the main consumers of electricity. Moreover, the topic of electrical drives design and optimization has become of considerable importance especially for the automotive sector and for hybrid and electric traction applications. In particular, in the last two decade, this sector has undergone a considerable technological development thanks to the exponential evolution of power electronics, the use of increasingly performing electric machines and new control techniques. In this scenario, the design and optimization of control algorithms for interior permanent magnet synchronous machines (IPMSM) has became of considerable interest in the scientific and technological community. In detail, the IPMSM is one of the most used electrical machine typologies in the electric traction applications due to the high efficiency and flux-weakening capability. The purpose of the research project *"Realization of innovative algorithms for the minimization of the losses in synchronous brushless motors for automotive application"* consists in the design and development of innovative *Loss Model Algorithm* (LMA) for interior permanent magnet synchronous machines (PMSM). The LMAs goal is the identification of the working points of the machine at minimum losses through the optimal determination of the control variables values. Therefore, the use of LMAs in electric drives can be of considerable utility in terms of energy savings especially for automotive application where energy autonomy is a crucial parameter. In detail, a LMA is a control algorithm based on the knowledge of the dynamic mathematical model of the IPMSM. Therefore, the performances of LMA are strictly dependent on the accuracy of the mathematical model and of its electrical and magnetic parameters. In this regard, the research carried out during the PhD course focused on the four macro topics, reported as chapters of the PhD thesis:

1. loss minimization control techniques for PMSM: state of art;

2. performances analysis of the power loss mathematical models;
3. efficiency measurement of electric drives equipped with interior permanent magnets synchronous machine (IPMSM);
4. enhanced mathematical modelling of IPMSM.

The first chapter describes the state of art of main *Loss Minimization control Algorithms* (LMA) for electric drives equipped with PMSM. The LMAs can be classified into two general approaches named *Search control* and *Loss Model Control*, respectively. The main features of each approach are presented and discussed. Particular attention is devoted to the conventional IPMSM modelling approach employed in the LMC. Finally, the LMA chosen as a case of study is illustrated.

The second chapter describes the performances analysis of the power loss mathematical models for LMC. In detail, the conventional IPMSM modelling approach and the IPMSM modelling approach that take into account the magnetic self-saturation effects and the variability the iron loss with the supply frequency are studied and discussed. In order to evaluate the performances of each modelling approach, several experimental investigations have been carried out on an electric drive equipped with an IPMSM.

The third chapter is focused on the design and validation of accurate efficiency measurement approach for electrical drives equipped with IPMSMs. In particular, the efficiency measurement approaches for electrical drives described by the international standards and by the scientific literature are described and discussed. Particular attention was paid to the new standard IEC61800 and their prescriptions have been employed for the efficiency estimation of the electric drive under test. Finally, a new measurement approach for the comparison of the electrical drive efficiency, when it is controlled with several control algorithms, is presented and experimentally validate.

The last chapter describes the enhanced mathematical modelling of IPMSM that take into account the magnetic saturation, cross-coupling, spatial harmonics and iron loss effects. This activity was carried out in collaboration with the Institute of Power Electronics System (ELSYS) of the “Technische Hochschule Nürnberg Georg-Simon Ohm” during the PhD visiting period. In particular, the research activity was focused on the finite element modelization and analysis of IPMSMs and the *Ansys Maxwell* simulation environment (FE software) has been used for the simulation of the IPMSM under test. In detail, in order to define a high-fidelity IPMSM mathematical model, a

large number of FEA investigations have been carried out. In this regard, the enhanced IPMSM mathematical model is described, implemented in Matlab®/Simulink environment and, for validation purpose, its performances have been compared with those of the IPMSM implemented in *Ansys Maxwell* environment.

Chapter 1 Loss minimization control techniques for PMSM: state of art

1.1 Introduction

In the previous century, the synchronous motors were used in those applications where a constant speed operation was required since the speed is related to the supply frequency. In addition, this kind of machine requires a power supply in order to energize the rotor winding and they have not the skill to be self-starting machines. In the past, these features made this type of electrical machines unattractive for small and medium power applications, especially for traction or vehicular applications, where direct current and induction machines were widely used.

The evolution of power electronics systems, that allowed to have variable frequency power supply at competitive costs, have made it possible to successfully use the synchronous machines in variable speed applications. In this sense, the Permanent Magnet Synchronous Machines (PMSM), that employ the permanent magnet in order to produce the main magnet field, has undergone exponential development that allowed its use in several sectors, especially for automotive and vehicular applications. In particular, at the same power, this kind of machine present better dynamic performances and efficiency in comparison to the DC and induction machines. The main drawback is linked to the cost of rare-earth PM although in recent years they have achieved sustainable costs. In this chapter, the main typologies of PMSMs, the electrical and mechanical features and the conventional dynamic and mathematical model of PMSMs are described. Furthermore, the state of art of main Loss Minimization Algorithm control (LMA) for electric drives equipped with PMSM is presented and carefully discussed.

1.2 PMSM typologies

The PMSMs are diffused in the industrial field, especially in the small and medium electric drives, and in the automotive and vehicular field. In particular, this kind of machine is widely used in high-performances drives, where high efficiency and high dynamic performances justify the costs due to the use of PMs.

The stator and the rotor present both a laminated iron structure and they are separated by a thin air gap. The polyphase stator winding can be both distributed that

concentrated. The PMs are mounted in the rotor and their magnetic permeability is similar to that of the air. On the base of the rotor structure, a function of the placement of the PMs in the rotor, it is possible to obtain isotropic and anisotropic rotor structures. In literature, a first classification is made on the base of magnetic behaviour in:

- Surface-mounted Permanent Magnet Synchronous Machines (SPMSM) that present isotropic magnetic behaviour;
- Interior-mounted Permanent Magnet Synchronous Machines (IPMSM) that present anisotropic magnetic behaviour.

In machines with an isotropic rotor, electromechanical conversion is actuated according to the principle of electrodynamic systems, as for the DC motor. The electromechanical conversion is based on the interaction between the stator conductors and the magnetic fields create by permanent magnets. In the anisotropic machine, the electromechanical conversion follows the double principle of the electrodynamic and reluctance systems. The torque generated by this motor is given by the sum of the contributions of these two phenomena.

Within each kind of PMSM, it is possible to find several rotor configurations. Fig. 1 show the main common rotor configurations [I.1].

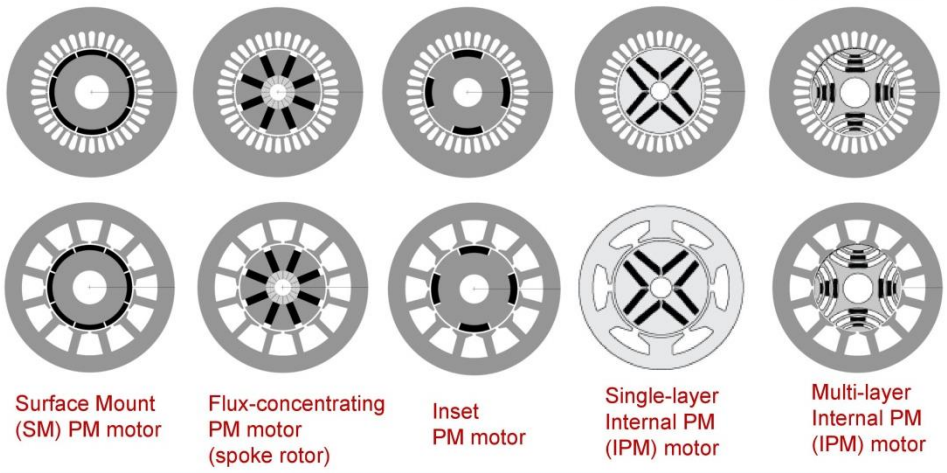

Fig. 1 Rotor configurations for SPMSMs and IPMSMs

The rotor and consequently the machines are classified into three main topologies: Interior PM (IPM) machines, Surface–mounted PM (SPM) machines and Inset PM machines (XPM). According to the magnetization direction of the PMs, the IPMSMs can be further distinguished in:

- Tangential magnetization IPMSM;

- Radial magnetization IPMSMs.

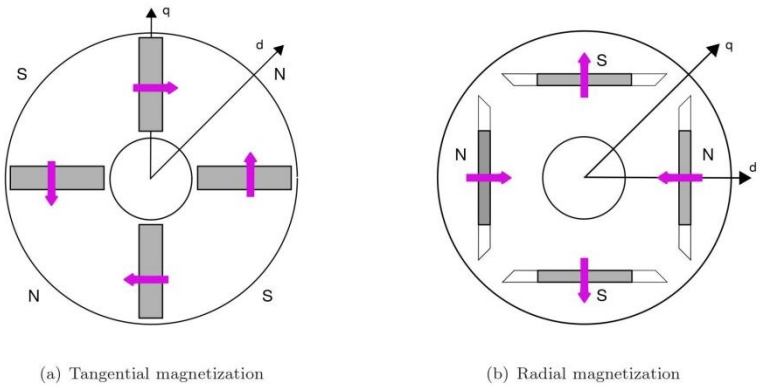

(a) Tangential magnetization (b) Radial magnetization

Fig. 2 Schematic representations of IPMSMs

In order to obtain an anisotropic magnetic behaviour, the IPMSM is not the only solution. In particular, there are other types of machines that can present an anisotropy rotor. One of those is the inset machine (XPMSM) that presents a rotor configuration similar to the rotor of SPMSM but between each couple of adjacent PMs, there is an iron tooth. As in the SPMSM, the main flux is due to the PMs placed on the rotor surface. In addition, the rotor teeth cause a rotor saliency. However, the achievable unsaturated saliency ratio is quite low and thus the contribution to the torque is limited. The tooth width is generally not optimized in order to minimize the torque ripple or to obtain a positive incremental saliency ratio, even at high currents.

A further classification can be made on the base of the spatial distribution of the induction airgap wave. In particular, the PMSM can be classified in:

- Trapezoidal PMSM or BLDCM (Brushless Direct Current machines);
- Sinusoidal PMSM or BLACM (Brushless Alternate Current machines):

The trapezoidal PMSMs have a trapezoidal spatial distribution of the induction of the airgap wave, while the sinusoidal ones have a sinusoidal type. In this case, the machines are appropriately controlled to obtain this type of operation. In this discussion, we will refer exclusively to the motors of the second type, that is to say those with magnetic induction field distribution of the sinusoidal type.

1.3 Conventional mathematical and circuital modelling theory of IPMSM

1.3.1 IPMSM mathematical model in the stator reference frame

In order to study the electric and magnetic behaviour of the IPMSM in several working conditions, it is necessary to know the dynamic and mathematical machine model and its electrical and magnetic parameters. In literature, several dynamic and mathematical IPMSM models are described [I.1]-[I.5]. In this chapter, the conventional dynamic and mathematical machine models are presented. The simplify hypothesis at the base of the conventional dynamic and mathematical IPMSM model are:

- sinusoidal spatial distribution of the magneto-motive force in the air gap;
- linear magnetic behaviour of the machine;
- absence of hysteresis and eddy currents in the iron core;
- absence of cross-coupling effects;
- absence of slot harmonics effects;
- absence of the temperature effects on the machine.

Referring to a three-phase IPMSM, the general voltage equations are:

$$\begin{cases} v_a = Ri_a(t) + \dfrac{d\lambda_a(t,\theta_e)}{dt} \\ v_b = Ri_b(t) + \dfrac{d\lambda_b(t,\theta_e)}{dt} \\ v_c = Ri_c(t) + \dfrac{d\lambda_c(t,\theta_e)}{dt} \end{cases} \tag{4.1}$$

Where θ_e is the rotor electrical position (given by the product from the number of the pole-pair p and the mechanical position θ_r), and:

- $v_a,\ v_b,\ v_c$ are the instantaneous phase voltages;
- $i_a,\ i_b,\ i_c$ are the instantaneous phase currents;
- $\lambda_a, \lambda_b, \lambda_c$ are the instantaneous magnetic phase flux linkage;
- R is the phase resistance, that it is supposed to be equal for all three-phase.

Flux linkage to the stator phases are both a function of the currents circulating in each stator phase and of the magnetic flux emanating from the rotor permanent magnets. It is assumed that the rotor and the stator of the machine exhibit constant magnetic permeability, or rather the linear magnetic behaviour and that the losses in the machine iron are negligible. The flux linkage can be expressed with the following relationships:

$$\begin{cases} \lambda_a(t) = \lambda_{a,i}(t) + \lambda_{PMa}(t) \\ \lambda_b(t) = \lambda_{b,i}(t) + \lambda_{PMb}(t) \\ \lambda_c(t) = \lambda_{c,i}(t) + \lambda_{PMc}(t) \end{cases} \quad (4.2)$$

Where $\lambda_{n,i}$ is the flux linkage produced by stator current excitation and λ_{PMn} is the flux linkage produced by permanent magnets. On the base of the model hypothesis, it is possible to assume sinusoidal the flux linkage λ_{PMa}, $\lambda_{PMb,}$ and λ_{PMc}:

$$\begin{cases} \lambda_{PMa} = \lambda_{PM} \cos p\theta_r \\ \lambda_{PMb} = \lambda_{PM} \cos(p\theta_r - \frac{2}{3}\pi) \\ \lambda_{PMc} = \lambda_{PM} \cos(p\theta_r - \frac{4}{3}\pi) \end{cases} \quad (4.3)$$

Where λ_{PM} represents the peak value of flux linkage of each phase due to the permanent magnets. The flux linkage produced by stator current excitation can be expressed with the following relationships:

$$\begin{cases} \lambda_{a,i} = L_{aa} i_a + L_{ab} i_b + L_{ac} i_c \\ \lambda_{b,i} = L_{ba} i_a + L_{bb} i_b + L_{bc} i_c \\ \lambda_{c,i} = L_{ca} i_a + L_{cb} i_b + L_{cc} i_c \end{cases} \quad (4.4)$$

where the L_{aa}, $L_{bb,}$ and L_{cc} are the self-inductances of the three phases, L_{ab}, L_{bc} and L_{ac} are the mutual-inductances between one phase to the other ones. The auto and mutual inductances can be considered dependent on the rotor position and then also on the time. The self-inductances can be expressed as follow:

$$\begin{cases} L_{aa} = L_{\sigma s} + L_{ms0} + L_m \cos 2p\theta_r \\ L_{bb} = L_{\sigma s} + L_{ms0} + L_m \cos(2p\theta_r - \frac{2}{3}\pi) \\ L_{cc} = L_{\sigma s} + L_{ms0} + L_m \cos(2p\theta_r - \frac{4}{3}\pi) \end{cases} \quad (4.5)$$

that is given by the sum of a sinusoidal term with a double electrical frequency (of amplitude L_m) and a constant term ($L_{\sigma s}$+L_{ms0}). The constant $L_{\sigma s}$ represents the leakage inductance and it is relative to the stator flux which encloses in the air without interesting the rotor. L_{ms0} and L_m represent, the constant component and the amplitude of the anisotropy component ($2p\theta r$ angle function) of the magnetization inductance, respectively. The mutual inductances take into account the flux linked by each winding due to the current flowing in the other windings. These also depend from anisotropy of the machine and can be expressed through the following relationships:

$$\begin{cases} L_{ab} = L_{ba} = -M_s + L_m \cos(2p\theta_r - \frac{2}{3}\pi) \\ L_{bc} = L_{cb} = -M_s + L_m \cos(2p\theta_r) \\ L_{ca} = L_{ac} = -M_s + L_m \cos(2p\theta_r - \frac{4}{3}\pi) \end{cases} \quad (4.6)$$

where M_s is the average coefficient of mutual induction between the phases of the stator winding. The relationships described above can also be expressed in matrix form as follows:

$$\begin{bmatrix} v_a \\ v_b \\ v_c \end{bmatrix} = \begin{bmatrix} R & 0 & 0 \\ 0 & R & 0 \\ 0 & 0 & R \end{bmatrix} \begin{bmatrix} i_a \\ i_b \\ i_c \end{bmatrix} + \frac{d \begin{bmatrix} \lambda_a \\ \lambda_b \\ \lambda_c \end{bmatrix}}{dt} \quad (4.7)$$

$$\begin{bmatrix} \psi_a \\ \psi_b \\ \psi_c \end{bmatrix} = \begin{bmatrix} L_{aa} & L_{ab} & L_{ac} \\ L_{ba} & L_{bb} & L_{bc} \\ L_{ca} & L_{cb} & L_{cc} \end{bmatrix} \begin{bmatrix} i_a \\ i_b \\ i_c \end{bmatrix} + \begin{bmatrix} \lambda_{PMa} \\ \lambda_{PMb} \\ \lambda_{PMc} \end{bmatrix} \quad (4.8)$$

The expressions (1.7) and (1.8) can also be expressed in compact form:

$$[v] = [R][i] + \frac{d[\lambda]}{dt} \quad (4.9)$$

$$[\psi] = [L][i] + [\lambda] \quad (4.10)$$

Replacing the equation (1.8) in the equation (1.7) of the electric voltage, it is possible to obtain the following relationship:

$$\begin{aligned} [v] &= [R][i] + \frac{d}{dt}([L][i] + [\lambda]) = [R][i] + \frac{d[L]}{dt}[i] + \frac{d[i]}{dt}[L] + \frac{d[\lambda]}{dt} = \\ &= [R][i] + \frac{d\theta_r}{dt}\frac{d[L]}{d\theta}[i] + \frac{d[i]}{dt}[L] + \frac{d\theta_r}{dt}\frac{d[\lambda]}{d\theta_r} = \\ &= [R][i] + \omega_r \frac{d[L]}{d\theta_r}[i] + [L]\frac{d[i]}{dt} + \omega_r \frac{d[\lambda]}{d\theta_r} \end{aligned} \quad (4.11)$$

Where:

- $[R][i]$ are the drop voltages component in each phase *a*, *b*, *c*;
- $[L]\frac{d[i]}{dt}$ are the back electromotive forces auto and mutually induced in the stator windings;
- $\omega \frac{d[L]}{d\theta_r}[i]$ are the rotational back electromotive forces due to the anisotropy of the machine;
- $\omega \frac{d[\lambda]}{d\theta_r}$ are the rotational back electromotive forces induced by the flux of the permanent magnets.

Multiplying both members of equation (1.11), for the transposed vector of the currents $[i]^T$, it is possible to obtain the expression of the input power of IPMSM:

$$[P_e] = [i]^T[v] = [i]^T[R][i] + [i]^T[L]\frac{d[i]}{dt} + \omega_r[i]^T\frac{d[L]}{d\theta_r}[i] + \omega_r[i]^T\frac{d[\lambda]}{d\theta_r} \tag{4.12}$$

Where:

- $P_e = [i]^T[v]$ represents the input electric power absorbed by the machine;
- $P_{cu} = [i]^T[R][i]$ represents the joule losses in the stator windings;
- $[i]^T[L]\frac{d[i]}{dt}$ represents the power stored in the magnetic field;
- $P_m = \omega_r[i]^T\frac{d[L]}{d\theta_r}[i] + \omega_r[i]^T\frac{d[\lambda]}{d\theta_r}$ represents the mechanical power of the motor shaft.

Therefore it is also possible to obtain the expression of the electromechanical torque to the shaft with the following relation:

$$T_{em} = \frac{P_m}{\omega_r} = [i]^T\frac{d[L]}{d\theta_r}[i] + [i]^T\frac{d[\lambda]}{d\theta_r} =$$
$$= [i_a\, i_b i_c]\frac{d}{d\theta_r}\begin{bmatrix} L_{aa} & L_{ab} & L_{ac} \\ L_{ba} & L_{bb} & L_{bc} \\ L_{ca} & L_{cb} & L_{cc} \end{bmatrix}\begin{bmatrix} i_a \\ i_b \\ i_c \end{bmatrix} + [i_a\, i_b i_c]\frac{d}{d\theta_r}\begin{bmatrix} \lambda_{PMa} \\ \lambda_{PMb} \\ \lambda_{PMc} \end{bmatrix} \tag{4.13}$$

Where:

- $[i_a\, i_b i_c]\frac{d}{d\theta_r}\begin{bmatrix} L_{aa} & L_{ab} & L_{ac} \\ L_{ba} & L_{bb} & L_{bc} \\ L_{ca} & L_{cb} & L_{cc} \end{bmatrix}\begin{bmatrix} i_a \\ i_b \\ i_c \end{bmatrix}$ represents the reluctance torque component, or the torque developed by the machine in the absence of permanent magnets;
- $[i_a\, i_b i_c]\frac{d}{d\theta_r}\begin{bmatrix} \lambda_{PMa} \\ \lambda_{PMb} \\ \lambda_{PMc} \end{bmatrix}$ represents the torque component developed by the machine through the interaction between the flux produced by the permanent magnets and the currents circulating in the stator phases.

The mathematical model of the synchronous permanent-magnet motor thus found consists of a system of differential equations with non-constant coefficients, whose solutions are not easy to determine. This difficulty is overcome by resorting to a mathematical artifice which consists in transforming the coordinates from the *abc* stator reference frame system to the *dqo* reference frame system rotating at synchronism.

1.3.2 IPMSM mathematical model in *dqo* synchronous reference frame

The mathematical model in the stator reference frame system determined in the previous paragraph is formed by three differential equations with variable coefficients. The use of such a mathematical model for the purpose of controlling an IPMSM is not simple to implement. In order to obtain differential equations with constant parameters, it is possible to use linear mathematical transformations. Specifically, the Park transformation allows the transition from a three-phase stator reference system to a two-phase reference frame system, that is rotating at the electrical rotor speed ω_r and with the real axis coincident to the polar rotor axis. In particular, this transformation has the advantage of being reduced to a system of equations in the reference (*dqo*) where the coefficients of self and mutual inductions are independent of the rotor position and therefore constant over time. To obtain the Park model, a first coordinate transformation is carried out from the stator reference system (*a,b,c*) to the fixed two-phase reference system (α, β), as shown in Fig. 3.

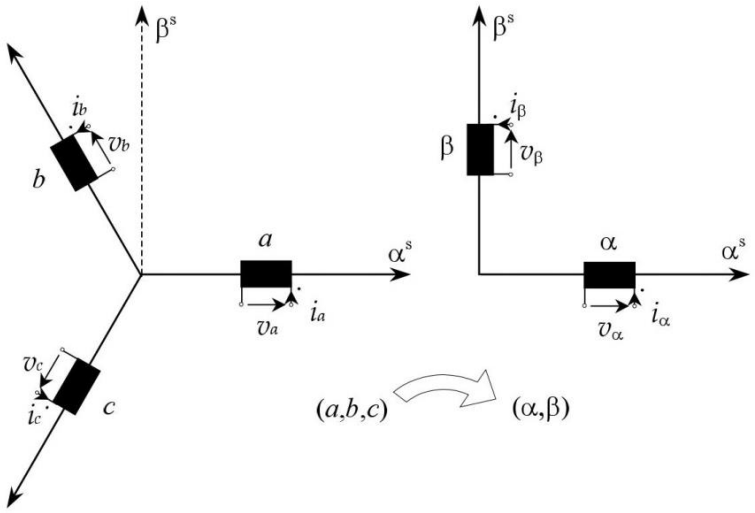

Fig. 3 Transformation of coordinates from the stator reference system (a, b, c) to the fixed two-phase reference system (α,β)

With such a transformation is obtained a system that there are only two windings arranged at 90° degrees and therefore, magnetically decoupled. This model has the stator and rotor quantities evaluated with reference to the corresponding physical reference frame, i.e. the inductive coefficients are still a function of the angular position of the rotor. Therefore a further transformation is needed which allows to express stator and rotor quantities under a single reference. A system of axes (*d,q,o*) rotating integrally with the rotor is considered, where the rotor quantities are referred to this system. This

further coordinates transformation, where e stator quantities referred to the system (α,β) are reported to the system (d,q), is shown in Fig. 4.

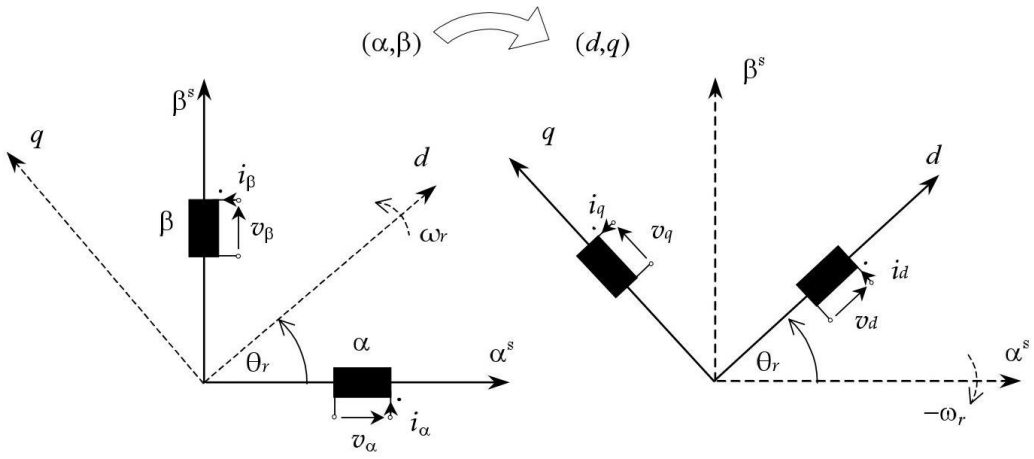

Fig. 4 Transformation of coordinates from the fixed two-phase reference system (α,β) to rotating (*d,q,o*) system.

The transformation of the quantities from the three-phase reference system (a,b,c) to the reference system (d,q,o) is carried out through the following transformation matrix:

$$[T] = \frac{2}{3}\begin{bmatrix} \cos p\theta_r & \cos(p\theta_r - \frac{2}{3}\pi) & \cos(p\theta_r - \frac{4}{3}\pi) \\ -\sin p\theta_r & -\sin(p\theta_r - \frac{2}{3}\pi) & -\sin(p\theta_r - \frac{4}{3}\pi) \\ \frac{1}{2} & \frac{1}{2} & \frac{1}{2} \end{bmatrix} \tag{4.14}$$

It is also possible to define the inverse matrix which allows the transformation of the quantities from the coordinate system (d,q,o) to the three-phase coordinate system (a,b,c):

$$[T]^{-1} = \frac{2}{3}\begin{bmatrix} \cos p\theta_r & -\sin p\theta_r & 1 \\ \cos(p\theta_r - \frac{2}{3}\pi) & -\sin(p\theta_r - \frac{2}{3}\pi) & 1 \\ \cos(p\theta_r - \frac{4}{3}\pi) & -\sin(p\theta_r - \frac{4}{3}\pi) & 1 \end{bmatrix} \tag{4.15}$$

The electrical quantities in (d,q,o) reference system are defined with the following relationships:

$$[v_{d,q,o}] = [T][v_{a,b,c}] = \frac{2}{3}\begin{bmatrix} \cos p\theta_r & \cos(p\theta_r - \frac{2}{3}\pi) & \cos(p\theta_r - \frac{4}{3}\pi) \\ -\sin p\theta_r & -\sin(p\theta_r - \frac{2}{3}\pi) & -\sin(p\theta_r - \frac{4}{3}\pi) \\ \frac{1}{2} & \frac{1}{2} & \frac{1}{2} \end{bmatrix}\begin{bmatrix} v_a \\ v_b \\ v_c \end{bmatrix} \tag{4.16}$$

$$\left[i_{d,q,o}\right] = [T]\left[i_{a,b,c}\right] = \frac{2}{3}\begin{bmatrix} \cos p\theta_r & \cos(p\theta_r - \frac{2}{3}\pi) & \cos(p\theta_r - \frac{4}{3}\pi) \\ -\sin p\theta_r & -\sin(p\theta_r - \frac{2}{3}\pi) & -\sin(p\theta_r - \frac{4}{3}\pi) \\ \frac{1}{2} & \frac{1}{2} & \frac{1}{2} \end{bmatrix}\begin{bmatrix} i_a \\ i_b \\ i_c \end{bmatrix} \quad (4.17)$$

$$\left[\lambda_{d,q,o}\right] = [T]\left[\psi_{a,b,c}\right] = \frac{2}{3}\begin{bmatrix} \cos p\theta_r & \cos(p\theta_r - \frac{2}{3}\pi) & \cos(p\theta_r - \frac{4}{3}\pi) \\ -\sin p\theta_r & -\sin(p\theta_r - \frac{2}{3}\pi) & -\sin(p\theta_r - \frac{4}{3}\pi) \\ \frac{1}{2} & \frac{1}{2} & \frac{1}{2} \end{bmatrix}\begin{bmatrix} \lambda_a \\ \lambda_b \\ \lambda_c \end{bmatrix} \quad (4.18)$$

Applying the aforementioned transformation of coordinates to the IPMSM mathematical model, the flux equation is:

$$\left[\lambda_{d,q,o}\right] = [T]\left[\lambda_{a,b,c}\right] = [T][L]\left[i_{a,b,c}\right] + [T]\left[\lambda_{a,b,c}\right] =$$

$$= [T][L][T]^{-1}\left[i_{d,q,o}\right] + [T][T]^{-1}\left[\lambda_{d,q,o}\right] = \begin{bmatrix} L_d & 0 & 0 \\ 0 & L_q & 0 \\ 0 & 0 & L_o \end{bmatrix}\begin{bmatrix} i_d \\ i_q \\ i_o \end{bmatrix} + \begin{bmatrix} \lambda_{PM} \\ 0 \\ 0 \end{bmatrix} \quad (4.19)$$

Where each inductance component is:

$$L_d = L_s + M_s + \frac{3}{2}L_m \quad (4.20)$$

$$L_q = L_s + M_s - \frac{3}{2}L_m \quad (4.21)$$

$$L_o = L_s - 2M_s \quad (4.22)$$

$$L_s = L_{\sigma s} + L_{ms0} \quad (4.23)$$

The voltage balance equations results:

$$\left[v_{d,q,o}\right] = [T]\left[v_{a,b,c}\right] = [T][R]\left[i_{a,b,c}\right] + [T]\frac{d\left[\lambda_{a,b,c}\right]}{dt} =$$

$$= [T][R][T]^{-1}\left[i_{d,q,o}\right] + [T]\frac{d([T]^{-1}\left[\lambda_{d,q,o}\right])}{dt} =$$

$$= \begin{bmatrix} R & 0 & 0 \\ 0 & R & 0 \\ 0 & 0 & R \end{bmatrix}\begin{bmatrix} i_d \\ i_q \\ i_o \end{bmatrix} + [T][T]^{-1}\frac{d\begin{bmatrix} \lambda_d \\ \lambda_q \\ \lambda_o \end{bmatrix}}{dt} + [T]\omega_r\frac{d\left[[T]^{-1}\right]}{d\theta}\begin{bmatrix} \lambda_d \\ \lambda_q \\ \lambda_o \end{bmatrix} = \quad (4.24)$$

$$= \begin{bmatrix} R & 0 & 0 \\ 0 & R & 0 \\ 0 & 0 & R \end{bmatrix}\begin{bmatrix} i_d \\ i_q \\ i_o \end{bmatrix} + \frac{d\begin{bmatrix} \lambda_d \\ \lambda_q \\ \lambda_o \end{bmatrix}}{dt} + p\omega_r\begin{bmatrix} -\lambda_q \\ \lambda_d \\ 0 \end{bmatrix}$$

Replacing equation (1.19) in equation (1.24), the voltage equation became:

$$\begin{bmatrix} v_d \\ v_q \\ v_o \end{bmatrix} = \begin{bmatrix} R & 0 & 0 \\ 0 & R & 0 \\ 0 & 0 & R \end{bmatrix} \begin{bmatrix} i_d \\ i_q \\ i_o \end{bmatrix} + \begin{bmatrix} L_d & 0 & 0 \\ 0 & L_q & 0 \\ 0 & 0 & L_o \end{bmatrix} \frac{d \begin{bmatrix} i_d \\ i_q \\ i_o \end{bmatrix}}{dt} + p\omega_r \begin{bmatrix} -L_q i_q \\ L_d i_d + \lambda_{PM} \\ 0 \end{bmatrix} \tag{4.25}$$

The balance of powers in the (*d*,*q*,*o*) coordinate system is given by the following expression:

$$P_i = \left[i_{a,b,c}\right]^T \left[v_{a,b,c}\right] = \left[i_{d,q,o}\right] ([T]^{-1})^T [T]^{-1} \left[v_{d,q,o}\right] = \frac{3}{2}(v_d i_d + v_q i_q + v_o i_o) \tag{4.26}$$

Developing this equation it is possible to obtain:

$$\begin{aligned} P_i &= \left[i_{a,b,c}\right]^T \left[v_{a,b,c}\right] = \left[i_{d,q,o}\right] ([T]^{-1})^T [T]^{-1} \left[v_{d,q,o}\right] = \\ &= \left[i_{d,q,o}\right] ([T]^{-1})^T [T]^{-1} \left\{ [R]\left[i_{d,q,o}\right] + \left[L_{d,q,o}\right] \frac{d}{dt}\left[i_{d,q,o}\right] + p\omega_r \begin{bmatrix} -\lambda_q \\ \lambda_d \\ 0 \end{bmatrix} \right\} = \\ &= \left[i_{d,q,o}\right] ([T]^{-1})^T [T]^{-1} [R] \left[i_{d,q,o}\right] + \left[i_{d,q,o}\right] ([T]^{-1})^T [T]^{-1} \left[L_{d,q,o}\right] \frac{d}{dt}\left[i_{d,q,o}\right] \\ &+ \left[i_{d,q,o}\right] ([T]^{-1})^T [T]^{-1} p\omega_r \begin{bmatrix} -\lambda_q \\ \lambda_d \\ 0 \end{bmatrix} \end{aligned} \tag{4.27}$$

Where the first term represents the joule losses in the stator windings P_{cu}, the second term represents variation in the time unit of the energy stored in the magnetic field produced by the armature ampere-turns (P_{mf}) and the last term represents the output electromechanical power P_m. The electromechanical power P_m is equal to:

$$\begin{aligned} P_m &= \left[i_{d,q,o}\right] ([T]^{-1})^T [T]^{-1} p\omega_r \begin{bmatrix} -\lambda_q \\ \lambda_d \\ 0 \end{bmatrix} = \frac{3}{2} p\omega \left[\lambda_d i_q - \lambda_q i_d\right] = \\ &= \frac{3}{2} p\omega_r \left[\lambda_{PM} i_q + \left(L_d - L_q\right) i_d i_q\right] \end{aligned} \tag{4.28}$$

From this equation, it is possible to obtain the expression of electromechanical torque:

$$T_{em} = \frac{3}{2} p\left[\lambda_d i_q - \lambda_q i_d\right] = \frac{3}{2} p\left[\lambda_{PM} i_q + \left(L_d - L_q\right) i_d i_q\right] \tag{4.29}$$

The expression of electromechanical torque is composed of two components, where the first, named fundamental torque, is a function of the flux linkage produced by permanent magnets and of *q*-axis current and the second term, named reluctance torque, is a function of both *d*-*q*-axis currents and the saliency of the machine. Below, all the

equations of the IPMSM conventional dynamic and mathematical model, including the mechanical balance equation, are reported:

$$v_d = Ri_d + L_d \frac{di_d}{dt} - p\omega_r L_q i_q \tag{4.30}$$

$$v_q = Ri_q + L_q \frac{di_q}{dt} + p\omega_r L_d i_d + p\omega_r \lambda_{PM} \tag{4.31}$$

$$T_{em} = \frac{3}{2} p\left[\lambda_{PM} i_q + \left(L_d - L_q\right) i_d i_q\right] \tag{4.32}$$

$$T_{em} = T_r + F\omega_r + J\frac{d\omega}{dt} \tag{4.33}$$

$$\frac{d}{dt}\theta_r = \omega_r \tag{4.34}$$

The circuital model of the conventional IPMSM mathematical model is reported in Fig. 5. In particular, Fig. 5 (a) represent the electromagnetic phenomena that occur in the *d*-axis circuit, while Fig. 5 (b) represent the electromagnetic phenomena that occur in the *q*-axis circuit.

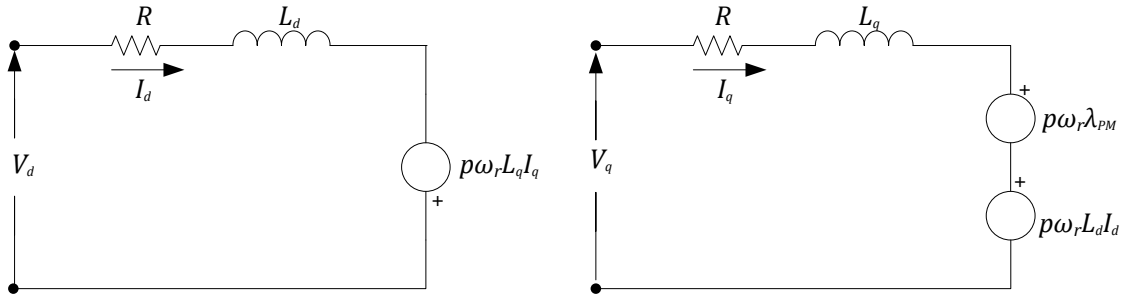

Fig. 5 Circuital model derived from conventional IPMSM mathematical model

1.3.3 IPMSM mathematical model that takes into account iron loss

The previous IPMSM dynamic and mathematical model has been defined without taking into account the iron loss. The power losses in an IPMSM are composed by the sum of joule power losses, iron power loss (hysteresis and eddy currents power losses), mechanical power losses and additional power losses. For control purposes, the power losses can be divided into controllable losses and uncontrollable losses. The joule power losses produced by the fundamental harmonic current component and the iron power loss produced by the fundamental harmonic flux component are part of controllable losses. The mechanical power losses, the additional power losses, the joule power losses produced by the other harmonic current components and the iron power loss produced

by the other harmonic flux components are part of uncontrollable power losses. On the base of the sinusoidal spatial distribution of the magneto-motive force in the air gap and linear magnetic behaviour of the machine, it is possible to define an IPMSM mathematical model that takes into account the iron power loss. In detail, it is possible to define a resistance R_c and a current i_c such that the product $R_c i_c^2$ returns the iron power losses. Employing the Park theory, it is possible to decouple the current i_c in the direct-axis component i_{cd} and in quadrature axis component i_{cq}. Therefore, it is possible to define the following equations that compose the IPMSM mathematical model that take into account the iron loss:

$$v_d = Ri_d + L_{1d}\frac{di_d}{dt} + L_{md}\frac{di_{od}}{dt} - p\omega_r L_q i_{oq} \tag{4.35}$$

$$v_q = Ri_q + L_{1q}\frac{di_q}{dt} + L_{mq}\frac{di_{oq}}{dt} + p\omega_r L_d i_{od} + p\omega_r \lambda_{PM} \tag{4.36}$$

$$T_{em} = T_r + F\omega_r + J\frac{d\omega_r}{dt} \tag{4.37}$$

Where:

$$i_{od} = i_d - i_{cd} \tag{4.38}$$

$$i_{oq} = i_q - i_{cq} \tag{4.39}$$

$$i_{cd} = \frac{-p\omega_r L_{mq} i_{oq} + L_{md}\frac{di_{od}}{dt}}{R_C} \tag{4.40}$$

$$i_{cq} = \frac{p\omega_r(\lambda_{PM} + L_d i_{od}) + L_{mq}\frac{di_{oq}}{dt}}{R_C} \tag{4.41}$$

$$L_d = L_{1d} + L_{md} \tag{4.42}$$

$$L_q = L_{1q} + L_{mq} \tag{4.43}$$

$$T_{em} = \frac{3}{2}p[\lambda_{PM} i_{oq} + (L_{md} - L_{mq}) i_{od} i_{oq}] \tag{4.44}$$

having indicated with:

- i_{cd}, i_{cq} the instantaneous value of dq-axis currents components of i_c current;
- R_c the resistance that allow to take into account the controllable iron power loss;
- L_{1d}, L_{1q} the dq-axis leakage inductances;
- L_{md}, L_{mq} the dq-axis magnetization inductances;
- L_d, L_q the dq-axis inductances;

The IPMSM mathematical model that takes into account the iron loss can be represented with the circuital model shown in Fig. 6.

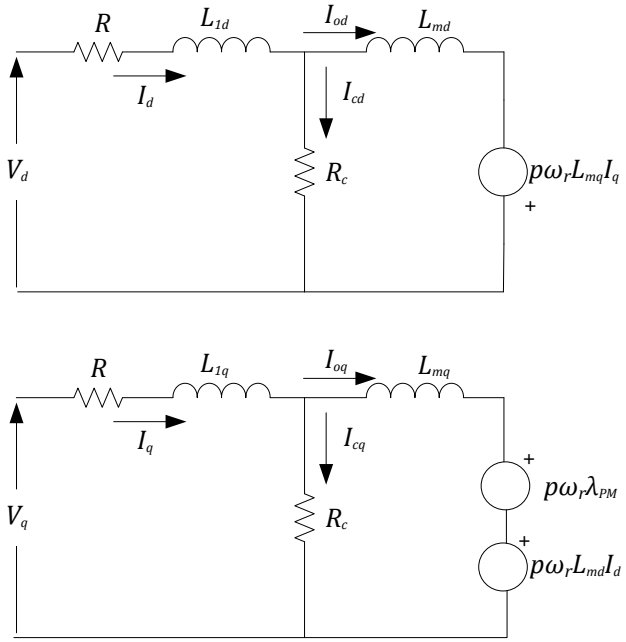

Fig. 6 Equivalent d-axis(a) and q-axis (b) circuital model of the dynamic mathematical model of the IPMMS that takes into account the iron power losses.

Neglecting the leakage inductances, it is possible to obtain a simplified IPMSM dynamic and mathematical model, where L_d=L_{md} and L_q=L_{mq}. In particular, the equations that compose the IPMSM mathematical model are:

$$v_d = Ri_d + L_d \frac{di_{od}}{dt} - p\omega_r L_q i_{oq} \tag{4.45}$$

$$v_q = Ri_q + L_q \frac{di_{oq}}{dt} + p\omega_r L_d i_{od} + p\omega_r \lambda_{PM} \tag{4.46}$$

$$T_{em} = \frac{3}{2} p[\lambda_{PM} i_{oq} + (L_d - L_q) i_{od} i_{oq}] \tag{4.47}$$

$$T_{em} = T_r + F\omega_r + J \frac{d\omega_r}{dt} \tag{4.48}$$

This mathematical model can be also represented with the circuital model shown in Fig. 7:

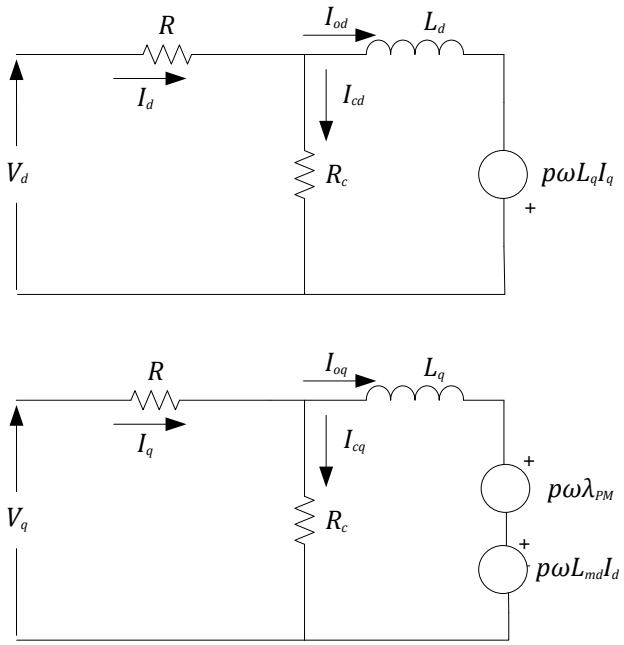

Fig. 7 Simplified d-axis(a) and q-axis (b) equivalent circuital models of the dynamic mathematical model of the IPMMS that takes into account the iron power losses.

On the base of this circuital and mathematical model, it is possible to define the expression of each component of the power losses:

$$P_{cu} = \frac{3}{2} R\left(i_d^2 + i_q^2\right) \tag{4.49}$$

$$P_{fe} = \frac{3}{2} R_c\left(i_{cd}^2 + i_{cq}^2\right) = \frac{3(p\omega_r)^2}{2R_c}\left[\left(L_q i_{oq}\right)^2 + (\lambda_{PM} + L_d i_{od})^2\right] \tag{4.50}$$

$$P_{mech} = K_m \omega_r \tag{4.51}$$

Where K_m is a proportional coefficient for the estimation of mechanical power losses. In details, defining with P_c the controllable losses, with P_L the total power losses, with P_{add} the additional power losses that take into account also the losses produced by the harmonic magnetic and electric quantities, with P_m the output mechanical power and with η the efficiency, it is possible to define the following relationships:

$$P_c = P_{cu} + P_{fe} \tag{4.52}$$

$$P_L = P_c + P_{mech} + P_{add} \tag{4.53}$$

$$P_m = T_{em} \omega_r \tag{4.54}$$

$$\eta = \frac{P_m}{P_{in}} = \frac{P_m}{P_m + P_L} \tag{4.55}$$

1.4 State of art of Loss Minimization Control Algorithms for PMSM

In recent years, the problem of environmental pollution has grown exponentially, arousing the interest of both political administrations and public opinion. In this sense, the levels of environmental pollution are closely linked to the electricity generation and consumption. In particular, the efforts of several national and international european policies have focused on encouraging sustainable development and energy savings, such as greater use of renewable sources and the promotion of electric and hybrid mobility. The industrial world, on the other hand, has undergone great technological development, benefiting from sustainable development and energy-saving policies.

In reference to the industrial electrical drives field, especially for electric and hybrid automotive applications, the economic and technical benefits deriving from an increase in the overall efficiency of the power train system (including the electrical drive) can become decidedly relevant. In particular, in order to increase the autonomy of electric and hybrid vehicle operation, the main critical technical aspect of energy-saving became a fundamental factor.

In this sense, the world research efforts focused on both constructive aspects and aspects concerning control strategies. The latter is of considerable interest, as it can also be applied to existing electric drives that have not been designed with the aim of maximizing system performances. In this way, modifications to the hardware apparatus are not necessary but it is sufficient only to make modifications to the controller so as to apply control strategies for minimizing the power losses of the electric drive.

In recent years, above all due to the growing interest in the development of increasingly efficient hybrid and electric vehicles, the research line of development of control strategies, that aim to maximize the electric drive efficiency, has returned to be widely discussed in the literature [I.1]-[I.12]. In detail, the approach to carry out the control at minimum losses can be classified into two categories named "*Search control*" (SC) and "*Loss model control*" (LMC) or "*Loss model algorithm*" (LMA), respectively.

The SC is an adaptive control strategy that is not based on the knowledge of the mathematical and circuital model of the machine. This approach measures the input power of electric drive and iteratively change step by step the control variables until the power absorbed by the electric drive reaches the minimum for certain load and speed conditions [I.7],[I.13]-[I.14].

The LMC, contrariwise, is based on the accurate knowledge of the mathematical and circuital model of the machine in such a way to define a power losses mathematical model of electric drive, a function of the electric and magnetic machine parameters. Defined the mathematical model of power losses, it is possible to determine the values of the control variables that allow obtaining the minimum of electric drive power losses [I.1]-[I.7], [I.9]. These two approaches will be described with the accurate way in the following paragraphs.

1.4.1 Search control

The Search Control technique, as already mentioned, minimizes losses using the adaptive control techniques by the adjustment, during operation, of one or more control quantities so as to influence the amount of power absorbed by the electric drive, in order to identify, for a given state of operation, a condition for which the absorbed power is minimum.

The operation mode of said control technique at minimum losses consists into imposing on a selected control a variable small step variations and simultaneously measuring the power absorbed by the electric drive. After an appropriate time interval from setting a value to the control variable, such as to allow the system to return to steady-state conditions, the power absorbed by the electric drive is measured and compared with that absorbed in the previous working condition (before of the variation of the control variable). If the value of the newly absorbed power is less than the value measured in the previous working condition, a new step variation of the control variable is imposed and the procedure described above is repeated iteratively until an increase in the absorbed power is found. In the condition immediately prior to the said, if in the meantime no external disturbances have occurred (variations in load, speed, etc.), the electric drive working near the maximum efficiency.

A very important parameter for the minimization procedure optimization, described above, is the width of the step to be imposed on the control variable. It should be considered that the stepwise variation of the control variable inevitably involves stepwise variations of the output electromagnetic torque, which in some cases can also result in an undesired oscillation of the speed. Another problem, related to this type of approach, concerns the time taken by the controller to identify the minimum loss

operating condition. The search by the controllers of the point of maximum efficiency can be "slow" if compared to the times of duration of the external disturbances to which the variable speed electric drives are subjected. It is clear that if the electric drive undergoes frequent variations in the working point, the adjustment action is no longer effective and, therefore, the amount of energy-saving becomes not very significant. Moreover, in variable speed drives used in applications in which there is a frequent shift of the working point on the torque-speed plane and where the steady-state operating condition remains unaltered only for short periods of time, the controller, in addition to not being able to promptly reach the operating condition with minimum losses, can in unfavourable cases trigger oscillation phenomena of electric drive output quantities, making the operation of the electric drive unstable.

The choice of the control variable through which to minimize losses affects the electric drive performances in a decisive way, both in terms of efficiency and in terms of its dynamic performances. In [I.13], the authors choose like control variable the supply voltage. In detail, the authors show good performance at the steady-state condition. However, the search-based LMA presents the disturbance in response. A feedback stabilizer was applied together with the controller to reduce the oscillations in the response. Moreover, the adoption of this control method inevitably involves an appreciable deterioration of the dynamic performance of the electric drive, especially if compared with the performance that could be obtained by controlling the motor in order to maximize the ratio between the torque produced and the current absorbed (Maximum Torque Per Ampere-MTPA). In [I.15], Vaez et. al. defined the power loss as a function of the torque, speed and *d*-axis stator current component i_d. In steady-state conditions assuming that the torque and speed remain constant, it is possible to find the minimum loss by changing the value of i_d. But to define the optimum value of i_d it is necessary to develop an analytical model of i_d from basic equations of the motor. However, the parameters of the motor are not constants, and the current i_d found may not be the optimum value. Thus, the authors developed an adaptive loss minimization controller (ALMC), which is basically a search-based LMA for an IPMSM electric drive. However, the dynamic performance of the ALMC based IPMSM is not acceptable and hence, it is only used during steady-state conditions. This algorithm is implemented by comparing samples of speed error ($\delta\omega_r$). If the difference between these samples is less

than the defined minimum value, the steady-state can be assumed. So the SC is turned-on. During the transient period, the value of i_d is kept constant. When the system achieves the steady-state condition the value of i_d increases or decreases in a continuous slope. The SC compares samples of the input power, and when the difference between these samples is lower than a defined minimum value, the minimum power loss is achieved. In [I.16], the authors define the current angle β ($\beta = \tan^{-1}\frac{|i_d|}{i_q}$) as a control variable. In this way, the power loss can be defined as a function of torque, speed, and β. In steady-state conditions with torque and speed constants, if β varies the power loss changes too. The author approximated the power loss function using a polynomial approximation in some operating points obtained experimentally. It was found that there is a β^* in which the absorbed power is minimum. So the author designed a search control algorithm to find the optimal β. Authors used a β controller to achieve the optimum current angle β^* and a speed controller to find the optimum i_d and i_q corresponding to the maximum efficiency of the motor. The power loss of the proposed controller was compared with the $i_d=0$ controller and motor efficiency enhancement is found with the proposed β controller. But the authors did not show the dynamic performance of the electric drive. An example of a control scheme using the SC for determining the optimal value of *d*-axis stator current component is shown in Fig. 8. The adaptive controller establishes, for each iteration cycle, the reference value i_d^*, while the reference value of the component along the quadrature axis of the stator current (i_q^*) is generated by the speed regulator.

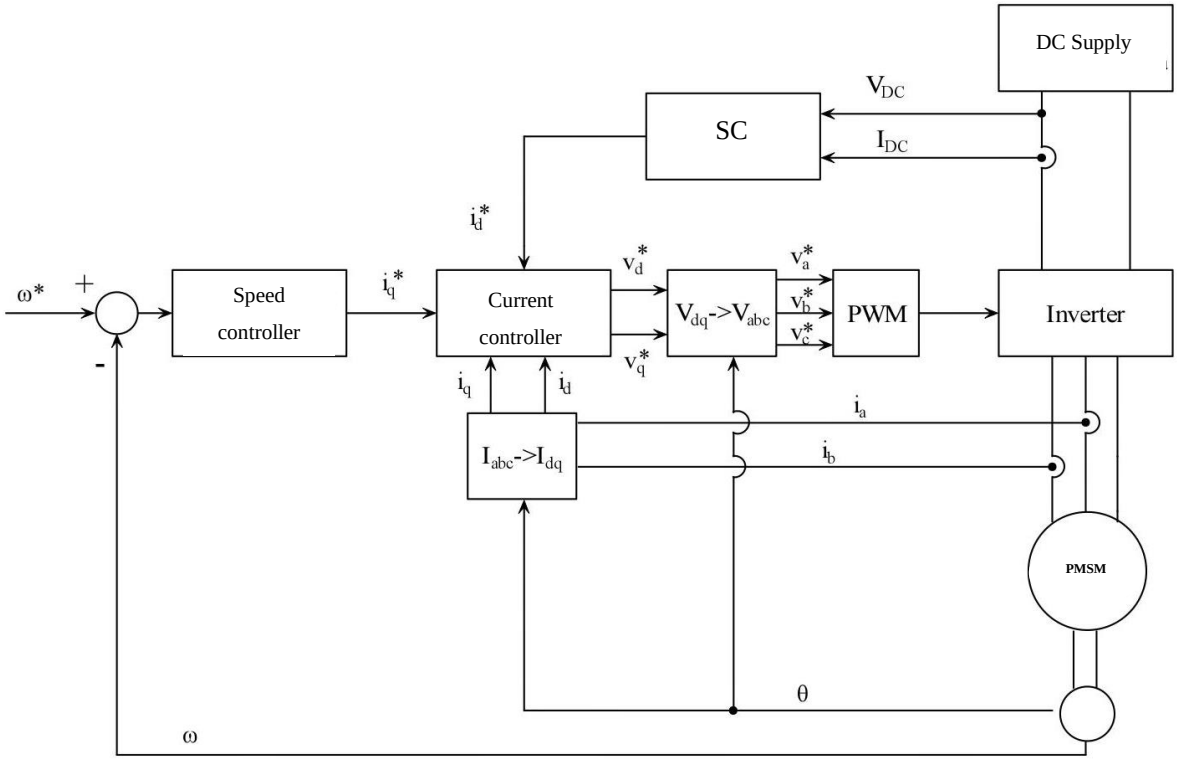

Fig. 8 Control diagram of electric drive controlled with adaptive SC.

Therefore, the main advantages of the SC techniques consist of robust behaviour towards parametric variations because is not necessary the knowledge of the machine mathematical model and the possibility to include the power loss of inverter. Contrariwise, the main disadvantages of the SC techniques consist in torque and speed oscillations caused by the step by step variation of the control variable and of the high convergence time necessary to find the minimum of absorbed power. In addition, when the optimum efficiency is found, the motor becomes very sensitive to load perturbations. This is not acceptable for high-performances drives where good dynamic performance is required.

1.4.2 Loss model control

The Loss Model Control is based on the development of the dynamic mathematical model of the PMSM that takes into account its iron losses. In detail, the LMC uses the power losses mathematical model to calculate the value of control variables corresponding to minimum power loss condition. The control quantity used in the LMC to impose the maximum efficiency is the amplitude of the stator current component

along with the direct axis i_d. The development of the motor mathematical model that takes into account the losses is carried out starting from the mathematical model of the PMSM expressed in the *dqo* reference frame. The advantages of LMC is that the control architecture is very similar to the control architecture of typical Field Oriented Control (FOC) usually employed in electrical drives equipped with PMSMs. The Fig. 9 shows a typical control diagram of electrical drive controlled by LMA and it is possible to deduce that, for all the drives already in use which use the usual digital controllers in *dqo* reference frame, the passage to LMC only involves the modification of some elements of the control software.

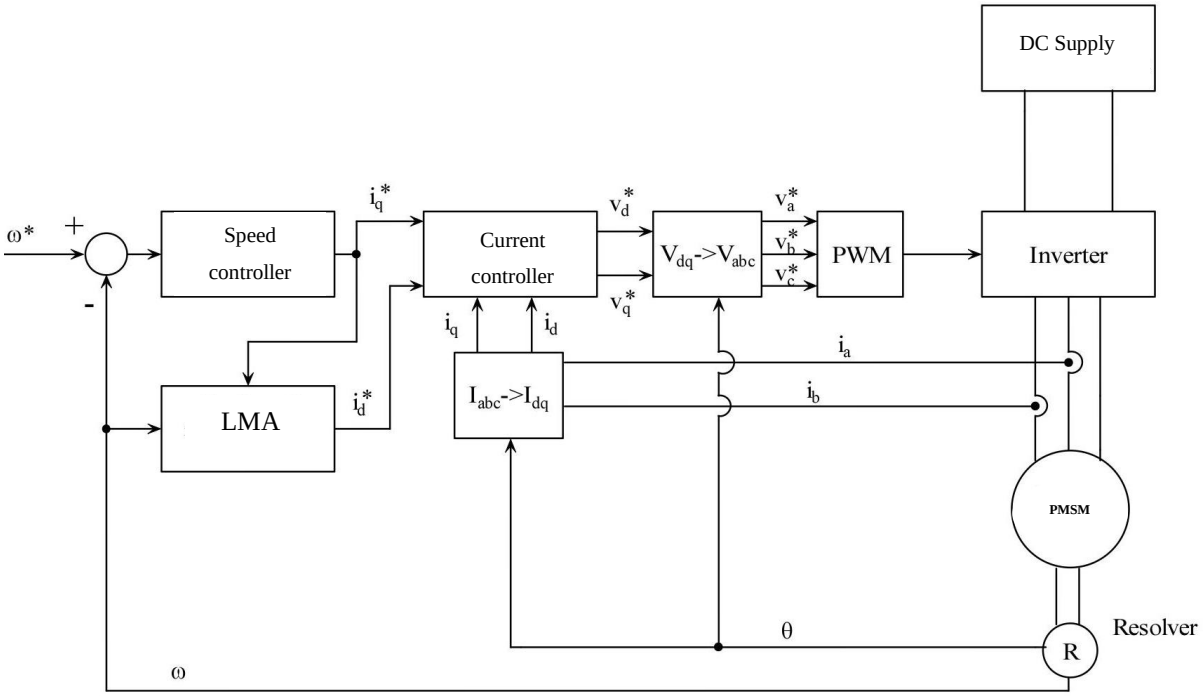

Fig. 9 Control diagram of electrical drive controlled by LMA

In correspondence with a generic set of loading conditions in the speed-torque plane, the speed controller calculates the value of the *q*-axis stator current component i_q. The reference mechanical speed ω^* and *q*-axis stator current component i_q represent the input quantities of LMA, which returns the reference value i_d^* necessary to obtain the minimization of the power losses in a generic working condition. The LMC, in relation to the accuracy of the model that takes into account the losses, allows to obtain more satisfactory results than those obtained with the SC technique. In particular, in LMC the response of the motor is fast and does not have torque ripple. However, the implementation of this model on the controller requires the preliminary measurement of

the electric and magnetic parameters of the machine mathematical model. Therefore, the LMC usually is not robust respect to the parametric variations of the machine forming part of the electric drive.

In recent years, in this sense, the efforts of the scientific community have focused on the possibility of improving this type of approach by taking into consideration the parametric variations of the machine [I.8], [I.17]-[I.20]. In [I.17], the authors design a loss minimizing control law for a fuel cell electric vehicle (FCEV) permanent magnet synchronous motor (PMSM) which reflects the effects of cross magnetic field saturation. In detail, the inductances are modelled as functions of *q*-axis current, based on the flux data obtained experimentally, and the current values, that minimize the losses, are searched from the experimental power loss data which are obtained for several values of *d*-axis current. In [I.18], a global permanent magnet synchronous machine (PMSM) loss minimization control method is proposed based on nonlinear optimization. In this case, in order to take into account the magnetic self-saturation, cross-coupling, and harmonics effects, a look-up table based PMSM flux-linkage model is introduced and the iron loss model is also numerically developed. In [I.19] a nonlinear programming optimization algorithm is implemented for the control of a PMSM to find the optimum current vector references which minimize the total copper and core losses in the entire operating region of the motor, including the field weakening mode. In this case, the loss determination in the equivalent circuit has been further improved by using a variable core loss resistance. It is shown that the efficiency is improved in the entire high-speed operating region of the machine up to 8% respect those obtained with Maximum Torque Per Ampere(MTPA) field oriented vector control method which inherently takes in to account the copper loss only. In [I.12], an online control method of interior permanent magnet synchronous machine (IPMSM) drives for traction applications considering machine parameters and inverter nonlinearities is presented. A model-based correction method using stator flux adjustment is proposed for an online quasi global MTPA achievement. It is proven that in the flux weakening (FW) region, due to the inverter nonlinearities, a lower than expected maximum achievable torque for a demanded speed and a higher than expected current magnitude for a demanded torque may be obtained. Hence, an inverter nonlinearity compensation

(INC) method exploiting the voltage feedback (FB) loop is introduced and its advantages over the conventional INC scheme are demonstrated.

In conclusion, it can be deduced that the control at minimum losses made with the Search Control technique, compared to that performed with the Loss Model Control technique, provides a less effective overall performance. Table 1 shows the main advantages and disadvantages discussed of each control technique.

Table 1 Comparison between SC and LMC

	Advantages	*Disadvantages*
SC	• No loss model necessary; • No dependency on the parameters; • Include the inverter losses (in some cases).	• Slow Convergence • Torque pulsations • Extra sensors for power measurement (in some cases)
LMC	• Fast response; • No torque pulsations; • Possibility of implementation on electric drives in service; • Simple to implement.	• Requires the knowledge of motor and loss mathematical model; • Dependency on the machine parameters.

1.5 Loss model Algorithm (LMA) chosen as a case of study

As widely described above, the LMAs have better overall performance in comparison to those obtained with the SC technique. Therefore, in this work, the LMA described in [I.21] has been taken into consideration and will be widely discussed. This choice was made on this algorithm, as it was studied, developed and tested at the SDESLAB laboratory of the University of Palermo and, therefore, available for possible upgrades and experimental analysis.

Taking into consideration the mathematical model of the machine in steady-state conditions that takes into account the power losses in the iron, the controllable power losses can be expressed as a function of the current components i_{od}, $i_{oq,}$ and the mechanical angular speed ω_r:

$$P_{cu}(i_{od}, i_{oq}, \omega_r) = \frac{3}{2} R \left\{ \left[\left(i_{od} - \frac{p\omega_r L_q i_{oq}}{R_C} \right)^2 + \left(i_{oq} + \frac{p\omega_r (\lambda_{PM} + L_d i_{od})}{R_C} \right)^2 \right] \right\} \quad (4.56)$$

$$P_{fe}(i_{od}, i_{oq}, \omega_r) = \frac{3(p\omega_r)^2}{2R_c} \left[\left(L_q i_{oq} \right)^2 + (\lambda_{PM} + L_d i_{od})^2 \right] \quad (4.57)$$

$$P_c(i_{od}, i_{oq}, \omega_r) = P_{cu}(i_{od}, i_{oq}, \omega_r) + P_{fe}(i_{od}, i_{oq}, \omega_r) \quad (4.58)$$

Combining the expression of controllable losses (1.58) and the expression of the developed electromagnetic torque (1.49), it is possible obtain an expression a relation that expresses the power losses of the motor as a function of the electromagnetic torque T_{em}, of the direct-axis current component i_{od} and of the mechanical angular speed ω_r:

$$P_c(i_{od}, T_{em}, \omega_r) = P_{cu}(i_{od}, T_{em}, \omega_r) + P_{fe}(i_{od}, T_{em}, \omega_r) \quad (1.59)$$

In steady-state conditions, at fixed values both of the electromagnetic torque T_{em} and the mechanical angular speed ω_r, the total controllable losses only depend on the value of current component i_{od}, and then they can be minimized by adjusting the direct-axis current i_d. In order to determine the optimal value of current i_{od}, consequently the value of direct-axis current i_d, it is sufficient to derive the equation (1.59) respect to current i_{od} and set it equal to zero. The condition of minimum power losses is given by:

$$AB = {T_{em}}^2 C \quad (4.59)$$

Where:

$$A = p^2 [R R_c^2 i_{od} + {\omega_r}^2 L_d (R + R_c)(L_d i_{od} + \lambda_{PM})] \quad (4.60)$$

$$B = [\lambda_{PM} + (1 - k) L_d i_{od}]^3 \quad (4.61)$$

$$C = [R R_c^2 + (R + R_c)(\omega k L_d)^2](1 - k) L_d \quad (4.62)$$

k represents the saliency ratio ($k=L_q/L_d$). For PMSM with isotropic rotor structure (SPMSM), the saliency ratio $k=1$ and the above relationships become easier to treat. However, for PMSM without isotropic rotor structure, it is no easy the determination of the optimal value of current component i_{od} because the relationships (1.60-1.62) present nonlinear nature. In literature, there are proposed several approaches to solve this problem. In this case, the LMA use an interval-reduction algorithm that results useful and robust for all those functions that feature in the search interval only a local minimum. The flowchart of this approach is reported in Fig. 10.

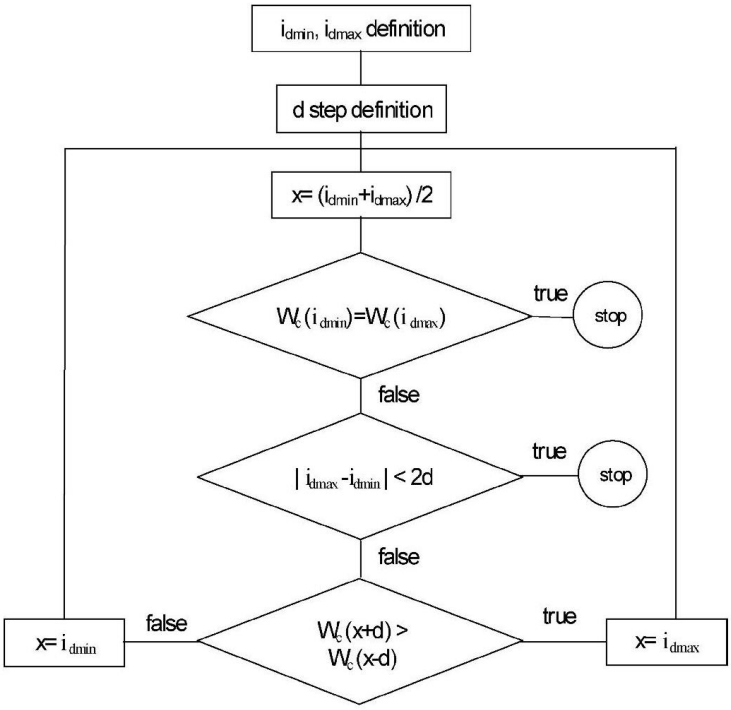

Fig. 10 Flowchart of the LMA.

It can be seen how this approach is substantially a "binary search" algorithm. The input quantities of LMA are the minimum value (i_{dmin}) and the maximum value (i_{dmax}) of the direct-axis current search interval i_d and the search step amplitude d. By fixing the input quantities, the midpoint x is calculated. After, if $P_c(x-d)>P_c(x+d)$ ($W_c(x-d)>W_c(x+d)$) then $x=i_{dmax}$, contrariwise $x=i_{dmin}$. This calculation is iterated until $|i_{dmax} - i_{dmin}| < 2d$ giving the value of direct-axis current i_d which minimizes the power consumption of the electrical drive. In [I.21] is shown that this approach requires a very low number of iterations. However, it must be affirmed that the accurate identification of the minimum losses operation point is a function of the accuracy of the loss model used. The latter

depends on the electrical and magnetic parameters of the mathematical model that are not constant but that are function of machine working conditions. Therefore, in the next chapter, will be analyzed the performance of the conventional power loss model, which use constant parameter values for all working conditions, and loss model that takes into account the nonlinear magnetic behaviour of the machine.

References

[I.1]. S. A. Odhano, R. Bojoi, M. Popescu and A. Tenconi, "Parameter identification and self-commissioning of AC permanent magnet machines - A review," 2015 IEEE Workshop on Electrical Machines Design, Control and Diagnosis (WEMDCD), Torino, 2015, pp. 195-203.

[I.2]. J. Liu and W. Chen, "Generalized DQ model of the permanent magnet synchronous motor based on extended park transformation," 2013 1st International Future Energy Electronics Conference (IFEEC), Tainan, 2013, pp. 885-890.

[I.3]. S. L. Kellner and B. Piepenbreier, "General PMSM d,q-model using optimized interpolated absolute and differential inductance surfaces," 2011 IEEE International Electric Machines & Drives Conference (IEMDC), Niagara Falls, ON, 2011, pp. 212-217.

[I.4]. M. N. Uddin, M. M. Rahman, B. Patel and B. Venkatesh, "Performance of a Loss Model Based Nonlinear Controller for IPMSM Drive Incorporating Parameter Uncertainties," in IEEE Transactions on Power Electronics, vol. 34, no. 6, pp. 5684-5696, June 2019.

[I.5]. N. Bianchi and S. Bolognani, "Magnetic models of saturated interior permanent magnet motors based on finite element analysis," Conference Record of 1998 IEEE Industry Applications Conference. Thirty-Third IAS Annual Meeting (Cat. No.98CH36242), St. Louis, MO, USA, 1998, pp. 27-34 vol.1.

[I.6]. A. M. Bazzi and P. T. Krein, "Review of Methods for Real-Time Loss Minimization in Induction Machines," in *IEEE Transactions on Industry Applications*, vol. 46, no. 6, pp. 2319-2328, Nov.-Dec. 2010.

[I.7]. F. C. F. Azevedo and M. N. Uddin, "Recent advances in loss minimization algorithms for IPMSM drives," *2014 IEEE Industry Application Society Annual Meeting*, Vancouver, BC, 2014, pp. 1-9.

[I.8]. K. D. Hoang and H. K. A. Aorith, "Online Control of IPMSM Drives for Traction Applications Considering Machine Parameter and Inverter Nonlinearities," in *IEEE Transactions on Transportation Electrification*, vol. 1, no. 4, pp. 312-325, Dec. 2015.

[I.9]. T. Jerčic, D. Žarko, J. Matuško and M. Martinovic, "Minimum loss control of interior permanent magnet traction motor," *2015 IEEE International Electric Machines & Drives Conference (IEMDC)*, Coeur d'Alene, ID, 2015, pp. 992-998.

[I.10]. B. Gallert, G. Choi, K. Lee, X. Jing and Y. Son, "Maximum efficiency control strategy of PM traction machine drives in GM hybrid and electric vehicles," *2017 IEEE Energy Conversion Congress and Exposition (ECCE)*, Cincinnati, OH, 2017, pp. 566-571.

[I.11]. M. Bonislawski and R. Palka, "Efficiency optimal control system of hybrid excited machines," *2016 21st International Conference on Methods and Models in Automation and Robotics (MMAR)*, Miedzyzdroje, 2016, pp. 163-167.

[I.12]. K. D. Hoang and H. K. A. Aorith, "Online Control of IPMSM Drives for Traction Applications Considering Machine Parameter and Inverter Nonlinearities," in *IEEE Transactions on Transportation Electrification*, vol. 1, no. 4, pp. 312-325, Dec. 2015.

[I.13]. S. Vaez, V. I. John and M. A. Rahman, "Adaptive loss minimization control of inverter-fed IPM motor drives," *PESC97. Record 28th Annual IEEE Power Electronics Specialists Conference. Formerly Power Conditioning Specialists Conference 1970-71. Power Processing and Electronic Specialists Conference 1972*, Saint Louis, MO, USA, 1997, pp. 861-868 vol.2.

[I.14]. E. S. Sergaki, P. S. Georgilakis, A. G. Kladas and G. S. Stavrakakis, "Fuzzy logic based online electromagnetic loss minimization of permanent magnet synchronous motor drives," *2008 18th International Conference on Electrical Machines*, Vilamoura, 2008, pp. 1-7.

[I.15]. S. Vaez, V. I. John and M. A. Rahman, "An on-line loss minimization controller for interior permanent magnet motor drives," *1997 IEEE International Electric Machines and Drives Conference Record*, Milwaukee, WI, USA, 1997, pp. MC3/6.1-MC3/6.3.

[I.16]. M. Cao, "Online Loss Minimization Control of IPMSM for Electric Scooters," *The 2010 International Power Electronics Conference - ECCE ASIA -*, Sapporo, 2010, pp. 1388-1392.

[I.17]. J. Lee, K. Nam, S. Choi and S. Kwon, "A Lookup Table Based Loss Minimizing Control for FCEV Permanent Magnet Synchronous Motors," *2007 IEEE Vehicle Power and Propulsion Conference*, Arlington, TX, 2007, pp. 175-179.

[I.18]. H. Ge, B. Bilgin and A. Emadi, "Global loss minimization control of PMSM considering cross-coupling and saturation," *2015 IEEE Energy Conversion Congress and Exposition (ECCE)*, Montreal, QC, 2015, pp. 6139-6144.

[I.19]. A. Rabiei, T. Thiringer and J. Lindberg, "Maximizing the energy efficiency of a PMSM for vehicular applications using an iron loss accounting optimization based on nonlinear programming," *2012 XXth International Conference on Electrical Machines*, Marseille, 2012, pp. 1001-1007.

[I.20]. Z. Li and H. Li, "MTPA control of PMSM system considering saturation and cross-coupling," *2012 15th International Conference on Electrical Machines and Systems (ICEMS)*, Sapporo, 2012, pp. 1-5.

[I.21]. C. Cavallaro, A. O. Di Tommaso, R. Miceli, A. Raciti, G. R. Galluzzo and M. Trapanese, "Efficiency enhancement of permanent-magnet synchronous motor drives by online loss minimization approaches," in *IEEE Transactions on Industrial Electronics*, vol. 52, no. 4, pp. 1153-1160, Aug. 2005.

Chapter 2 Performances analysis of the power loss mathematical models

2.1 Introduction

The performances of loss model control is strictly dependent on the accuracy of the mathematical model of IPMSM. Therefore, in order to evaluate the overall performances of the control algorithm, it is necessary to study the performance of the power loss mathematical model described in the previous chapter. In this sense, two power loss models have been taken into account. The first is derived by IPMSM conventional mathematical model that takes into account the iron losses, where the model parameters are constant. This power loss model doesn't take into account the non-linear magnetic behaviour of the machine and the variability of the iron losses with the supply frequency of the machine. The second power loss model takes into account the self and cross saturation effects and the variation of iron loss with the variation of the supply frequency of the machine. For this purpose, several experimental investigations have been conducted on a prototype of IPMSM. This chapter describes the electric drive under test, the experimental investigations conducted for the characterization of the IPMSM prototype, and the study of the performances of the loss models conducted in the Matlab environment.

2.2 IPMSM electric drive under test

The IPMSM electric drive under test is composed of:

- a three-phase, six-pole brushless machine (Magnetic S.r.l., type BLQ-40 Fig. 11(a)), with SmCo permanent magnets (HITACHI Inc., type H- 18B, with maximum specific energy equal to 143 kJ/m3) radially mounted with tangential magnetization (Fig. 11 (b)). The stator winding is a three-phase, double-layer, shortened pitch, located into 27 slots. In Table 2 and Table 3 are reported the main rated values and the geometrical data of the IPMSM under test, respectively;
- a DPS 30 A power converter (Automotion Inc.), equipped with two LEM current sensors (Fig. 12). The converter has a rectifier and an inversion stage and is powered directly by the electrical grid. The main features are reported in Table 4.

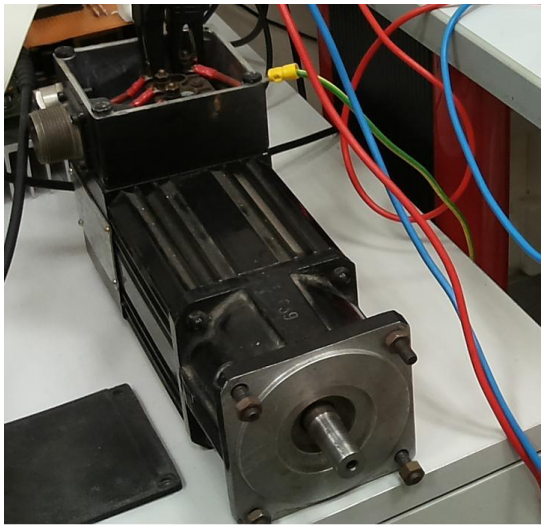

(a)

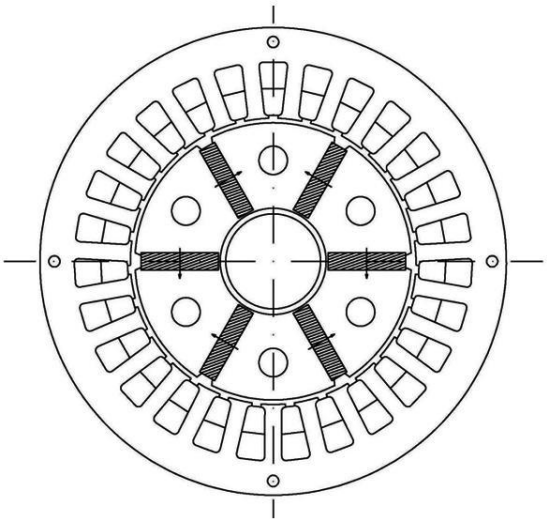

(b)

Fig. 11 IPMSM under test (a) and its cross-section (b).

Table 2 Rated values of the IPMSM under test.

Quantity	***Value***
Voltage [V]	132
Current [A]	3.6
Speed [rpm]	4000
Torque [Nm]	1.8
Pole pairs	3

Table 3 Geometrical data of the IPMSM

Geometrical data	***Value***
External stator diameter [mm]	81
Inner stator diameter [mm]	49.6
External rotor diameter [mm]	48
Inner rotor diameter [mm]	18.46
Axial rotor length [mm]	59
PMs width [mm]	13.45
PMs thickness [mm]	3
Airgap [mm]	0.8
Slot depth [mm]	9.2

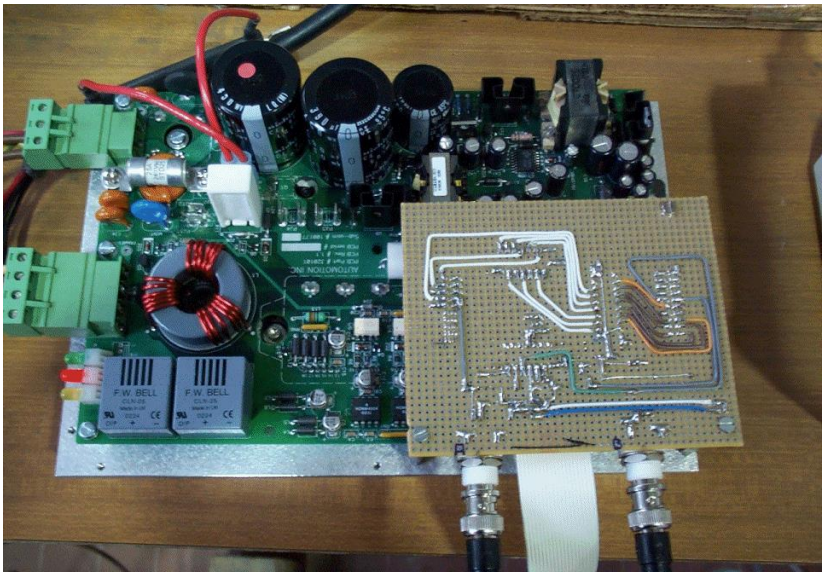

Fig. 12 DSP 30 A power converter

Table 4 Main features of the power converter.

Model	DSP 30
Input rated voltage	230 V
Peak value of maximum output current	30 A
Nominal power	6.5 kW
DC link voltage	310 V
PWM modulation frequency	5÷20 kHz

- a dSPACE® rapid prototyping control board, in order to drive the IGBT bridge of the converter;
- a PC with the dSPACE®-based electrical drive user interface, which allows performing the real-time control and the supervision of the main electrical and mechanical quantities of the electric drive;
- an HD-715-8NA hysteresis brake (Magtrol Inc.), which allows performing experimental tests with different load conditions;
- a DSP6001 high-speed programmable dynamometer controller (Magtrol Inc.), used to drive the brake in real-time (Fig. 13). The dynamometer digital interface provides the mechanical torque, speed and mechanical power values measured at the shaft of the motor. Furthermore, the dynamometer allows sending the measured electrical signals of speed and torque to other acquisition systems. In

Table 5 the main features of hysteresis brake and the measurement accuracy of dynamometer DSP6001 are reported;

- an ARTUS resolver (type 26SM19 U452), which is connected to the motor shaft in order to measure the motor speed.

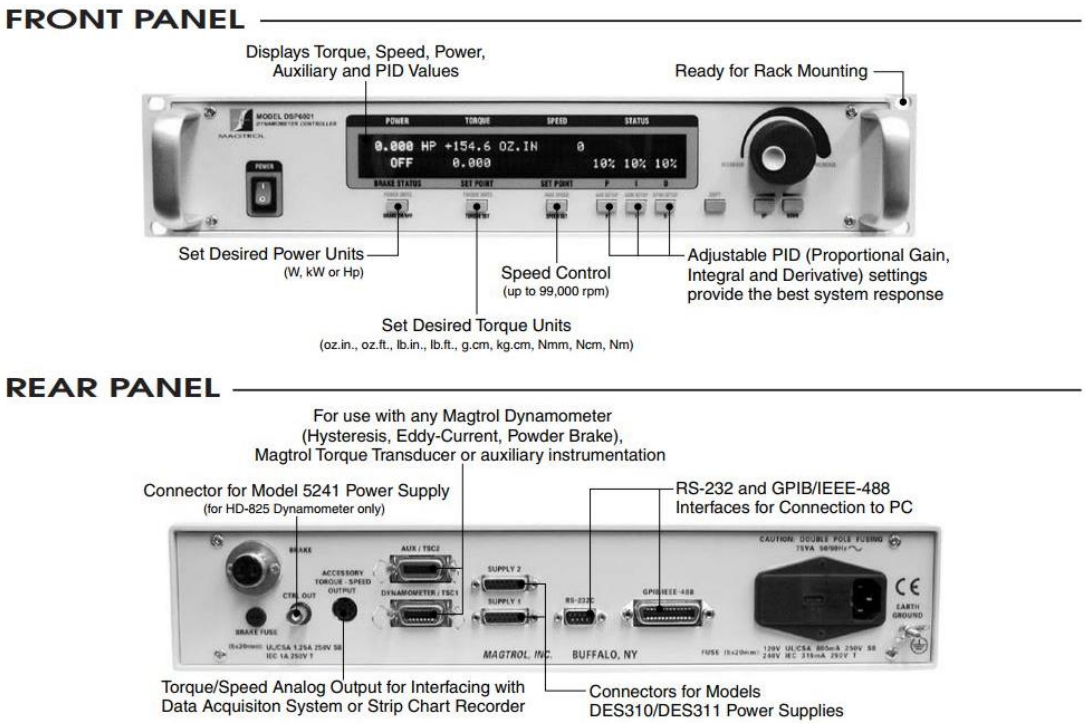

Fig. 13 Front panel and rear panel of dynamometer DSP6001

Table 5 Main features of Magtrol hysteresis brake and dynamometer DSP6001

Hysteresis brake Magtrol model	HD-715-8NA
Maximum torque	6.2 Nm
Maximum speed	25000 rpm
Nominal input inertia	1.449×10^{-3} kgm^2
Accuracy	Speed: 0.01% of reading from 10 rpm to 100,000 rpm TSC1: 0.02% of range (±1 mV) TSC2: 0.02% of range (±2 mV)
Maximum torque input	TSC1: ±5 V DC TSC2: ±10 V DC
Torque/Speed Output	Torque: ±10 V DC Speed: ±10 V DC

In Fig. 14 and Fig. 15 are reported respectively a picture and a schematic representation of the electric drive under test.

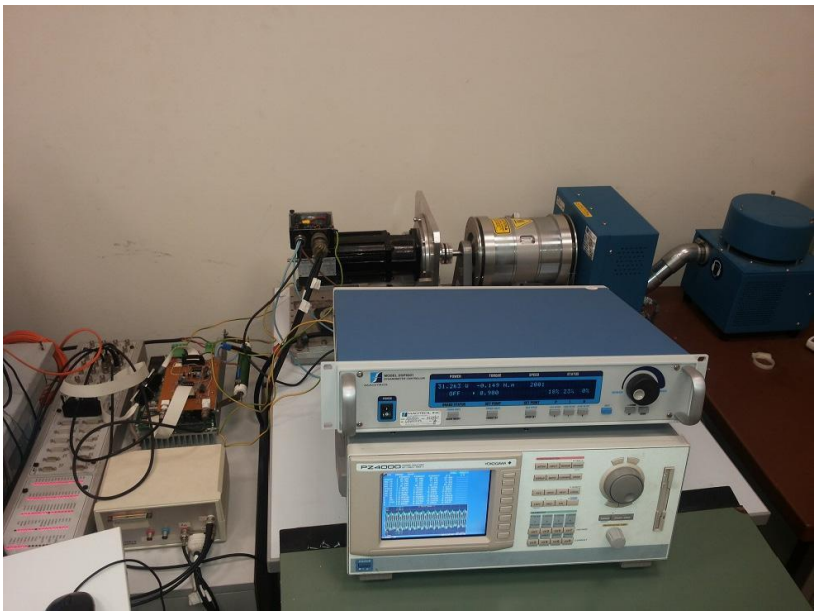

Fig. 14 Electric drive under test

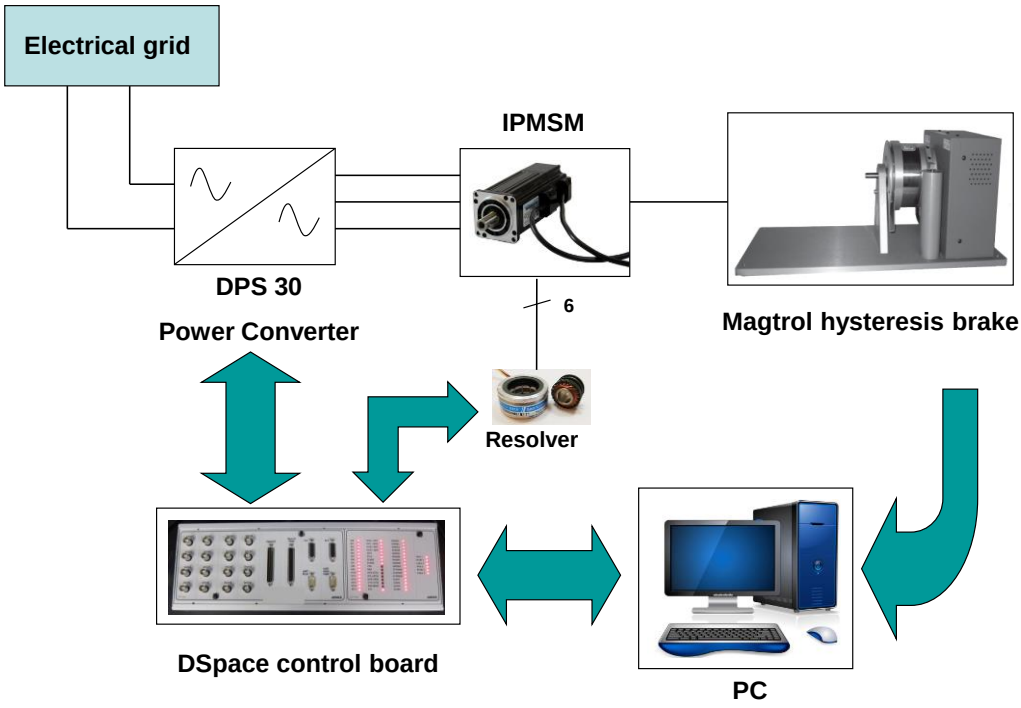

Fig. 15 Schematic representation of the electric drive under test.

A Field Oriented Control strategy (FOC) is implemented in dSPACE® rapid prototyping control board system. The FOC strategy has been used for the speed control of the IPMSM and in Fig. 16 is shown the simplified scheme of the related electrical drive. The reference angular speed ω^* is compared with the output angular speed ω from the

resolver-to-digital converter, determining a feedback control and this error is processed by speed controller block that gives the reference value of *q*-axis current i_q. The level of magnetization of the machine can be controlled by acting on the i_{dref} block. The reference values of the *d*-*q* currents are compared with the real values of *d*-*q* currents obtained by the LEM current sensors. The current controller processes the current error and calculates the reference values of *d*-*q*-axis voltage. These are reported in the three-phase reference frame *abc* through the transformation of coordinates *dq/abc*. The voltage signals are then processed with the PWM control technique and applied to the machine through the DSP 30 converter.

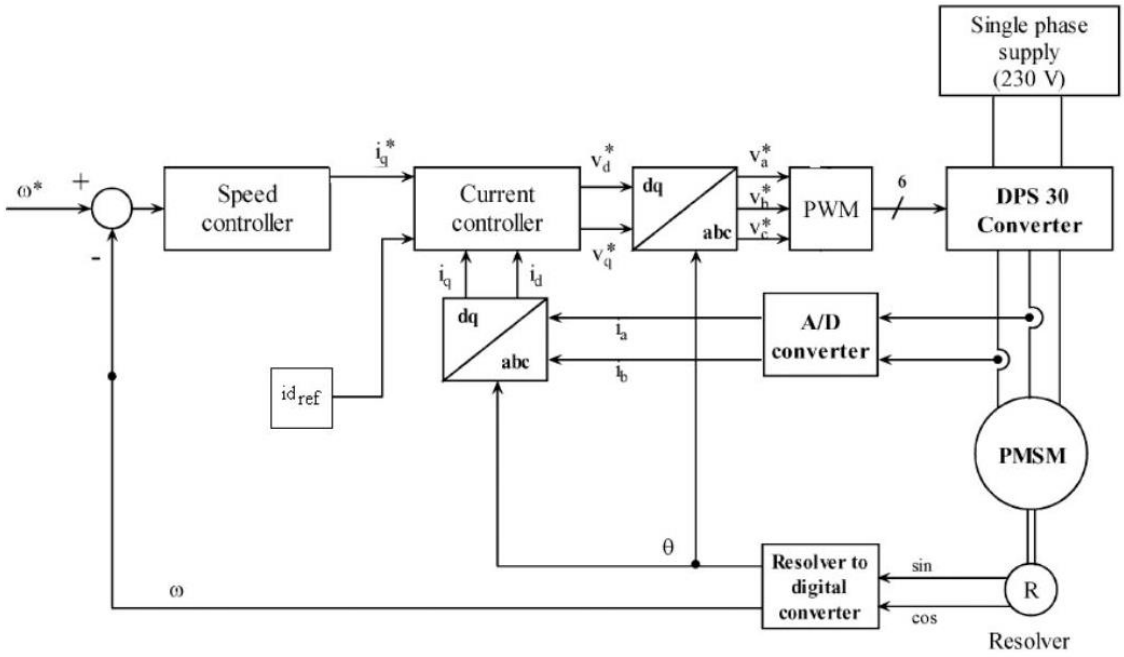

Fig. 16 Field oriented control (FOC) block diagram

2.3 Experimental characterization of IPMSM

For simulations and developing of loss model control algorithm purpose, accurate parameters models is necessary to successfully estimate the electric drive performances. Regarding the topic of estimation of PMSMs parameters, standards procedures are not established. In detail, at present, a draft standard exists for testing and parameter determination of PMSMs: BS IEC/TS 60034-20-2 [II.1]. However, this is brief and inaccurate. The growing interest in PM motors, due to their high power density and high efficiency compared to more conventional drives, has brought about a great contribution of scientific researches to this topic [II.2]-[II.8]. Furthermore, IEEE Power and Energy Society and IEEE Industry Applications Society created an Electric Machines-committee with intent to have a unified and definitive guide for testing PMSMs, encompassing all kinds of machines (all frames, voltages, configurations (surface, inset, and IPM), and power ranges, kilowatts – multi-mega-watts). In this sense, the recent approved IEEE Std 1812 [II.9] describes the instructions for conducting tests to determine the performance characteristics and machine parameters of PMSMs. This IEEE trial guide and other scientific contributions [II.2]-[II.8] have been taken into account for the characterization of the IPMSM prototype. In details, the IPMSM parameters are:

- the resistance of three-phase stator winding R;
- the value of stator flux linkage due to the PMs λ_{PM};
- the value of dq-axes inductance L_d, L_q;
- the value of the core losses resistance R_c.

The tests carried out for the estimation of the aforementioned parameters are described below.

2.3.1 Three-phase stator winding resistance measurement

For the purpose concerning the estimation of the three-phase stator winding resistance, it has been employed a 4-wires measurement. In detail, a digital micro-ohmmeters AOIP model *OM 21* is used. It measures from 0,1 μΩ up to 26 kΩ (OM 21) with an accuracy of 0.03 %. The Fig. 17 shows the measurement scheme used for the described measure.

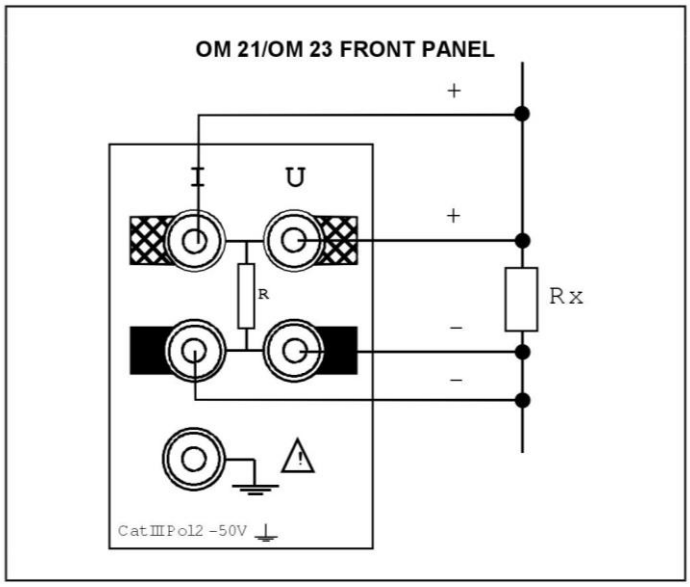

Fig. 17 Measurement scheme of the three-phase stator winding resistance

The measurement was carried out between each phase terminal and the neutral point of the winding being accessible. The measurement was carried out at a temperature of 20°C and for greater accuracy, the measurement was repeated three times for each phase.

In Fig. 18 is reported a picture of the test bench and in Table 6 are reported the winding phase resistance measured. The values obtained indicate the presence of a slight dissymmetry of the winding, but which can be considered negligible. Therefore, the average value between the three-phase resistances equal to 2.32 Ω is assumed as the reference value.

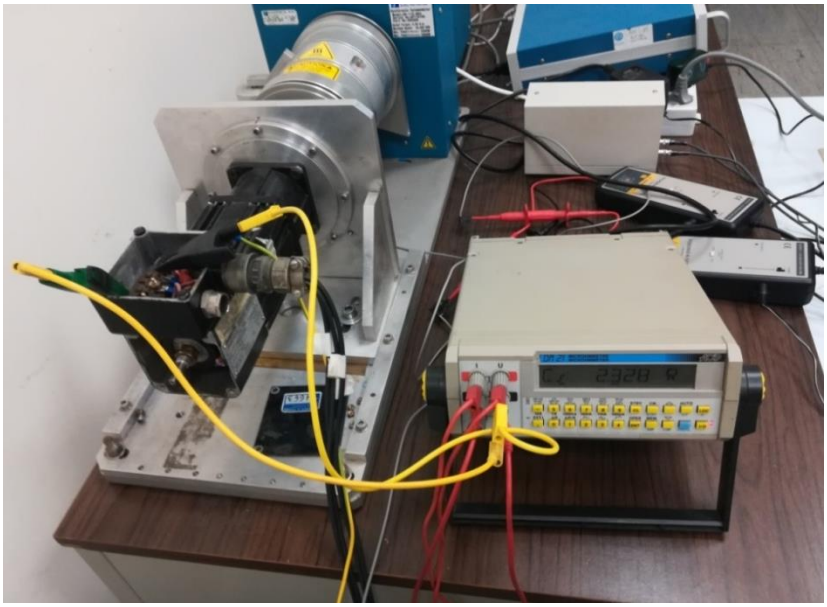

Fig. 18 Test bench for the evaluation of three-phase stator winding resistance

Table 6 Phase resistance values measured

	1st measure	*2st measure*	*3st measure*	*Medium value*
R_a [Ω]	2.300	2.301	2.301	2.300
R_b [Ω]	2.323	2.322	2.322	2.322
R_c [Ω]	2.331	2.330	2.329	2.330

2.3.2 Stator flux linkage due to the PMs measurement

The simplest way to estimate the stator flux linkage due the PMs is to perform an open circuit test with a drive motor used to bring the IPMSM up to the desired test speed and measuring the open-circuit voltage [II.9]. The IPMSM of the electric drive under test it is not coupled with a drive motor. Therefore, it is not possible to perform this test. An alternative way for the estimation of the stator flux linkage due to the PMs is to perform a static test with torque transducer [II.7]-[II.8]. This test is a rotor block test where the winding phases must be properly connected and DC supplied in such a way as to obtain a system capable of being fed respectively along the direct axis and along the quadrature axis. The Fig. 19 (a) and Fig. 19 (b) show respectively the phase winding connection schemes to obtain the alignment of rotor *d*-axis or the PM magnet field and the alignment of rotor *q*-axis with the magnetic axis of phase *a*.

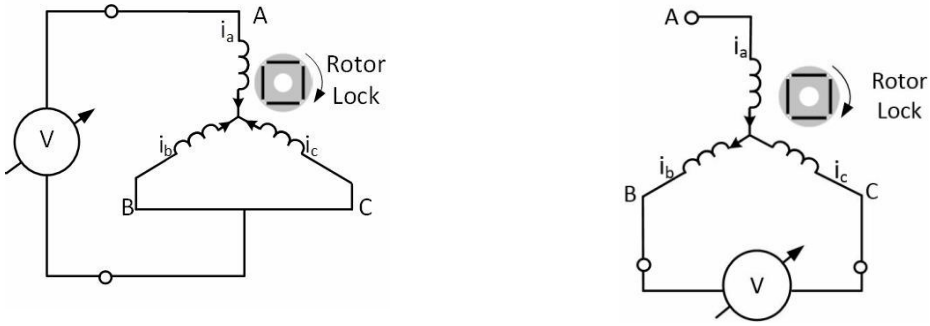

Fig. 19 Positioning of rotor along *d*-axis (a) and *q*-axis (b).

Therefore, the value of stator flux linkage due the PMs λ_{PM} is obtained by holding the rotor in *q*-axis position with the following relationship:

$$\lambda_{PM} = \frac{2T_{em}}{3pi_q} \tag{2.1}$$

The test is simple to carry out, it only requires a DC supply, the measurement of the DC supply current and allows to evaluate the influence of cross-saturation effects on stator

flux linkage due the PMs λ_{PM}. The main drawback consists of torque measurement that is not very accurate. Another solution is to supply the IPMSM by inverter. In this case, it is not necessary to connect the phase winding according to the scheme of Fig. 19 (b). Each electric drive is equipped with inverter and, therefore, it doesn't require additional cost for this test. In this work, both tests were carried out. In details, the stator flux linkage due the PMs λ_{PM} is obtained for positive and negative values of *q*-axis current i_q, where for negatives value of i_q doesn't' mean a generator operation of the IPMSM but only an inversion of the electromagnetic torque and, therefore, of the rotor speed direction. A Fluke A40B-20 A precision shunt resistor and a Teledyne LeCroy WaveRunner 6Zi, oscilloscope have been employed in order to perform the estimation of stator flux linkage due to the PMs with DC power supply (Fig. 20). In Fig. 21 the values of λ_{PM}, obtained by DC power supply with i_q that varies from 0.5 A to 5.5 A with a step equal to 0.5 A, are reported. The two trends of λ_{PM} reported show similar behaviour, but they are slightly different in amplitude. This result can be associated to several factors, but mainly due to the accuracy of the mechanical torque sensor. The average value of stator flux linkage due the PMs λ_{PM} is calculated and it used to evaluate the *rms* value of the induced voltage at nominal speed and compared to the value reported in the nameplate of IPMSM under test (132 V):

$$\lambda_{PM\_average} = 0.086 \text{ Wb} \tag{2.2}$$

$$V_{rms} = \sqrt{\frac{3}{2}}\lambda_{PM\_average} p\omega = \sqrt{\frac{3}{2}} 0.086 \cdot 3 \cdot 4000 \cdot \left(\frac{2\pi}{60}\right) = 132.4 \text{ V} \tag{2.3}$$

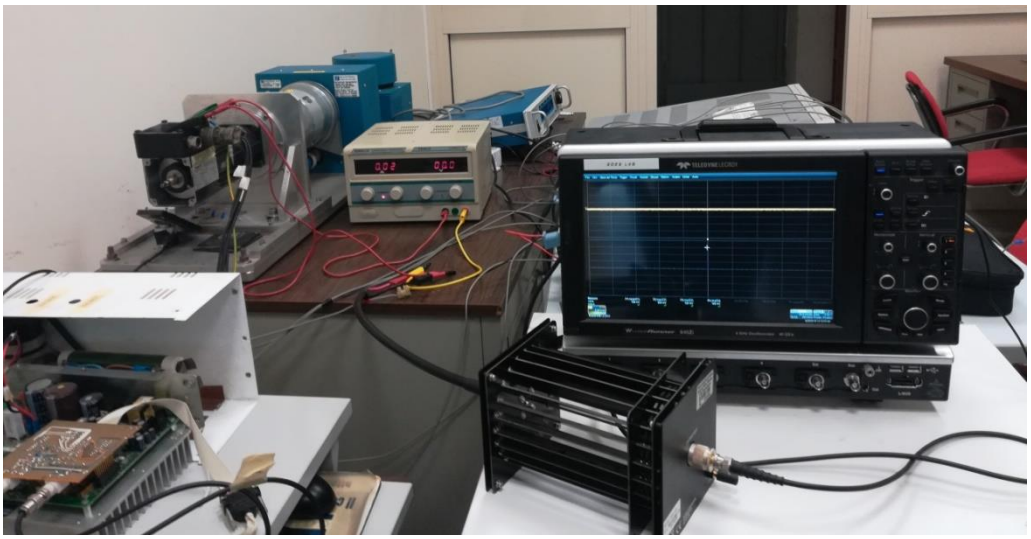

Fig. 20 Test bench for the estimation of stator flux linkage due to the PMs λ_{PM} with DC power supply.

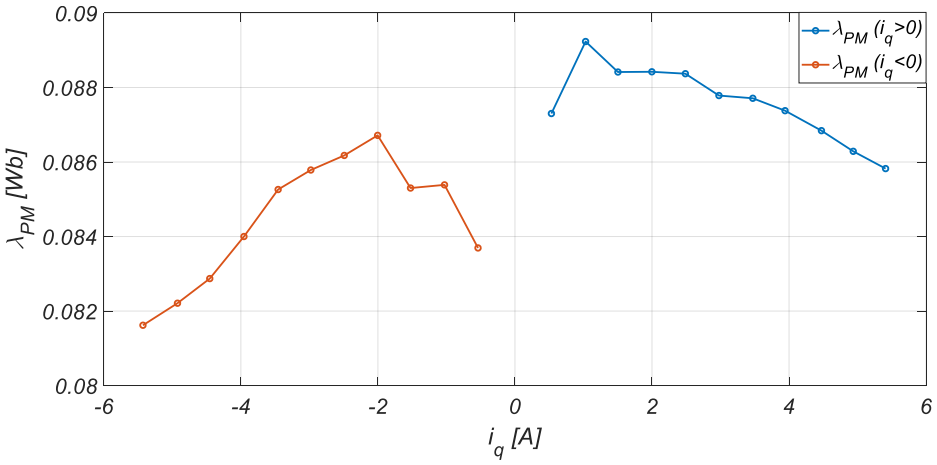

Fig. 21 Stator flux linkage due to the PMs λ_{PM} as a function of *q*-axis current *iq* obtained by DC power supply

In Fig. 22 are reported the values of λ_{PM} obtained by the inverter power supply with i_q that varies from 0.5 A to 6 A with a step equal to 0.5 A. The two trends of λ_{PM} reported show a similar behaviour than those obtain with DC power supply. Also, in this case, there is an amplitude difference between the two trends of stator flux linkage due to the PMs λ_{PM}. This result can be associated to several factors, but mainly due to the accuracy of the mechanical torque sensor. In this sense, the average value of stator flux linkage due the PMs λ_{PM} is calculated and it used to evaluate the *rms* value of the induced voltage at nominal speed and compared to the value reported in the nameplate of IPMSM under test (132 V):

$$\lambda_{PM\_average} = \frac{\sum_{i=1}^{n} \lambda_{PM\_i}}{n} = 0.0842 \text{ Wb} \tag{2.4}$$

$$V_{rms} = \sqrt{\frac{3}{2}} \lambda_{PM\_average} p\omega = \sqrt{\frac{3}{2}} 0.0842 \cdot 3 \cdot 4000 \cdot \left(\frac{2\pi}{60}\right) = 129.6 \text{ V} \tag{2.5}$$

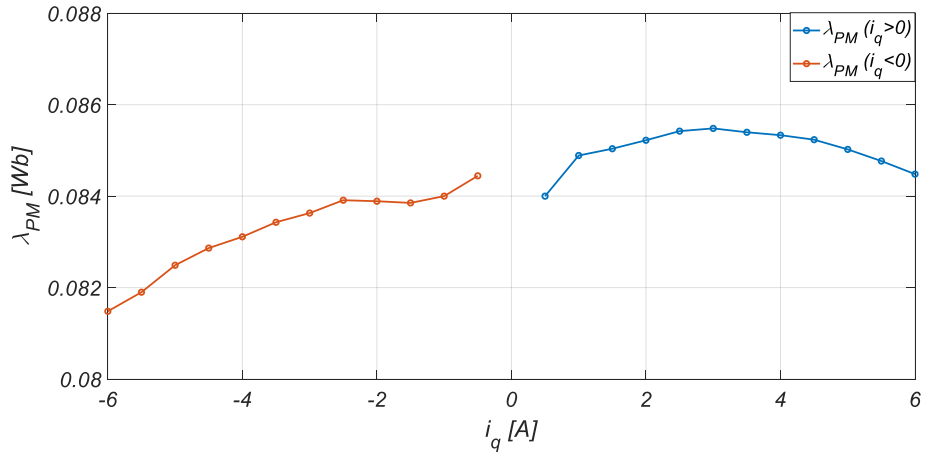

Fig. 22 Stator flux linkage due to the PMs λ_{PM} as a function of *q*-axis current i_q obtained by the inverter power supply.

It is possible to see that the average value $\lambda_{PM\_average}$, in both cases, provides a value of the induced voltage at a nominal speed that is near to the value reported in the nameplate of the machine (132 V). Therefore, this value $\lambda_{PM\_average}$ is taken as a reference for the conventional mathematical model of the IPMSM.

2.3.3 *dq*-axes inductances measurements

The measurement of *dq*-axes inductances is the most critical step in the estimation of parameters of IPMSMs. In the standard IEEE Std 1812, an open circuit test and a short circuit test are employed in order to estimate the back-emf and the synchronous inductance or the *d*-axis inductance. Contrariwise, a method to determine the *q*-axis inductance is not included in the standard. A great number of research studies are available in the literature for the estimation of *dq*-axes inductances. In detail, the measurement approaches can be classified in standstill tests and running tests. The standstill tests of IPMSM consists of rotor block tests, where a variable voltage at constant frequency is applied such that the absorbed current is constant [II.5]-[II.8]. This is the measurement method most employed in industry filed by the manufacturers of PMSMs. Another solution is to perform a rotor block test with a DC supply and measure a DC step response of the machine [II.4], [II.8]. In this case, the *dq*-axes inductances (L_d, L_q) are obtained from the estimation of the time constant of IPMSM. Tests at standstill conditions neglect slot harmonics and core losses, but they are easy to carried out. Simplified measurement requirements are needed and it is not necessary the use of the drive. The running tests present the advantage to take into account the effects of the PWM power supply and estimate the *dq*-axes inductances in various conditions (both no-load than under load conditions) [II.5],[II.10]-[II.12]. Respect to the standstill tests, the running tests requires sophisticated measurement equipment and post-processing requires special care. In this work, AC standstill tests are employed for the estimation of *dq*-axes inductances. In detail, the test procedure requires the alignment of the rotor in *d*-axis and *q*-axis that can be obtained employing the phase winding connection schemes shown in Fig. 19 (a-b). A variable auto-transformer (Variac Inc.), is used as a sinusoidal voltage supply. The voltage applied, the current and power absorbed by the machine are measured through PZ 4000 three-phase power analyzer

(Yokogawa Inc). Starting from the stator winding resistance, the determination of the inductance is simple with the following relationships:

$$Z = \frac{V_{rms}}{I_{rms}} \tag{2.6}$$

$$L_d = \frac{2}{3}\frac{\sqrt{Z^2 - R^2}}{2\pi f} \tag{2.7}$$

$$L_q = \frac{2}{3}\frac{\sqrt{Z^2 - R^2}}{2\pi f} \tag{2.8}$$

In Fig. 23 and in Fig. 24, the direct and quadrature axis inductances, as functions of i_d and i_q respectively, are reported. The *d*-axis inductance L_d appears to increase with the current while the *q*-axis inductance L_q, as the current changes, it initially grows and then decreases due to high current values. The increase in *d*-axis inductance L_d and the decrease of *q*-axis inductance L_q may be attributed to the magnetic self-saturation with increasing current. It is possible to notice that the maximum L_d value is 33% higher than the minimum L_d value and that the maximum L_q value is 12% higher than the minimum L_q value. The average value of *dq*-axes inductances are calculated and they chose as a reference value of *dq*-axes inductances (L_d, L_q):

$$L_{d\_average} \cong 7.5 \text{ mH} \tag{2.9}$$

$$L_{q\_average} \cong 11 \text{ mH} \tag{2.10}$$

Furthermore, it is possible to use variable values of the *dq*-axes inductances as a function of *dq*-axes currents such that to take into account the effects of the magnetic self-saturation.

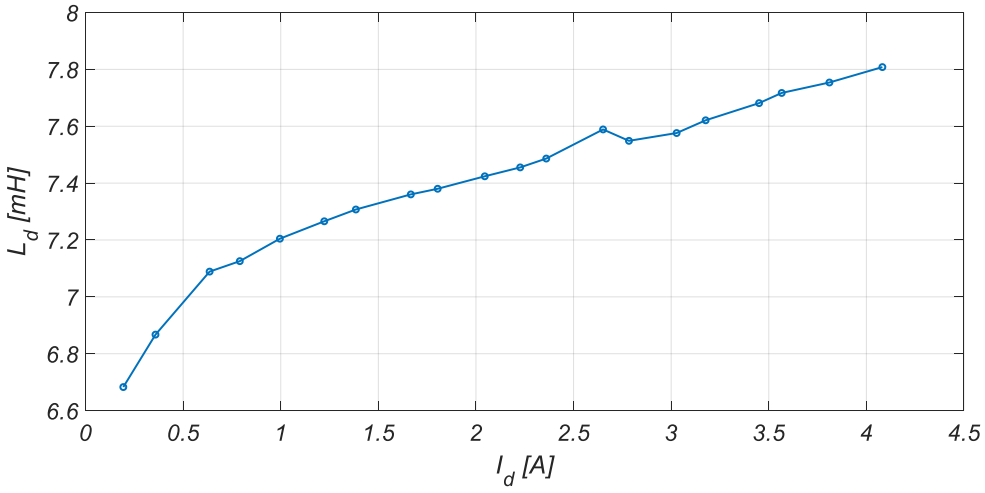

Fig. 23 Direct axis inductance L_d as a function of i_d.

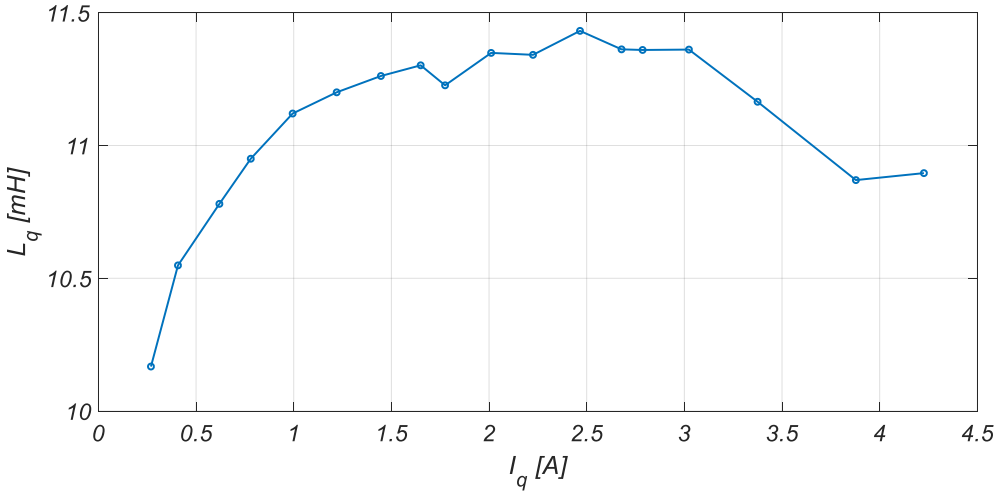

Fig. 24 Quadrature axis inductance L_q as a function of i_q.

2.3.4 No-load test

The goal of the no-load test is the estimation of iron loss at fundamental harmonic and consequently the core loss resistance of conventional mathematical model of IPMSM. The test procedure provides to bring the motor at a fixed value of rotor mechanical speed and to measure the absorbed power and the *rms* values of input voltages and currents. The no-load input power P_{oc} is equal to:

$$P_{oc} = P_{cu} + P_{fe} + P_m \tag{2.11}$$

Where P_{cu}, P_{fe} and P_m are respectively the copper losses, the iron core losses, and mechanical losses. The core losses resistance R_c can be derived from iron core loss with the following relationship:

$$R_c = \frac{V_{rms}^2}{P_{fe}} \tag{2.12}$$

Where V_{rms} is the *rms* value of line to line voltage. In order to bring the motor to the desired value of mechanical speed, the IPMSM is controlled with FOC implemented in the electrical drive described before. This involves the PWM power supply from the inverter which is reflected in a large harmonic content in the supply voltage. For this purpose, a PZ 4000 three-phase power analyzer (Yokogawa Inc), have been used to measure the input electrical quantities (line to line voltage, phase voltage, input currents, absorbed active power). The PZ 4000 three-phase power analyzer is equipped with a digital filtering option that allows performing the measurement eliminating most of the harmonic content. In detail, the minimum filtering frequency is equal to 500 Hz

and it has been chosen for the test. The no-load test can be performed with two measurement schemes, respectively, the typical three phase-four wire system measurement scheme (3P4W) (Fig. 25 (a)) and Aron measurement scheme (Fig. 25 (b)).

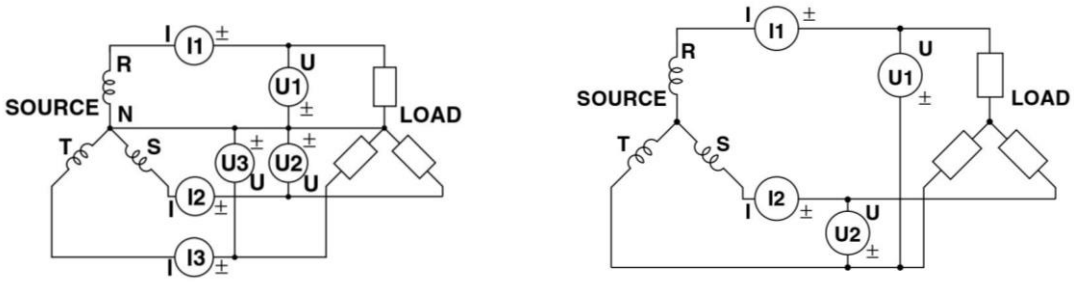

(a) (b)

Fig. 25 3P4W measurement scheme (a) and Aron measurement scheme (b)

In the first case, the phase voltage is acquired, while in the second scheme the line to line voltage is acquired. The phase voltage is affected by the presence of the third harmonic which can have a non-negligible amplitude and can determine an inaccurate estimate of the *rms* value of the fundamental harmonic of the line to line input voltage. Furthermore, the filtering frequency of 500 Hz may be ineffective at low supply frequencies. Although there are no third harmonics in the system of absorbed currents of IPMSM, therefore the power is not affected by the third harmonic of the phase voltage but this latter can influence the determination of R_c. In the second case, the line to line voltage is not affected by the presence of a third harmonic. The determination of iron core losses requires the estimation of copper losses P_{cu} and mechanical losses P_m. The copper losses P_{cu} can be determined for 3P4W scheme and Aron scheme with the following relationships, respectively:

$$P_{cu} = \sum_{i=1}^{3} R I_{oci}^2 \tag{2.13}$$

$$P_{cu} = 3R I_{oc\ average}^2 \tag{2.14}$$

Where I_{oci} is the rms value of each phase current absorbed and $I_{oc\ average}$ is the average value between the *rms* values of two-phase input currents measured with Aron scheme. Although in the first case, the *rms* values of the currents of each phase are known and, therefore, it is possible to accurately estimate the copper losses of each phase and therefore the overall ones, while in the second case the copper losses estimated could be not very accurate due to the possible dissymmetry that could be present in the three

input currents absorbed by the IPMSM. In this work, two no-load tests have been carried out, respectively, employing the measurement schemes described. In detail, 11 measurement points were taken into consideration with a mechanical rotor speed n_r ranging from 200 to 5000 rpm, with steps of 500 rpm starting from the value of 500 *rpm*. In Fig. 26 the sum between the iron core losses and mechanical losses obtained in each test as function of mechanical speed n_r are reported.

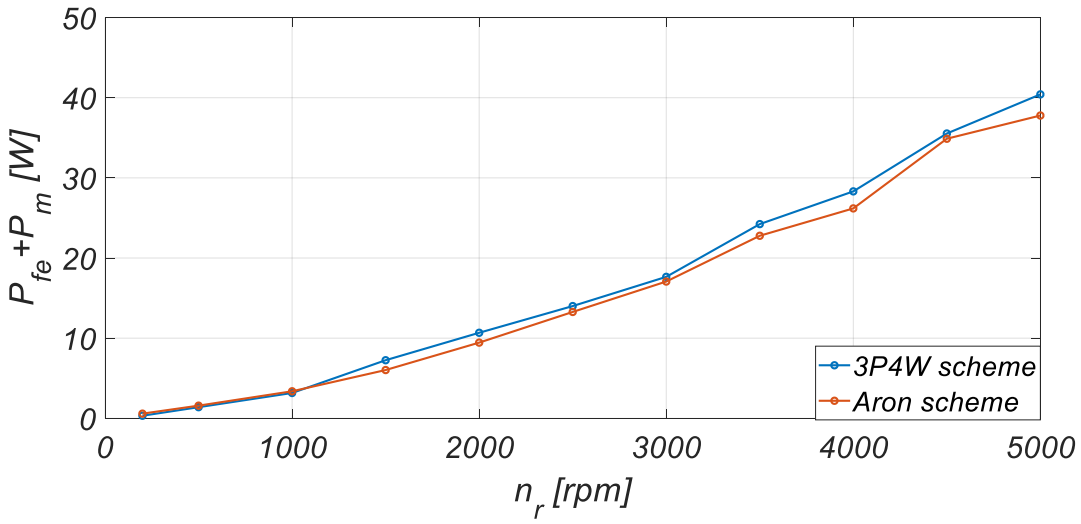

Fig. 26 Iron core losses and mechanical losses sum estimated.

It is possible to note that the difference between the results returned by the tests is slightly different only at high speeds. Therefore, the results obtained from both tests can be considered valid. In some case studies, mechanical losses are neglected and the iron core losses are simply equalled as the difference between the no-load absorbed power and the copper losses. According to IEEE Std 1812 [II.9], it is possible to estimate the mechanical losses as a function of mechanical speed with retardation or coast-down test. This test is used to determine the cinematic stored energy in the machine as the stored energy is related to the loss that tends to decelerate the rotor during free coast-down. This test relies on the relationship between the deceleration rate and the total losses. In detail, the goal is the determination of the total decelerating torque of the test machine, that is:

$$T_{dec} = J\frac{d\omega_r}{dt} \tag{2.15}$$

Where J and ω_r are respectively the total moment of inertia of the test machine and the rotor mechanical speed in [rad/s]. The machine mechanical losses as a function of mechanical speed can then be obtained as:

$$P_m = \omega_r T_{dec} \tag{2.16}$$

This test requires the knowledge of inertia of the test machine that usually is given by the manufacturer and the time-derivative of the machine speed. In this work, a retardation test has been carried out, bringing the machine to nominal speed and recording the deceleration transient. The mechanical speed signal of resolver has been acquired with dSPACE® rapid prototyping control board and suitably filtered to eliminate any overlapping noise as the latter would be profoundly amplified with a time-derivative operation. In Fig. 27 the trend of filtered mechanical speed n_r as function of the time is reported.

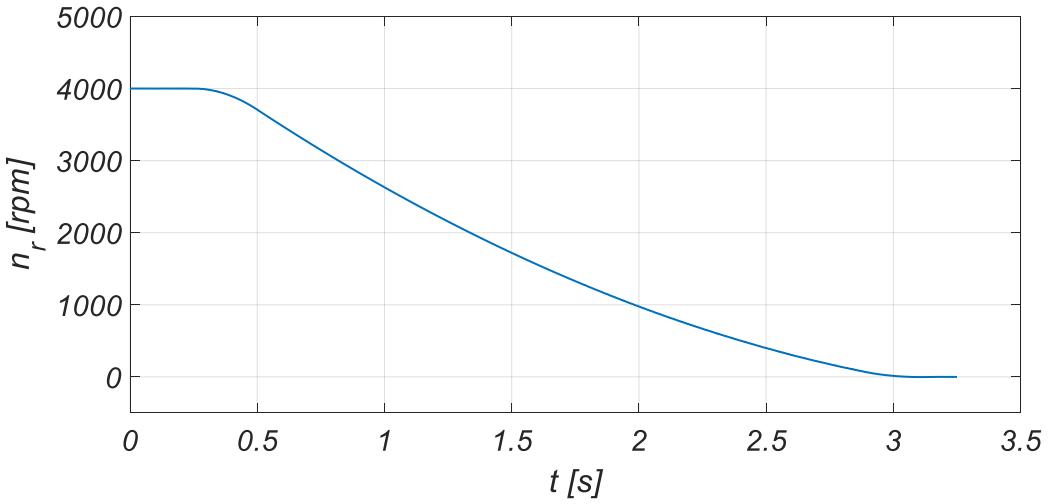

Fig. 27 Mechanical speed of retardation test.

From the acquired speed data, the mechanical losses are obtained and a polynomial function is used to fit its trend as a function of mechanical speed. In this way, it is possible to estimate the mechanical loss above the nominal mechanical speed. In Fig. 28, the trend of mechanical losses as a function of mechanical speed n_r is reported.

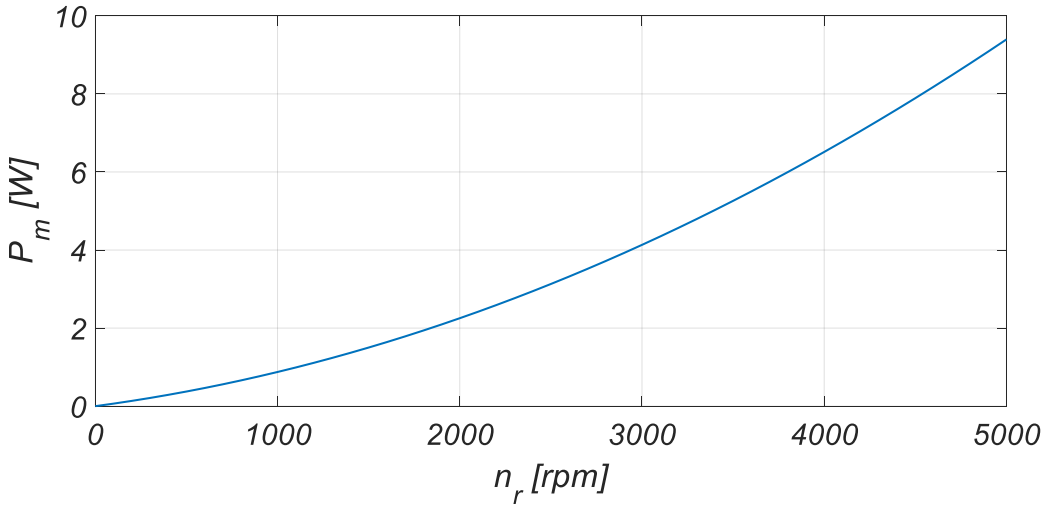

Fig. 28 Mechanical losses obtained with retardation test.

The obtained values of mechanical losses are used to obtain the iron core losses. Furthermore, a fit curve is employed between the two trends of iron core losses obtained. In Fig. 29 the trend of iron core losses as a function of rotor mechanical speed n_r obtained with 3P4W scheme, Aron scheme and with the fit curve are reported.

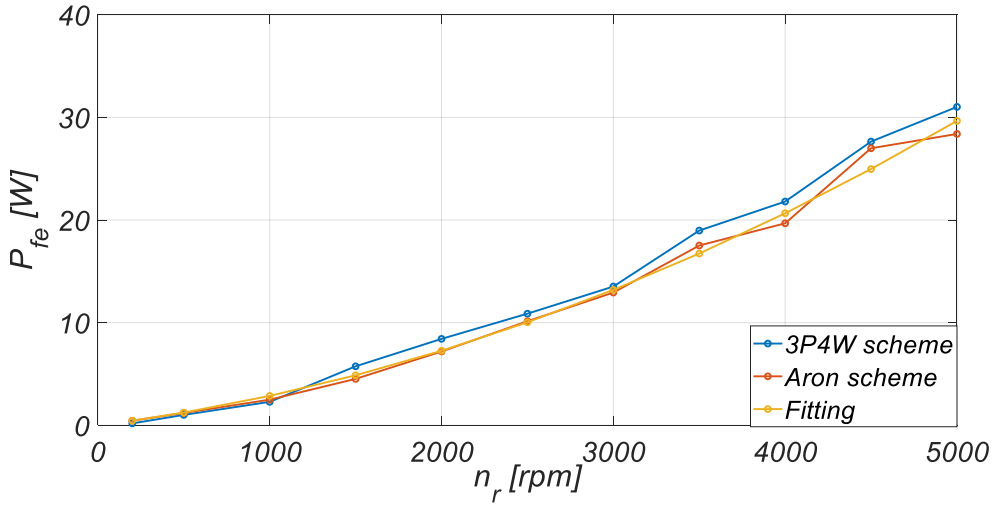

Fig. 29 Iron core losses estimated.

The values of the core loss resistance R_c as a function of rotor mechanical speed n_r obtained from the iron core losses fit curve are reported in Fig. 30.

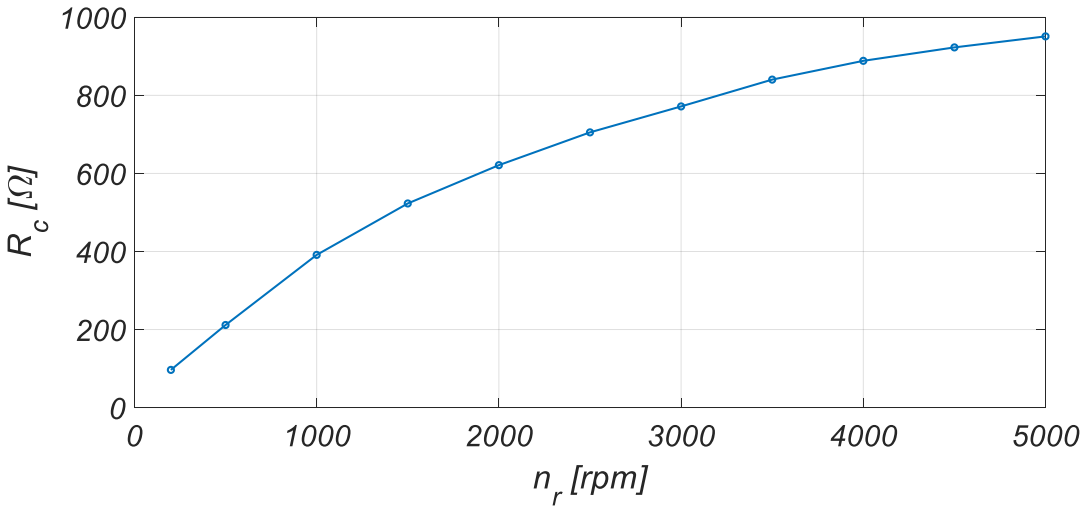

Fig. 30 Core loss resistance.

2.4 Experimental investigations for the determination of minimum loss operation points

In order to study the performances of loss models, several experimental tests have been carried out on electric drive under test. The goal is the determination of minimum loss operation points of IPMSM in stationary working conditions or for fixed values of mechanical speed and load torque. In detail, two experimental investigations were carried out. In the first experimental investigation, the IPMSM performances at fundamental harmonic of electrical quantities have been analyzed. While in the second experimental investigation, in addition to the IPMSM performances, the performances of the entire electrical drive or Power Drive System (PDS), including the inverter, have been analyzed considering the entire harmonic content of electrical quantities. In this way, it is possible to evaluate the possible advantages derived by the use of the loss model control on the overall electric drive performances. For this purpose, a WT330 power analyzer (Yokogawa Inc) and a PZ 4000 three-phase power analyzer (Yokogawa Inc) have been employed, respectively, to measure the absorbed power at the input section of the converter and at the input section of IPMSM. The output mechanical power of IPMSM has been measured by the digital dynamometer DSP6001 of hysteresis brake. In Fig. 31, a schematic representation of the test bench is reported.

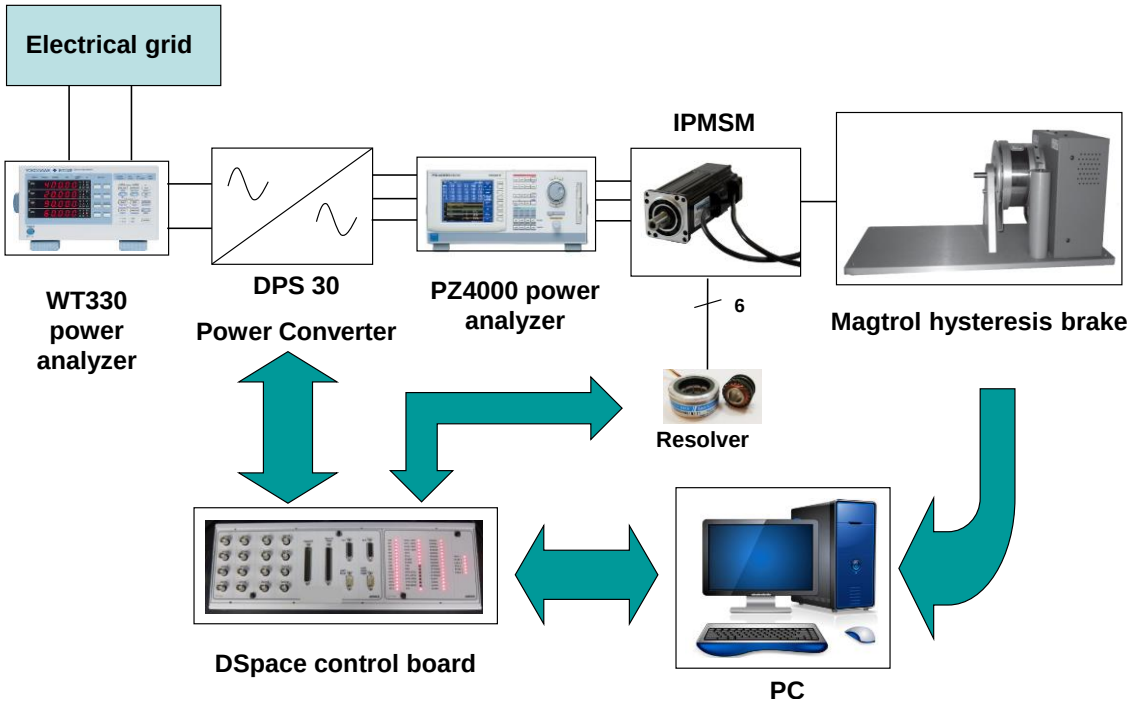

Fig. 31 Schematic representation of the test bench.

The sampling frequencies are 100 kHz and 1 MHz, for WT330 power analyzer and PZ 4000 three-phase power analyzer, respectively. The experimental investigations carried out and the results obtained are described in detail below.

2.4.1 Experimental investigations on electrical drive performance in correspondence of electrical quantities fundamental harmonic

In order to achieve the goals described in the previous section, through the use of the implemented FOC, the motor has been driven with a reference speed in the range 500 to 4000 rpm, with steps of 500 rpm, obtaining eight different speed tests. In addition, for each speed condition, several torque load has been applied to the motor shaft, from 0% (no-load condition) to 100% (full load condition) of load torque rated value T_n with steps of 25%, obtaining 40 overall working conditions with defined values of speed and load. Furthermore, for each test, a specified IPMSM magnetization level has been set by acting on the value of the direct-axis current i_d of the control system. In particular, the i_d value has been varied from -2.4 A to +2.4 A with steps of 0.2 A. In detail, for each test, 25 different magnetization conditions have been employed. Hence, from the measurement system of the proposed test bench, it is possible to detect the i_d values that minimize the absorbed power or the power losses of IPMSM for each working condition. As example, the power losses trends of the IPMSM ΔP_{mot} as a function of i_d at 500 rpm and 3000 rpm, for each load condition, are reported in Fig. 32 and Fig. 33 respectively.

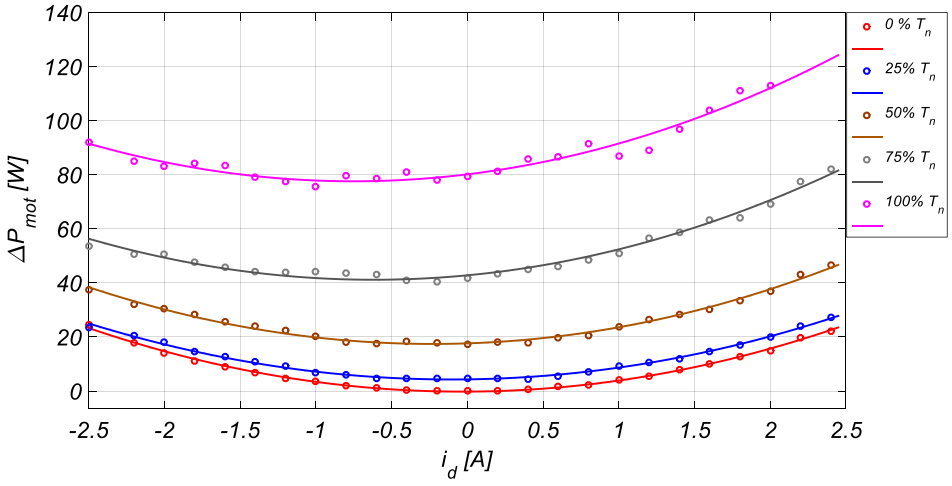

Fig. 32 Power losses vs i_d for different load conditions at 500 rpm.

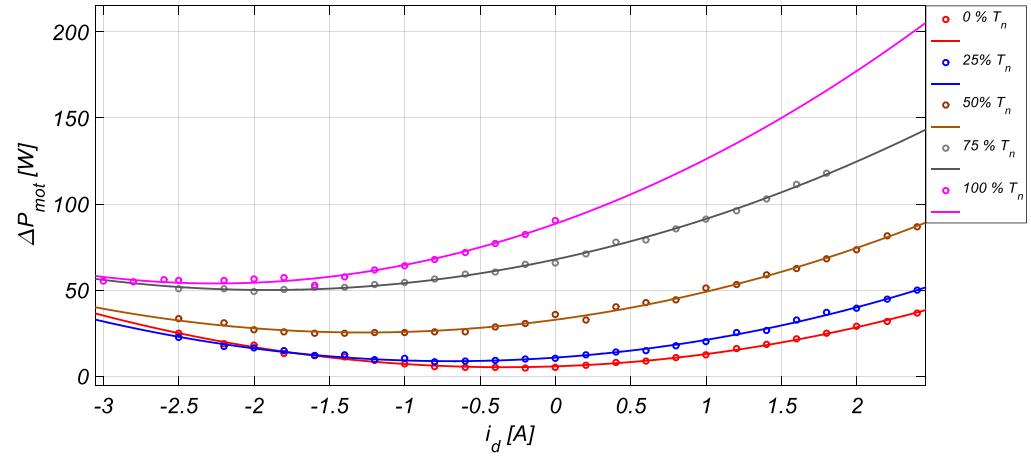

Fig. 33 Power losses vs i_d for different load conditions at 3000 rpm.

As it is possible to notice, the minimum value of power losses ΔP_{mot} is obtained for a negative value of the i_d current. By changing the applied load, the minimum value of ΔP_{mot} slides through higher negative values of the direct-axis current i_d, as shown in the figures above mentioned. Fig. 34 and Fig. 35 show the ΔP_{mot} vs i_d characteristics parametrized as a function of the reference speed, maintaining the applied load fixed at 50% and 100% of its rated value, respectively.

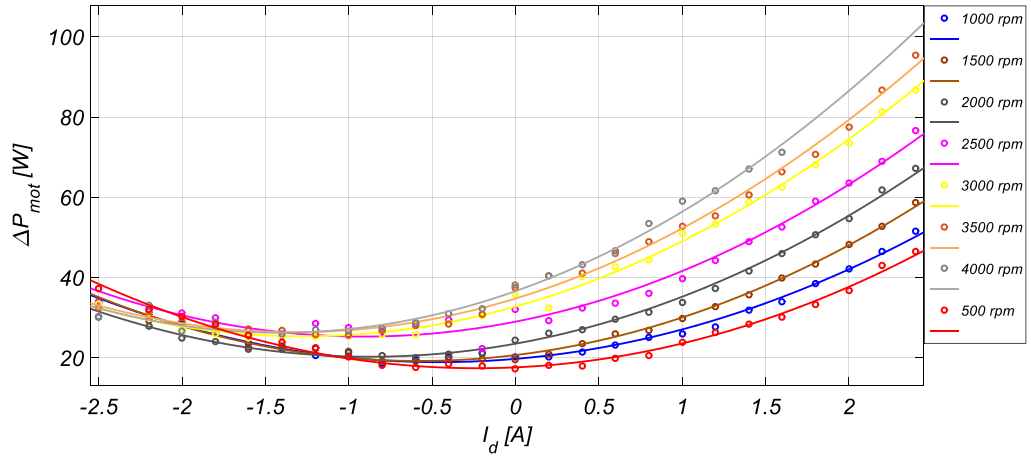

Fig. 34 Power losses vs i_d for different reference speeds at 50% of its rated load.

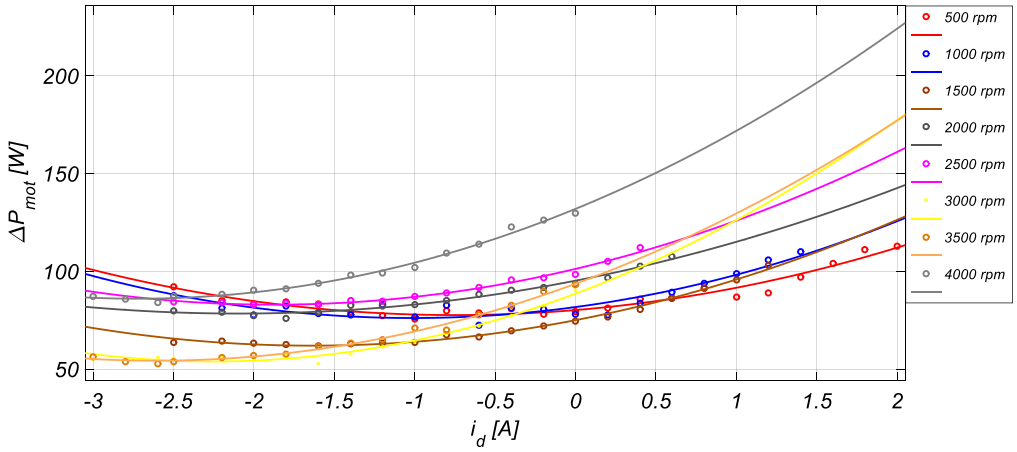

Fig. 35 Power losses vs i_d for different reference speeds at its rated load.

As expected, it can be noticed that the minimum values of power losses ΔP_{mot} are obtained for negative values of i_d. In addition, by increasing the applied load, the related peaks are detected for higher negative values of i_d. Furthermore, the trends of detected values of *dq*-axis currents of minimum power loss operating points as a function of the applied load and angular speed are reported in Fig. 36 and Fig. 37, respectively.

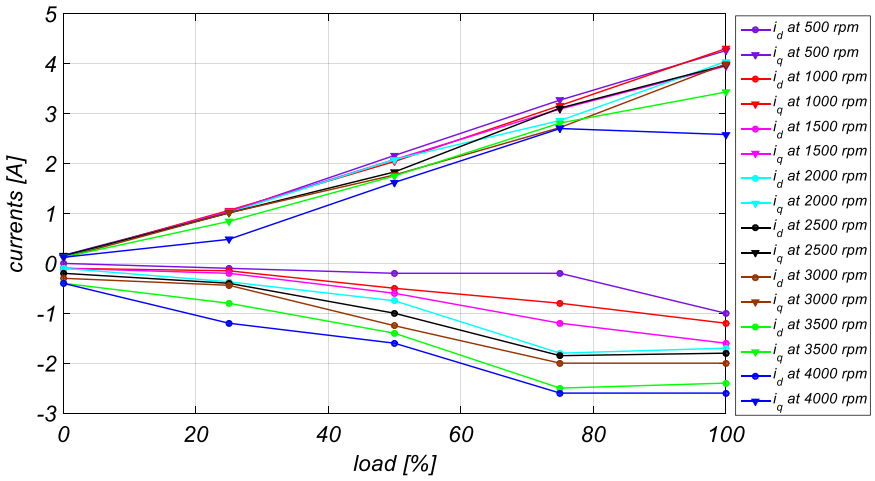

Fig. 36 Direct-axis and quadrature-axis current values as a function of the applied load for each reference speed.

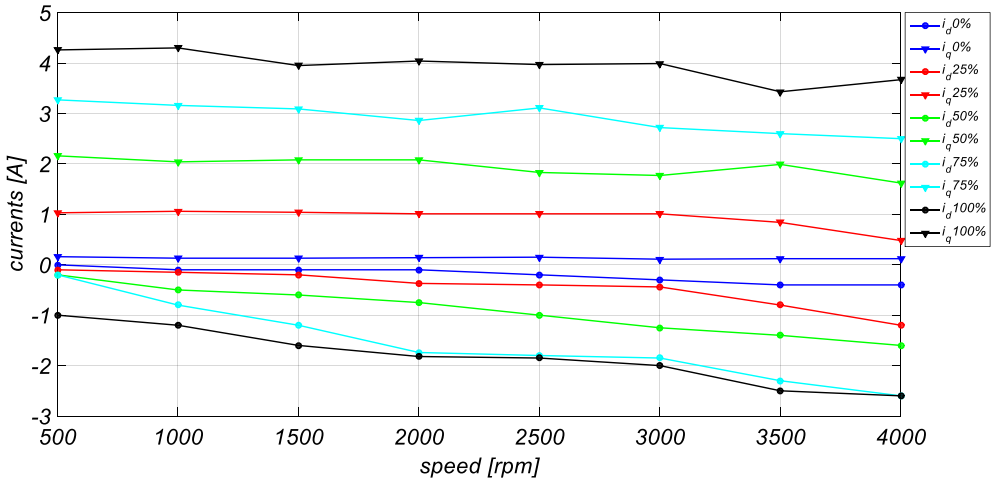

Fig. 37 Direct-axis and quadrature-axis current values as a function of the reference speed for each load condition.

As it is possible to notice, a load increase determines a significant increase of the i_q component, while the i_d value is smoothly decreasing. Instead, the angular speed increase determines a significant decrease of the i_d component, while the i_q component maintains a value almost equal to its rated value. It appears evident that the minimum value of the power losses is obtained for values of i_d that increase towards negative values when the angular reference speed is increased. The behaviour of the amplitude of *dq*-axis currents is justified by the expression of output electromagnetic torque (1.47), where, for constant values of the generated electromagnetic torque, an i_q decrease implies an increase of the i_d amplitude. However, these variations are not linear. Thus, with the measurements here shown, it can be stated that it is always possible to determine, for each motor operating condition, a specified i_d value that minimizes the power losses (or maximizes the IPMSM efficiency). The results obtained will be used to validate the performances of loss models.

2.4.2 Experimental investigations on electrical drive performances considering the entire harmonic content of the electrical quantities

The previous experimental investigation provides the data needed to validate the loss mathematical models derived by the IPMSM mathematical model, at fundamental harmonic, previous described. In order to evaluate the possible real impact of the Loss Model Algorithm (LMA) about the overall performance of the electrical drive, it is necessary to evaluate the performances of electrical drive respect to the entire harmonic content of electrical quantities. Moreover, it is not sufficient to evaluate only the

IPMSM performance but also those of the converter and, therefore, of the entire power drive system (PDS). In this sense, in order to evaluate the performances of electrical drive respect to the entire harmonic content of electrical quantities, several experimental investigations have been performed. With the aid of the test bench (Fig. 31), it is possible to detect the i_d values that minimize the absorbed power or the power losses of IPMSM and PDS for each working condition. In detail, through the use of the implemented FOC, the IPMSM has been driven with a reference speed in the range of 1000 to 4000 rpm, with steps of 1000 rpm, obtaining four different speed tests. In addition, for each speed condition, several torque load has been applied to the motor shaft, from 0% (no-load condition) to 100% (full load condition) of load torque rated value T_n with steps of 25%, obtaining 20 overall working conditions with defined values of speed and load. Furthermore, for each test, a specified IPMSM magnetization level has been set by acting on the value of the direct-axis current i_d of the control system. In particular, since from the previous experimental investigations it is clear that the minimum of power losses is in correspondence of negative values of i_d, the i_d range has been slightly reduced in comparison with the previous investigation and the i_d value has been varied from -2.4 A to +1.8 A with steps of 0.2 A. In detail, for each test, 22 different magnetization conditions have been employed. As example, the power losses trends of the PDS ΔP_{pds} and of IPMSM ΔP_{mot} as a function of i_d at 1000 rpm and 4000 rpm, for each load condition, are reported in Fig. 38, Fig. 39, Fig. 40 and, respectively.

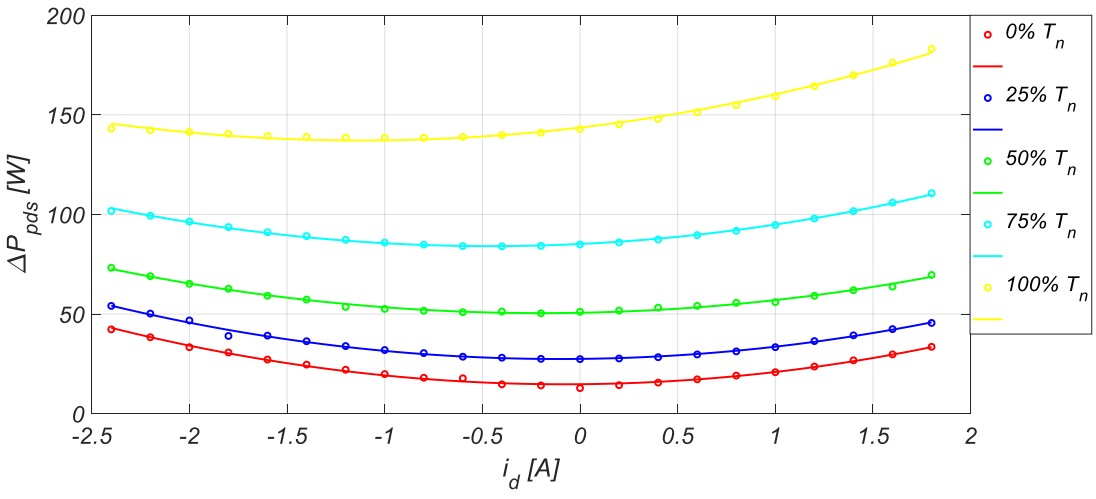

Fig. 38 PDS power losses vs i_d for different load conditions at 1000 rpm.

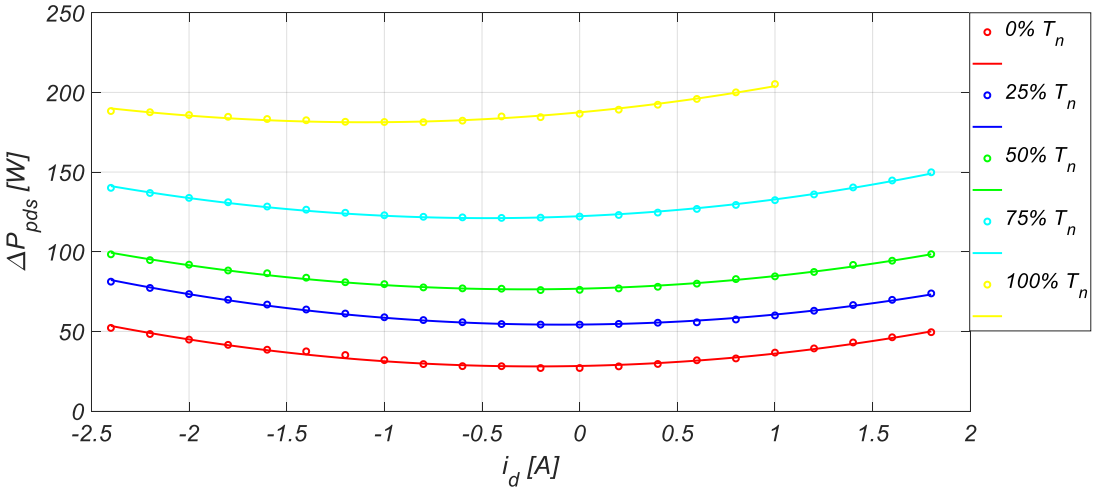

Fig. 39 PDS power losses vs i_d for different load conditions at 4000 rpm.

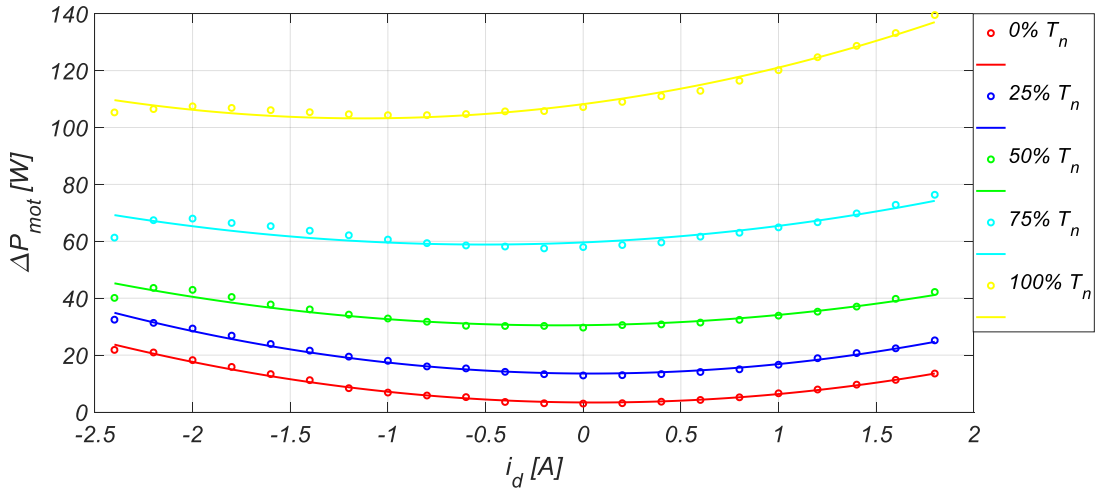

Fig. 40 Motor power losses vs i_d for different load conditions at 1000 rpm.

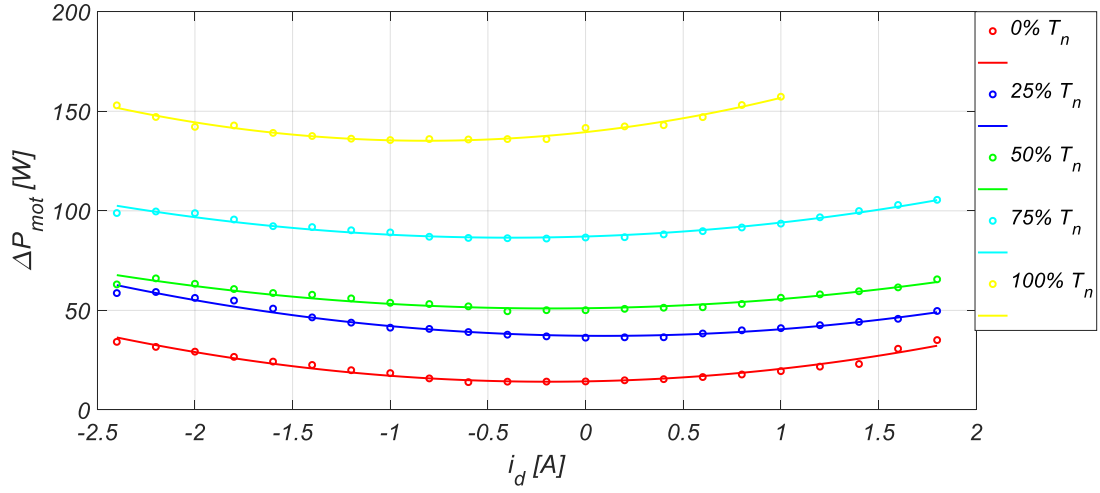

Fig. 41 Motor power losses vs i_d for different load conditions at 4000 rpm.

As it is possible to notice, the minimum value of power losses of PDS ΔP_{pds} and the motor ΔP_{mot} is obtained in correspondence of negative values i_d current. Moreover, unlike the results obtained from the experimental investigations at the fundamental harmonic, both for the PDS and for the motor, the trend of power losses, for applied load until to 75 % of rated value, is fairly flattened near the minimum value or in correspondence of negative value of i_d current. This fact implies, as the current decreases towards negative values, a negligible or no appreciable reduction in power losses. Fig. 42, Fig. 43, Fig. 44 and Fig. 45 show the trend of ΔP_{pds} and ΔP_{mot} as a function of i_d current parametrized as function of the reference speed, maintaining the applied load fixed at 50% and 100% of its rated value, respectively.

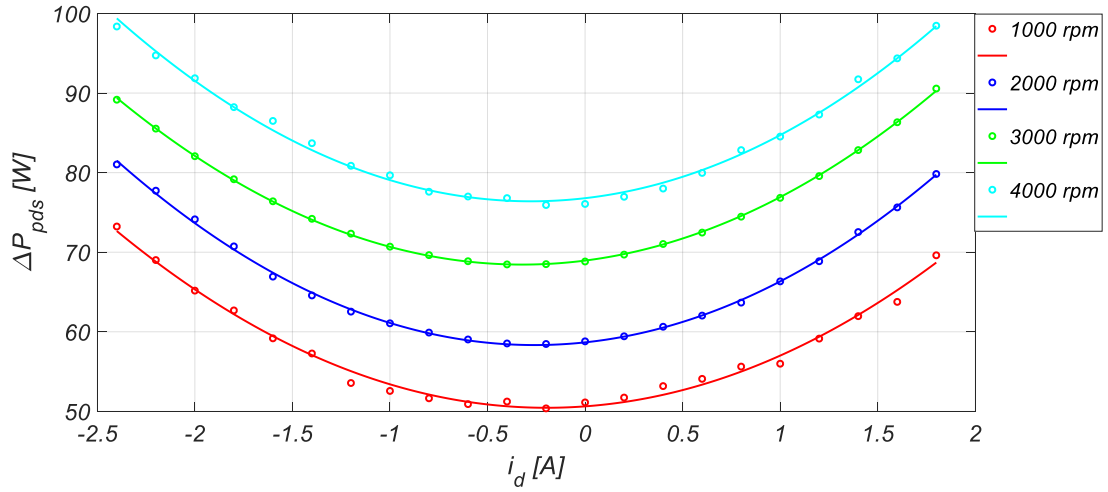

Fig. 42 PDS power losses vs i_d for different reference speeds at 50% of its rated load.

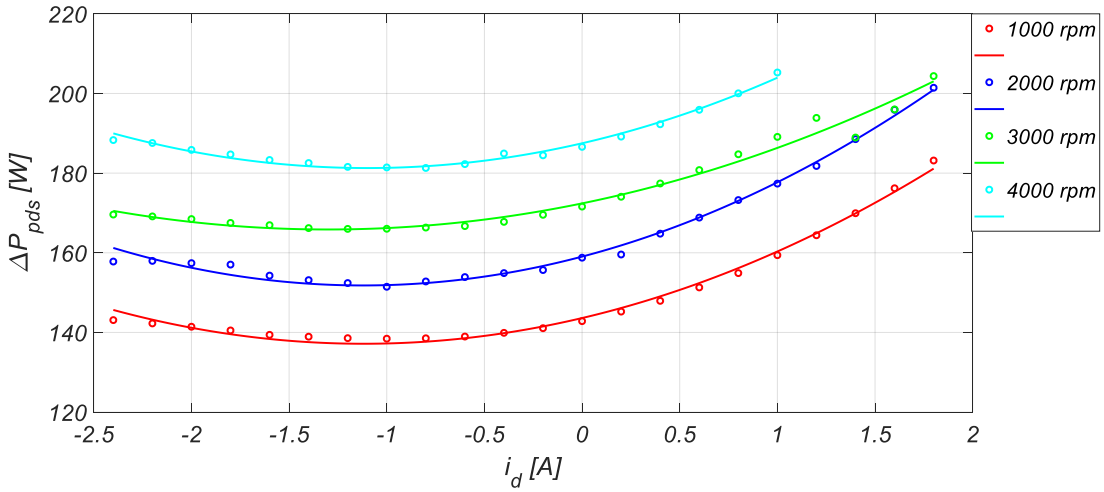

Fig. 43 PDS power losses vs i_d for different reference speeds at its rated load

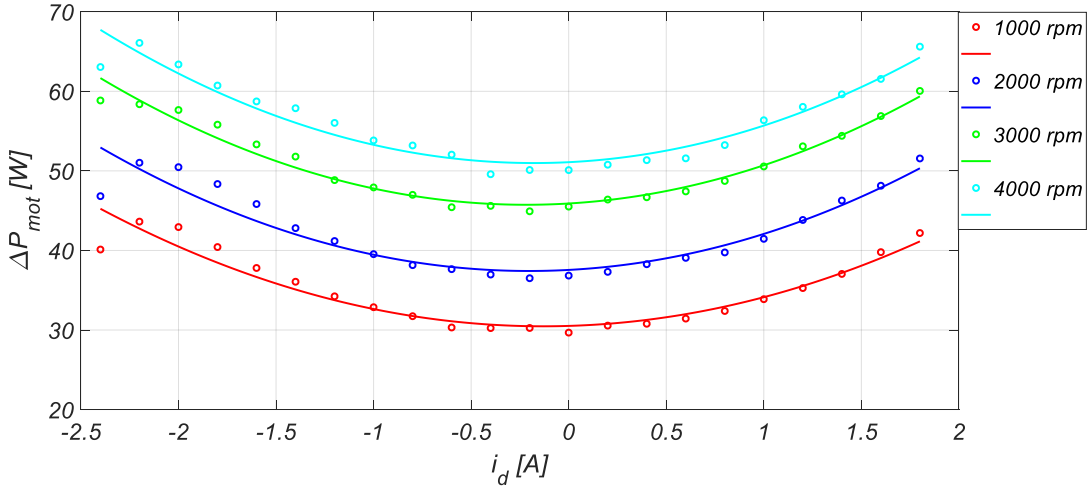

Fig. 44 Motor power losses vs i_d for different reference speeds at 50% of its rated load.

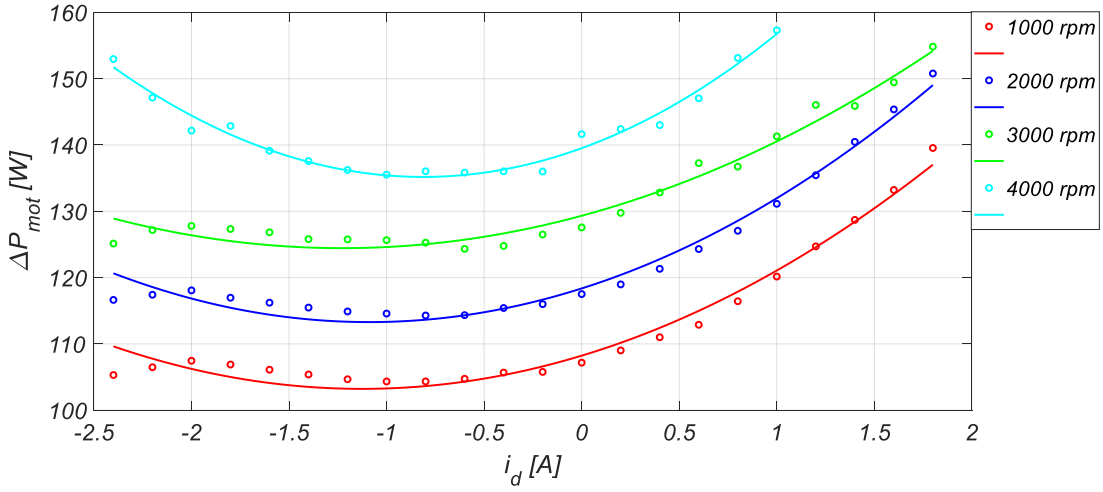

Fig. 45 Motor power losses vs i_d for different reference speeds at its rated load.

As expected, it can be noticed that the minimum values of power losses ΔP_{pds} and ΔP_{mot} are obtained for negative values of i_d current. In details, at 50 % of rated load, it is possible to see that the minimum of power losses, both for PDS and for the motor, are obtained for i_d current value slightly negative or close to 0 A. Similar results were also obtained for lower values of the applied load (<50% T_n). Only at high applied load, the related minimum of power losses is detected for higher negative values of i_d current. The trends of detected values of *dq*-axis currents of minimum power loss operating points as a function of the applied load and angular speed are reported in Fig. 46, Fig. 47, Fig. 48 and Fig. 49, respectively.

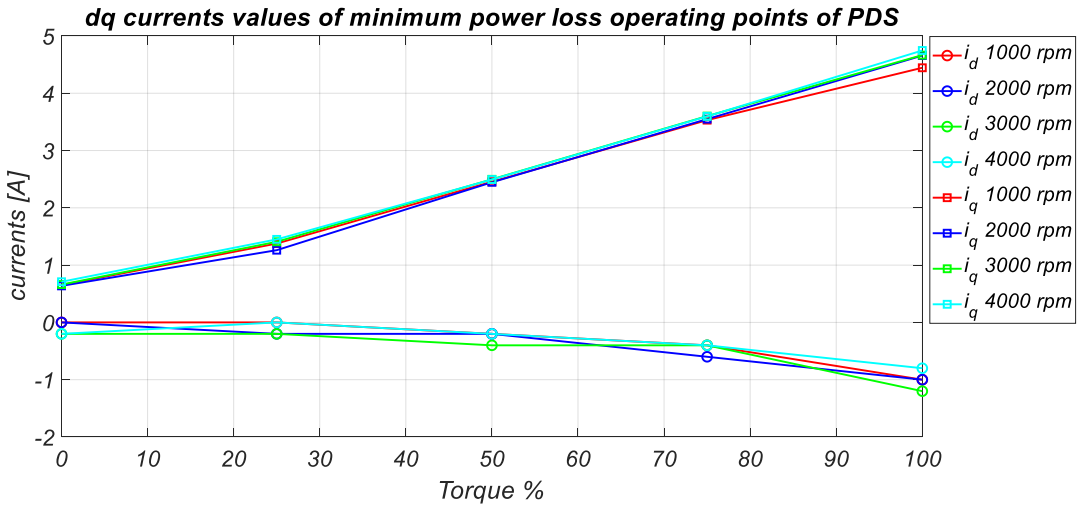

Fig. 46 *dq* current values of minimum power loss operating points of the PDS as a function of the applied load at each reference speed.

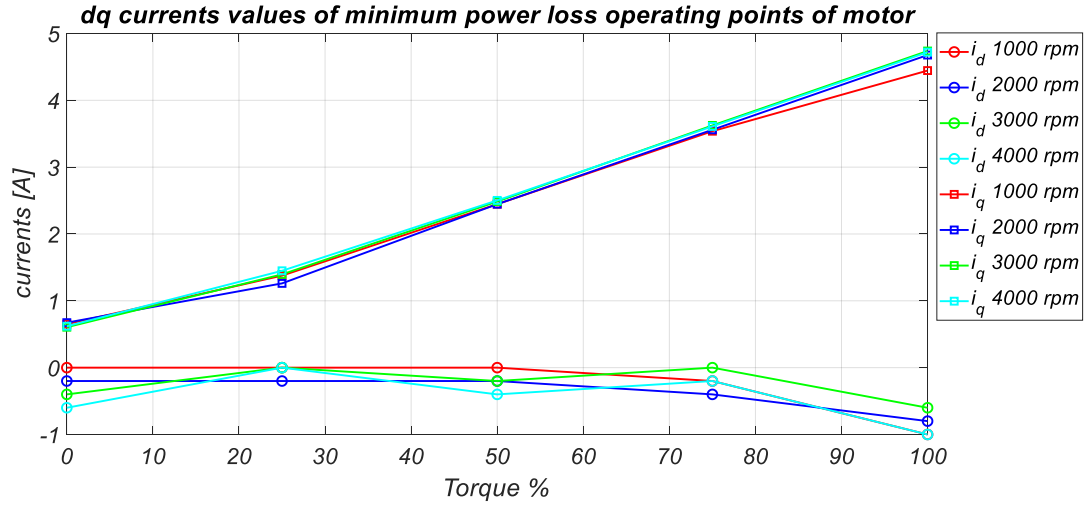

Fig. 47 *dq* current values of minimum power loss operating points of the motor as a function of the applied load at each reference speed.

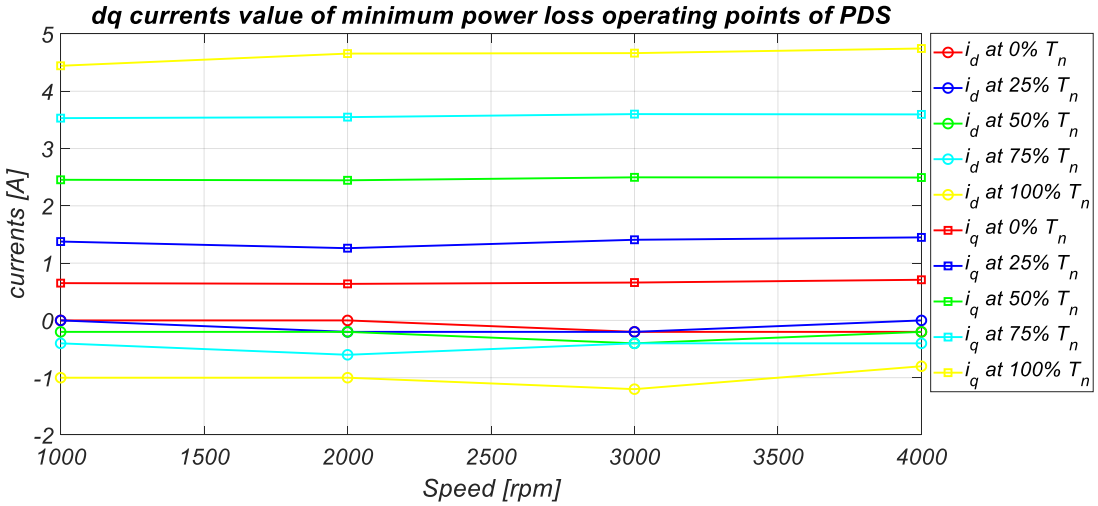

Fig. 48 *dq* current values of minimum power loss operating points of the PDS as a function of the reference speed at several load conditions.

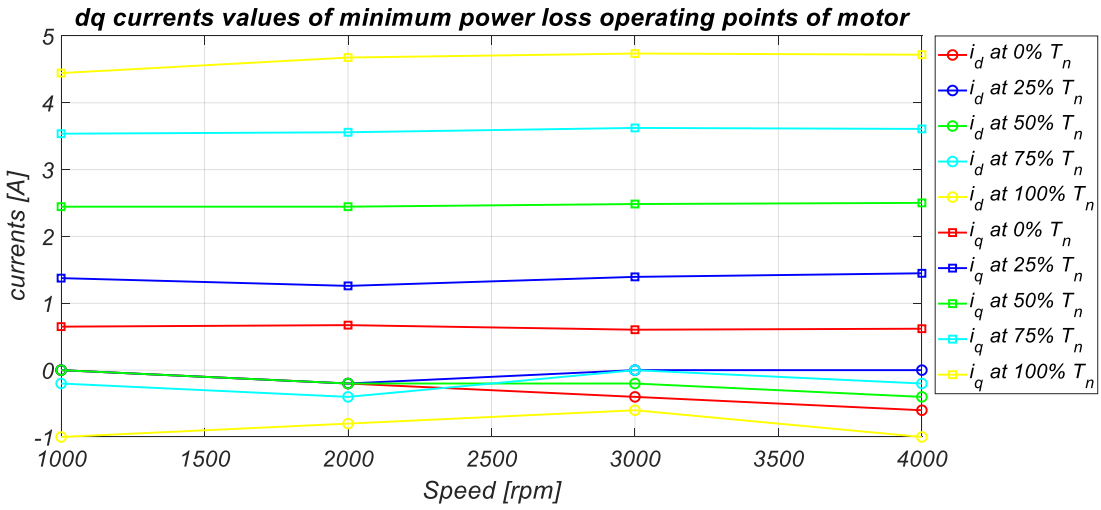

Fig. 49 *dq* current values of minimum power loss operating points of the PDS the motor as a function of the reference speed at several load conditions.

As it is possible to notice, a load increase determines a significant increase of the i_q current, while the i_d value is smoothly decreasing. Instead, the angular speed increase determines a slight decrease of the i_d current, while the i_q component maintains a value almost equal to its rated value. These observations are valid both for power losses of PDS ΔP_{pds} and for power losses of the motor ΔP_{mot}. Also, in this case, the behaviour of the amplitude of *dq*-axis currents are not linear. Respect to the results obtained from the previous experimental investigations, the minimum value of the power losses is obtained for lower negative values of i_d current, especially for high load and high speed. These results will be used to evaluate the possible effectiveness of LMAs on the overall performances of the electric drive under test.

2.5 Performances study of IPMSM mathematical models in Matlab® environment

An accurate estimate of the minimum losses or maximum efficiency operating point of IPMSM, for fixed speed and load conditions, is necessary to obtain good performances with the use of LMAs. The mathematical model of power losses are derived by the IPMSM conventional mathematical model that take into account the iron losses, described in section 1.3.3, and, in details, the expressions of controllable power losses are:

$$P_{cu}(i_{od}, i_{oq}, \omega_r) = \frac{3}{2} R \left\{ \left[\left(i_{od} - \frac{p\omega_r L_q i_{oq}}{R_C} \right)^2 + \left(i_{oq} + \frac{p\omega_r (\lambda_{PM} + L_d i_{od})}{R_C} \right)^2 \right] \right\} \tag{2.17}$$

$$P_{fe}(i_{od}, i_{oq}, \omega_r) = \frac{3(p\omega_r)^2}{2R_c} \left[\left(L_q i_{oq} \right)^2 + (\lambda_{PM} + L_d i_{od})^2 \right] \tag{2.18}$$

$$P_c(i_{od}, i_{oq}, \omega_r) = P_{cu}(i_{od}, i_{oq}, \omega_r) + P_{fe}(i_{od}, i_{oq}, \omega_r) \tag{2.19}$$

The total controllable losses are a function of ω_r, i_{od}, i_{oq}, L_d, L_q, λ_{PM}, R and R_c. The last five elements are not adjustable parameters and, for a stated motor working condition (namely load and speed), neither ω_r or i_{oq} can be used to control the motor losses. Therefore, the motor efficiency can be controlled only by acting on the i_{od} value, but, since for a stated motor working condition the i_{cd} value is constant, the power losses can be controlled by directly adjusting the direct-axis current i_d. In order to carry out an accurate estimation of the minimum losses point, it is necessary to take into account the variation of the motor parameters that influence its efficiency. For this purpose, two power loss models are taken into account. In the first loss model, a traditional approach is taken into account where the parameters are constant. In this case, the self and cross-saturation phenomena and the variation of iron loss resistance with the supply frequency are not take in consideration. The second loss model is a variable parameter model, where the values of parameters are a function of working conditions or *dq*-axis currents of the IPMSM. The goal is to take into account the effects of self-saturation in *dq*-inductances ($L_d(i_d)$, $L_q(i_q)$), the cross saturation effect in the stator flux linkage due the PMs $\lambda_{PM}(i_q)$ and the variation of iron loss resistance R_c with the supply frequency or the mechanical speed ω_r of the IPMSM. From the experimental characterization carried out, both the values of nominal parameters to be used in the constant parameters loss model and the parametric variations to be used in the variable parameter loss model have been

deduced. In detail, as values of nominal parameters, the average values of each parameter were chosen and they are reported in Table 7.

Table 7 Rated values of the parameters of IPMSM under test

Average stator resistance R	2.32 Ω
Direct-axis inductance L_d	7.5 mH
Direct-axis inductance L_q	11 mH
PMs stator flux linkage λ_{PM}	0.0842 Wb
Iron loss resistance R_c	540 Ω

Contrariwise, through a polynomial interpolation, the equations, that describe the variation of the parameters according to the working conditions of the machine, have been deduced and listed below:

$$\lambda_{PM}(i_q) = a_\lambda \cdot i_q^2 + b_\lambda \cdot i_q + c_\lambda \quad (2.20)$$

$$L_d(i_d) = a_{L_d} \cdot i_d^2 + b_{L_d} \cdot |i_d| + c_{L_d} \quad (2.21)$$

$$L_q(i_q) = a_{L_q} \cdot i_d^2 + b_{L_q} \cdot |i_q| + b_{L_q} \quad (2.22)$$

$$R_c(\omega_r) = a_R \omega_r^2 + b_R \cdot \omega_r + c_R \quad (2.23)$$

where the coefficients values are reported below:

$a_\lambda \left[\frac{\mathrm{Wb}}{\mathrm{A}^2}\right]$	$b_\lambda \left[\frac{\mathrm{Wb}}{\mathrm{A}}\right]$	c_λ[Wb]	$a_{L_d} \left[\frac{\mathrm{H}}{\mathrm{A}^2}\right]$	$b_{L_d} \left[\frac{\mathrm{H}}{\mathrm{A}}\right]$	c_{L_d}[H]
$-12.65 \cdot 10^{-5}$	$81.62 \cdot 10^{-5}$	0.0841	$-3.222 \cdot 10^{-5}$	$-3.979 \cdot 10^{-4}$	$7.582 \cdot 10^{-3}$

$a_{L_q} \left[\frac{\mathrm{H}}{\mathrm{A}^2}\right]$	$b_{L_q} \left[\frac{\mathrm{H}}{\mathrm{A}}\right]$	b_{L_q}[H]	$a_R \left[\frac{\Omega \cdot \mathrm{s}^2}{\mathrm{rad}^2}\right]$	$b_R \left[\frac{\Omega \cdot \mathrm{s}}{\mathrm{rad}}\right]$	c_R[Ω]
$-6.14 \cdot 10^{-4}$	$-3.069 \cdot 10^{-4}$	$13.46 \cdot 10^{-3}$	$-3.416 \cdot 10^{-5}$	0.3423	75.65

Therefore, in order to validate the loss mathematical models, a comparison study with experimental data obtained by the experimental investigations, have been performed in the Matlab environment.

2.5.1 Implementation of the IPMSM mathematical model in Matlab environment

For the purpose concerning the determination of the minimum loss operating point of IPMSM, the loss models, previous described, have been implemented in a script in the Matlab environment. Regarding the implementation of the mathematical model of IPMSM, it is necessary to define which quantities are mathematical independent and which are mathematically dependent. In this study, the *dq*-currents have been chosen as independent variables, making all the other quantities of interest dependent on them. In detail, in order to define the elements of each current component vector ([i_d],[i_q]), the minimum value, the maximum value and the amplitude of the step between two consecutive elements are defined. Therefore, from each possible combination of *dq*-axis current, defined the values of the parameters and the value of supply frequency or the mechanical speed, the values of each current components of the mathematical model of IPMSM are determined with the following relationships:

$$i_{od} = \left(i_d + \frac{i_q \omega_e k L_d}{R_c} - \frac{{\omega_e}^2 k L_d \lambda_{PM}}{{R_c}^2} \right) / \left(1 + \frac{{\omega_e}^2 k L_d \lambda_{PM}}{{R_c}^2} \right) \tag{2.24}$$

$$i_{oq} = i_q - \omega_e \left(\frac{\lambda_{PM} + L_d i_{od}}{R_c} \right) \tag{2.25}$$

$$i_{cd} = i_d - i_{od} \tag{2.26}$$

$$i_{cq} = i_q - i_{oq} \tag{2.27}$$

From these quantities, it is possible to obtain the values of the copper losses, iron losses, total controllable losses and the electromagnetic torque with the equation (2.17), (2.18), (2.19) and (1.47), respectively. In detail, each pair of (i_d, i_q) values represents a possible working condition of the IPMSM to which corresponds a defined value of the components of the controllable losses and of the electromagnetic torque. In Fig. 50, Fig. 51, Fig. 52 and Fig. 53 the trends of total controllable losses, copper losses, iron losses and electromagnetic torque as a function of *dq*-axis currents i_d, i_q are shown.

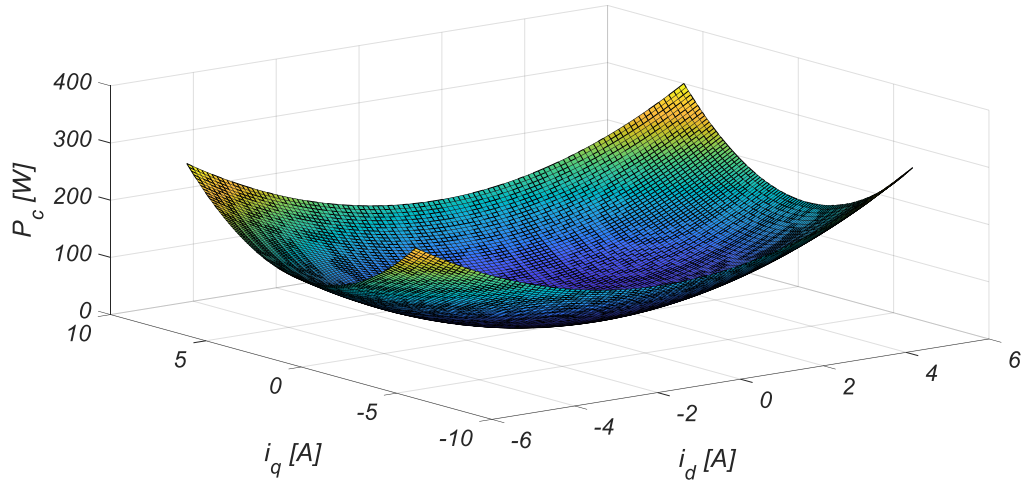

Fig. 50 Total controllable losses as function of *dq*-axis currents i_d, i_q.

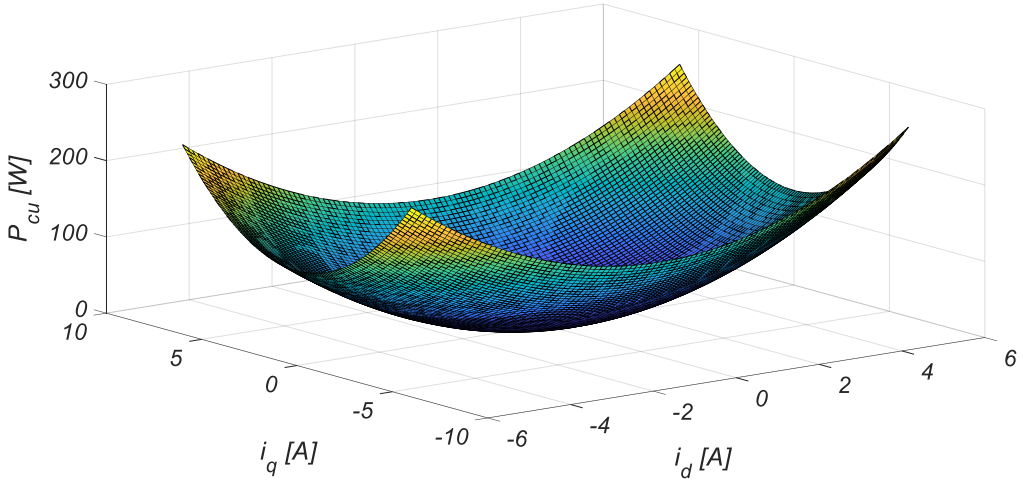

Fig. 51 Copper losses as function of *dq*-axis current i_d, i_q.

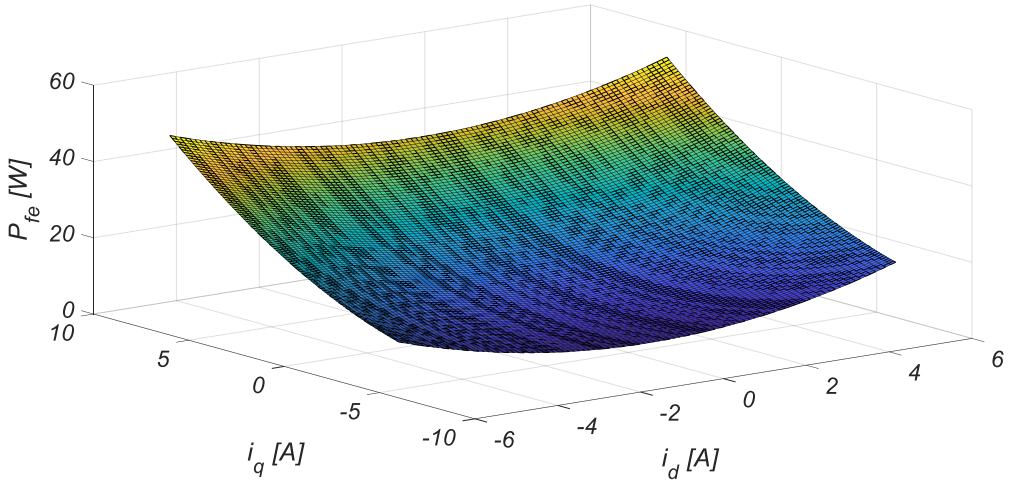

Fig. 52 Iron losses as function of *dq*-axis current i_d, i_q.

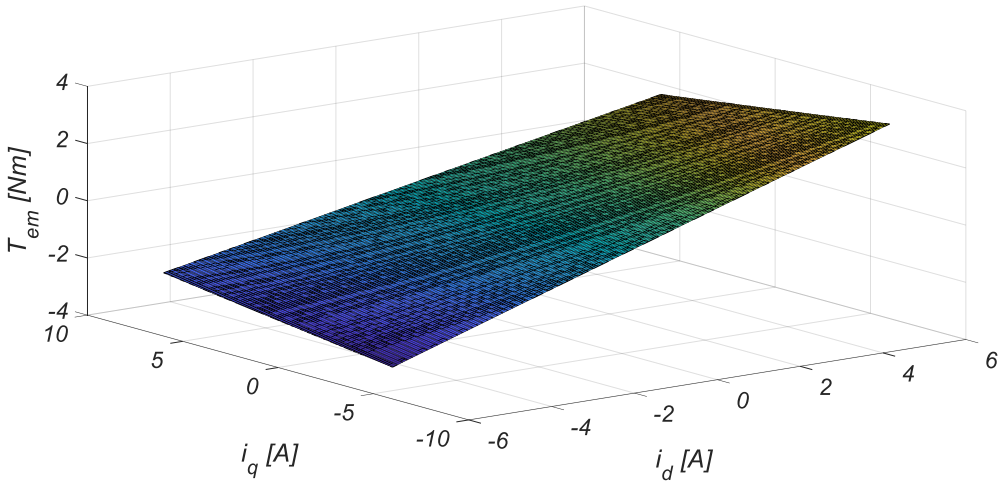

Fig. 53 Electromagnetic torque as a function of *dq*-axis current i_d, i_q.

The problem concerns the detection of the minimum loss operating point for fixed working conditions, in terms of speed and load torque, presents multidimensional character. In detail, it is necessary for the identification of *dq*-currents values that generate a precise torque value. This step is obtained with a binary research algorithm that finds all element of torque matrix [T_{em}] that satisfy the following relationships:

$$T_{em\,min} < T_{em} < T_{em\,max} \tag{2.28}$$

$$T_{em\,max} = T_{em}^{*} + 0.01 * T_n \tag{2.29}$$

$$T_{em\,min} = T_{em}^{*} - 0.01 * T_n \tag{2.30}$$

Where T_{em}^{*}, $T_{em\,min}$, and $T_{em\,max}$ are the desired value of load torque, the maximum and minimum research extremes of the desired value of load torque, respectively. Consequently, it is possible to identify the values of each component of controllable power loss and of each current component. For example, in Fig. 54 the trend of controllable losses, copper losses and iron losses as function of *d*-axis current i_d at 3000 rpm and without torque load applied is shown.

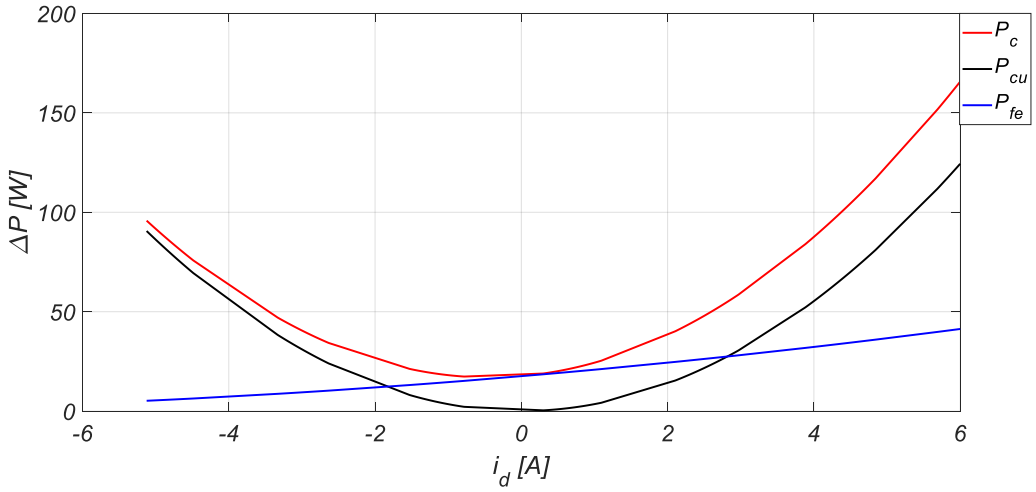

Fig. 54 Total controllable losses P_c, copper losses P_{cu} and iron losses P_{fe} as a function of *d*-axis current i_d at 3000 rpm and without load applied.

Below the comparison between the data obtained from the loss models and the experimental data are shown and discussed.

2.5.2 Results and comparison analysis

For the purpose concerning the validation of loss models, the reference working conditions of the machine, analyzed in the experimental tests, have been taken into consideration. In detail, the reference speed varies in the range 1000 to 4000 rpm, with steps of 1000 rpm and for each reference speed, the load torque varies from 0% (no-load condition) to 100% (full load condition) of load torque rated value T_n with steps of 25%. A first comparison is performed with the experimental data acquired at fundamental harmonic. In Fig. 55, Fig. 56 and Fig. 57 the comparison between each component of controllable losses obtained from the constant parameter loss model and from the experimental investigation, at fundamental harmonic, at 2000 rpm and for no-load condition, applied load torque equal to 50% and 100% of rated load, are shown, respectively.

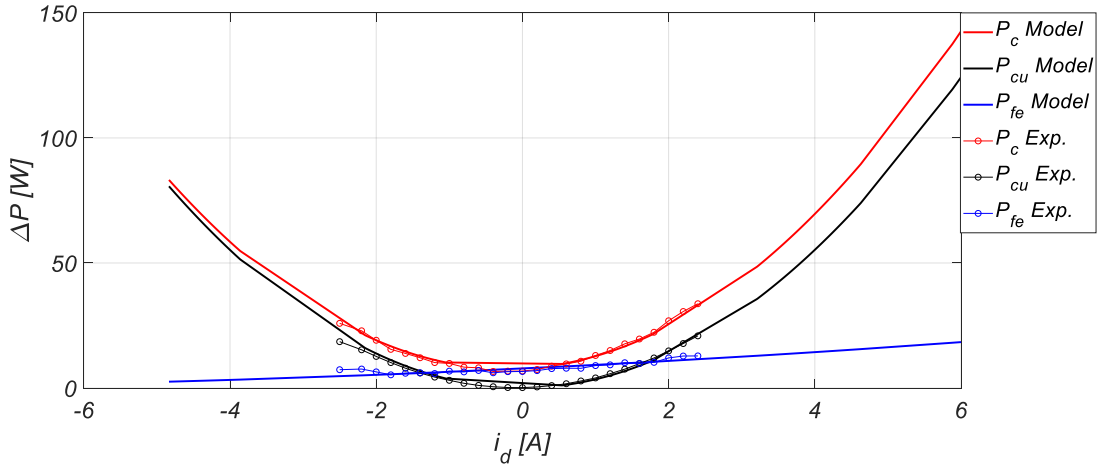

Fig. 55 Comparison between each component of controllable losses obtained from constant parameter loss model and from experimental investigation at fundamental harmonic (2000 rpm, T_{em}^{*}=0% T_n).

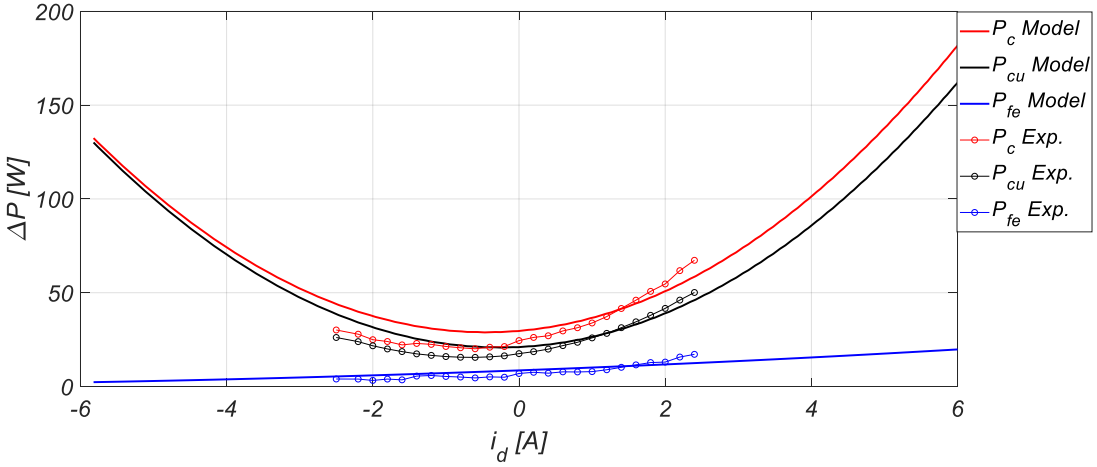

Fig. 56 Comparison between each component of controllable losses obtained from constant parameter loss model and from experimental investigation at fundamental harmonic (2000 rpm, T_{em}^{*}=50% T_n).

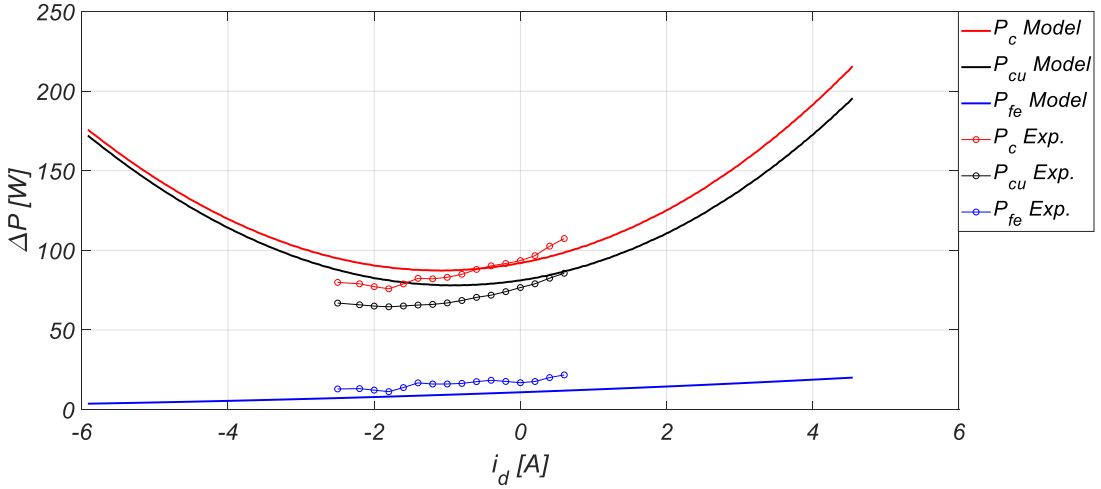

Fig. 57 Comparison between each component of controllable losses obtained from constant parameter loss model and from experimental investigation at fundamental harmonic (2000 rpm, T_{em}^{*}=100% T_n).

As it is possible to notice, the controllable losses evaluated with the constant parameter model differ to a greater extent from experimental ones at fundamental harmonic, in correspondence of high load torque ($T_{em}^{*} \geq 50\%\ T_n$). Moreover, as the speed increases, this difference is enhanced. This behaviour can be deduced from Fig. 58, Fig. 59 and Fig. 60, where the comparisons between the controllable losses of constant parameters loss model and those obtained from experimental investigations at 3000 rpm are reported.

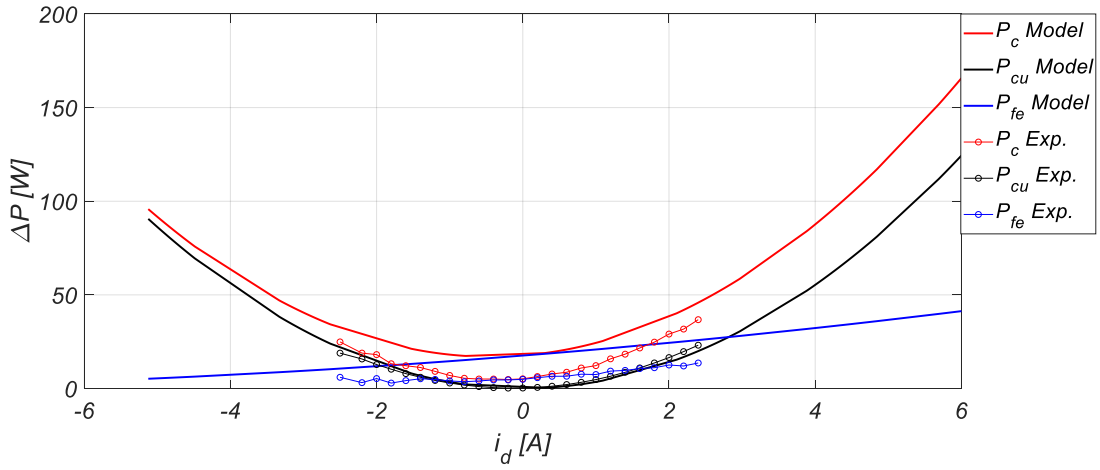

Fig. 58 Comparison between each component of controllable losses obtained from constant parameter loss model and from experimental investigation at fundamental harmonic (3000 rpm, $T_{em}^{*}=0\%\ T_n$).

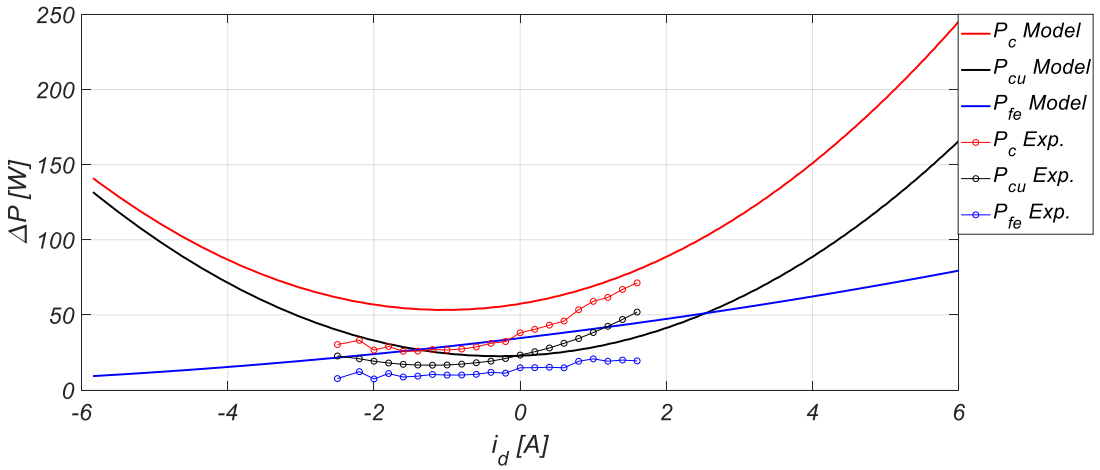

Fig. 59 Comparison between each component of controllable losses obtained from constant parameter loss model and from experimental investigation at fundamental harmonic (3000 rpm, $T_{em}^{*}=50\%\ T_n$).

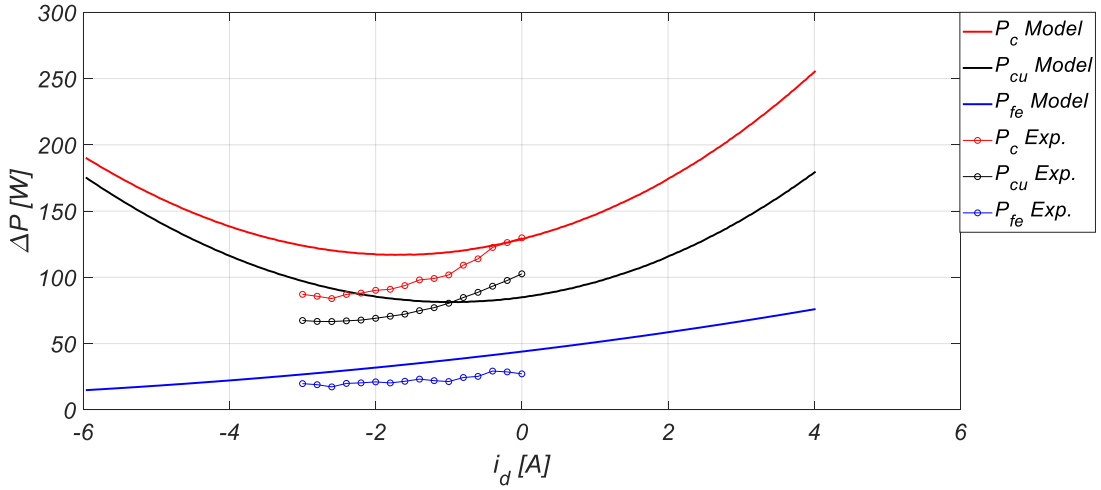

Fig. 60 Comparison between each component of controllable losses obtained from constant parameter loss model and from experimental investigation at fundamental harmonic (3000 rpm, T_{em}^{*}=100% T_n).

These results are justified by the increase in the mechanical speed and the applied load which results in an increase in the absorbed current which determines parametric variations that are not taken into consideration by this loss model. The same investigation has been performed for the variable parameters loss model. In particular, in Fig. 61, Fig. 62 and Fig. 63 the comparison between each component of controllable losses obtained from the variable parameter loss model and from the experimental investigation, at fundamental harmonic, at 2000 rpm and for no-load condition, applied load torque equal to 50% and 100% of rated load, are shown, respectively.

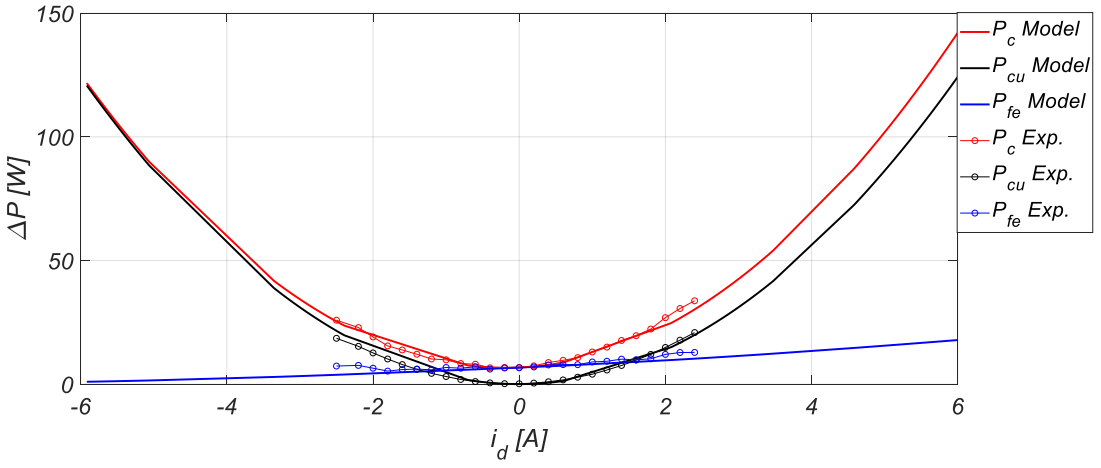

Fig. 61 Comparison between each component of controllable losses obtained from the variable parameter loss model and from the experimental investigation at fundamental harmonic (2000 rpm, T_{em}^{*}=0% T_n).

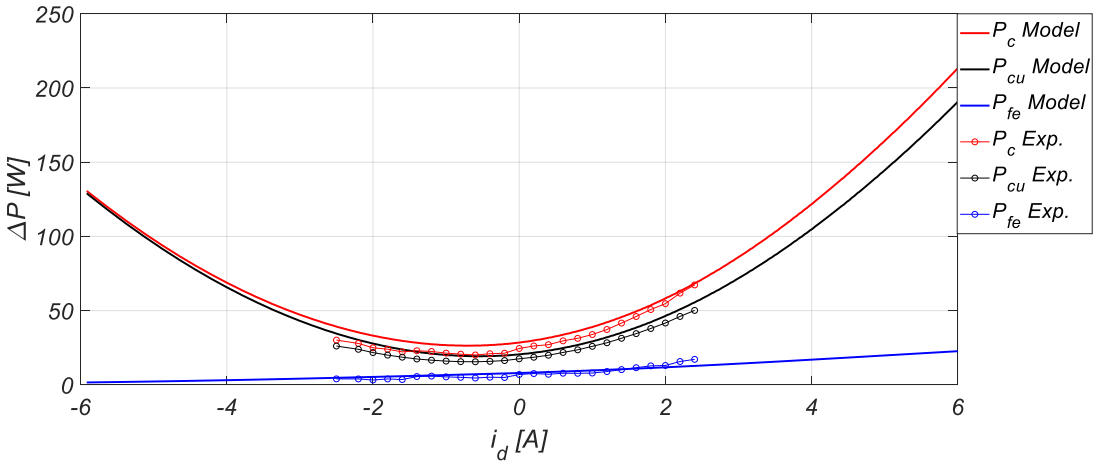

Fig. 62 Comparison between each component of controllable losses obtained from the variable parameter loss model and from the experimental investigation at fundamental harmonic (2000 rpm, T_{em}^{*}=50% T_n).

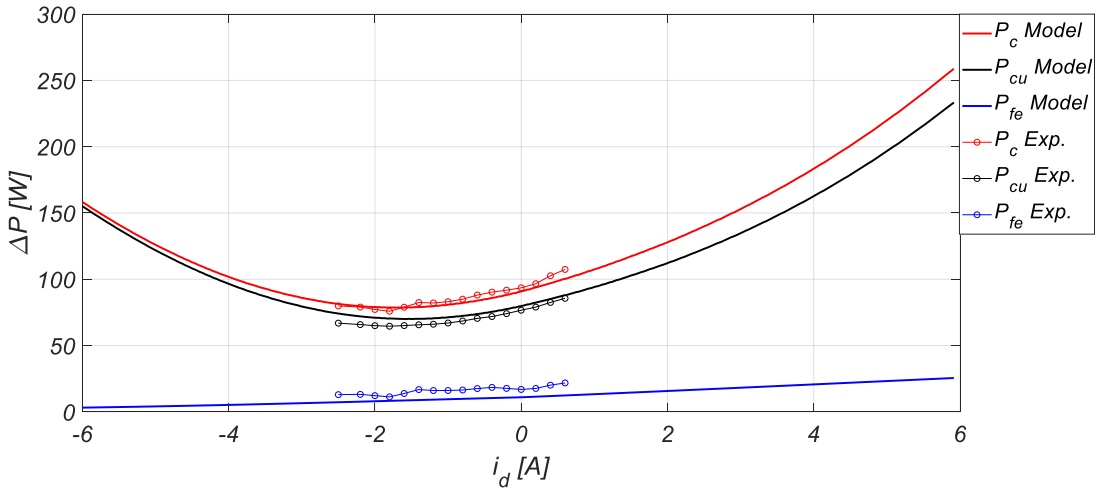

Fig. 63 Comparison between each component of controllable losses obtained from the variable parameter loss model and from the experimental investigation at fundamental harmonic (2000 rpm, T_{em}^{*}=100% T_n).

In this case, as it possible to be noticed, the controllable losses evaluated with the variable parameters loss model are more accurate compared to the previous ones when the applied load increases. Similar results are obtained also for high-speed values. This behaviour can be appreciated by the results reported in Fig. 64, Fig. 65 and Fig. 66, where the comparisons between the controllable losses of variable parameters loss model and those obtained from experimental investigations, at nominal mechanical speed of 4000 rpm, at same torque load conditions, are reported.

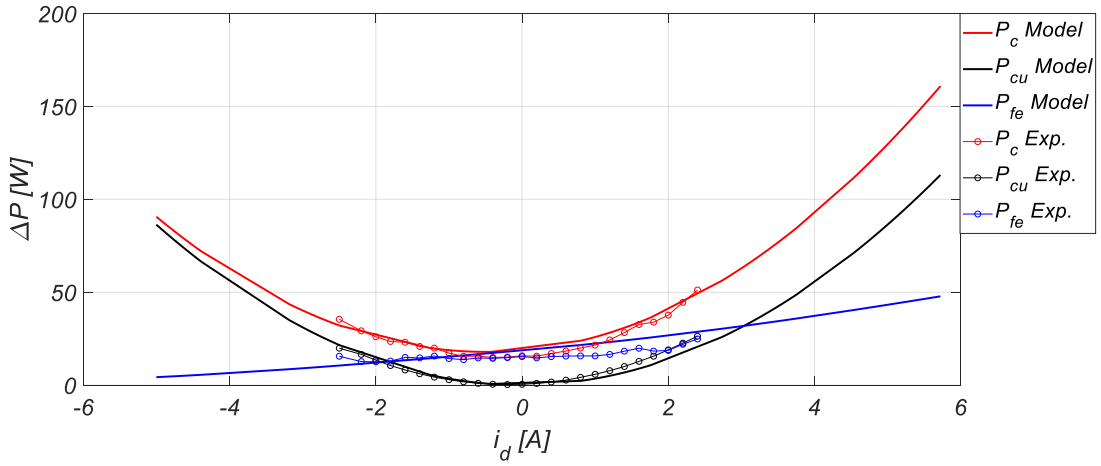

Fig. 64 Comparison between each component of controllable losses obtained from the variable parameter loss model and from the experimental investigation at fundamental harmonic (4000 rpm, T_{em}^{*}=0% T_n).

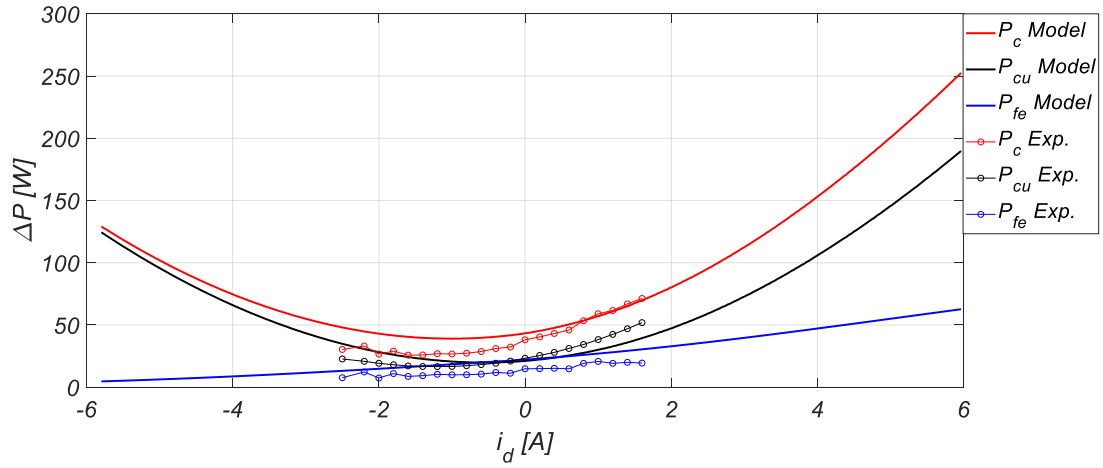

Fig. 65 Comparison between each component of controllable losses obtained from the variable parameter loss model and from experimental investigation at fundamental harmonic (4000 rpm, T_{em}^{*}=50% T_n).

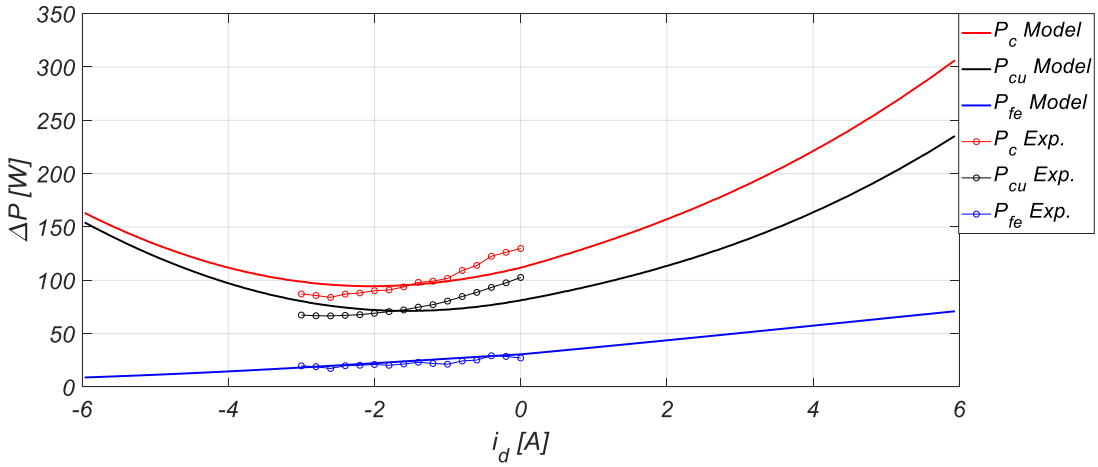

Fig. 66 Comparison between each component of controllable losses obtained from the variable parameter loss model and from the experimental investigation at fundamental harmonic (4000 rpm, T_{em}^{*}=100% T_n).

The analysis for the other reference speeds and torque load conditions provides similar results with respect to the study cases described. Therefore, it is possible to assert that taking into consideration the parameter variations determines a greater accuracy in the estimation of controllable losses at the fundamental harmonic. Particular attention must be paid to minimum loss operating points, especially to the value of *d*-axis current i_d where they are detected. This analysis is fundamental since the *d*-axis current i_d is the control variable of LMAs. Therefore, in Table 8, Table 9, Table 10 and Table 11 the minimum loss operating points detected with constant parameters model (*LM1*), with variable parameters model (*LM2*) and experimental tests at fundamental harmonic are reported (*Tests 1st harmonic*).

Table 8 Minimum loss operating points detected with LM1, LM2 and experimental test at fundamental harmonic at 1000 rpm.

ω_r=1000 rpm	*LM1*		*LM2*		*Tests 1st harmonic*	
	$i_{d\ LM1}$ [A]	$P_{c\ LM1}$ [W]	$i_{d\ LM2}$[A]	$P_{c\ LM2}$[W]	$i_{d\ exp}$ [A]	$P_{c\ exp}$[W]
T_{em}=0% T_n	-0.055	1.953	-0.075	2.732	-0.2	1.608
T_{em}=25% T_n	-0.055	7.230	-0.265	8.075	0	4.354
T_{em}=50% T_n	-0.215	21.999	-0.565	21.880	-0.8	18.572
T_{em}=75% T_n	-0.585	46.026	-1.106	43.019	-0.8	43.914
T_{em}=100% T_n	-0.986	78.667	-1.626	72.868	-1.4	72.360

Table 9 Minimum loss operating points detected with LM1, LM2 and experimental test at fundamental harmonic at 2000 rpm.

ω_r=2000 rpm	*LM1*		*LM2*		*Tests 1st harmonic*	
	$i_{d\ LM1}$ [A]	$P_{c\ LM2}$ [W]	$i_{d\ LM2}$[A]	$P_{c\ LM2}$[W]	$i_{d\ exp}$ [A]	$P_{c\ exp}$[W]
T_{em}=0% T_n	-0.135	7.769	-0.174	6.645	-0.4	6.620
T_{em}=25% T_n	-0.195	13.462	-0.390	12.253	-0.4	8.064
T_{em}=50% T_n	-0.505	28.883	-0.751	26.349	-0.6	20.114
T_{em}=75% T_n	-0.655	53.684	-1.255	47.917	-1.8	47.254
T_{em}=100% T_n	-1.146	87.258	1.832	78.597	-1.8	75.860

Table 10 Minimum loss operating points detected with LM1, LM2 and experimental test at fundamental harmonic at 3000 rpm.

ω_r=3000 rpm	LM1		LM2		Tests 1st harmonic	
	$i_{d\,LM1}$ [A]	$P_{c\,LM2}$ [W]	$i_{d\,LM2}$[A]	$P_{c\,LM2}$[W]	$i_{d\,exp}$ [A]	$P_{c\,exp}$[W]
T_{em}=0% T_n	-0.175	17.230	-0.311	11.570	-0.2	4.810
T_{em}=25% T_n	-0.605	23.232	-0.53	17.450	-0.8	8.504
T_{em}=50% T_n	-0.766	39.451	-0.857	31.886	-1.4	24.870
T_{em}=75% T_n	-0.986	65.323	-1.337	53.99	-1.4	48.986
T_{em}=100% T_n	-1.416	100.164	-1.774	85.489	-1.6	87.822

Table 11 Minimum loss operating points detected with LM1, LM2 and experimental test at fundamental harmonic at 4000 rpm.

ω_r=4000 rpm	LM1		LM2		Tests 1st harmonic	
	$i_{d\,LM1}$ [A]	$P_{c\,LM2}$ [W]	$i_{d\,LM2}$[A]	$P_{c\,LM2}$[W]	$i_{d\,exp}$ [A]	$P_{c\,exp}$[W]
T_{em}=0% T_n	-0.625	29.345	-0.246	18.124	-0.4	14.898
T_{em}=25% T_n	-0.746	36.137	-0.682	24.105	-0.8	11.048
T_{em}=50% T_n	-1.036	53.279	-0.944	39.010	-1.6	25.800
T_{em}=75% T_n	-1.296	80.376	-1.403	61.780	-2	52.460
T_{em}=100% T_n	-1.776	116.927	-1.982	94.440	-2.4	83.980

The minimum loss operating points of the loss model, which are closer to those found experimentally, are highlighted in green. As it is possible to notice, the variable parameters loss model provides *d*-axis current value more accurate in comparison to those obtained with constant parameters loss model in most of the analyzed working conditions. In detail, the performances of the variable parameter loss model are better at high load torque and, only for low load torque, are slightly worse or comparable than those obtained with constant parameter loss model. Moreover, the controllable losses, detected with experimental investigations, show a decreasing trend as the current i_d increases towards negative values, especially for medium/high load torque. Therefore, since the detected values of the current i_d with constant loss parameters model are higher than those obtained with the variable parameter loss model, the latter leads to lower controllable losses.

In order to evaluate the possible real impact of LMAs, that employ the loss models described, about the overall performance of the electrical drive, an additional analysis is performed about the losses evaluated by considering the entire harmonic content of electrical quantities. In detail, the comparisons between the controllable losses of constant parameters loss model and those obtained from experimental investigations at 1000 rpm, evaluated on the entire harmonic content of the electrical quantities, are reported in Fig. 67, Fig. 68 and Fig. 69.

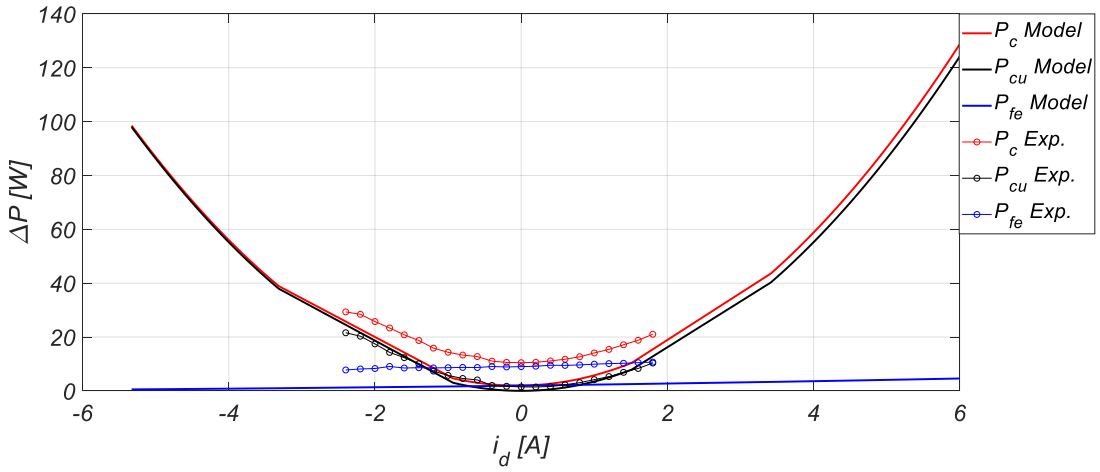

Fig. 67 Comparison between each component of controllable losses obtained from constant parameter loss model and from experimental investigation at entire harmonic content (1000 rpm, T_{em}^{*}=0% T_n).

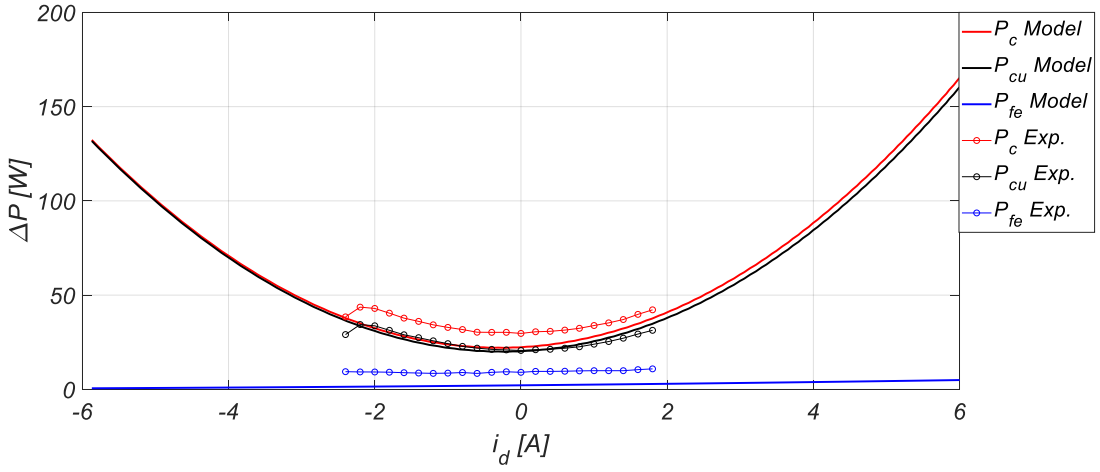

Fig. 68 Comparison between each component of controllable losses obtained from constant parameter loss model and from experimental investigation at entire harmonic content (1000 rpm, T_{em}^{*}=50% T_n).

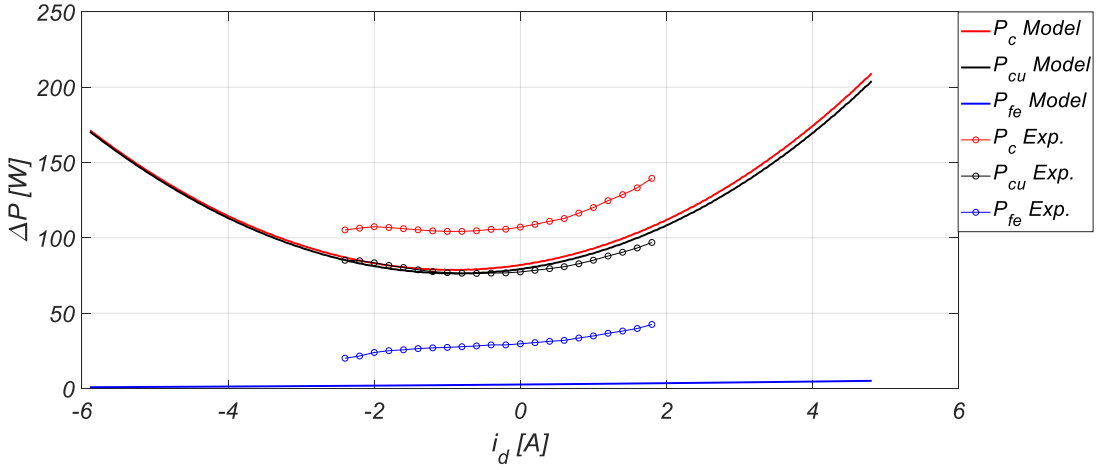

Fig. 69 Comparison between each component of controllable losses obtained from constant parameter loss model and from experimental investigation at entire harmonic content (1000 rpm, T_{em}^{*}=100% T_n).

As it is possible to notice, the controllable losses evaluated with constant parameters loss model present a lower amplitude in comparison with those obtained from experimental investigations. In particular, the difference between the total controllable losses obtained can be attributed to the difference between the amplitudes of the iron losses, unlike those of copper which are very similar. This behaviour can be explained on the base that the absorbed currents by the machine present reduced harmonic content, due to the filtering action of the machine inductances, while the applied voltage present high harmonic content, due to the Pulse Width Modulation (PWM) of the inverter. Moreover, as the speed increases, similar results have been obtained. By way of example, the comparisons between the controllable losses of constant parameters loss model and those obtained from experimental investigations at 3000 rpm are reported in Fig. 70, Fig. 71 and Fig. 72.

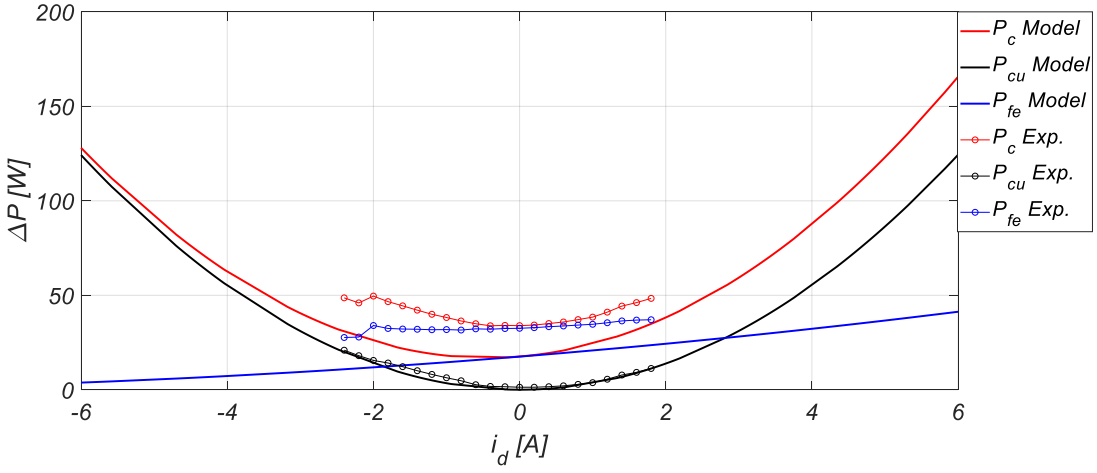

Fig. 70 Comparison between each component of controllable losses obtained from constant parameter loss model and from experimental investigation at entire harmonic content (3000 rpm, T_{em}^{*}=0% T_n).

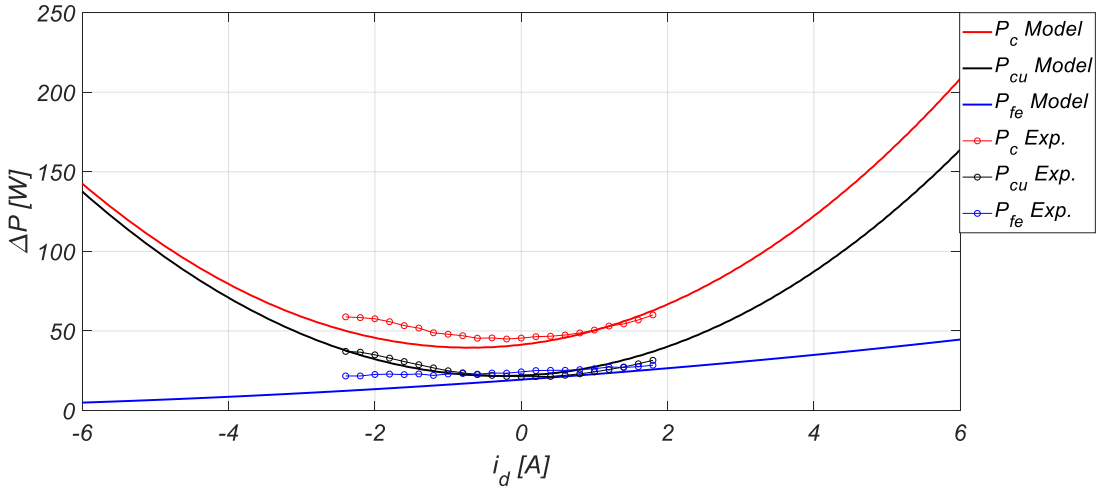

Fig. 71 Comparison between each component of controllable losses obtained from constant parameter loss model and from experimental investigation at entire harmonic content (3000 rpm, T_{em}^{*}=50% T_n).

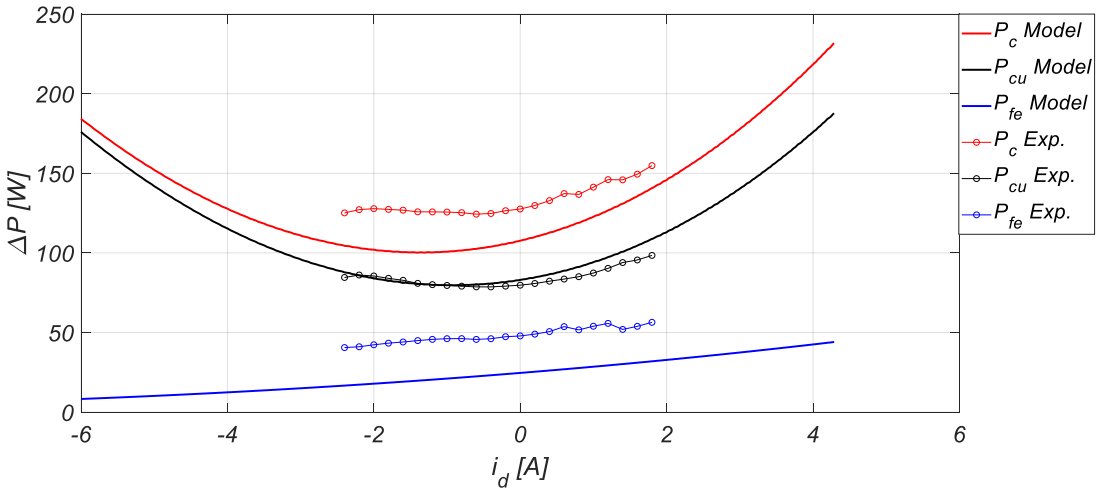

Fig. 72 Comparison between each component of controllable losses obtained from constant parameter loss model and from experimental investigation at entire harmonic content (3000 rpm, T_{em}^{*}=0% T_n).

The same investigation has been performed for the variable parameters loss model. In particular, the comparison between each component of controllable losses obtained from the variable parameter loss model and from experimental investigation, evaluated on the entire harmonic content of the electrical quantities, at 1000 rpm and for no-load condition, applied load torque equal to 50% and 100% of rated load, are shown in Fig. 73, Fig. 74 and Fig. 75, respectively.

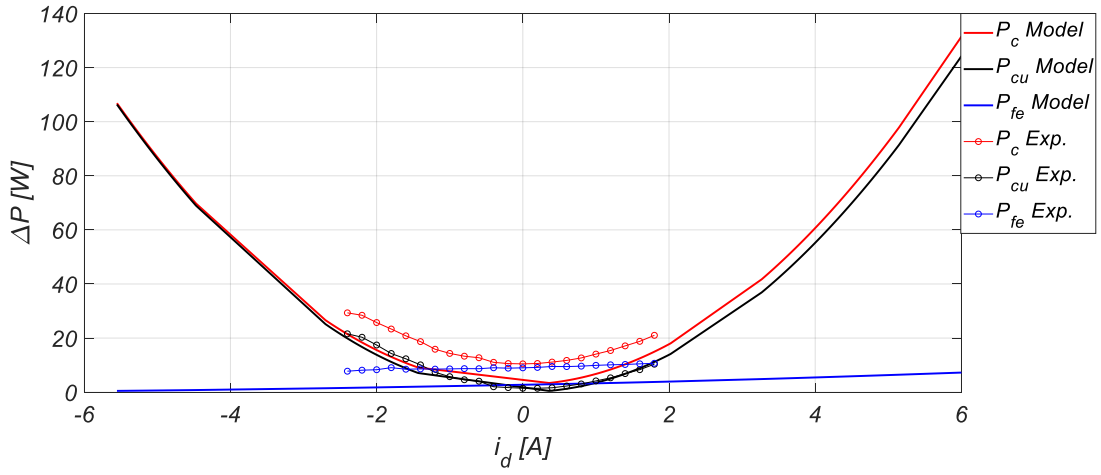

Fig. 73 Comparison between each component of controllable losses obtained from variable parameter loss model and from experimental investigation at entire harmonic content (1000 rpm, T_{em}^{*}=0% T_n).

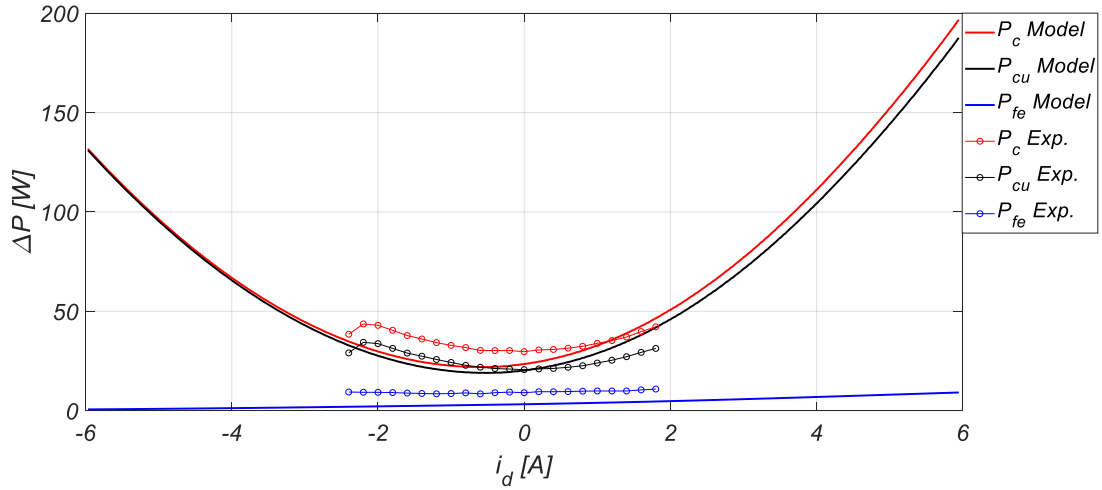

Fig. 74 Comparison between each component of controllable losses obtained from the variable parameter loss model and from experimental investigation at entire harmonic content (1000 rpm, T_{em}^{*}=50% T_n).

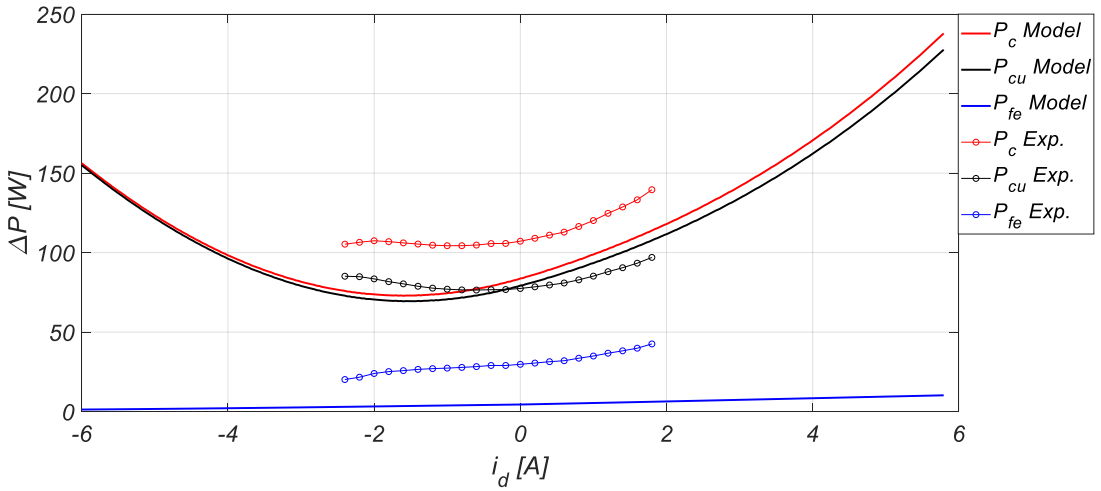

Fig. 75 Comparison between each component of controllable losses obtained from the variable parameter loss model and from the experimental investigation at entire harmonic content (1000 rpm, T_{em}^{*}=100% T_n).

Also in this case, for the same reasons before mentioned, the controllable losses evaluated with the variable parameters model present lower amplitude in comparison with those obtained from experimental investigations. Compared to the previous case, when the applied load torque increases, there is a greater difference between the estimated copper losses and those obtained from the experimental investigations. Moreover, as the speed increases, similar results have been obtained. By way of example, the comparisons between the controllable losses of variable parameters loss model and those obtained from experimental investigations at 3000 rpm are reported in Fig. 76, Fig. 77 and Fig. 78.

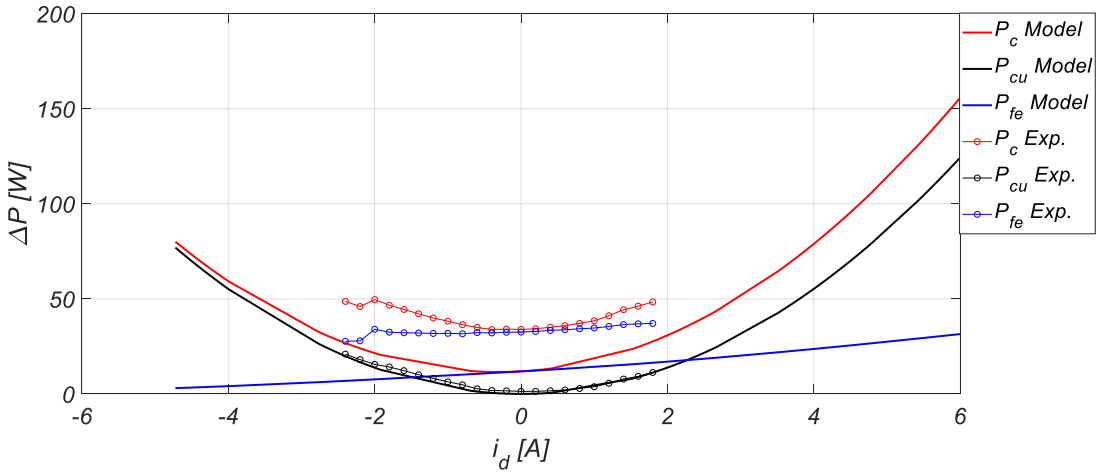

Fig. 76 Comparison between each component of controllable losses obtained from the variable parameter loss model and from the experimental investigation at entire harmonic content (3000 rpm, T_{em}^{*}=0% T_n).

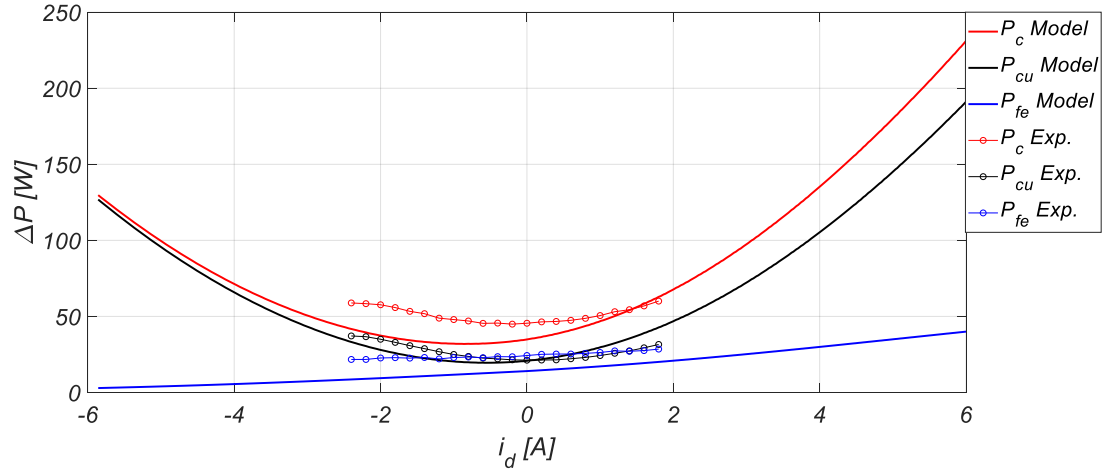

Fig. 77 Comparison between each component of controllable losses obtained from the variable parameter loss model and from the experimental investigation at entire harmonic content (3000 rpm, T_{em}^{*}=50% T_n).

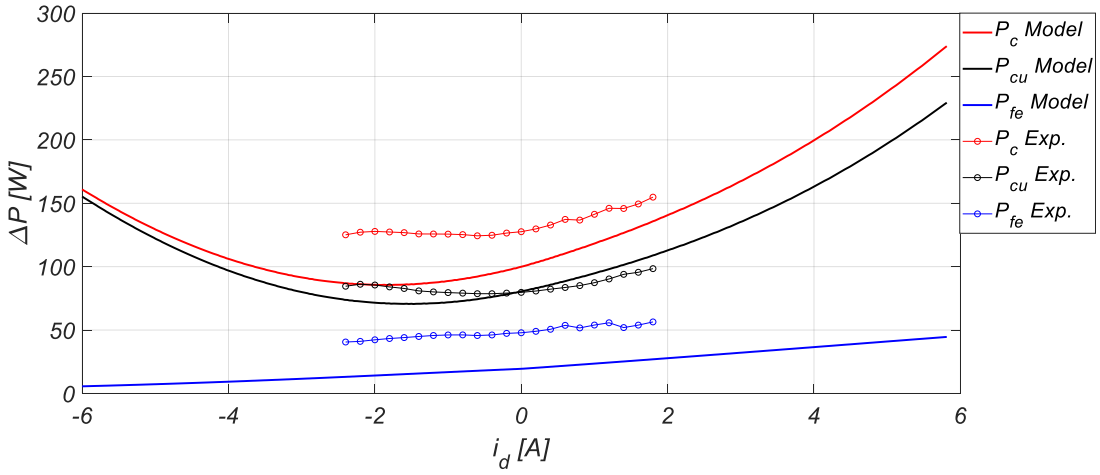

Fig. 78 Comparison between each component of controllable losses obtained from the variable parameter loss model and from the experimental investigation at entire harmonic content (3000 rpm, T_{em}^{*}=100% T_n).

The analysis for the other reference speeds and torque load conditions provides similar results with respect to the study cases described. Particular attention must be paid to minimum loss operating points, especially to the value of *d*-axis current i_d where they are detected. In Table 12, Table 13, Table 14 and Table 15 the minimum loss operating points detected with constant parameters model (*LM1*), with variable parameters model (*LM2*) and experimental tests at entire harmonic content are reported (*Tests-all harmonics*).

Table 12 Minimum loss operating points detected with LM1, LM2 and experimental test at entire harmonic content, at 1000 rpm.

ω_r=1000 rpm	*LM1*		*LM2*		*Tests-all harmonics*	
	$i_{d\,LM1}$ [A]	$P_{c\,LM1}$ [W]	$i_{d\,LM2}$[A]	$P_{c\,LM2}$[W]	$i_{d\,exp}$ [A]	$P_{c\,exp}$[W]
T_{em}=0% T_n	-0.055	1.953	-0.0751	2.732	0	10.46
T_{em}=25% T_n	-0.055	7.231	-0.265	8.075	0	12.843
T_{em}=50% T_n	-0.215	21.999	-0.565	21.88	0	29.673
T_{em}=75% T_n	-0.585	46.026	-1.106	43.019	-0.2	57.510
T_{em}=100% T_n	-0.986	78.667	-1.626	72.868	-1	104.33

Table 13 Minimum loss operating points detected with LM1, LM2, and experimental test at entire harmonic content, at 2000 rpm.

ω_r=2000 rpm	*LM1*		*LM2*		*Tests-all harmonics*	
	$i_{d\,LM1}$ [A]	$P_{c\,LM2}$ [W]	$i_{d\,LM2}$[A]	$P_{c\,LM2}$[W]	$i_{d\,exp}$ [A]	$P_{c\,exp}$[W]
T_{em}=0% T_n	-0.1353	7.7691	-0.174	6.645	-0.2	21.997
T_{em}=25% T_n	-0.195	13.462	-0.390	12.253	-0.2	18.460
T_{em}=50% T_n	-0.505	28.883	-0.751	26.349	-0.2	36.510
T_{em}=75% T_n	-0.655	53.684	-1.255	47.917	-0.4	66.990
T_{em}=100% T_n	-1.146	87.258	1.832	78.597	-0.8	114.28

Table 14 Minimum loss operating points detected with LM1, LM2, and experimental test entire harmonic content, at 3000 rpm.

ω_r=3000 rpm	*LM1*		*LM2*		*Tests-all harmonics*	
	$i_{d\,LM1}$ [A]	$P_{c\,LM2}$ [W]	$i_{d\,LM2}$[A]	$P_{c\,LM2}$[W]	$i_{d\,exp}$ [A]	$P_{c\,exp}$[W]
T_{em}=0% T_n	-0.175	17.230	-0.311	11.570	-0.4	33.890
T_{em}=25% T_n	-0.605	23.232	-0.530	17.450	0	26.667
T_{em}=50% T_n	-0.766	39.451	-0.857	31.886	-0.2	44.920
T_{em}=75% T_n	-0.986	65.323	-1.337	53.990	0	76.300
T_{em}=100% T_n	-1.416	100.164	-1.774	85.489	-0.8	124.330

Table 15 Minimum loss operating points detected with LM1, LM2, and experimental test at entire harmonic content, at 4000 rpm.

ω_r=4000 rpm	*LM1*		*LM2*		*Tests-all harmonics*	
	$i_{d\,LM1}$ [A]	$P_{c\,LM2}$ [W]	$i_{d\,LM2}$[A]	$P_{c\,LM2}$[W]	$i_{d\,exp}$ [A]	$P_{c\,exp}$[W]
T_{em}=0% T_n	-0.625	29.345	-0.246	18.124	-0.4	46.983
T_{em}=25% T_n	-0.746	36.137	-0.682	24.105	0	36.307
T_{em}=50% T_n	-1.036	53.280	-0.944	39.010	-0.4	49.578
T_{em}=75% T_n	-1.296	80.376	-1.403	61.780	-0.4	86.077
T_{em}=100% T_n	-1.776	116.927	-1.982	94.440	-1	135.530

As it is possible to notice, the minimum loss operating points have been identified in correspondence of i_d negative value lower than those identified in the tests at fundamental harmonic, especially for high load torque ($T_{em}^* \geq 50\%\ T_n$). Furthermore, the variation of the i_d values of minimum loss operating points is very reduced respect those

of the tests at fundamental harmonic, both when the applied load torque and reference speed varies. Similar results are obtained for the losses of the entire power drive system (PDS), which includes the losses of the inverter. Regarding the controllable losses obtained from the experimental tests at entire harmonic content, as opposed to those obtained from the fundamental harmonic tests, they have comparable values for different negative values of i_d or their variation is very limited in amplitude, especially for high load torque. All this implies, that a significant variation of the i_d current corresponds to very small or negligible variations in overall controllable losses and consequently making the action of the LMAs ineffective. In order to highlight this result, in Table 16, Table 17, Table 18 and Table 19 the minimum loss operating points of IPMSM and PDS detected with experimental tests are reported.

Table 16 Minimum loss operating points of IPMSM and PDS detected with the experimental test at 1000 rpm.

ω_r=1000 rpm	IPMSM-1st harmonic		IPMSM-all harmonics		PDS-all harmonics	
	$i_{d\,exp}$ [A]	$i_{d\,exp}$ [A]	$i_{d\,exp}$ [A]	$P_{c\,LM2}$[W]	$i_{d\,exp}$ [A]	$P_{c\,exp}$[W]
T_{em}=0% T_n	-0.2	1.608	0	10.460	0	19.420
T_{em}=25% T_n	0	4.354	0	12.843	0	27.340
T_{em}=50% T_n	-0.8	18.572	0	29.673	-0.2	50.370
T_{em}=75% T_n	-0.8	43.914	-0.2	57.510	-0.4	84
T_{em}=100% T_n	-1.4	72.360	-1	104.330	-1	138.430

Table 17 Minimum loss operating points of IPMSM and PDS detected with the experimental test at 2000 rpm.

ω_r=2000 rpm	IPMSM-1st harmonic		IPMSM-all harmonics		PDS-all harmonics	
	$i_{d\,exp}$ [A]	$i_{d\,exp}$ [A]	$i_{d\,exp}$ [A]	$P_{c\,LM2}$[W]	$i_{d\,exp}$ [A]	$P_{c\,exp}$[W]
T_{em}=0% T_n	-0.4	6.620	-0.2	21.997	0	30.420
T_{em}=25% T_n	-0.4	8.064	-0.2	18.460	-0.2	34
T_{em}=50% T_n	-0.6	20.114	-0.2	36.510	-0.2	58.470
T_{em}=75% T_n	-1.8	47.254	-0.4	66.990	-0.6	96.130
T_{em}=100% T_n	-1.8	75.860	-0.8	114.280	-1	151.470

Table 18 Minimum loss operating points of IPMSM and PDS detected with the experimental test at 1000 rpm.

ω_r=3000 rpm	IPMSM-1st harmonic		IPMSM-all harmonics		PDS-all harmonics	
	$i_{d\,exp}$ [A]	$i_{d\,exp}$ [A]	$i_{d\,exp}$ [A]	$P_{c\,LM2}$[W]	$i_{d\,exp}$ [A]	$P_{c\,exp}$[W]
T_{em}=0% T_n	-0.2	4.810	-0.4	33.890	-0.2	41.20
T_{em}=25% T_n	-0.8	8.504	0	26.667	-0.2	48.47
T_{em}=50% T_n	-1.4	24.870	-0.2	44.920	-0.4	68.47
T_{em}=75% T_n	-1.4	48.986	0	76.300	-0.4	107.87
T_{em}=100% T_n	-1.6	87.822	-0.8	124.330	-1.2	166

Table 19 Minimum loss operating points of IPMSM and PDS detected with the experimental test at 4000 rpm.

ω_r=3000 rpm	IPMSM-1st harmonic		IPMSM-all harmonics		PDS-all harmonics	
	$i_{d\,exp}$ [A]	$i_{d\,exp}$ [A]	$i_{d\,exp}$ [A]	$P_{c\,LM2}$[W]	$i_{d\,exp}$ [A]	$P_{c\,exp}$[W]
T_{em}=0% T_n	-0.4	14.898	-0.4	46.983	0	52.50
T_{em}=25% T_n	-0.8	11.0478	0	36.307	0	54.23
T_{em}=50% T_n	-1.6	25.800	-0.4	49.578	-0.2	75.93
T_{em}=75% T_n	-2	52.460	-0.4	86.077	-0.4	121.23
T_{em}=100% T_n	-2.4	83.980	-1	135.530	-1	181.30

From results reported, it is possible to deduce that the values of i_d current of minimum loss operating points of PDS are similar to those detected for IPMSM at the correspondence of the entire harmonic content of electrical quantities. These results undoubtedly assert that the performances of the electric drive deriving from the use of LMAs, based on a mathematical model defined at the fundamental harmonic, should not be evaluated only with respect to the fundamental harmonic of the electrical quantities, but they must be evaluated with respect to the entire harmonic content of the same quantities.

2.6 Discussion and considerations

The conducted analysis at fundamental harmonic shows that the use of LMA based on loss model, that take into account the parameters variation with the working operating conditions, would allow obtaining better performances in terms of efficiency on the electric drive under test than the those obtainable with LMA based on constant parameters loss model. However, if we refer to the experimental analysis carried out with respect to the entire harmonic content of the electrical quantities, it is clear that the performances of the two loss models are comparable. This study highlights how the harmonics of electrical quantities, such as supply voltages and absorbed currents, generate a no-negligible contribution of active power with respect to that evaluated at the fundamental harmonic and such as to compromise the effectiveness of the LMAs based on IPMSM mathematical models defined at fundamental harmonic. Although this result may be characteristic of the electric drive under test, and different results can be obtained for other electric drives especially for high power electrical drives, it is necessary to highlight some critical aspects identified during the experimental investigations. In detail, a crucial aspect concern to make an accurate analysis of the harmonic contents of the electrical quantities and to identify the frequency limit beyond which any power contributions are negligible. This analysis is fundamental for the accurate selection of the sampling frequencies.

Another critical aspect found concerns the measurement of the active power absorbed at the input section both of the motor and the PDS. In particular, at steady-state conditions, it presents no-neglible variations that make its average estimate complex to achieve. This behaviour must certainly be attributed to the controller that acts instant by instant on the control variables or the inverter used. Therefore, in order to evaluate the efficiency or the power losses of the electrical drive in an accurate way and make the active power variations negligible, it is necessary to carry out an analysis at the mean values with respect to the time.

In addition, particular attention must be paid to the uncertainty of measurement concerning both systematic and random errors, identifying possible causes and actions to be taken to limit their effects. Therefore, any benefits deriving from the use of a control algorithm require the accurate determination of the efficiency of the electric drive being tested. In the experimental investigations carried out, these aspects have not

been neglected, and specific measures have been taken regarding the measurement instruments used, such as the choice of high sampling rates. However, the three-phase power analyzers used are not very flexible to carry out accurate investigations on the critical aspects listed. By way of example, the three-phase power analyzers are equipped with a function that evaluates the average value of the quantities of interest on multiple acquisitions but with pre-implemented mathematical relationships that cannot be modified. In the next chapter, in order to define an accurate way to estimate the efficiency of the electric drives, these aspects will be addressed and accurately analyzed.

References

[II.1]. IEC Pub. 34-4: Methods for determining synchronous machine quantities from tests, 1985.

[II.2]. R. Dutta, M.F. Rahman, “A Comparative Analysis of Two Test Methods of Measuring d-q Axes Inductances of Interior Permanent- Magnet Machine”, IEEE Transactions on Magnetics, Vol.42, Issue.11, pp.3712-3718, Nov 2006.

[II.3]. Yuting Gao, Ronghai Qu and Yang Liu, "An improved AC standstill method for inductance measurement of interior permanent magnet synchronous motors," 2013 International Conference on Electrical Machines and Systems (ICEMS), Busan, 2013, pp. 927-931.

[II.4]. M. Kazerooni and N. C. Kar, "Methods for determining the parameters and characteristics of PMSM," 2011 IEEE International Electric Machines & Drives Conference (IEMDC), Niagara Falls, ON, 2011, pp. 955-960.

[II.5]. H. B. Ertan and İ. Şahin, "Evaluation of inductance measurement methods for PM machines," 2012 XXth International Conference on Electrical Machines, Marseille, 2012, pp. 1672-1678.

[II.6]. S. A. Odhano, R. Bojoi, M. Popescu and A. Tenconi, "Parameter identification and self-commissioning of AC permanent magnet machines - A review," 2015 IEEE Workshop on Electrical Machines Design, Control and Diagnosis (WEMDCD), Torino, 2015, pp. 195-203.

[II.7]. S. A. Odhano et al., "Identification of Three-Phase IPM Machine Parameters Using Torque Tests," in IEEE Transactions on Industry Applications, vol. 53, no. 3, pp. 1883-1891, May-June 2017.

[II.8]. V. Rallabandi, N. Taran, D. M. Ionel and P. Zhou, "Inductance testing according to the new IEEE Std 1812-application and possible extensions for IPM machines," *2017 IEEE Energy Conversion Congress and Exposition (ECCE)*, Cincinnati, OH, 2017, pp. 4302-4308.

[II.9]. “IEEE trial-use guide for testing permanent magnet machines,” IEEE Std 1812-2014, pp. 1–56, Feb 2015.

[II.10]. J. G. Cintron-Rivera, A. S. Babel, E. E. Montalvo-Ortiz, S. N. Foster and E. G. Strangas, "A simplified characterization method including saturation

effects for permanent magnet Machines," 2012 XXth International Conference on Electrical Machines, Marseille, 2012, pp. 837-843.

[II.11]. S. Hall, F. J. Márquez-Fernández and M. Alaküla, "Dynamic Magnetic Model Identification of Permanent Magnet Synchronous Machines," in IEEE Transactions on Energy Conversion, vol. 32, no. 4, pp. 1367-1375, Dec. 2017.

[II.12]. S. Wiedemann, S. Hall, R. M. Kennel and M. Alaküla, "Dynamic Testing Characterization of a Synchronous Reluctance Machine," in IEEE Transactions on Industry Applications, vol. 54, no. 2, pp. 1370-1378, March-April 2018.

Chapter 3 Efficiency measurement of electric drives equipped with IPMSM

3.1 Introduction

The achievement of high efficiency, in the electric drives field, leads to a reduction in the total power losses and therefore a considerable energy saving. Following the instructions of the various performance standards required for the electric motors and drives, it is now very important to evaluate their performance with the most accurate measurement methods possible. In recent years, standardized methods have been recently proposed and discussed in the literature in order to determine the efficiency of electric drives [III.1]-[III.10]. In detail, until to the 2014/2015, the only existing international standards were the standard IEC 60034-2-1/2 [III.1]-[III.2], that describe the standard methods for determining losses and efficiency from tests of rotating electrical machines fed by electrical grid, and the standard IEC 60034-2-3 [III.3], that describes the specific test methods for determining losses and efficiency of converter-fed AC induction motors. These international standards are an excellent reference for induction machines, dc machines, and wound-field synchronous machines but there are not specific prescriptions with regard to PMSMs. Moreover, the machines for traction vehicles are not part of the application fields of these international standards. The recent guide IEEE Std 1812-2014 [III.4] describes the instructions for conducting tests to determine the performance characteristics and machine parameters of PMSMs. This last reference focuses on the determination of the parameters and the efficiency of PMSMs but does not provide clear and detailed instructions on determining the efficiency of the whole electric drive. In this sense, the new standard IEC 61800-9 [III.5]-[III.6] tries to fill the gaps present in the previous international standards, describing not only the test methods for determining the efficiency of the machine fed by power electronics converters but also the efficiency of each component of the adjustable speed electrical power drive systems and, therefore, the total efficiency of electrical drive. In this chapter, the prescriptions of standards IEC 60034-2, IEEE Std 1812-2014 and IEC 61800-9 are presented and discussed. Furthermore, with reference to the topic of comparison between the performances of the electric drive controlled with different control algorithms, an innovative method for determining the efficiency variation of the

adjustable speed electrical power drive systems is described. In detail, the design of the test bench and the experimental validations are described and discussed.

3.2 Measurement methods of electric drives efficiency

The efficiency of any electrical machines or any other energy system is defined as the ratio between the output power P_{out} and the input power P_{in}:

$$\eta = \frac{P_{out}}{P_{in}} \tag{3.1}$$

The efficiency is an index of the system ability to limit the losses that are inevitably present. Referring to the field of electrical drives, the international standard IEC 61800-9 defines the electrical drive as an extended product (EP) formed by several parts (Fig. 79). In details, there are:

- the complete drive module (CDM) consisting of the electronic power converter connected between the electric supply and a motor as well as extensions such as protection devices, transformers, and auxiliaries;
- the power drive system (PDS) that includes CDM and the motor;
- the motor system (MS) that includes the PDS and motor control equipment (motor starter, contactor, etc);
- the driven equipment (DE) consisting of equipment mechanically connected to the shaft of the motor, including the load.

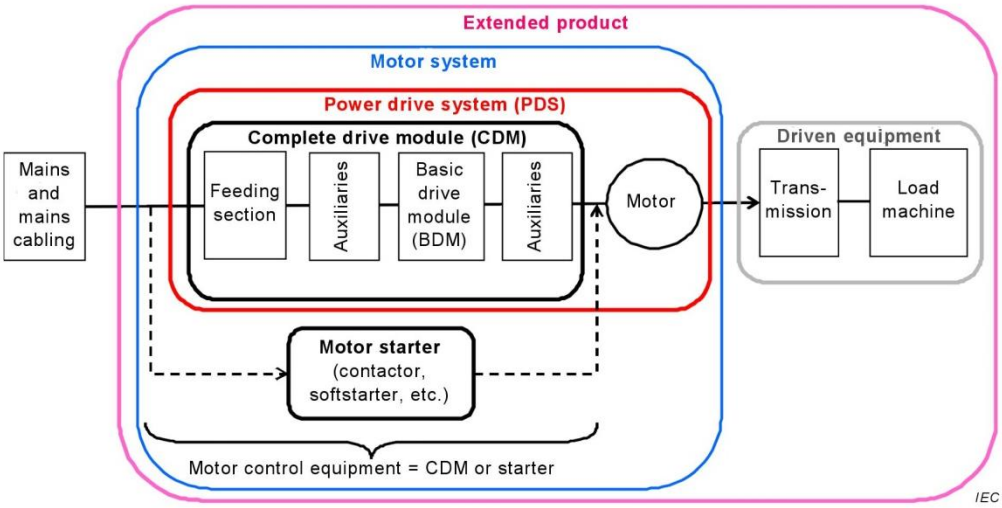

Fig. 79 Illustration of the extended product (EP).

For the purpose of this research work on the electrical drive described in the previous chapter, the electrical drive diagram, reported in Fig. 80, will be used as reference.

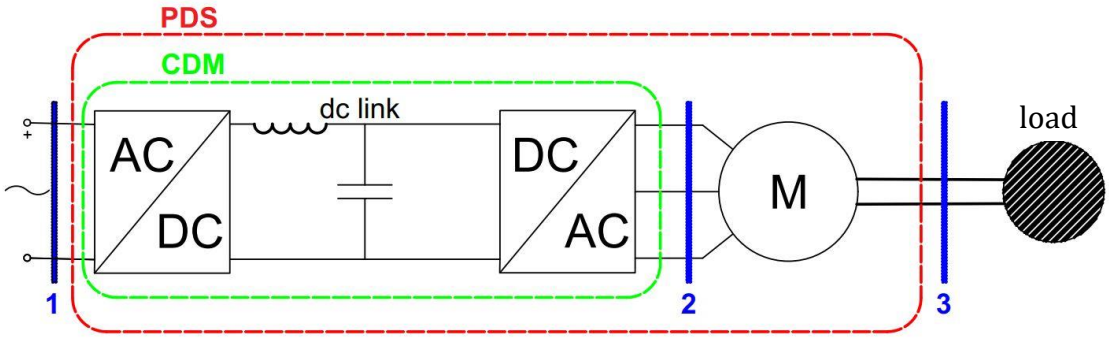

Fig. 80 Diagram of electrical drive.

In detail, the input section of PDS (1), the output section of CDM (2) and the output section of PDS (3) are highlighted with blue segments. Therefore it is possible to define the efficiency of PDS, the efficiency of CDM and the efficiency of the motor with the following relationships:

$$\eta_{PDS} = \frac{P_3}{P_1} \tag{3.2}$$

$$\eta_{CDM} = \frac{P_2}{P_1} \tag{3.3}$$

$$\eta_M = \frac{P_3}{P_2} \tag{3.4}$$

Therefore, it is possible to estimate each efficiency component by means the measurement of the electrical power at the PDS input section, at the CDM output section and the mechanical power at the motor output section. This procedure represents the direct measurement method of the PDS efficiency. Otherwise, it is possible to estimate each efficiency component with an indirect measurement method that requires the estimation of each component of power losses and, consequently, the total power losses ΔP. To measure the efficiency of an electric machine with the indirect method, the standard IEC 60034-2-1 provides the following relationships:

$$\eta = \frac{P_{in} - \Delta P}{P_{in}} \tag{3.5}$$

$$\eta = \frac{P_{out}}{P_{out} + \Delta P} \tag{3.6}$$

Where the equation (3.5) is suggested for motor operation, while the equation (3.6) is suggested for generator operation. In details, for the case study, the complete drive

module total losses ΔP_{CDM} and the motor total losses ΔP_M can be defined with the following relationships:

$$\Delta P_{CDM} = P_1 - P_2 \tag{3.7}$$

$$\Delta P_M = P_2 - P_3 \tag{3.8}$$

Therefore the equation for the determining of PDS efficiency with the indirect method is:

$$\eta_{PDS} = \frac{P_1 - (\Delta P_{CDM} + \Delta P_M)}{P_1} \tag{3.9}$$

In this case, the estimation of PDS efficiency requires only the measurement of the powers in each section showed before (Fig. 80). Otherwise, in order to estimate the value of ΔP_{CDM} and the ΔP_M, with indirect method, the evaluation of each component of motor power losses and of complete drive module power losses is necessary. The requirements suggested by each international standard for estimating the efficiency with direct and indirect measurement methods are described in more detail below.

3.2.1 Standard IEC 60034-2

As already mentioned, the standard IEC 60034-2-1/2 deals with the methods of measuring the efficiency of electrical machines directly connected to the electrical grid or powered with sinusoidal voltage. Instead, the standard IEC60034-2-3 concerns the induction machines powered by an inverter, or with distorted voltage and current waveforms. The main limitation of these standards is the application field that doesn't include the PMSMs, the electrical machines for traction vehicles and, regard the IEC60034-2-3, it is valid only for the induction machine. However, the main prescriptions reported in these standards can be taken into account and extended to the PMSMs. In this discussion, reference is made to the standard IEC60034-2-1, since the standard IEC60034-2-2 represents a supplement for high-power machines and, therefore, not of interest for the purposes of this work. In detail, the methods recommended for efficiency estimation by the standard IEC60034-2-1 vary depending on the size, type of machine and objective measurement uncertainty.

For induction machines with a size lower than 1 kW, the direct method is recommended as it presents lowest uncertainty. A second low uncertainty method is the method with two twin machines in mechanical opposition with separate power supplies. Between the

two methods, the first is easier to apply, since it does not require two twin machines. If the size of the induction machine is greater than 1 kW, the indirect method is required with the determination of the additional load losses starting from the residual load losses. A low uncertainty method that exploits the measurement of total losses is that with two twin machines in mechanical opposition, but with the same electrical power supply. Other methods present medium or high uncertainty. For methods that use calorimeters or calibrated machines, the standard does not provide any indication about the uncertainty. Table 20 summarizes the efficiency measurement methods described.

Table 20 Efficiency measurement methods according to IEC 60034-2-1 for induction machines.

INDUCTION MACHINES		
Method	Method suggested	Uncertainty
Direct method, including a measure of speed and torque	Single-phase and polyphase machines with $P_n \leq 1$ kW	Low
Direct method, with two twin machines in mechanical opposition, with separate power supplies		Low
Indirect method, with the determination of the additional load losses	Three-phase machines with $1\text{kW} \leq P_n \leq 150$ kW	Low
Indirect method, with two twin machines in mechanical opposition, with the same electrical power supply		Low
Calorimeter		To be determined
Calibrated machine		To be determined
Other method		Medium/High

For synchronous machines, the standard proposes similar methods. In this case, the limit within which the direct low uncertainty method can be applied is given in terms of height *H* of the shaft axis line with respect to the support plane. The method with two twin machines in mechanical opposition with separate electrical connections presents, now, medium uncertainty. See for more details the Table 21.

Table 21 Efficiency measurement methods according to IEC 60034-2-1 for synchronous machines.

SYNCHRONOUS MACHINES		
Method	Method suggested	Uncertainty
Direct method, including a measure of speed and torque	Machines with $H \leq 180$ mm	Low
Direct method, with two twin machines in mechanical opposition, with separate power supplies		Medium
Indirect method, with the determination of the additional load losses	Machines with $H > 180$ mm	Low
Indirect method, with two twin machines in mechanical opposition, with the same electrical power supply		Low
Calorimeter		To be determined
Calibrated machine		To be determined
Other method		Medium/High

Regarding the power supply voltage and frequency features, they must comply with IEC 60034-1. The standard suggests that the analog instruments should preferably be used over 2/3 of their full-scale value. The accuracy class, for the measurement of electrical

quantities, must be 0.2%. The torque meter, if used, must have an accuracy of ± 0.2% of the full-scale value. The frequency meter must have an accuracy of ± 0.2% of the full-scale value. The speed measurement should be accurate to 0.1% or 1 rpm, using the one that gives the minor error. Finally, the temperature measurement must have a precision of ± 1°C. Regarding the determination of the efficiency with the indirect method or of the separate losses, the description of the main test is reported for induction and synchronous machines.

In detail, for induction machines, the tests to be carried out are the no-load test and the load test. In the no-load test, the input power P_0, the current I_0, the voltage U_0, the resistance of stator winding R_0 are measured. Measurements must be made when P_0 does not change more than 3% within 30 minutes. The input voltage is varied between approximately 110% and 30% of nominal voltage U_n, detecting the above values for each working point. The constant losses P_k are obtained with the following equation:

$$P_k = P_0 - \frac{3}{2} R_0 I_0^2 \tag{3.10}$$

Interpolating the work points in the plane (U^2, P_k) a straight line is obtained, whose intercept at the origin corresponds to the losses due to zero voltage, or the mechanical losses due to friction and windage P_{fw}. The iron losses are:

$$P_{fe} = P_k - P_{fw} \tag{3.11}$$

In the load test, the machine is initially brought into the nominal working conditions and then the rated current I_n, the input power P_n, the rated voltage U_n, the slip s, the resistance R of the stator windings, the room temperature θ_c and that of the windings θ_n are measured. Measurements are carried out when the temperature does not vary more than 0.5°C within 15 minutes. The copper losses in the stator windings are then calculated:

$$P_{cu} = \frac{3}{2} R I_n^2 \tag{3.12}$$

For the induction machines with a wound rotor, it is possible to calculate the copper losses in the rotor in the same way. While, for the induction machines with a squirrel-cage rotor, the rotor copper losses P_R are calculated with the following equation:

$$P_R = s\left(P_n - P_{cu} - P_{fe}\right) \tag{3.13}$$

For the calculation of the load additional losses, it is necessary to carry out tests with variable load, with no less than six working points between 125% and 25% of the rated

load, of which two are over 100% on rated load. These tests must be carried out immediately after the test at a nominal load to limit the temperature variations of the windings. The resistance must be brought back to the average temperature between θ_n and θ_c. Torque T and number of revolutions per second n are also measured. The residual losses for the single working point $P_{L,i}$ are:

$$P_{L,i} = P_{in} - P_{out} - P_{cu} - P_R - P_k \tag{3.14}$$

Where P_{in} is the input power and P_{out} is the output power or the mechanical power at the shaft of the machine ($P_{out}=2\pi nT$). The additional losses at load P_{LL} are obtained through linear regression analysis. If k is the number of work points, then:

$$A = \frac{k\sum_{i=1}^{n} P_{L,i}T_i^2 - \left(\sum_{i=1}^{n} P_{L,i}\right)\left(\sum_{i=1}^{n} T_i^2\right)}{k\sum_{i=1}^{n} T_i^4 - \left(\sum_{i=1}^{n} T_i^2\right)^2} \tag{3.15}$$

$$P_{LL} = AT^2 \tag{3.16}$$

The copper losses must be reported to the reference temperature ($\theta_r=75\ ^\circ C$), thus obtaining $P_{cu\theta r}$ and $P_{r\theta r}$:

$$P_{cu\theta_r} = k_\vartheta P_{cu} \tag{3.17}$$

$$P_{R\theta_r} = k_\vartheta P_R \tag{3.18}$$

Where K_θ is the temperature coefficient. In conclusion, the total power losses are:

$$\Delta P = P_k + P_{cu\theta_r} + P_{R\theta_r} + P_{LL} \tag{3.19}$$

For synchronous machines, the no-load test and load tests are similar to those described for the induction machine. The constant losses P_k and their components P_{fe} and P_{fw} are evaluated in the same way. The copper stator losses P_{cu} are evaluated in the test at rated load and then reported to the reference temperature. The standard defines the losses in the excitation system P_e, including within it the rotor copper losses P_R, those in the exciter P_{Ed} and those in brushes P_b, that is:

$$P_e = P_R + P_{Ed} + P_b \tag{3.20}$$

There are conventional methods, described in the standard, for the evaluation of the last two components. The additional load losses can be assessed in two ways. The first involves a short circuit test with a generator operation. A coupled dragging machine is used. Then the additional load losses corresponding to the rated current are:

$$P_{LL,n} = 2\pi nT - P_{fw} - P_{cu} \tag{3.21}$$

while those for any current value I are thus obtained:

$$P_{LL} = P_{LL,n}\left(\frac{I}{I_n}\right)^2 \tag{3.22}$$

The second method provides for motor operation with a fixed supply voltage (preferably about 1/3 of the nominal value or the minimum value for which stable operation can be had). The armature current is adjusted by varying the excitation of the machine. In order to estimate the additional load losses, the standard suggests considering at least six work points between 125% and 25% of the rated current value and measure the input power P_{in}, the absorbed current I and the supply voltage U. In this case, the additional load losses for each working point are:

$$P_{LL} = P_{in} - P_k - P_{cu} - P_e \tag{3.23}$$

In conclusion, the total power losses are:

$$\Delta P = P_k + P_{cu\theta_r} + P_{LL} + P_e \tag{3.24}$$

Regarding the electric drives field, the electrical machines are powered by voltage source inverter (VSI). In this case, the voltage at the machine terminals is not sinusoidal but it is distorted. In most cases, the supply voltage is obtained with PWM (Pulse Width Modulation) or SVPWM (Space Vector Pulse Width Modulation) modulation and it has a distorted waveform as shown in Fig. 81. The harmonic content of the voltage introduces additional harmonic losses which must be measured and take into account in the calculation of the total power losses of the motor.

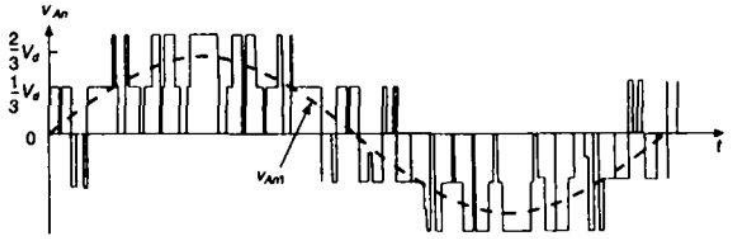

Fig. 81 Output phase voltage from a PWM-VSI.

For this purpose, IEC 60034-2-3 [10] can be of great help. The methods in this technical specification apply to induction motors used with variable frequency drives. However, the application to other AC motors or DC motors and converters is not excluded. The methods are mainly intended for motors fed by voltage source converters. Furthermore, the additional harmonic losses determined by the use of this technical specification are for comparison of different motor designs, but they are not appropriate to be used for

efficiency determination of a PDS in a driven application with its wide range of torque versus speed operating points. The requirements to be met for the test are [6]:

- Use of VSI inverters;
- No current or slip control;
- Fundamental harmonic of power supply voltage value equal to the nominal one;
- Supply frequency equal to the nominal;
- The switching frequency equal to 4 kHz.

The choice of the switching frequency and the reference voltage has crucial importance in the modulation technique to be used. In any case, overmodulation must be avoided. The input voltage of the inverter must be set to a value that guarantees the nominal voltage of the motor avoiding overmodulation but without supplying voltage higher than that required for this condition. Particular care must be taken during no-load tests, where the converter output voltages can be so high as to lead to overmodulation [6]. In order to evaluate the additional harmonic losses, four tests must be performed, in the order established as follows:

1. **Load test with sinusoidal power supply**, to determine the additional load losses P_{LL} in sinusoidal regime;
2. **No-load test with sinusoidal power supply**, to determine the no-load losses P_0 in sinusoidal regime;
3. **Load test with power supply by the inverter**, to determine additional load losses $P_{LL,C}$ in distorted regime;
4. **No-load test with inverter power supply**, to determine the no-load losses $P_{0,C}$ in the distorted regime.

The standard suggests making the measurement, in each test, with three wattmeters. The determination of P_{LL} and $P_{LL,C}$ requires a linear regression analysis like described before. The additional harmonic losses are calculated as the difference between the losses in the distorted regime and those in the sinusoidal regime. In particular, the load losses and no-load losses will be respectively [1] [6]:

$$P_{HL,L} = P_{LL,C} - P_{LL} \tag{3.25}$$

$$P_{HL,0} = P_{0,c} - P_0 \tag{3.26}$$

The total additional harmonic losses are:

$$P_{H,L} = P_{HL,L} + P_{HL,0} \tag{3.27}$$

The latter, added to the total losses ΔP with sinusoidal power supply, give the total losses $\Delta P_{T,C}$ with inverter power supply. In conclusion, the motor efficiency is:

$$\eta_M = \frac{P_{in} - \Delta P_{T,C}}{P_{in}} \tag{3.28}$$

Moreover, the standard defines a coefficient r_{HL}, used as an efficiency index to classify the motors supplied by the inverter. In details, it is:

$$r_{HL} = \frac{\Delta P_{T,C}}{\Delta P} 100 \tag{3.29}$$

3.2.2 Guide IEEE Std 1812-2014

The IEEE Std 1812-2014 suggests the direct efficiency measurement method for small power PMSMs and for larger power PMSMs, where the mechanical power cannot be measured accurately the indirect measurement method. For the last case, the loss components to be used in determining the efficiency of a PM machine are as follows:

- Core loss;
- Friction and windage loss;
- Additional losses due to inverter voltage harmonics;
- Stray-load loss;
- Armature loss using the armature current at the specified load and the dc armature resistance corrected to a specified temperature.

In order to determine these loss components, the guide sets out various methods for performing no-load, short-circuit and load tests. For the last two, there are no differences compared to traditional synchronous machines and the methods are the same as those already seen in IEC 60034-2-1. Regarding the determination of the core loss and friction and windage loss, there are substantial differences with respect to the procedures described before for wound synchronous machines. In fact, in a PMSM, the excitation is fixed and cannot be reduced to zero because is established by the permanent magnets. While in a traditional synchronous machine, friction and windage loss can be measured directly in a no-load test without excitation. The same procedure is not possible for PMSMs. The Guide suggests replacing the permanent magnets rotor with a second one that is identical but without permanent magnets. In this case, a drive motor is used to bring the rotor to the speed of interest and thus the measurement of friction and windage losses can be performed directly

or indirectly. Once the friction and windage losses have been measured directly, the losses in the iron can be calculated by subtracting the losses just measured from the losses measured in the no-load test with the permanent magnet rotor. In any case, performing this replacement of the rotor is in practice quite difficult and only possible for the manufacturer. The guide suggest other procedures like the direct measurement of the mechanical power transmitted by a tared machine method, or with retardation or coast-down test. The last method was used for the characterization of the PMSM under test and described in the previous chapter. With regard to load losses, the substantial difference with wound synchronous machines lies in the absence of rotor circuits in the PMSMs. Therefore, the load losses will be given by the sum of the copper stator losses and additional losses or stray-load loss. On the other hand, although the electrical conductivity of the magnets is lower than that of copper, there may be non-negligible eddy currents in the rotor, higher than those of a traditional machine. The contribution of eddy currents becomes appreciable in particular geometric configurations of the magnets, such as in the case of SPMSMs. This contribution to power losses is incorporated in the additional losses, which can be calculated as described before. The method introduced by IEC 60034-2-3 for the determination of additional losses due to inverter voltage harmonics is the same as reported in the guide. Therefore, it will be necessary to carry out a no-load test and a load test both with sinusoidal power supply and with inverter power supply and process the measurement results in order to obtain the additional harmonic losses. Otherwise, the guide suggests to measure directly the total losses from output and input power, and the component losses are subtracted from total losses to obtain an estimate of the stray-load losses including those due to inverter harmonics.

3.2.3 Standard IEC61800-9

The standard IEC 61800-9 is a valid reference for evaluating the efficiency of electric motors, CDMs and also of PDS. The real innovation introduced by this standard, respect to the past, is the definition of general methodology to energy efficiency standardization for any extended product by using the guidance of the extended product approach (EPA). Moreover, the standard introduces efficiency standards for each kind

of motors, CDM and PDS. Contrariwise, the standard IEC 60034-30 [III.11]-[III.12] carried out the efficiency standards classification only for induction motors. The contents of the standard can be summarized as follows:

- Introduction of the "extended product" approach (EPA);
- Classification of motors, CDMs and PDSs;
- Efficiency at partial loads of CDM and PDS.

The "extended product" approach aims to take into account not only the efficiency of the motor but of the whole electric drive with its load. This means combining the efficiency of the motor and the converter. The efficiency of the electric drive is determined by considering the sum of motor and CDM losses as total losses. Once this is done, the efficiency indices can be derived. These last ones constitute a parameter of considerable interest to be able to compare several drives between them and thus aim at the energy optimization of the whole power drive system. There are three efficiency classes for CDMs: IE0, IE1, and IE2. For each size, a reference CDM (Reference Complete Drive Module, RCDM) is introduced, whose efficiency is a reference value. In fact, if the efficiency of a CDM is within ± 25% of that of the RCDM, then the CDM has IE1 efficiency class. Below -25% of the RCDM efficiency, the class is IE0, over +25% of the RCDM efficiency it is IE2 (Fig. 82). The efficiency must be determined by making the converter work at 100% of the rated output current and at 90% of the nominal motor frequency. With regard to the motor efficiency classification, the IEC 61800-9 refers to the classification of the standard IEC 60034-30. The standard IEC 60034-30-1 [III.11] approved in 2008 and updated in 2014, distinguishes four efficiency classes for motors powered by the electricity grid or by sinusoidal voltage supply: IE1 (standard efficiency), IE2 (high efficiency), IE3 (premium efficiency) and IE4 (super premium efficiency). The standard specifies efficiency classes for single-speed electric motors that have a rated power P_n from 0.12 kW to 1000 kW, a rated voltage U_n above 50 V to 1 kV and have 2, 4, 6 or 8 poles. Instead, the standard IEC 60034-30-2 [III.12] specifies efficiency classes for variable speed rotating electric machines not covered in IEC 60034-30-1 and, therefore, for electrical machines powered with electronic converters. In detail, the efficiency classes are the same described before and they are valid also for electric machines that have a rated speed ω_n from 600 rpm to 6000 rpm. In the same way, we introduce the efficiency of Reference Power Drive System RPDS that

is obtained by combining the efficiency of RCDM and of Reference Motor RM where which has IE2 efficiency class. For the PDS, three efficiency classes are defined in the same way, naming them IES0, IES1, and IES3, where S means "system". To define the IES1 class, the range of variation now is ± 20% with respect to the reference value (Fig. 82). Furthermore, the working point in which to perform the evaluation is 100% of the rated current and 100% of the rated speed. Since the electric drive generally finds itself working under different conditions of torque and speed, the standard defines the work points at partial loads at which the manufacturers must evaluate and declare the performance of the PDS. Based on this information, buyers can also calculate the return for any work condition by interpolation. For the PDS there are eight work points, obtained with a load torque of 25%, 50% and 100% of the rated value and a speed of 0%, 50% and 100% of the rated value (Fig. 83).

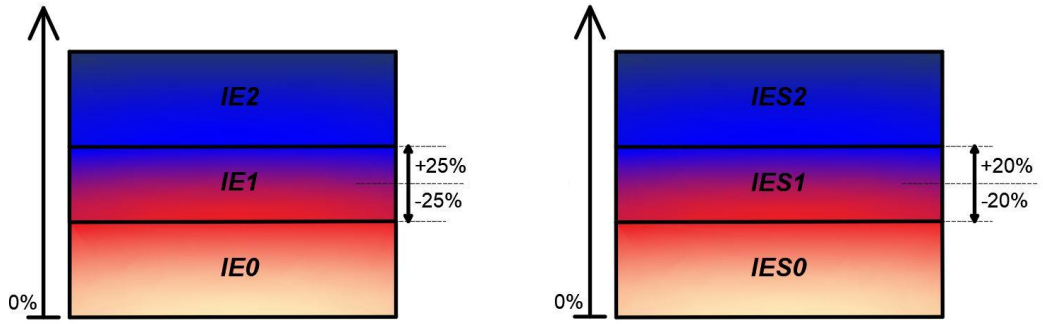

Fig. 82 Definition of efficiency classes for CDM (left) and PDS (right).

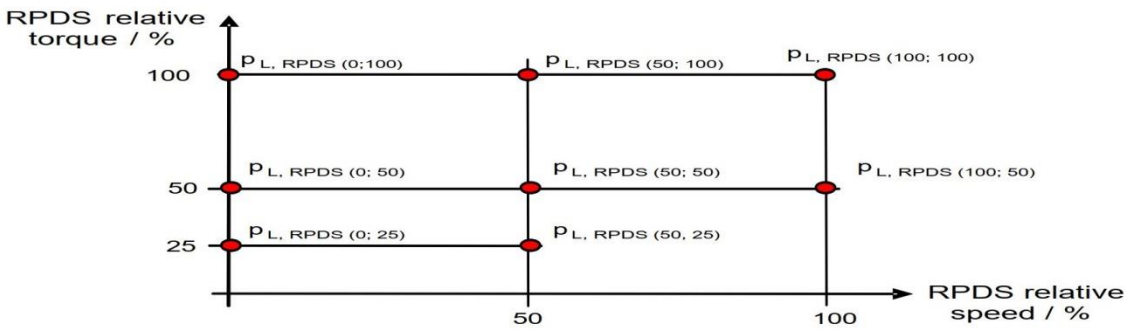

Fig. 83 RPDS working points defined by IEC 61800-9-2.

In detail, the IEC 61800-9-2 [III.6] specifies the procedures for measuring motor, CDM and PDS losses, and it provides the reference values of efficiency in relation to the size of the electric drive and defines the efficiency classes. There are three recommended methods for estimation of CDM losses:

- direct method (the difference between input power and output power);

- indirect method (evaluation of each losses component);
- calorimetric method.

The most accurate method, according to the standard, is the indirect method.

For PDS there are two recommended methods:

- direct method (the difference between input power and output power);
- indirect method (evaluation of each loss component).

In detail, the direct method is suggested when the PDS is equipped with a small power motor ($P_n \leq 1$ kW), otherwise, it is suggested the indirect method. Finally, we want to highlight some of the specifications that the instrumentation and the measurement technique must meet:

- For each working point it is necessary to take measurements for at least 1-3 minutes;
- The bandwidths of the instrumentation must be adequate for the detection of voltage and current frequency components. In details, a bandwidth ranging from 0 to 10 times the switching frequency f_{PWM} is considered adequate for measuring the output power from the CDM;
- The measurement range must be chosen in relation to the measurement of currents and voltages;
- The instrumentation must meet the specifications given by IEC 60034-2-1.

3.2.4 Final considerations

An accurate description of the measurement methods required by international standards and the guide IEEE Std 1812-2014 has been carried out. In detail, the methods recommended by the IEC standards vary according to the size and type of machine. In general, for small power machines, the direct method is the one recommended by the standard, while for medium/high power machines the indirect method is recommended. The direct method is easier than the indirect method and requires only the measurement of input power and the output power from the analyzed system (motor, CDM, PDS). In particular, in the case of whole PDS, the critical aspect consists of the measurement of the output mechanical power that requires accurate transducer or instrumentations that usually is expensive. Contrariwise, the indirect method requires the measurement of each power losses component. In detail, the IEC

61800-9 reports the procedure to evaluate each power losses component not only for the AC machine but also for the CDM. The advantage of this methodology consists in the possibility of performing the efficiency measurement with only electrical equipment which is very accurate and economically sustainable. The main drawback is represented by the measurement procedure that is more complex than the measurement procedure of the direct method. Despite the indirect method is suggested for medium/high power machines, in the literature it has been shown that, even for medium/high power motors, the direct method can provide low uncertainty values, comparable to those obtainable with the indirect method [III.7]. Based on the considerations made and since the IPMSM under test present nominal power lower than 1 kW, the direct method has been adopted in order to evaluate the efficiency of PDS under test. Furthermore, the speed and torque transducer, employed in the electrical drive under test, satisfy the measurement requirement of IEC 60034-2 [III.1].

3.3 Preliminary analysis and tests for the design of test bench

3.3.1 Harmonic analysis

For a correct design of the measurement system, preliminary experimental investigations or tests have been carried out. The goal of these preliminary investigations is to evaluate the features of the measurement quantity as amplitude and their spectrum content. In order to choose the measurement system minimum requirements, such as the sampling rates and the bandwidths, this analysis is fundamental. In reference to the electric drive under test and its schematic representation (Fig. 80), several harmonic analyses of electrical quantities at CDM input and output sections, and of the mechanical quantities at the motor output section have been carried out. In detail, at the CDM input section, the current is the quantity that has the highest harmonic content since the CDM is fed by the grid and, therefore, with sinusoidal voltage. Instead, at the CDM output section or IPMSM input section, the voltage is the quantity with the highest harmonic content due to the SVPWM (Space Vector Pulse Width Modulation) and the current harmonic content is limited due to the filtering action of IPMSM inductances. A Teledyne LeCroy WaveRunner 6Zi equipped with voltage and current probes have been employed for this analysis. All the measurements reported in this paragraph are performed at a speed of 2000 rpm and a

load torque of 1 Nm. Since the IPMMS under test has three pole pairs, the fundamental electric frequency is 100 Hz at speed of 2000 rpm. For the purposes of this analysis, other surveys have been carried out in correspondence of other values of mechanical speed and load torque, providing results very similar in terms of harmonic content to those relative to the working point analyzed and reported here. The sampling frequency f_s and the measurement time T_w are equal to 10 MHz and 100 ms, respectively. In Fig. 84, the trend of the current I_{CDM} at the CDM input section and its FFT (Fast Fourier Transform) are reported. From Fig. 85, it is possible to note that harmonic content is very limited beyond the frequency of 10 kHz and, in particular, the IHD (Individual Harmonic Distortion), the ratio between the amplitude value of the individual harmonic and the amplitude value of the fundamental, presents values approximately equal to 10^{-3}. In Fig. 86, the trend of the CDM supply voltage V_{CDM} and its FFT are reported. From Fig. 87, it is possible to see the absence of harmonics component with high amplitude and, therefore, the IHD is lower than 10^{-3} at the frequency of 1 kHz.

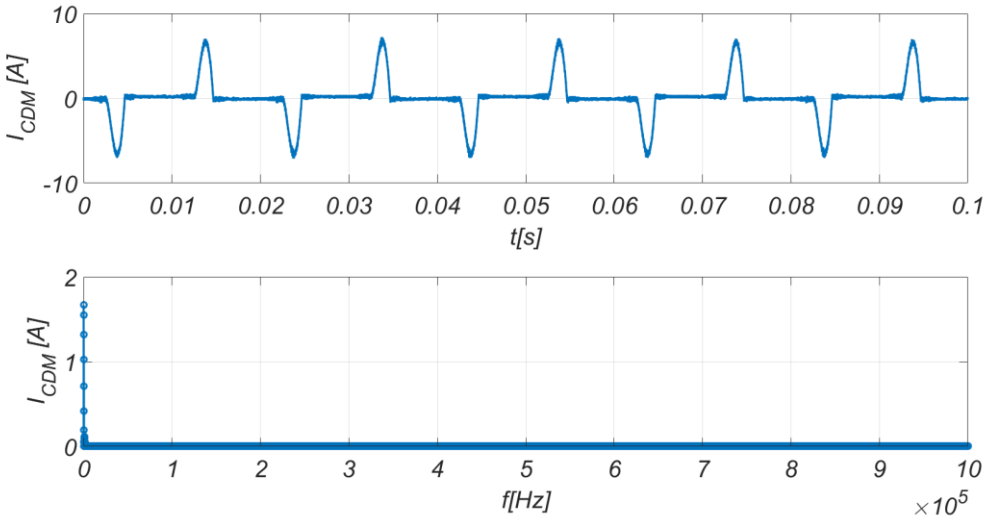

Fig. 84 Current waveform and its FFT.

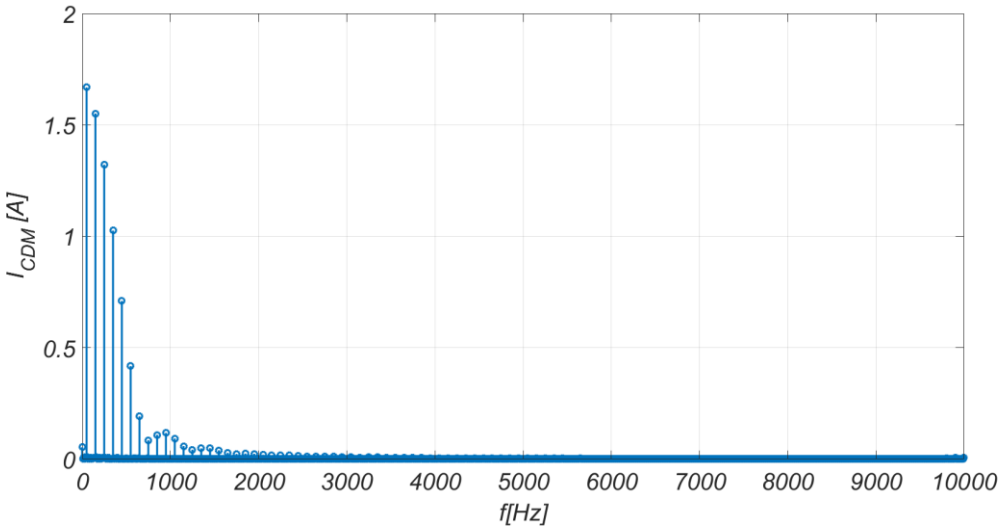

Fig. 85 Detail of current FFT.

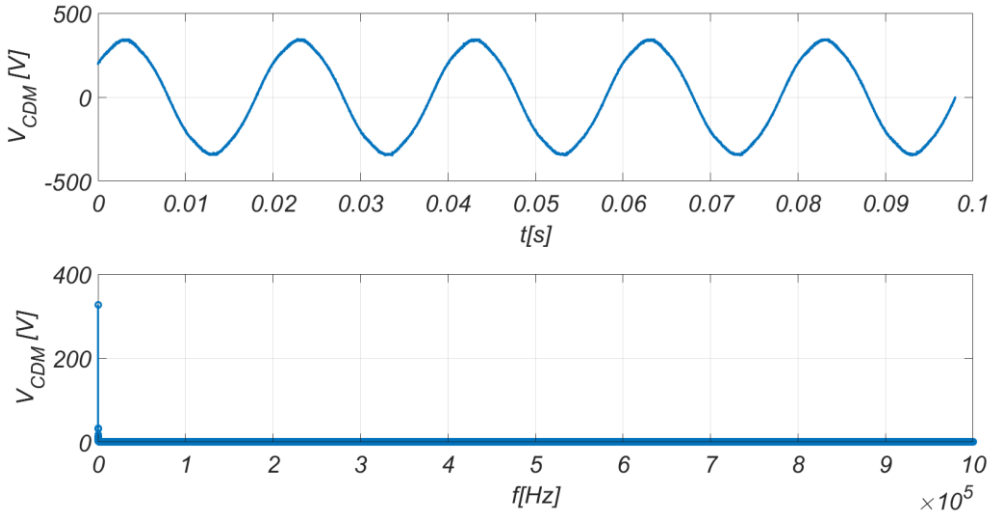

Fig. 86 Voltage waveform and its FFT.

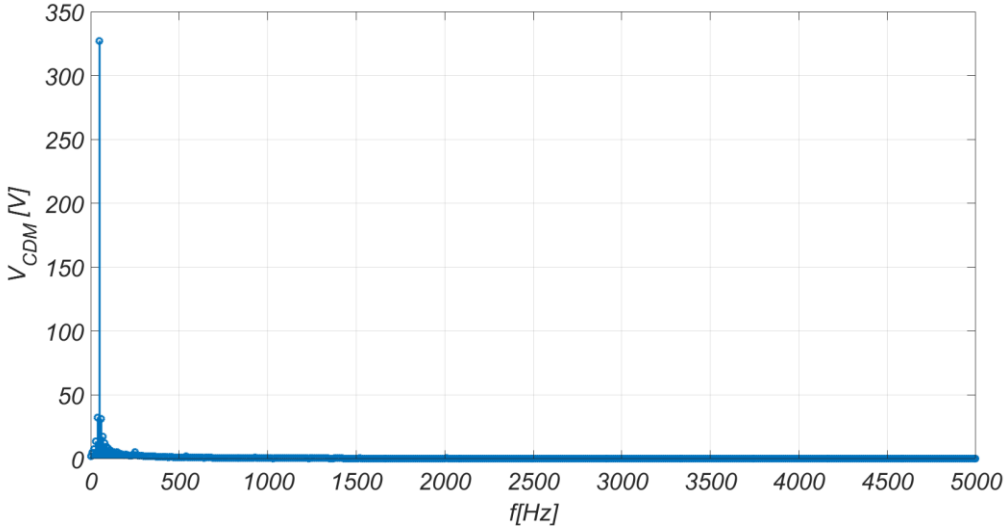

Fig. 87 Detail of voltage FFT.

In Fig. 88, the trend of the output current of CDM or the supply current of IPMSM I_{mot} and its FFT is reported. From Fig. 89, it is possible to see the presence of fundamental harmonic at 100 Hz and of the harmonic components multiple of the switching frequency equal to 10 kHz. Moreover, at 40 kHz the current harmonic component present peak values about equal to 10 mA and, therefore, IHD lower than to 10^{-2}. Instead, the output line voltage of CDM V_{CDM} presents heavier harmonic content respect those of the current and it is possible to see several voltage harmonic components multiple of the switching frequency (Fig. 90). From Fig. 91, it is possible to see that the harmonic components at 200 kHz present amplitude about equal to 4 V and, therefore, IHD about equal to 10^{-1}. IHD values below 10^{-2} occur only for frequencies above 500 kHz.

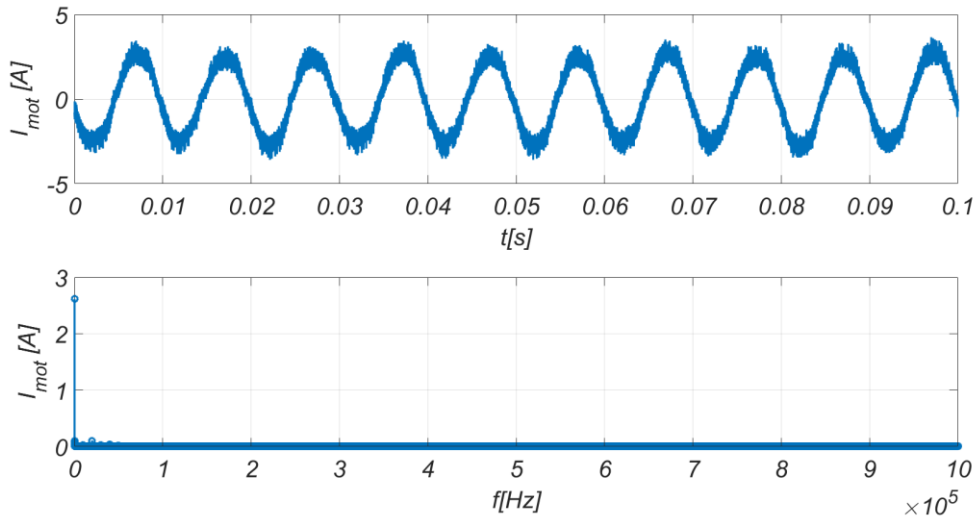

Fig. 88 Output current waveform of CDM and its FFT.

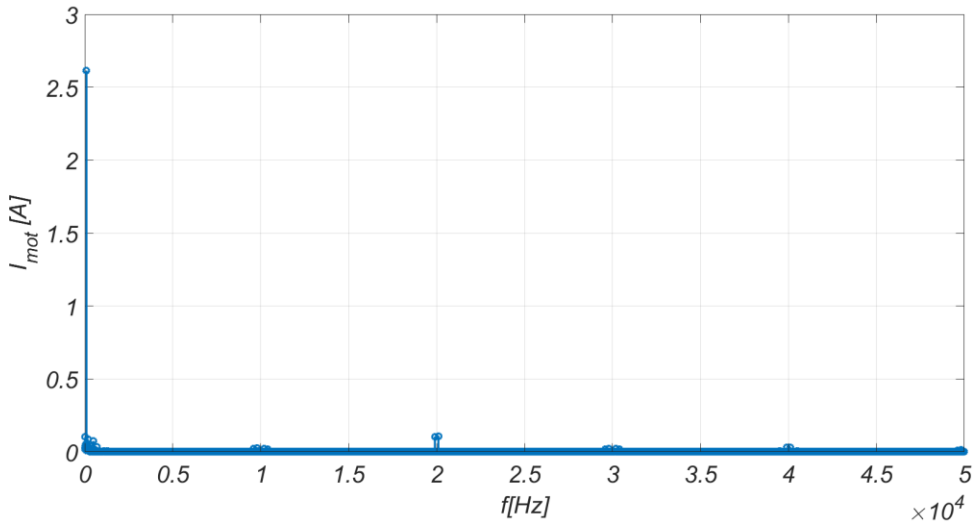

Fig. 89 Detail of output current FFT of CDM.

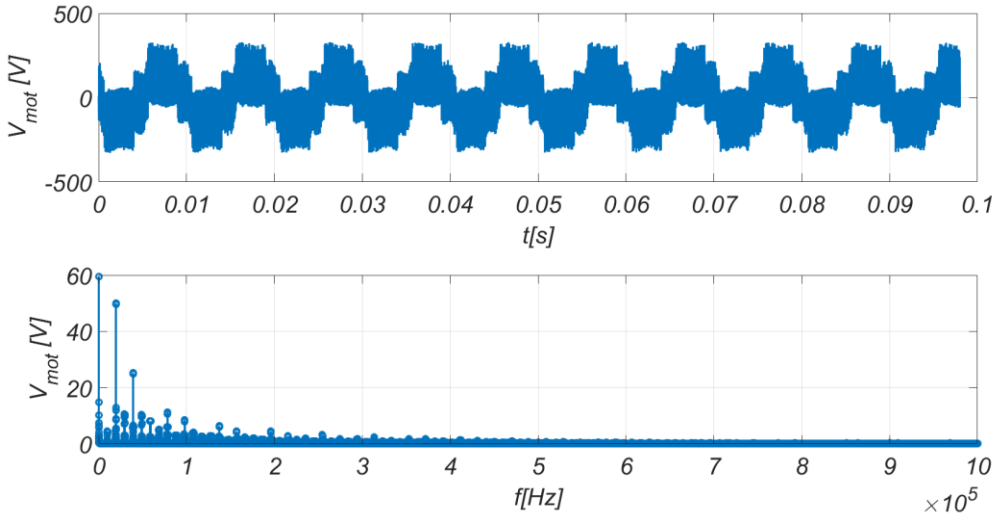

Fig. 90 Output line voltage waveform of CDM and its FFT.

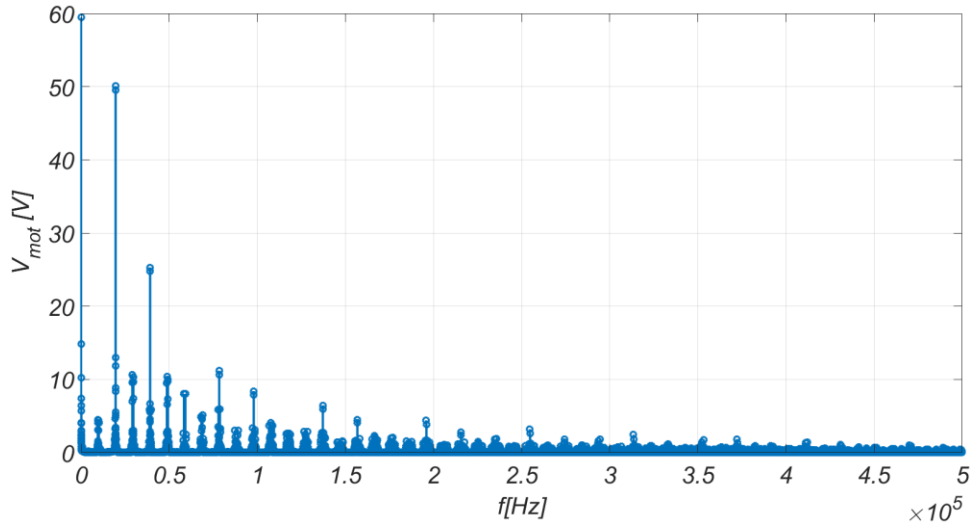

Fig. 91 Detail of output line voltage FFT of CDM.

A further investigation was carried out, through the use of the oscilloscope, on the instantaneous power both in the single-phase input section of CDM and in the three-phase output section of CDM. In particular, for the output section of CDM, the instantaneous power of a single-phase was taken into consideration and analyzed here. The results obtained for this phase have been compared to those obtained on the other two phases and they are very similar. Therefore, the considerations on one phase are valid for the other two phases. In detail, in Fig. 92 and Fig. 93 the spectrum of instantaneous power and the cumulative power of each measurement section, highlighted in blue and in red, are reported, respectively. The cumulative power is the sum of instantaneous power spectrum amplitude as a function of the frequency. The amplitude of each spectrum component is expressed in relative value respect to the

value of the fundamental component, instead, the cumulative power is expressed in relative values respect to the total value of instantaneous power.

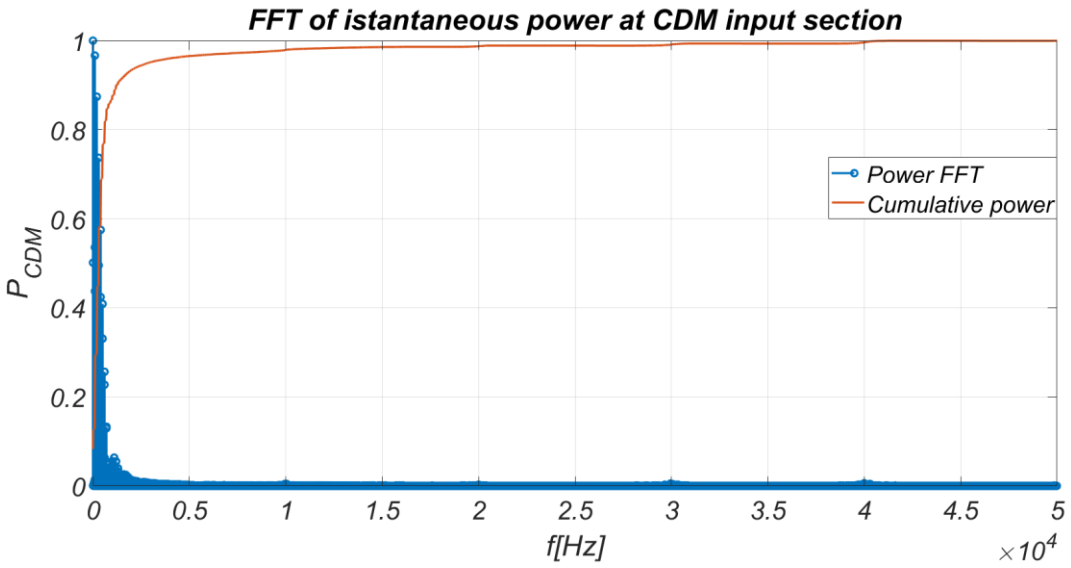

Fig. 92 Instantaneous power FFT at CDM input section.

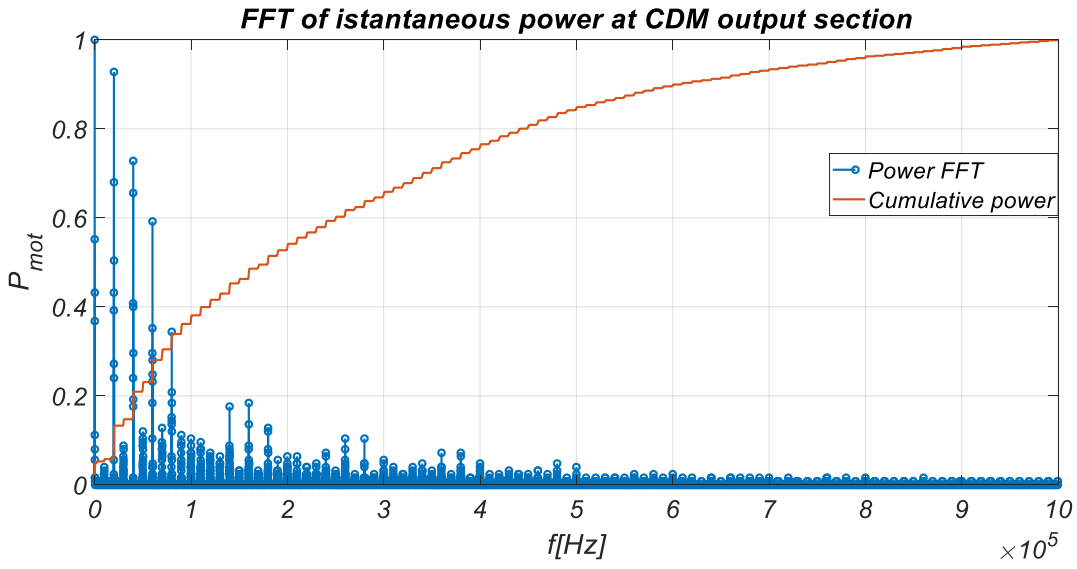

Fig. 93 Instantaneous power FFT at CDM output section.

Therefore, respect to the instantaneous power at the CDM input section, it is possible to deduce that the contributions of instantaneous power spectrum components above 20 kHz can be considered negligible. Instead, respect to the instantaneous power at the CDM output section, it is possible to deduce that the contributions of instantaneous power spectrum components above 800 kHz can be considered negligible. Although the frequency spectrum of instantaneous power does not add information for the correct choice of measurement equipment for the evaluation of electric drive efficiency, it can

be useful to quantify reactive power. Instead, it may be of great interest to evaluate the influence of voltage and current harmonics components on the active power. This study was carried out in the three-phase CDM output section where the voltages and currents show heavier harmonic content. This analysis was conducted by using the acquisition module of National Instruments NI PCI 6110-E in Labview environment. In detail, the study was carried out according to the following steps:

- Voltage and current are acquired at sample frequency f_c of 4 MHz, with measurement time T_w of 10 s;
- Filtering, through a digital filter, of current and voltage with cut frequency f_{cut} variable by the operator;
- Calculation of active power with unfiltered quantities P and of active power with filtered quantities P_{filt};
- Calculation of the relative percentage difference between the unfiltered active power and the filtered active power, when f_c varies:

$$\Delta P\% = \frac{P - P_{filt}}{P} 100 \tag{3.30}$$

The results of this analysis are reported in Table 22.

In conclusion, the analysis conducted highlighted the following aspects:

- At the CDM input section, the voltage and current harmonics components are negligible above the frequency of 1 kHz;
- At the CDM output section, the line voltage present heavier harmonic content and they only can be negligible above the frequency of 500 kHz (IHD<10^{-2}) while the current present harmonic content reduced compared those of the voltage;
- the harmonic content of voltage and current does not affect the active power only above 250 kHz.

Therefore, on the basis of the highlighted aspects, it is possible to deduce the minimum measurement requirements necessary for the design of the test bench. The measurement transducers, the acquisition boards used and their main characteristics are shown below.

Table 22 Relative percentage difference between unfiltered active power and the filtered active power as a function of cur frequency.

f_c	$\Delta P\% = \frac{P - P_{filt}}{P} 100$
2 MHz	Negligible
1 MHz	Negligible
250 kHz	Negligible
100 kHz	0.393 %
50 kHz	0.753 %
5 kHz	1.971 %
10 kHz	4.356 %
1 kHz	4.483 %
500 Hz	4.525 %
250 Hz	5 %

3.3.2 Test bench

Regarding the test bench, it was chosen to use National Instruments acquisition modules programmable in the *Labview* environment. In this way, the measurement system presents a high degree of flexibility, the ability to acquire a large number of signals, and in addition, the operator can design and define a virtual measurement instrument and its measurement features in real-time.

In order to measure the input power of PDS at the CDM single-phase input section, two measurements are required, one voltmetric and one amperometric. In Fig. 94 the measurement scheme at the CDM input section is reported. The single-phase voltage is measured through a direct connection to the NI DAQ 9225 acquisition module, whose specifications are shown in Table 23. Voltage transducers are not necessary since the voltage range of the module is higher than the input voltage value of the CDM. The current is measured both through a Fluke i400 current probe (Table 24) and through a non-inductive Fluke A40B shunt resistor (Table 25), whose output signals are sent to the NI DAQ 9215 acquisition module (Table 26). This resistance is placed on the neutral wire. We choose to use two current transducers to compare the measurement results obtained with a first method with greater accuracy and cost (the one with the

shunt resistance) and a second method less accurate but cheaper (the one with the current probe).

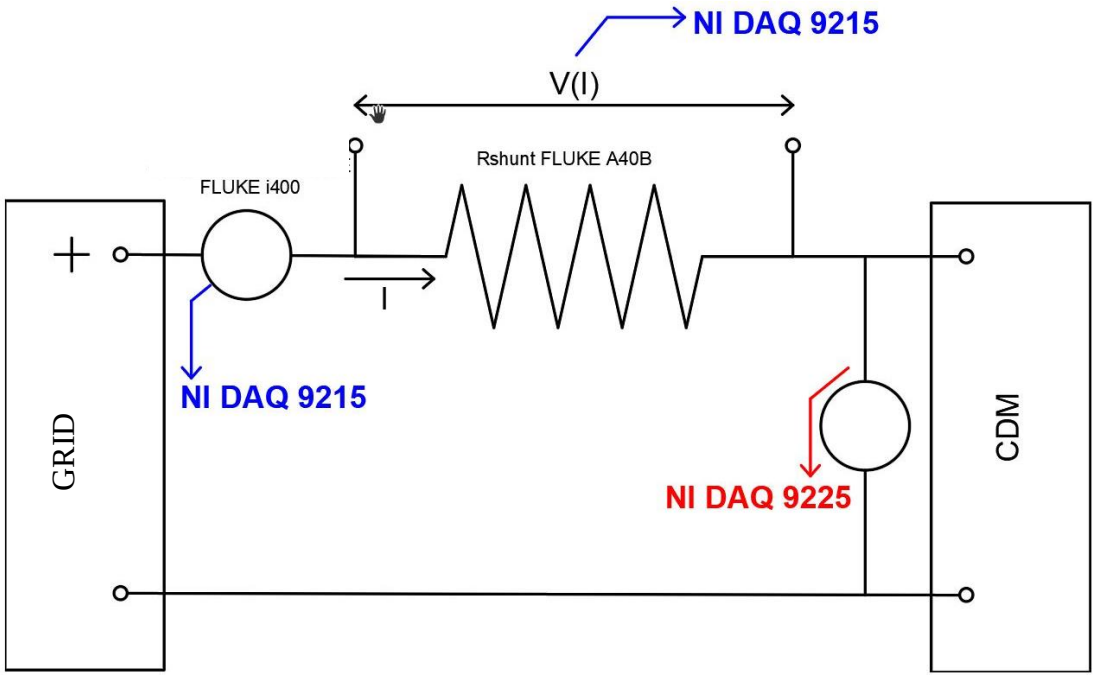

Fig. 94 Measurement scheme at the CDM input section.

From the tables of the adopted instrumentations, it can be seen how the bandwidth of the single components is adequate to measure the electrical quantity of the CDM input section. Another important parameter for a careful choice of the measuring instrument is the nominal range. The NI 9225 is suitable for the acquisition of supply sinusoidal voltage of the grid (240 V_{rms}) since it can reach 300 V_{rms} of the input voltage. As for the current, it reaches peak values of the order of the ampere unit. The shunt resistor has an already adequate value of the nominal range, while it is chosen to arrange 4 turns on the pass-through current probe to make it work at values close to the full-scale. It is easy to calculate the output voltages from the probe and from the shunt resistance and verify that these values do not exceed the acquisition module NI 9215 full-scale value of 10 V. Third parameter to consider, no less important than the previous ones, it is the uncertainty. Generally, the uncertainties introduced by the acquisition modules are negligible compared to those given by the transducers. The shunt resistance has a lower and better accuracy compared to the current probe. Furthermore, the shunt resistance has a wider bandwidth than the current probe.

Table 23 Acquisition module NI 9225 features.

NI 9225		
Number of channels	4	
ADC resolution	24 bit	
ADC typology	Delta-sigma	
Sampling	Simultaneous	
Sample rate f_s	1.613÷50 kS/s	
Nominal Voltage	300 Vrms	
Bandwidth	0.453 *fs*	
Accuracy	Gain error	Offset error
	±0.05%	±0.008%
THD	-95 dB	

Table 24 Current probe fluke i400 features.

CURRENT PROBE FLUKE i400	
Temperature reference	23±5°C;
Current range	1÷400 Arms or 1÷40 Arms
Output	1 mA/A
Accuracy	2%+0,06 A, 45 Hz fino a 400 Hz
Bandwidth	5÷20000 Hz

Table 25 Shunt fluke A40 B features.

SHUNT RESISTOR FLUKE A40B						
Nominal current	20 A					
Nominal resistor	0,04 Ω					
Bandwidth	0÷100 kHz					
Accuracy [±µA/A] (confidence level 95%)	DC	1 kHz	10 kHz	30 kHz	100 kHz	
	26	43	52	70	113	
Maximum current	<5 s			Indefinitely		
	42 A			22 A		
Phase angle error [degree]	1 kHz		10 kHz		100 kHz	
	< 0.013		< 0.125		< 1.250	
Work temperature range	13÷33 °C					

Table 26 Acquisition moduleNI 9215 features.

NI 9215		
Number of channels	4	
ADC resolution	16 bit	
ADC typology	SAR	
Sampling	Simultaneous	
Sample rate f_s	100 kS/s	
Input range	± 10 V	
Bandwidth	420 kHz	
Accuracy	Gain error	Offset error
	±0.02%	±0.0014%

Figure 3.7 shows the measurement scheme for the CDM three-phase output section. Aron measurement scheme is used to measure the active power at the CDM output section. In particular, the currents I_1, I_3 and the line voltages V_{12} and V_{32} are measured. The active power transferred to the motor, or the power P_2 measured in the CDM output section, is:

$$P_{outCDM} = P_2 = V_{12}I_1 \cos\varphi_{12} + V_{32}I_3 \cos\varphi_{32} \tag{3.31}$$

Where φ_{12} and φ_{32} are the phase displacements between the voltages and currents, respectively.

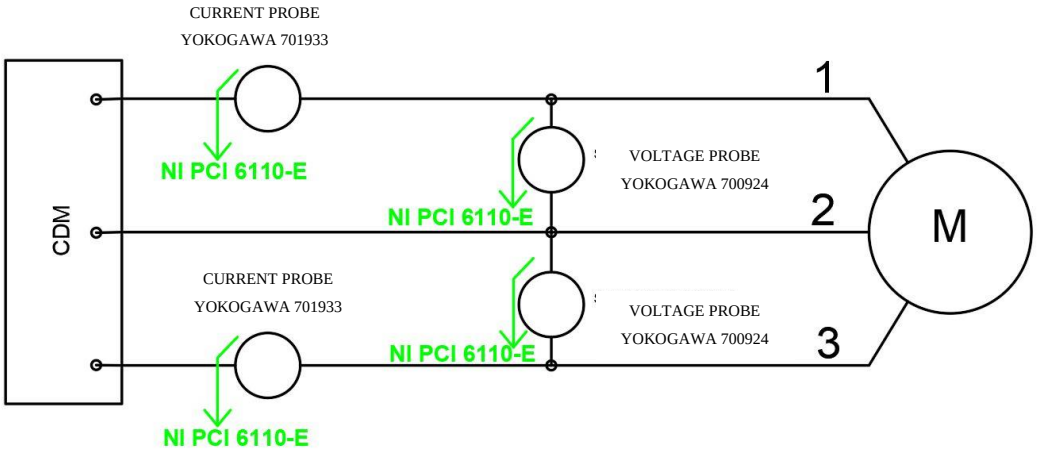

Fig. 95 Measurement scheme at the CDM output section.

As extensively discussed above, the electrical quantities of the output section of CDM have a much higher harmonic content than the electrical quantities of the CDM input section. Consequently, it is necessary to use probes and acquisition modules with a wide bandwidth. The choice obviously must not compromise the accuracy and, once again,

be adequate to the range of the electrical quantity to be measured. In detail, the voltage probes Yokogawa 700924 and current probes Yokogawa 709133 are used and their main features are reported in Table 27 and Table 28, respectively. From these tables, it is possible to see that the bandwidths fully satisfy the measurement requirements described in the harmonic analysis. A NI PCI 6110-E acquisition module is used for the acquisition of the probes output signal. In detail, this module presents the maximum sample frequency equal to 5 MHz. This value is much larger than the upper limit of the frequency range where significant contributions to the active power by the voltage and current harmonic components have been detected.

Table 27 Voltage probe Yokogawa 700924 features

VOLTAGE PROBE YOKOGAWA 700924		
Input	Differential	
Attenuation ratio	1:100 or 1:1000	
Bamdwidth (-3 dB)	0÷100 MHz	
Range	±1400 V (DC + AC peak) or 1000 Vrms with attenuation ratio of 1000:1; ±350 V (DC + AC peak) or 250 Vrms with attenuation ratio of 100:1	
Accuracy	Gain error	Offset error
	±2% (-400V≤common mode voltage ≤ 400 V); ±3% (-1000≤ common mode voltage ≤ 1000 V);	±7.5 mV
Work temperature range	5÷40 °C	

Table 28 Current probe Yokogawa 709133 features

Current probe YOKOGAWA 701933	
Output	0,1 V/A
Bandwidth (-3 dB)	0÷50 MHz
Peak current value in continuous operation	30 Arms
Maximum peak current	50 Arms
Accuracy	±1.0% of reading value ±1 mV
Noise	2.5 mArms
Work temperature range	0÷40 °C

Table 29 PCI Acquisition module NI 6110-E features

NI PCI 6110-E			
Number of channels	4		
ADC resolution	12 bit		
Sampling	Simultaneous		
Sample rate f_s	1÷5000 kS/s/chanel		
Input range	Selectable		
Bandwidth (-3 dB)	5 MHz		
ENOB	11 bit		
Accuracy	Gain error	Offset error	Background noise
	0.0571%	2.971 mV	5.073 mV

Fig. 96 shows the measurement scheme of the mechanical section.

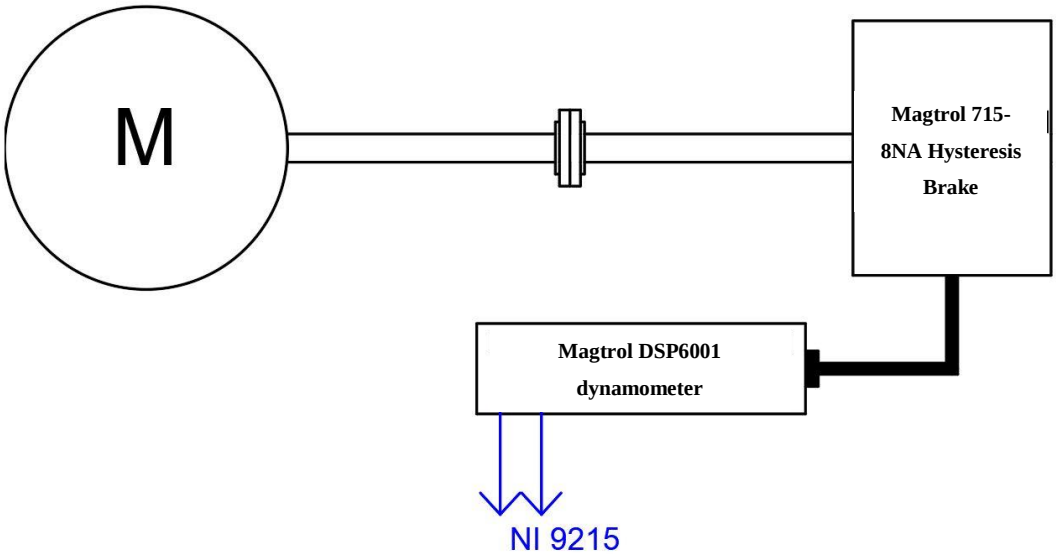

Fig. 96 Measurement scheme of the mechanical section.

The mechanical load of the motor consists of a Magtrol HD-715-8NA hysteresis brake. The brake presents the maximum torque equal to 6.5 Nm, maximum speed of 25000 rpm, maximum power for 5 minutes equal to 3360 W and maximum continuous power equal to 2985 W. The main features of the brake have already been described in the previous chapter (Table 5). The torque offered by the brake can be adjusted in real-time by means of a Magtrol digital dynamometer model DSP6001, whose interface already provides the torque, speed and power values measured at the shaft motor.

Furthermore, the digital dynamometer provides the torque and speed measurement signals can be sent to other acquisition systems. In this work, the acquisition module NI DAQ 9215 is used to acquire the torque and speed measurement signals.

3.4 Losses and efficiency measurements of PDS, CDM, and motor

The efficiency measurement or power losses measurement of PDS and of its two subsystems (CDM and motor) is a goal of this research work. As widely described before, the direct method is employed for efficiency measurement. The acquisition of electrical and mechanical quantities is carried out through the transducers and acquisition modules of *National Instrument*, previously described, in *Labview* environment. The acquisition is carried out with the Express Virtual Instrument (VI) DAQ Assistants, characterized by:

- Sampling frequency f_s;
- Single acquisition time or measurement time T_M.

The number of samples in one acquisition is:

$$N_s = T_M f_s \tag{3.32}$$

During the single acquisition time, the instantaneous values of electrical and mechanical quantities are acquired and the instantaneous value of electrical power of each measurement section and of mechanical power is calculated. Through the use of "VI BASIC DC RMS" the *rms* value of the voltages and currents, the mean value of instantaneous electric powers (or the active powers) and the mean value of mechanical quantities are calculated respect to the time T_M. In this way, into measurement time T_M, it is possible to obtain one sample for each electrical and mechanical quantity. Whit this choice, it is possible to repeat this procedure and perform a measurement with a high duration time window without weighing down the PC memory with a large number of samples. Furthermore, with several measurement samples, it is possible to evaluate the average value and the measurement deviation for each quantity. The single measure, characterized by T_M and f_s, is implemented then in a single iteration of a for loop. The number N of loop iterations corresponds to the number of measurement samples desired. The total observation time or the total acquisition time is equal to:

$$T_w = NT_M \tag{3.33}$$

At the output of each for loop iteration, the measurement sample is stored in an external array. At the end of the cycle, an array is obtained for each quantity of interest, consisting of scalar elements. The measurement arrays obtained are:

CDM input section	• Single-phase voltage *rms* value V_m; • Current acquired with Fluke probe $I_{m,p}$; • Current acquired with Fluke shunt resistor $I_{m,\,sh}$; • PDS input active power acquired with Fluke current probe $P_{PDS,p}$; • PDS input active power acquired with Fluke shunt resistor $P_{PDS,sh}$.
CDM output section	• Line voltage V_{12} • Line voltage V_{32} • Phase current I_1 • Phase current I_3 • Three-phase active power absorbed by the motor P_{mot};
Mechanical section	• Output torque T_{em}; • Mechanical speed of the motor ω_m; • Mechanical power P_M.

The efficiencies of PDS, CDM, and motor are calculated within the for loop, using the values of the active powers evaluated in the various sections, adopting the relationships already known for the direct method. Therefore, the following efficiency arrays are defined and measured:

- PDS efficiency evaluated with the Fluke probe $\eta_{PDS,p}$;
- PDS efficiency evaluated with the Fluke shunt resistor $\eta_{PDS,sh}$;
- CDM efficiency evaluated with the Fluke probe $\eta_{CDM,p}$;
- CDM efficiency evaluated with the Fluke probe $\eta_{CDM,sh}$;
- Motor efficiency η_{mot};

In order to evaluate the average value, the standard deviation and the variance for each array obtained, the "*VI standard Deviation and Variance*" is employed in the measurement software. Finally, the sampling frequency values f_s and acquisition time T_M adopted for the two DAQ Assistants are reported below:

DAQ of PDS input and output sections	• $f_s = 50$ kHz • $T_M = 60$ s
DAQ of CDM output section	• $f_s = 1$ MHz • $T_M = 60$ s

In order to have synchronous sampling between the measurement sections, the same measurement time was chosen. The number of samples acquired at the CDM output section is much higher than those acquired at the PDS input and output sections. The choice of sampling frequency f_s of 50 kHz is in agreement with the measurement requirements of the PDS input section because, as deduced from the spectrum analysis, at 10 kHz the current presents IHD about of 10^{-3}, while the voltage has a much more limited spectrum. The NI 9215 and the NI 9225 acquisition modules used for the acquisition of the PDS input section quantities, can reach this frequency.

Respect to the output mechanical section, since this is characterized by almost constant quantities, the harmonic content of the acquired signals is reduced respect to that of the electrical quantities. Therefore, the sampling frequency used for the PDS input section is widely sufficient for the mechanical quantities acquisition.

Particular attention must be paid to the sampling frequency for the CDM three-phase output section. The IEC 91800-9-2 standard establishes that it is necessary to sample at a frequency such that the bandwidth goes from 0 to 10 times the frequency f_{SVPWM} of the SVPWM modulation. Since f_{SVPWM} is equal to10 kHz for the electric drive under test, the bandwidth must be at least 0 ÷ 100 kHz, or at least the sampling frequency equal to 200 kHz must be adopted. In addition, the harmonic analysis performed in the CDM output three-phase section allows concluding that over 250 kHz the voltages and current harmonics components contribute to the three-phase active power in a negligible way. The choice of f_s equal to 1 MHz for the acquisition of the CDM three-phase output section quantity is largely justified. In any case, with the PCI 6110-E it could reach the frequency of 5 MHz, which would involve the acquisition of an excessively high number of samples.

The torque and speed signals present some oscillations, due to the actions of the controller. Moreover, it was noticed that the frequencies of these oscillations are a function of the control variables variations. We proceed with an FFT analysis of these

signals. The lowest frequency harmonic is 3.43 Hz and the corresponding period is equal to 0.29 s. Therefore, in order to acquire all the oscillatory components of torque and speed, it is necessary a measurement time T_M> 0.29 s. The choice of measurement time T_M equal to 60 s allows to respect this constraint. Furthermore, IEC 91800-9-2 recommends a measurement time of 1-3 minutes.

Finally, the total observation time T_w has been set equal to 2400 s or 40 minutes. This allows for a large number of samples to guarantee the repeatability of the measurements.

3.4.1 Results and analysis

As suggested by the IEC 61800-9-2 standard, the IPMSM working points, take into consideration the efficiency measurement, are reported in Table 30:

Table 30 IPMSM working points

Working points	$\boldsymbol{\omega_m = \omega_n}$	$\boldsymbol{\omega_m = 50\%\omega_n}$	$\boldsymbol{\omega_m = 0}$
$\boldsymbol{T_{em} = T_n}$	1) $\omega_n; T_n$	2) $50\%\omega_n; T_n$	3) $0; T_n$
$\boldsymbol{T_{em} = 50\%T_n}$	4) $\omega_n; 50\%T_n$	5) $50\%\omega_n; 50\%T_n$	6) $0; 50\%T_n$
$\boldsymbol{T_{em} = 25\%T_n}$	7) $\omega_n; 25\%T_n$	8) $50\%\omega_n; 25\%T_n$	9) $0; 25\%T_n$

where T_n and ω_n are the nominal value of the motor electromagnetic torque and of motor mechanical speed, respectively. The working points are numbered from 1 to 9, according to the sequence that was followed for the measurements. However, the standard introduces only eight working points and does not take into account the point 7). The latter has been considered here anyway. Regard to the speed ω_m=0, the standard refers to a sufficiently low speed, such that the motor supply frequency is lower than 12 Hz. For the IPMSM under tests, which has 3 pole pairs, this implies that the mechanical speed can be approximated to zero when it is in the range [0; 240] rpm. Therefore, we choose to take the measurement at 200 rpm. In order to simulate the behaviour of three different control algorithms, for each working point, the measurements are taken at three different values of the direct axis current I_d. These values are I_d = {−1; 0; 1} A. As already mentioned, 40 measurement samples are acquired for each the quantities of interest, previously defined. Each measurement sample of the 40 acquisitions present a

duration of 60 s and the total observation window is equal to 40 minutes. The respective arrays of voltage and currents *rms* and mean values of torque and speed are thus created. By way of example, the mean values of the quantities of interest for the first working point, evaluated respect to the total observation time, are reported in Table 31.

Table 31 Average values of the quantities acquired at the first working point, for the three I_d current values.

Average values									
1) $\omega_n; T_n$									
	$\mathbf{V_m}$ **[V]**	$\mathbf{I_{m,p}[A]}$	$\mathbf{I_{m,sh}[A]}$	$\mathbf{I_1[A]}$	$\mathbf{I_3[A]}$	$\mathbf{V_{12}[V]}$	$\mathbf{V_{32}[V]}$	**C[Nm]**	$\boldsymbol{\omega_m}\left[\frac{\mathbf{rad}}{\mathbf{s}}\right]$
$\mathbf{I_d}$**=1A**	230,181	6,514	6,479	3,62	3,593	220,56	218,48	1,801	420,60
$\mathbf{I_d}$**=0A**	230,441	6,402	6,368	3,404	3,372	214,15	212,08	1,801	420,61
$\mathbf{I_d}$**=-1A**	230,420	6,374	6,340	3,344	3,312	207,57	205,34	1,801	420,63

Furthermore, as regards the repeatability of the measurement and the evaluation of the measurement uncertainty, it is of considerable importance to evaluate the standard deviation for each quantity of interest. By way of example, the standard deviation average values of the quantities of interest for the first working point, evaluated respect to the total observation time, are reported in Table 32.

Table 32 Standard deviations of the quantities acquired at the first working point, for the three I_d current values

Standard deviation									
1) $\omega_n; T_n$									
	$\mathbf{V_m}$ **[V]**	$\mathbf{I_{m,p}[A]}$	$\mathbf{I_{m,sh}[A]}$	$\mathbf{I_1[A]}$	$\mathbf{I_3[A]}$	$\mathbf{V_{12}[V]}$	$\mathbf{V_{32}[V]}$	**C[Nm]**	$\boldsymbol{\omega_m}\left[\frac{\mathbf{rad}}{\mathbf{s}}\right]$
$\mathbf{I_d}$**=1A**	0.0142	0.002	0.0017	0.001	0.001	0.0088	0.0073	$2.81\ 10^{-4}$	$9.2\ 10^{-4}$
$\mathbf{I_d}$**=0A**	0.0162	0.004	0.0019	0.001	0.001	0.0078	0.0083	$5.81\ 10^{-4}$	$8.2\ 10^{-4}$
$\mathbf{I_d}$**=-1A**	0.0139	$4.6\ 10^{-4}$	$4.8\ 10^{-4}$	$1.6\ 10^{-4}$	$1.4\ 10^{-4}$	0.01	0.009	$1.5\ 10^{-6}$	$7.3\ 10^{-4}$

In Fig. 97-Fig. 102 the average values of each active power component (PDS input active power, active power absorbed by the motor and output mechanical power) for each case of study, I_d=1 A, I_d=0 A, and I_d=-1 A, are reported as function of mechanical speed n_m measured in rpm, respectively.

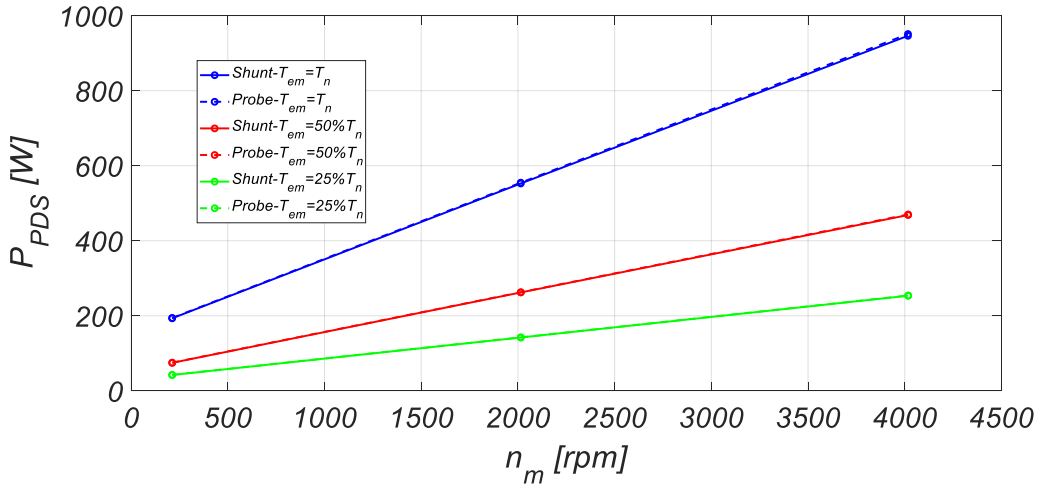

Fig. 97 PDS input active power measured with shunt resistor and fluke current probe at I_d=1 A.

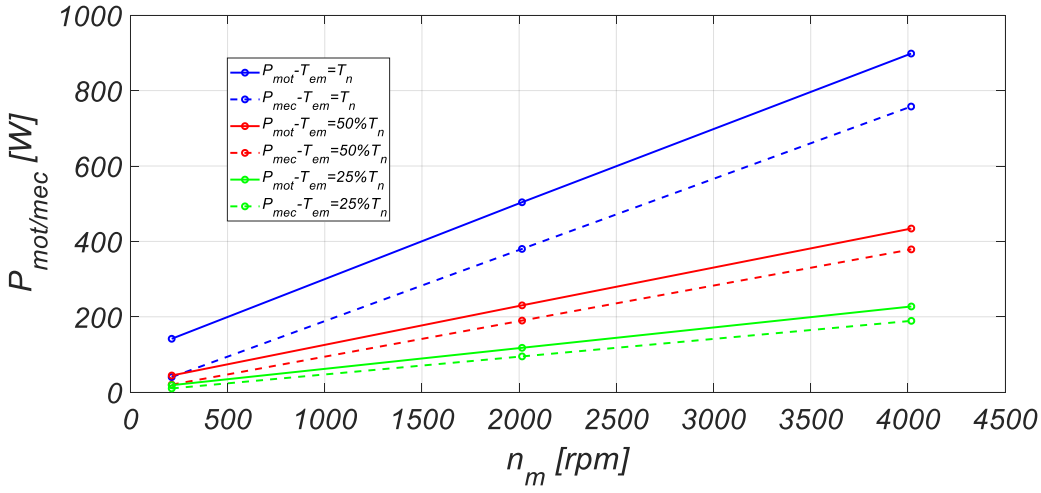

Fig. 98 Motor input active power and output mechanical power measured at I_d =1 A.

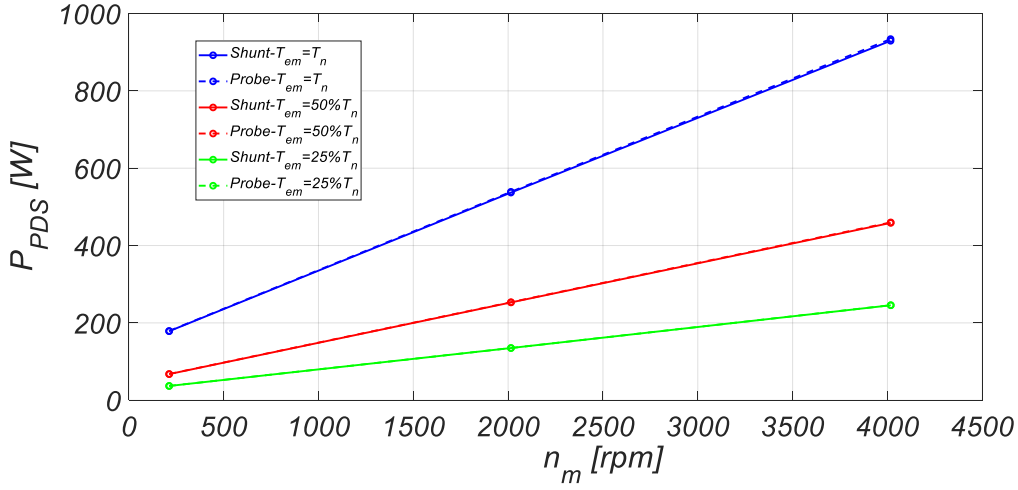

Fig. 99 PDS input active power measured with shunt resistor and fluke current probe at I_d =0 A.

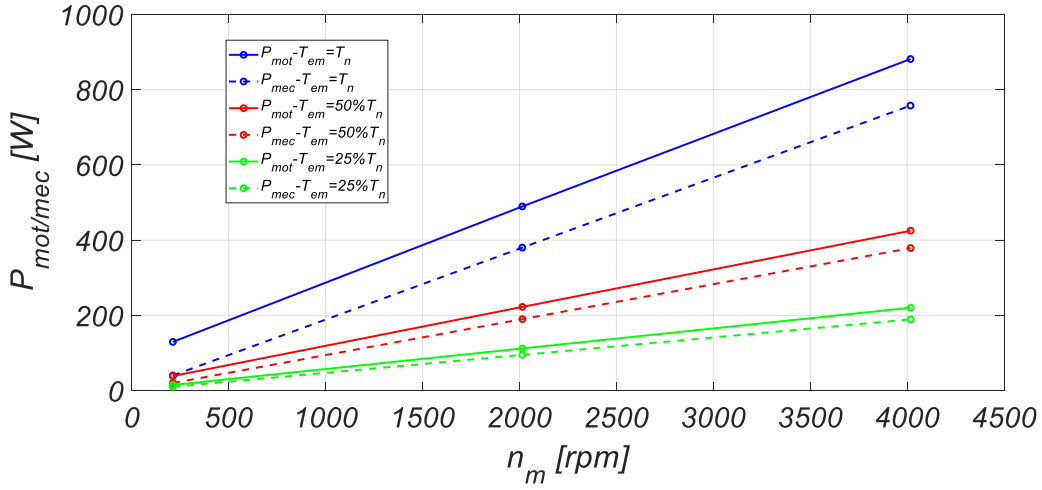

Fig. 100 Motor input active power and output mechanical power measured at I_d =0 A.

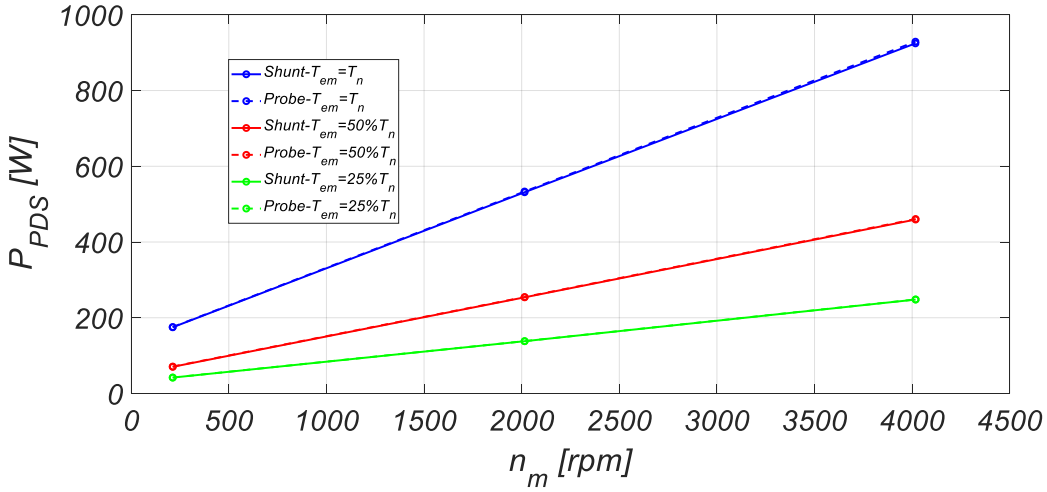

Fig. 101 PDS input active power measured with shunt resistor and fluke current probe at I_d =-1 A.

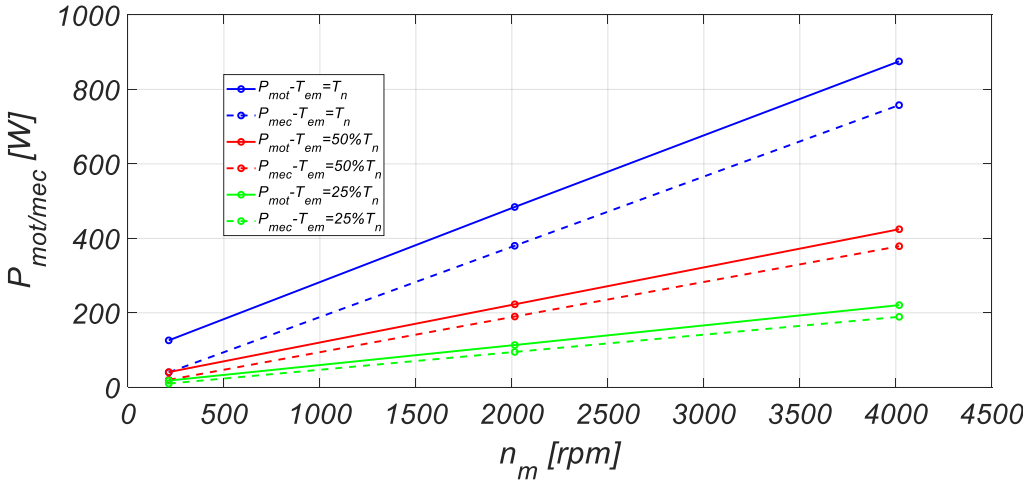

Fig. 102 Motor input active power and output mechanical power measured at I_d =-1 A.

From the acquired values of each active power component, it is possible to evaluate both the power losses than the efficiency of each part of the PDS or electric drive under

test. For simplicity, the efficiency mean values of CDM, motor, and PDS, evaluated respect to the total observation time, are reported in Fig. 103Fig. 111

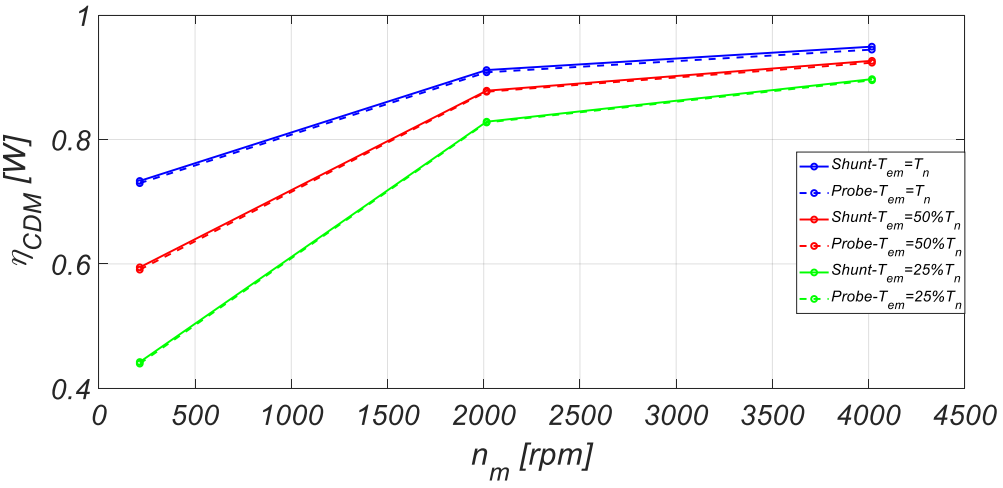

Fig. 103 CDM efficiency measured at I_d=1 A.

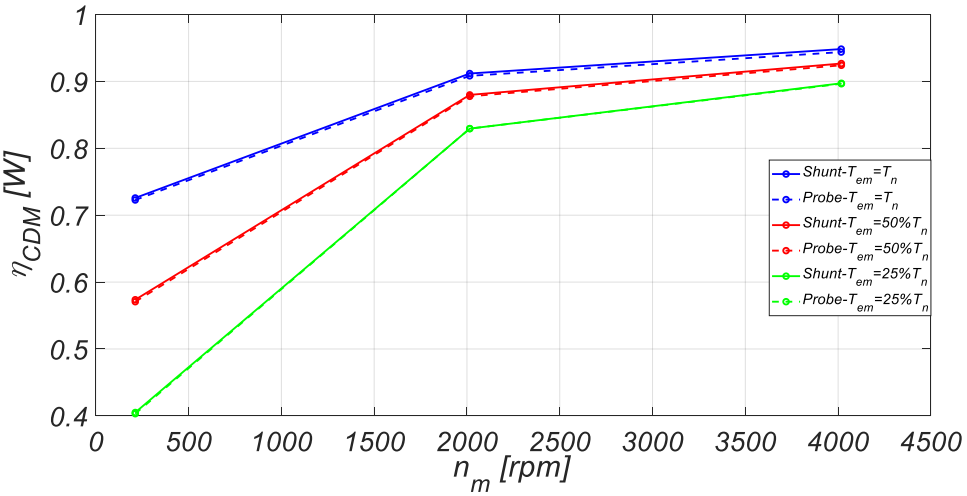

Fig. 104 CDM efficiency measured at I_d=0 A.

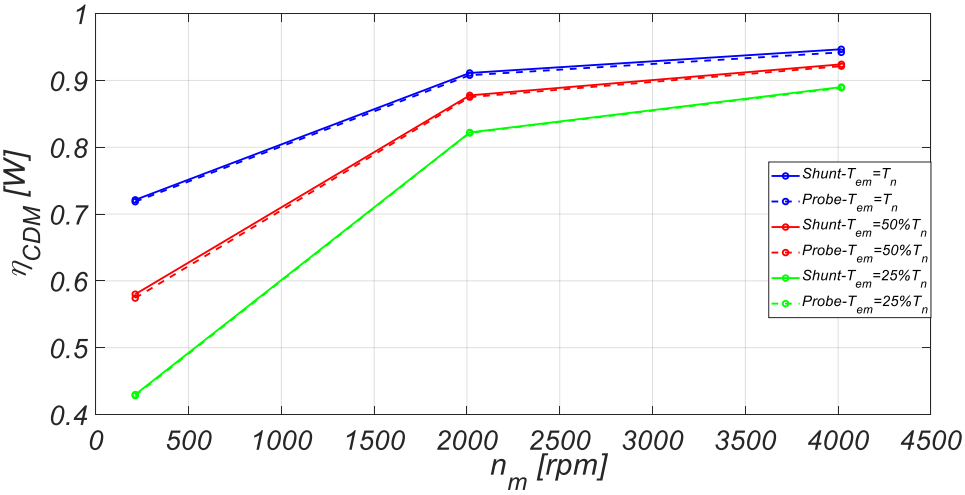

Fig. 105 CDM efficiency measured at I_d=-1 A.

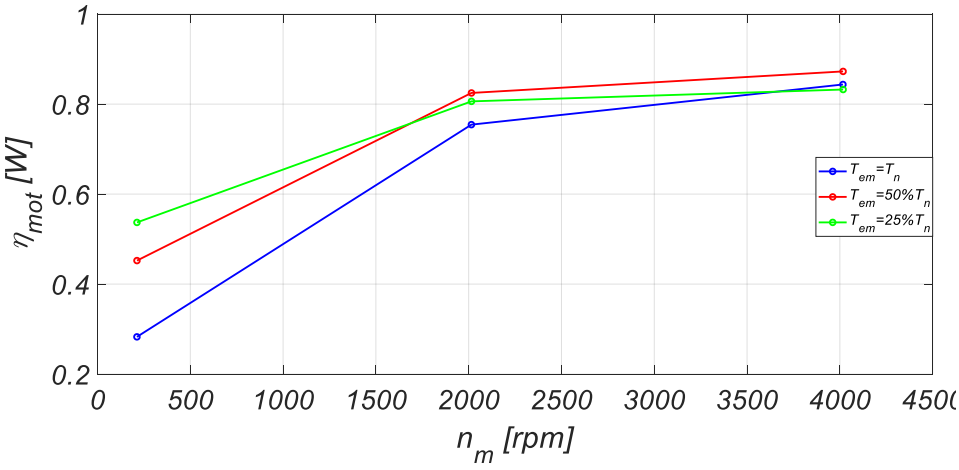

Fig. 106 Motor efficiency measured at I_d=1 A.

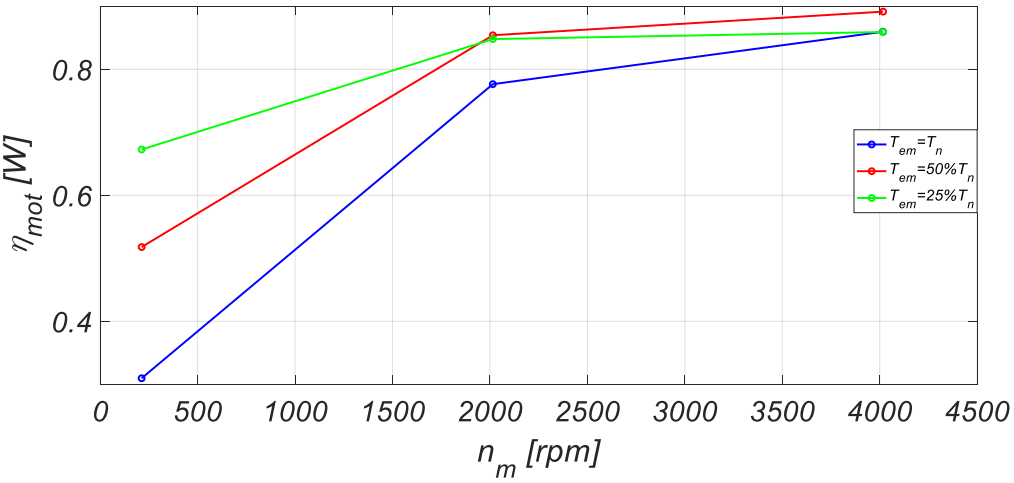

Fig. 107 Motor efficiency measured at I_d=0 A.

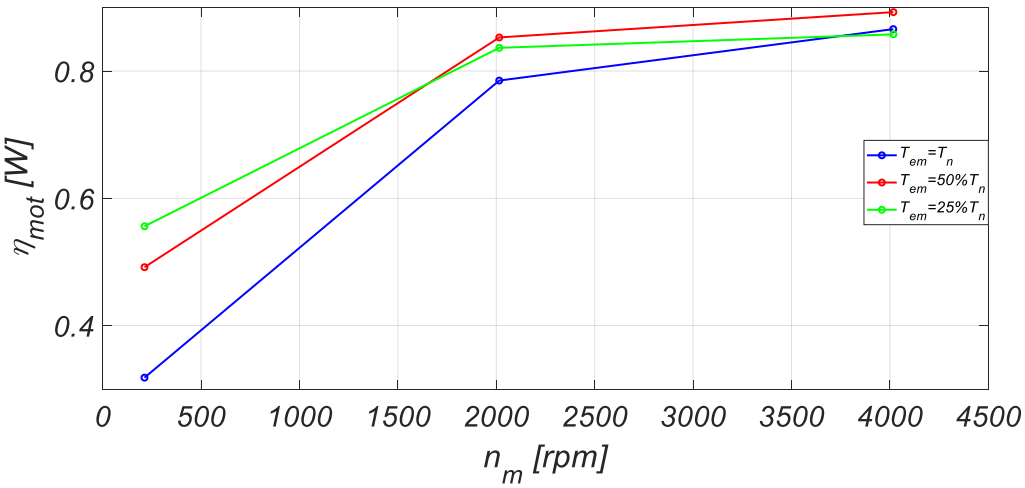

Fig. 108 Motor efficiency measured at I_d=-1 A.

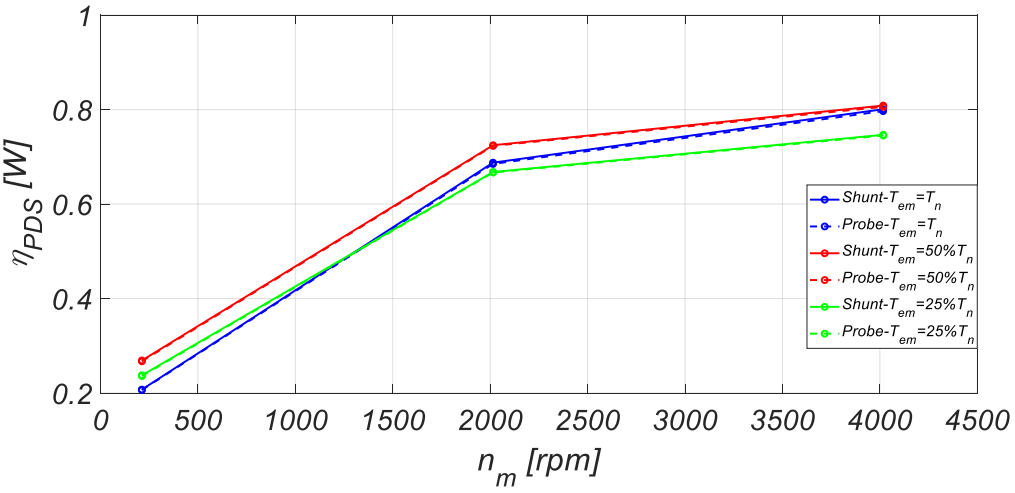

Fig. 109 PDS efficiency measured at I_d=1 A.

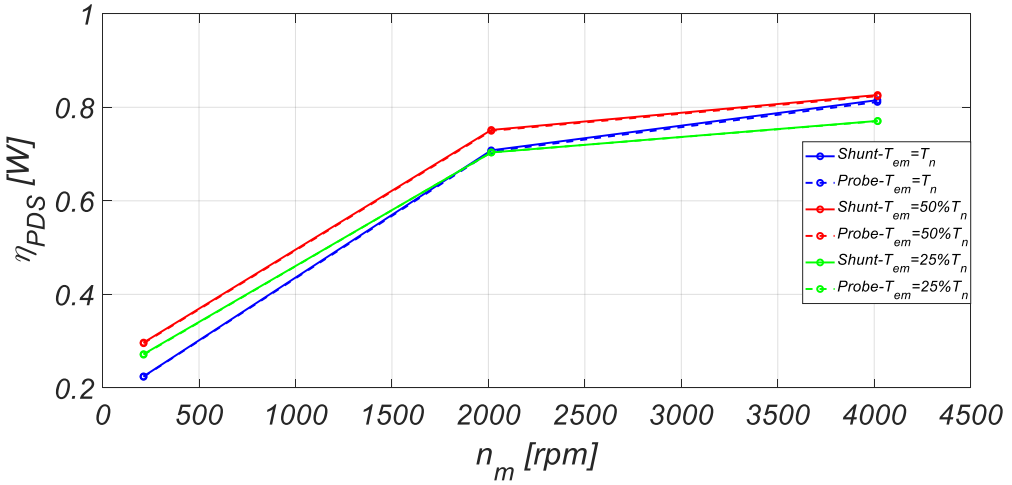

Fig. 110 PDS efficiency measured at I_d=0 A.

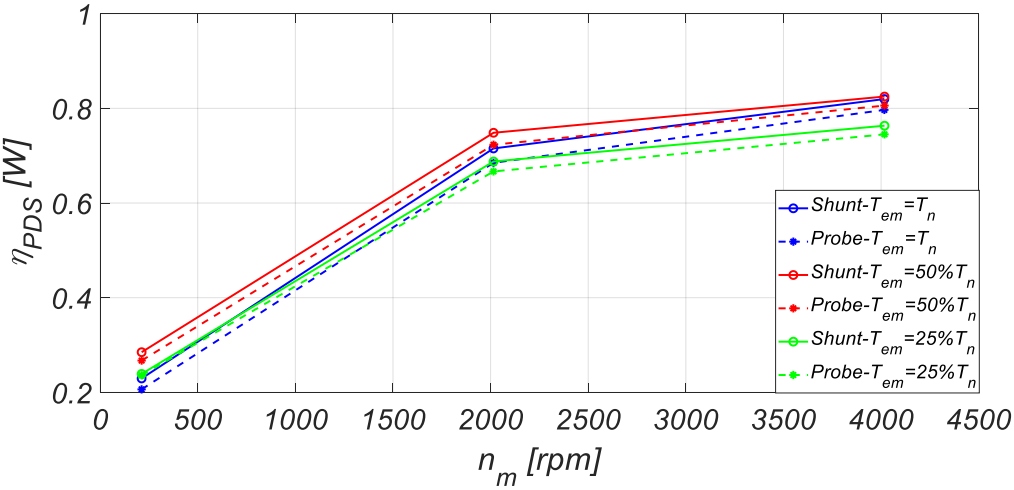

Fig. 111 PDS efficiency measured at I_d=-1 A.

In detail, the CDM (inverter) is the component that presents the highest values of efficiency at the correspondence of the working points analyzed. The values of CDM

efficiency increase as the load torque increase. In fact, for a converter, the performances improve when the working point is closer to the converter nominal working conditions. Although at nominal load torque T_n, the converter does not absorb its nominal current, this condition is nevertheless, compared to the other two, the one closest to the nominal working condition of the CDM. In addition, from Fig. 103 to Fig. 105, it is possible to see that the efficiency of CDM evaluated with shunt resistor is slightly higher than the efficiency evaluated with Fluke current probe for each *d*-axis current I_d value. Although also for the motor the efficiency increase as the load torque increase, a different efficiency behaviour has been detected compared to that of the CDM. In particular, for the condition $\omega_m=0$, the highest value of efficiency is obtained at the correspondence of the condition $T_{em}=25\%\ T_n$ for each *d*-axis current I_d value. While, for the conditions $\omega_m \geq 50\% \omega_n$, the highest value of efficiency is obtained at the correspondence of the condition $T_{em}=50\%\ T_n$ for each *d*-axis current I_d value (Fig. 106-Fig. 108). This behaviour can be attributed to the greater value of the current absorbed by the motor when it works at the nominal load torque $T_{em}=T_n$, which determinates an increase of the copper losses. The PDS efficiency behaviour is a combination of the behaviours before described. In detail, the highest efficiency values are obtained at correspondence of the load torque condition $T_{em}=50\%\ T_n$ for each *d*-axis current I_d value. Moreover, for the speed condition $\omega_m=0$, the PDS efficiency obtained at $T_{em}=25\%\ T_n$ are higher than the PDS efficiency obtained at $T_{em}=50\%\ T_n$. While for the speed conditions $\omega_m \geq 50\%\ \omega_n$, the PDS efficiency obtained at $T_{em}=25\%\ T_n$ is lower than the PDS efficiency obtained at $T_{em}=50\%\ T_n$. For all working points and for each *d*-axis current I_d value, the PDS efficiency values measured with shunt resistor are higher than those measured with Fluke current probe (Fig. 109-Fig. 111). A substantial difference between the PDS efficiency measured with the two mentioned systems was found when the IPMSM was powered with *d*-axis current $I_d=-1\ A$. The uncertainty, relating to the PDS efficiency measurement achieved with the two systems described, is analyzed below.

3.4.2 Uncertainty of the efficiency measurements

In this activity, the procedure for calculating the uncertainty is carried out only for the PDS efficiency. The latter is the one of greatest interest as it is an index of the performances of the entire electric drive under test and useful for the PDS energy

classification. The PDS efficiency uncertainty is affected by errors on power measurement in the PDS input single-phase section and by errors on power measurement in the PDS output mechanical section. Regarding the PDS input single-phase section, it is necessary to consider that there are two current transducers that have different accuracy. The uncertainty for the measurement of electrical power, with the system characterized by shunt resistance, has already been calculated in [III.13] and it is equal to 500 ppm or 0.05%. The expanded uncertainty with a confidence interval of 99% is then 0.13%. The measurement of the current through the Fluke current probe is affected by high uncertainty, since this probe has an error of 2% ± 0.06 A and its angle error is not known. An appropriate angle error value is set. This value is obtained by comparing the average specifications of the current probe transducer used with those of the same precision class, and, therefore, the value of 0.03 rad is reached. The expandend uncertainty on the measurement of PDS input single-phase power by Fluke current probe is equal to 9.3% (99% confidence interval).

The mechanical power measurement is mainly affected by the error introduced by the dynamometer, while the one introduced by the NI 9215 is negligible. Using the data provided by the dynamometer datasheet, the errors on torque and speed measurements are calculated. It is obtained that the expanded uncertainty, with a confidence interval of 99%, on the measurement of mechanical power is equal to 0.17%. The mechanical power can also be measured by direct reading of the dynamometer. The relative error committed, in this case, is obtained from the datasheet of the brake used, and is equal to 0.01% for the speed and to 0.5% for the torque. The expanded uncertainty with a confidence interval of 99% on the measurement of mechanical power with this second method is equal to 0.74%.

Finally, the relative uncertainties with a confidence interval of 99%, concerning the efficiency measurement with the first system, characterized by shunt resistance and acquisition of torque and speed, is 0.21%. Regarding the efficiency measurement with the measurement system characterized by Fluke current probe and acquisition of torque and speed, the relative uncertainty with a confidence interval of 99% is 9.4%. In both situations, the uncertainty reported is related to the worst case. The PDS efficiency measurement performed with the first measurement system complies with the IEC61800-9 uncertainty prescriptions and, therefore, can be used for the PDS energy

classification. While the PDS efficiency measurement performed with the first measurement system does not comply with the IEC61800-9 uncertainty prescriptions and, therefore, it cannot be used for the PDS energy classification. Therefore the analysis carried out underlines how high precision instrumentation is necessary and, therefore, economically expensive for the accurate efficiency measurement of electric drives under test.

3.5 New measurement approach for the comparison of electrical drive performances controlled by several control algorithms

The analysis carried out has shown that for accurate efficiency measurement of the electric drive under test, it is necessary to use accurate and, therefore, expensive measurement transducers. In this paragraph, a new and accurate measurement approach is presented which allows to compare the performances of an electric drive obtained using different control algorithm, also with low precision measurement instrumentation. This study was applied to the whole PDS taking into consideration the measurements made with the two measurement systems defined previously:

- A first measurement system composed of the acquisition module NI 9215 and high precision Fluke shunt resistor A40B;
- A second measurement system composed of the acquisition module NI 9215 and low precision Fluke current probe i400.

In the previous study, the PDS efficiency has been taken into consideration as a performance index of the electric drive under test, but the PDS power losses can be chosen in an equivalent manner. Let be $\Delta P_{PDS,Alg1,}$ and $\Delta P_{PDS,Alg2}$ the PDS power losses obtained with two control algorithms that supply the IPMSM with different *d*-axis current values, respectively. The PDS power losses are evaluated as the difference between the PDS input active power P_{PDS} and the PDS output mechanical power P_M. In general, the corresponding uncertainty of the PDS power losses measurement is:

$$u(\Delta P_{PDS}) = \sqrt{u^2(P_{PDS}) + u^2(P_M)} \tag{3.34}$$

where $u(P_{PDS})$ and $u(P_M)$ are the PDS input power measurement uncertainty and PDS output mechanical power measurement uncertainty, respectively. Each component of uncertainty includes both the contributions of systematic errors and random errors. Below, the quantity $\Delta\Delta P_{PDS}$ is defined as:

$$\Delta\Delta P_{PDS} = \Delta P_{PDS,Alg1} - \Delta P_{PDS,Alg2} \tag{3.35}$$

The $\Delta\Delta P_{PDS}$ represents an index of the power recovered passing from the first to the second control algorithm. In particular, since the use of the LMA involves the search for the optimal value of the *d*-axis current I_d which allows minimizing the power losses of the electric machine, the quantity $\Delta\Delta P_{PDS}$ can be used to compare the performance of LMA with other control algorithms. In this work the quantity $\Delta\Delta P_{PDS}$ is evaluated with

the two measurement system described and, therefore, the following two quantity are defined:

$$\Delta\Delta P_{PDS,shunt} = \left(\Delta P_{PDS,Alg1} - \Delta P_{PDS,Alg2}\right)_{shunt} \tag{3.36}$$

$$\Delta\Delta P_{PDS,probe} = \left(\Delta P_{PDS,Alg1} - \Delta P_{PDS,alg2}\right)_{probe} \tag{3.37}$$

where $\Delta\Delta P_{PDS,shunt}$ is evaluated with the shunt resistor and $\Delta\Delta P_{PDS,probe}$ is evaluated with the Fluke current probe. It is possible to prove that the $\Delta\Delta P_{PDS}$ measurement is not affected by uncertainty due to systematic errors. It is known that for the uncertainty propagation law, the uncertainty corresponding to a general quantity $y=f(x_1,x_2,....x_n)$, with $n \in N$, is:

$$u(y) = \sqrt{\sum_{i=1}^{n}\left(\frac{\partial f}{\partial x_i}\right)u^2(x_i) + 2\sum_{i=1}^{n-1}\sum_{j=i+1}^{n}\frac{\partial f}{\partial x_i}\frac{\partial f}{\partial x_j}r_{ij}u(x_i)u(x_j)} \tag{3.38}$$

where r_{ij} represents the correlation coefficient between the *i-th* and *j-th* quantities. For the singular case of the quantity $\Delta\Delta P_{PDS}$, it is:

$$y = \Delta\Delta P_{PDS} = \Delta P_{PDS,Alg1} - \Delta P_{PDS,Alg2} = P_{PDS,Alg1} - P_{M,Alg1} - P_{PDS,Alg2} + \\ + P_{M,Alg2} \tag{3.39}$$

Then, in the case under consideration, applying the relationship (3.38) we obtain:

$$u(\Delta\Delta P_{PDS}) = \left[u^2\left(P_{PDS,Alg1}\right) + u^2\left(P_{M,Alg2}\right) + u^2\left(P_{PDS,Alg2}\right) + u^2\left(P_{M,Alg2}\right) + \right. \\ -2r_{PDS,M}u\left(P_{PDS,Alg1}\right)u\left(P_{M,Alg1}\right) - 2r_{PDS,PDS}u\left(P_{PDS,Alg1}\right)u\left(P_{PDS,Alg2}\right) + \\ +2r_{PDS,M}u\left(P_{PDS,Alg2}\right)u\left(P_{M,Alg2}\right) + 2r_{PDS,M}u\left(P_{PDS,Alg2}\right)u\left(P_{M,Alg1}\right) + \\ \left. -2r_{M,M}u\left(P_{M,Alg1}\right)u\left(P_{M,Alg2}\right) - 2r_{PDS,M}u\left(P_{PDS,Alg2}\right)u\left(P_{M,Alg2}\right)\right]^{\frac{1}{2}} \tag{3.40}$$

Since both the input electric power and mechanical power are measured with the same measurement equipment and measured values are similar when the two control algorithms are employed, it is possible to assert that:

$$u(P_{PDS,Alg1}) = u(P_{PDS,Alg2}) = u(P_{PDS}) \tag{3.41}$$

$$u(P_{M,Alg1}) = u(P_{M,Alg2}) = u(P_M) \tag{3.42}$$

Let suppose that the uncertainty components are generated only by systematic errors. In this case, we can assert that, regarding the correlation coefficient, if the uncertainty quantities involved in the double product are both electrical or both mechanical, $r_ij=1$, while if the uncertainty quantities involved in the double product are one electrical and one mechanical, $r_ij=0$. The measurement uncertainty expression is:

$$u(\Delta\Delta P_{PDS}) = \sqrt{u^2(P_{PDS}) + u^2(P_M) + u^2(P_{PDS}) + u^2(P_M) - 2u(P_{PDS})u(P_{PDS}) - 2u(P_M)u(P_M)} \quad (3.43)$$

In conclusion, the following expression is obtained:

$$u(\Delta\Delta P_{PDS}) = \sqrt{2u^2(P_{PDS}) + 2u^2(P_M) - 2u^2(P_{PDS}) - 2u^2(P_M)} = 0 \quad (3.44)$$

This result is of considerable importance, as it emphasizes that $\Delta\Delta P_{PDS,shunt}$ and $\Delta\Delta P_{PDS,probe}$ are not affected by the uncertainties due to systematic errors. Therefore, the measurements of $\Delta\Delta P_{PDS,shunt}$ and of $\Delta\Delta P_{PDS,probe}$ should give coinciding results, except for a limited deviation due to random errors. After this theoretical premise, the experimental validation of the proposed measurement approach is shown below.

3.5.1 Experimental validation of the proposed measurement approach

In order to compare the performances of the electric drive under test controlled with I_d=1 A, I_d=0 A, and I_d=-1 A, respectively, the $\Delta\Delta P_{PDS,shunt}$ and $\Delta\Delta P_{PDS,probe}$ values are calculated from the experimental data acquired and for each IPMSM working condition. These values have been evaluated starting from the value of PDS power losses can be obtained from the PDS input power array acquired with Fluke shunt resistor $P_{PDS,shunt}$, the PDS input power array acquired with Fluke shunt resistor $P_{PDS,shunt}$, and PDS output mechanical power array P_M. The PDS power losses evaluated with the first measurement system $\Delta P_{PDS,shunt}$ and with the second measurement system $\Delta P_{PDS,probe}$ are calculated with the following relationships:

$$\Delta P_{PDS,shunt} = P_{PDS,shunt} - P_M \quad (3.45)$$

$$\Delta P_{PDS,probe} = P_{PDS,probe} - P_M \quad (3.46)$$

In detail, three cases of study can be defined:

- Comparison between the performances of the electric drive under test controlled with I_d=1A and with I_d=-1A (*Case 1*);
- Comparison between the performances of the electric drive under test controlled with I_d=1A and with I_d=0A (*Case 2*);
- Comparison between the performances of the electric drive under test controlled with I_d=0A and with I_d=-1A (*Case 3*);

In Fig. 112 $\Delta\Delta P_{PDS}$ evaluated when the IPMSM is supplied with I_d=1 A and I_d=-1 A for each motor working condition., Fig. 113 and Fig. 114 the mean values of $\Delta\Delta P_{PDS,shunt}$

and $\Delta\Delta P_{PDS,probe}$, evaluated respect to the total observation time T_w equal to 40 minutes, obtained for each case of study are reported.

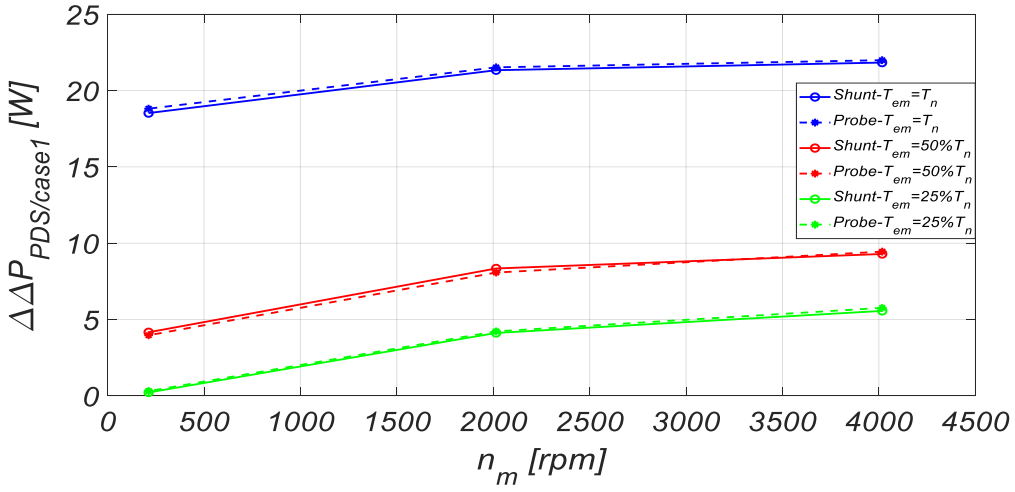

Fig. 112 $\Delta\Delta P_{PDS}$ evaluated when the IPMSM is supplied with I_d=1 A and I_d=-1 A for each motor working condition.

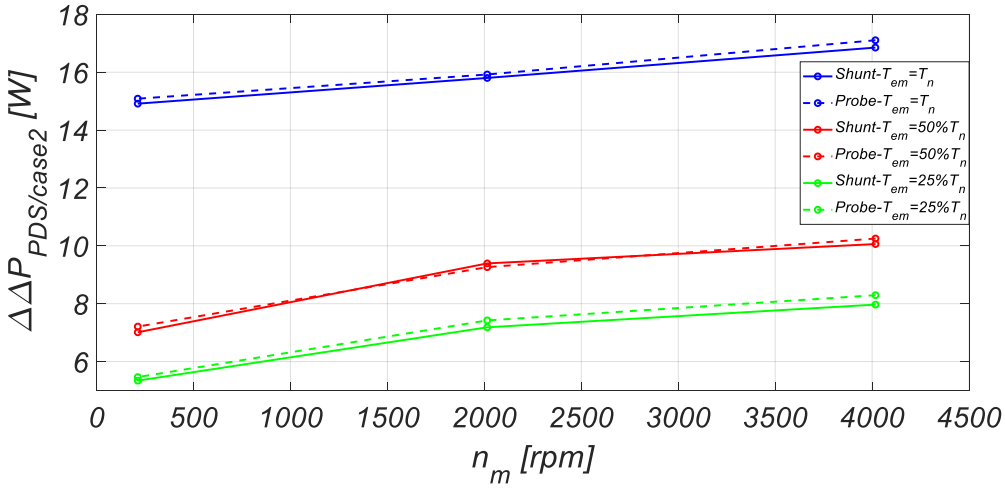

Fig. 113 $\Delta\Delta P_{PDS}$ evaluated when the IPMSM is supplied with I_d=1 A and I_d=0 A for each motor working condition.

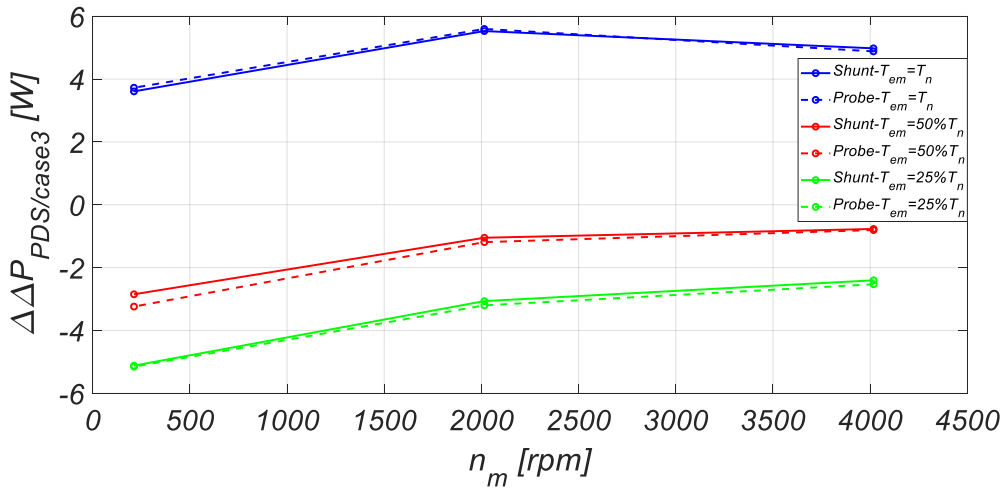

Fig. 114 $\Delta\Delta P_{PDS}$ evaluated when the IPMSM is supplied with I_d=0 A and I_d=-1 A for each motor working condition.

In detail, from the figures, it is possible to see how the value of $\Delta\Delta P_{PDS}$ evaluated with the shunt resistor and the Fluke current probe are very similar. A further analysis was carried out, calculating the percentage values $\Delta\Delta P_{PDS}\%$ of the quantity $\Delta\Delta P_{PDS,shunt,}$ and $\Delta\Delta P_{PDS,probe}$ respect the IPMSM mechanical power rated value $P_{M,n}$:

$$\Delta\Delta P_{PDS}\% = \frac{\Delta P_{PDS}}{P_{M,n}} 100 = \frac{\Delta P_{PDS}}{T_n \omega_n} 100 \tag{3.47}$$

In Fig. 115, Fig. 116 and Fig. 117 the mean values of $\Delta\Delta P_{PDS,shunt}\%$ and $\Delta\Delta P_{PDS,probe}\%$, evaluated respect to the total observation time T_w equal to 40 minutes, obtained for each case of study are reported.

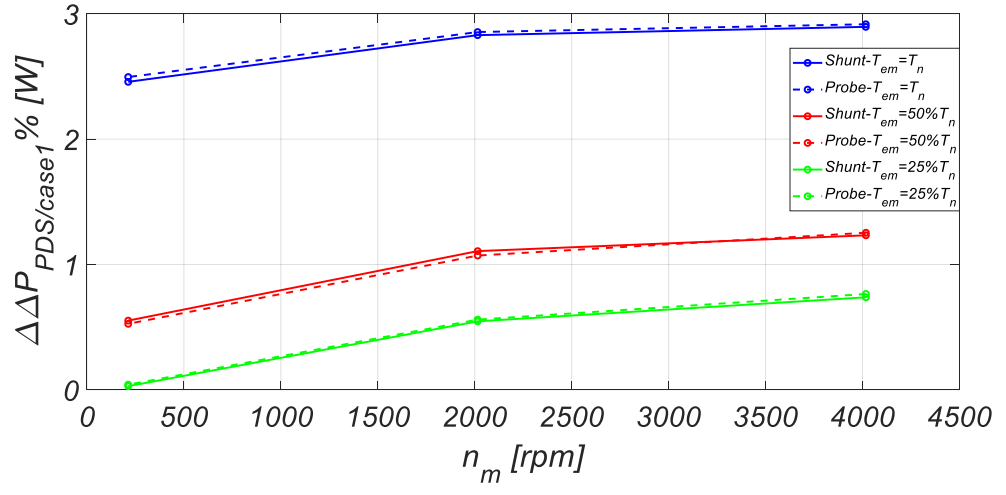

Fig. 115 $\Delta\Delta P_{PDS}\%$ evaluated when the IPMSM is supplied with I_d=1 A and I_d=-1 A for each motor working condition.

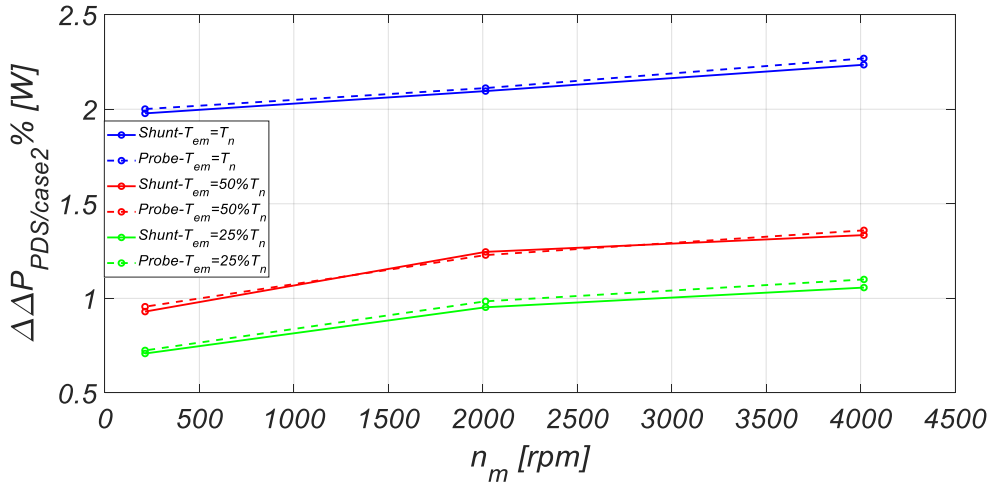

Fig. 116 $\Delta\Delta P_{PDS}\%$ evaluated when the IPMSM is supplied with I_d=1 A and I_d=0 A for each motor working condition.

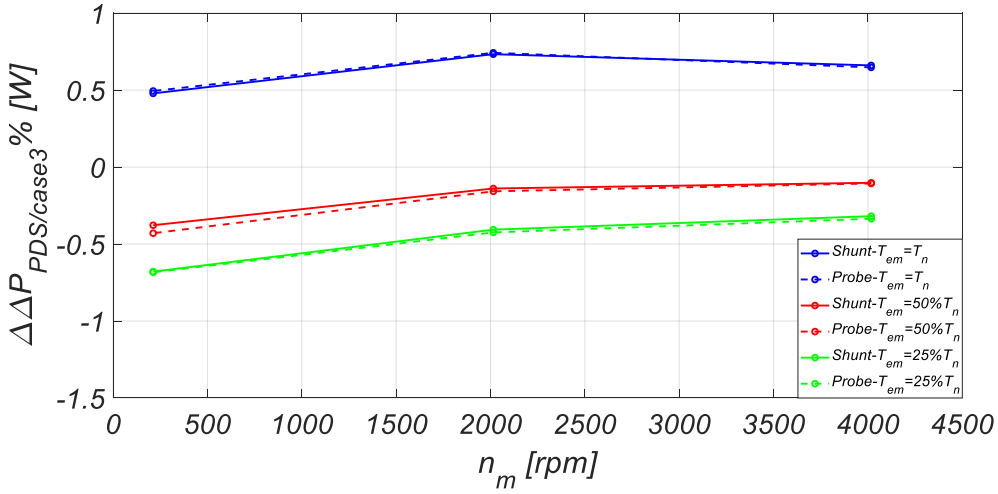

Fig. 117 $\Delta\Delta P_{PDS}\%$ evaluated when the IPMSM is supplied with I_d=0 A and I_d=-1 A for each motor working condition.

This analysis also confirms that the quantities $\Delta\Delta P_{PDS,shunt}\%$ and $\Delta\Delta P_{PDS,probe}\%$, have almost coincident values. In addition, the differences between the $\Delta\Delta P_{PDS,shunt}$ and $\Delta\Delta P_{PDS,probe}$ values and between the $\Delta\Delta P_{PDS,shunt}\%$ and $\Delta\Delta P_{PDS,probe}\%$ values are calculated with the following relationships for each case of study:

$$\Delta P_{case1} = \Delta\Delta P_{PDS,shunt/case1} - \Delta\Delta P_{PDS,probe/case1} \quad (3.48)$$

$$\Delta P_{case2} = \Delta\Delta P_{PDS,shunt/case2} - \Delta\Delta P_{PDS,probe/case2} \quad (3.49)$$

$$\Delta P_{case3} = \Delta\Delta P_{PDS,shunt/case3}\% - \Delta\Delta P_{PDS,probe/case3}\% \quad (3.50)$$

$$\Delta P_{case1}\% = \Delta\Delta P_{PDS,shunt/case1}\% - \Delta\Delta P_{PDS,probe/case1}\% \quad (3.51)$$

$$\Delta P_{case2}\% = \Delta\Delta P_{PDS,shunt/case2}\% - \Delta\Delta P_{PDS,probe/case2}\% \quad (3.52)$$

$$\Delta P_{case3}\% = \Delta\Delta P_{PDS,shunt/case3}\% - \Delta\Delta P_{PDS,probe/case3}\% \quad (3.53)$$

In Table 33 the numerical results of the differences before mentioned are reported. In particular, from the analysis of these numerical results, it is possible to see that the ΔP_{casei} absolute value does not exceed the value of 0.4 W and the $\Delta P_{casei}\%$ percentage value does not exceed the value of 0.055%. This conducted analysis confirms how the quantity $\Delta\Delta P_{PDS}$, even if evaluated with low precision instruments, can be used as an index to compare the performances of the same electric drive under test controlled with several control algorithms. Finally, in the next section, the evaluation of $\Delta\Delta P_{PDS}$ measurement uncertainty is reported in Table 33.

Table 33 Numerical results of the differences between the $\Delta\Delta P_{PDS,shunt}$ and $\Delta\Delta P_{PDS,probe}$ values and between the $\Delta\Delta P_{PDS,shunt}\%$ and $\Delta\Delta P_{PDS,probe}\%$ values

	ΔP_{case1}[W]	ΔP_{case2}[W]	ΔP_{case3}[W]	$\Delta P_{case1}\%$	$\Delta P_{case1}\%$	$\Delta P_{case1}\%$
1	-0.157	-0.253	0.096	-0.021	-0.034	0.013
2	-0.187	-0.119	-0.068	-0.025	-0.016	0.009
3	-0.288	-0.172	0.115	-0.038	-0.023	0.015
4	-0.155	-0.19	0.035	-0.021	-0.025	0.046
5	-0.267	0.128	0.14	0.035	0.017	0.018
6	0.194	-0.196	0.391	0.026	-0.026	0.052
7	-0.198	-0.325	0.126	-0.026	-0.043	0.017
8	-0.104	-0.238	0.134	-0.014	-0.031	0.018
9	-0.09	-0.123	0.033	-0.012	-0.016	0.004

3.5.2 Uncertainty calculation of the $\Delta\Delta P_{PDS}$ measurement

The innovative feature of the measurement approach proposed, for the comparison of the performances of an electric drive controlled by several control algorithms, is that allows to accurately measure the efficiency variation also by means of low accurate and cheaper measurement equipment thanks to the fact that the effects of the systematic errors balance out. Therefore, the $\Delta\Delta P_{PDS}$ measurement uncertainty includes only the measurement uncertainty due to random errors. This last contribution is equal to the $\Delta\Delta P_{PDS}$ standard deviation evaluated respect to the total observation time T_w equal to 40 minutes. This uncertainty allows defining the possible range values in which it is possible to find the value of the quantity of interest with a probability of 66%. In this analysis, we refer to the expanded uncertainty with a confidence interval of 99% that

can be obtained multiplying the deviation standard to 2.58. In particular, it is possible to define the maximum and minimum values of the range with the following relationships:

$$\Delta\Delta P_{PDS,max} = \Delta\Delta P_{PDS} + u(\Delta\Delta P_{PDS}) \quad (3.54)$$

$$\Delta\Delta P_{PDS,max} = \Delta\Delta P_{PDS} - u(\Delta\Delta P_{PDS}) \quad (3.55)$$

The expanded uncertainty of $\Delta\Delta P_{PDS}$ with a confidence interval of 99%, evaluated with shunt resistor $u_{shunt}(\Delta\Delta P_{PDS})$ and evaluated with Fluke current probe $u_{probe}(\Delta\Delta P_{PDS})$ for each case of study (named with subscript "1,2,3", respectively) and for each motor working condition, are reported in the Table 34, respectively.

Table 34 $\Delta\Delta P_{PDS}$ uncertainty for each case of study and for each working condition

Working points **n**	$u_{shunt,1}(\Delta\Delta P_{PDS})$ **[W]**	$u_{shunt,2}(\Delta\Delta P_{PDS})$ **[W]**	$u_{shunt,3}(\Delta\Delta P_{PDS})$ **[W]**	$u_{probe,1}(\Delta\Delta P_{PDS})$ **[W]**	$u_{probe,2}(\Delta\Delta P_{PDS})$ **[W]**	$u_{probe,3}(\Delta\Delta P_{PDS})$ **[W]**
1	0.42	0.54	0.42	0.24	0.51	0.47
2	0.29	0.24	0.27	0.27	0.23	0.26
3	0.46	0.29	0.45	0.26	0.24	0.35
4	0.24	0.23	0.24	0.21	0.21	0.19
5	0.27	0.26	0.27	0.17	0.17	0.13
6	0.26	0.26	0.26	0.27	0.27	0.27
7	0.2	0.21	0.18	0.18	0.1	0.17
8	0.17	0.21	0.15	0.11	0.12	0.12
9	0.31	0.22	0.29	0.22	0.22	0.2

In order to further highlight the accuracy of the proposed measurement method, it is possible to analyze the relationships between the mean values of $\Delta\Delta P_{PDS}$ evaluated with the two measurement systems and their range values obtained with the relationships (3.54) and (3.55). Referring to the 9 motor working points (Table 30), the mean values of $\Delta\Delta P_{PDS}$ and their range values obtained at correspondence of rated load torque T_n (motor working points 1,2,3), at correspondence of 50% of T_n (motor working points 4,5,6) and at correspondence of 25% of T_n (motor working points 7,8,9) are reported in Fig. 118, Fig. 119 and Fig. 120, respectively.

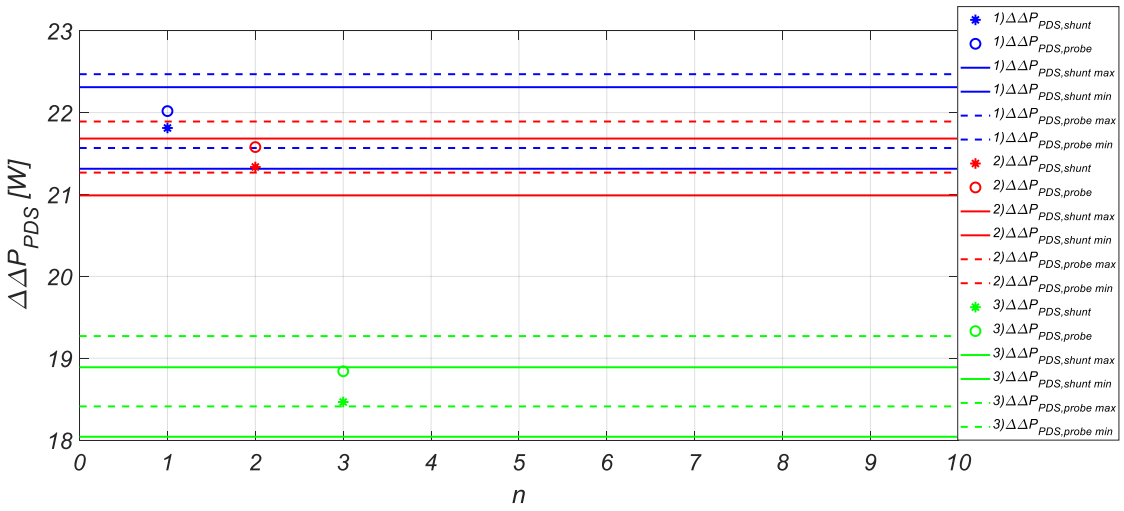

Fig. 118 $\Delta\Delta P_{PDS}$ mean values and their range values obtained at rated load torque T_n.

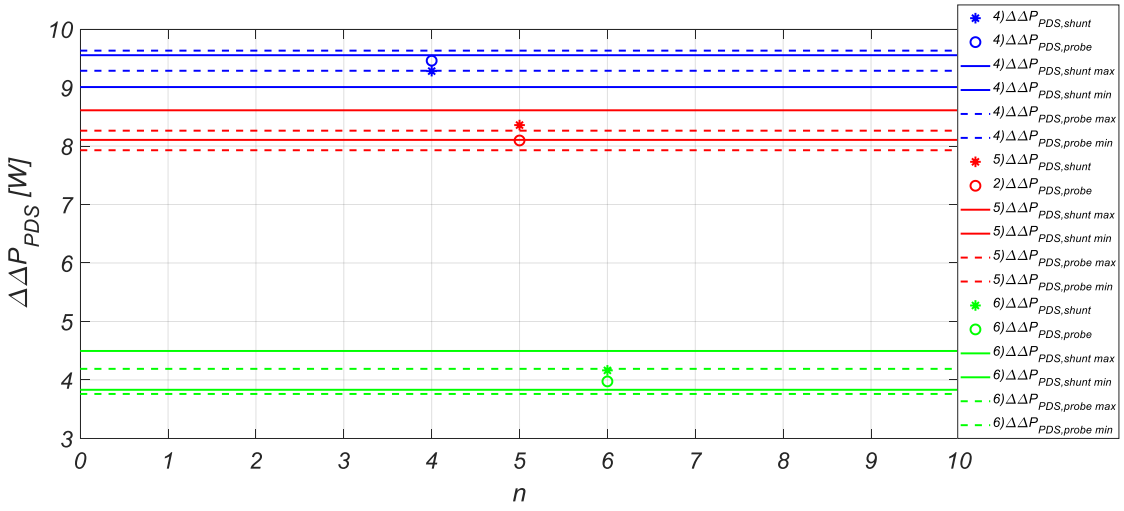

Fig. 119 $\Delta\Delta P_{PDS}$ mean values and their range values obtained at 50% of load torque T_n.

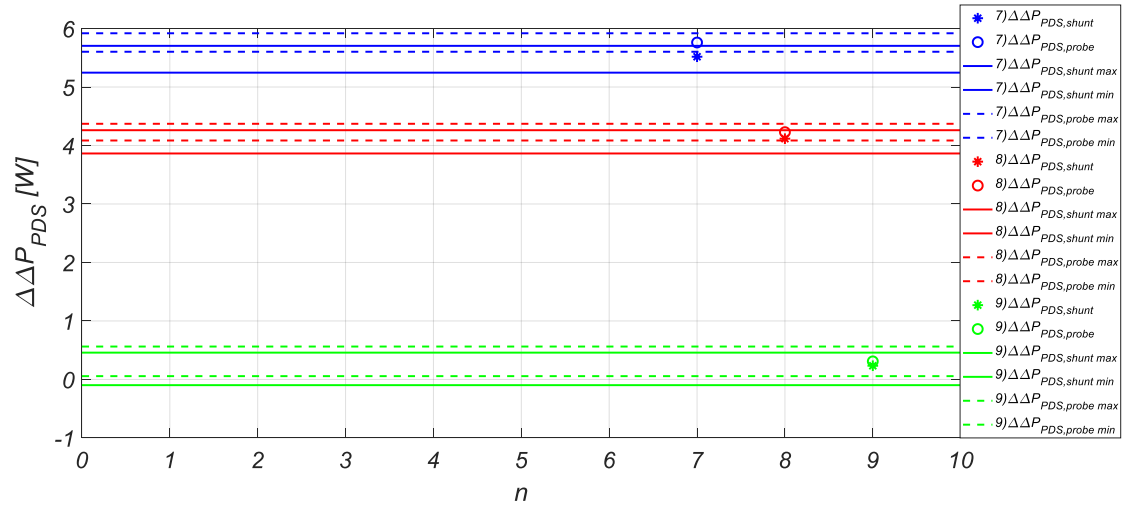

Fig. 120 $\Delta\Delta P_{PDS}$ mean values and their range values obtained at 25% of load torque T_n.

These figures, besides showing the small difference between the $\Delta\Delta P_{PDS}$ mean values, obtained with the two measurement system, for each motor working conditions, show how among the $\Delta\Delta P_{PDS}$ range values evaluated with measurement system equipped with shunt resistor and evaluated with the measurement system equipped with Fluke current probe there are intersections and, therefore, possible values of $\Delta\Delta P_{PDS}$ in common. This last observation allows us to assert that the difference between the possible $\Delta\Delta P_{PDS}$ values evaluated with the two measurement systems is quite limited.

References

[III.1] IEC 60034-2-1. Rotating electrical machines - Part 2-1: Standard methods for determining losses and efficiency from test., 2011.

[III.2] IEC 60034-2-2. Rotating electrical machines - Part 2-2: Specific methods for determining separate losses of large machines from tests - Supplement to IEC 60034-2-1.

[III.3] IEC 60034-2-3. Specific test methods for determining losses and efficiency of converter-fed AC motors, 2011.

[III.4] "IEEE trial-use guide for testing permanent magnet machines," IEEE Std 1812-2014, pp. 1–56, Feb 2015.

[III.5] IEC 61800-9-1. Adjustable speed electrical power drive systems - Part 9-1: Ecodesign for power drive systems, motor starters, power electronics and their driven applications - General requirements for setting energy efficiency standards for power driven equipment using the extended product approach (EPA) and semi analytic model (SAM).

[III.6] IEC 61800-9-2. Adjustable Speed Electrical Power Drive Systems—Part 9-2: Ecodesign for Power Drive Systems, Motor Starters, Power Electronics & Their Driven Applications—Energy Efficiency Indicators for Power Drive Systems and Motor Starters, 2017.

[III.7] G. Bucci, F. Ciancetta, E. Fiorucci and A. Ometto, "Uncertainty Issues in Direct and Indirect Efficiency Determination for Three-Phase Induction Motors: Remarks About the IEC 60034-2-1 Standard," in IEEE Transactions on Instrumentation and Measurement, vol. 65, no. 12, pp. 2701-2716, Dec. 2016.

[III.8] R. Antonello, F. Tinazzi e M. Zigliotto, «Energy efficiency measurements in IM: the non-trivial application of the norm IEC 60034-2-3:2013» in 2015 IEEE Workshop on Electrical Machines Design, Control and Diagnosis, Torino, 2015.

[III.9] E. B. Agamloh, "Power and efficiency measurement of motor-variable frequency drive systems," 2015 61st IEEE Pulp and Paper Industry Conference (PPIC), Milwaukee, WI, 2015, pp. 1-8.

[III.10] K. Stockman, S. Dereyne, D. Vanhooydonck, W. Symens, J. Lemmens and W. Deprez, "Iso efficiency contour measurement results for variable speed

drives," The XIX International Conference on Electrical Machines - ICEM 2010, Rome, 2010, pp. 1-6.

[III.11] IEC 60034-30-1. Rotating electrical machines - Part 30-1: Efficiency classes of line operated AC motors.

[III.12] IEC 60034-30-2. Rotating electrical machines - Part 30-2: Efficiency classes of variable speed AC motors (IE-code).

[III.13] A. Cataliotti, V. Cosentino, D. Di Cara, A. Lipari, S. Nuccio and C. Spataro, "A PC-Based Wattmeter for Accurate Measurements in Sinusoidal and Distorted Conditions: Setup and Experimental Characterization," in IEEE Transactions on Instrumentation and Measurement, vol. 61, no. 5, pp. 1426-1434, May 2012.

Chapter 4 Enhanced mathematical modelling of IPMSM

4.1 Introduction

The interior permanent magnet synchronous machine (IPMSM) is one of the most widely employed machine typology in many applications, such as automotive [IV.1]-[IV.4], aerospace [IV.5]-[IV.6], and marine industries [IV.7]. The conventional IPMSM mathematical model is commonly used in the study and simulation of IPMSM drive control system. In particular, the conventional IPMSM mathematical model is based on idealized hypotheses, such as the sinusoidal spatial distribution of the magneto-motive force in the air-gap, linear behaviour of the machine magnetic circuits that involves the absence of self-saturation and cross-coupling effects, spatial harmonics in phase voltages, iron core losses and the temperature effects on the machine behaviour. However, nonlinearity and temperature effects have a substantial influence on the IPMSM performances and characteristics. The conventional idealized IPMSM mathematical model in *dq*-reference frame may be unreliable in predicting the performances of saturated machines [IV.7]-[IV.10]. The parameters of the two-axes or *dq*-axes model vary nonlinearly, depending on operating conditions that change the level of saturation and magnetic field distribution in the motor. The self magnetic saturation and the cross magnetization have a substantial influence on the *dq*-axes inductances. In particular, saturation and cross-magnetization modelling of an anisotropic synchronous machine requires a great amount of data, regarding *dq*-axes magnetizing curves, evaluated for several working conditions. Although the *d*-axis magnetizing curve is generally known, the *q*-axis magnetizing curve is usually not available. In literature, several modelling approaches, that take into account the saturation and cross-coupling effects, are proposed [IV.8], [IV.11]. In addition, the presence of reluctance torque in IPMSM not only determines a nonlinear relationship between the electromagnetic torque and the armature current components but also leads to greater level of spatial harmonics in phase voltages due to the inherently large variation in the magnetic energy with the rotor position [IV.12], [IV.13]. Therefore, if the spatial harmonics and magnetic saturation effects in the stator and rotor cores are neglected, the conventional IPMSM *dq*-axes model, that employs constant values of *d*- and *q*-axis inductances, cannot accurately represent the IPMSM electromechanical behaviour [IV.14]. Moreover, this behaviour is emphasized when the IPMSM works in

the field weakening region where the phase voltage harmonics will distort the current waveforms due to the limited dc-link voltage. Since traction motors for automotive applications are designed to work in the constant power region or field weakening region and, therefore, they operate in highly nonlinear conditions, a high fidelity IPMSM model can be of great aid for the design of innovative control strategies and for the evaluation of their performances.

Therefore, without a high fidelity IPMSM machine model, a high-performance IPMSM machine control algorithm cannot be accurately evaluated in the simulation. Furthermore, since the performances of an electric drive controlled by the Loss Model Algorithm (LMA), especially in terms of efficiency, depends on the accuracy of the mathematical model of the IPMSM, the definition of a new and enhanced IPMSM mathematical model can be of considerable use. The goal of this work is to investigate and define an IPMSM mathematical model including saturation, cross-coupling, spatial harmonics and iron loss effects. For this purpose, the IPMSM under test, described in previous chapters, has been taken into consideration, implemented in *Ansys Maxwell* environment, and several finite element analysis (FEA) investigations have been carried out. In this way, the *dq*-axes flux linkages, variable with the *dq*-axes currents and the rotor position, were established via FEA transient simulations.

In detail, this chapter firstly describes the IPMSM enhanced mathematical model that takes into account the saturation, cross-coupling, and spatial harmonics effects, and secondly the FEA (Finite-element analysis) investigations conducted in *Ansys Maxwell* environment for the characterization of the IPMSM. Subsequently, the FEA investigations conducted for the definition of iron loss mathematical model and its integration in the previously defined model are described. Finally, in order to validate the IPMSM enhanced mathematical model, it has been implemented in Matlab/Simulink environment and its results have been compared with the results of the FEA investigations carried out on the IPMSM model implemented in *Ansys Maxwell* environment.

4.2 Enhanced mathematical modelling of IPMSM in order to that take into account saturation, cross-coupling and spatial harmonics effects

The conventional approach to modelling the IPMSM is based on the following voltage and torque equations:

$$v_d = Ri_d + L_d \frac{di_d}{dt} - \omega_e L_q i_q \tag{4.1}$$

$$v_q = Ri_q + L_q \frac{di_q}{dt} + p\omega_e L_d i_d + \omega_e \lambda_{PM} \tag{4.2}$$

$$T_{em} = \frac{3}{2} p\left[\lambda_{PM} i_q + \left(L_d - L_q\right) i_d i_q\right] \tag{4.63}$$

where v_d is the *d*-axis voltage, v_q is the *q*-axis voltage, i_d is the *d*-axis current, i_q is the *q*-axis current, R is the stator winding resistance, L_d is the *d*-axis inductance, L_q is the *q*-axis inductance, p is the number of pole pairs, m is the number of the phases, ω_e is the electrical angular speed, λ_{PM} is the permanent magnet flux linkage and T_{em} is the electromagnetic torque. In the conventional approach the parameters L_d, L_q and λ_{PM} present constant values. In literature, several modelling approaches, that take the saturation effects into account, have been proposed [IV.15]-[IV.20]. In detail, the *dq*-axes inductances are a function of *dq*-axes currents, respectively, and the PM flux linkage is a function of the *q*-axis current. These IPMSM modelling approaches only captures the effects of the fundamental components, whereas the harmonic field components resulting from the combination of saturation, cross-coupling, slotting, and permeance variance with the rotor position are neglected. Therefore, in order to analyze the problems associated with the IPMSM conventional modelling approach, below the definition of the new IPMSM modelling approach will be shown. The *dq*-axes flux linkages λ_d and λ_q are functions of the *dq*-axes currents i_d, i_q, since the currents are the main source of flux linkages in the IPMSM, and the cross-saturation between the *d*-axis and *q*-axis is inevitably present due to the imperfect construction symmetry of the machine. The spatial harmonics are present also due to the slotting effects and this phenomenon is a function of the rotor mechanical position θ_m. Therefore, in order to take into account the effect of saturation, cross-coupling and spatial harmonics effects it is necessary to define *dq*-axes flux linkages λ_d and λ_q as functions of the *dq*-axes currents i_d, i_q and the rotor position θ_m, as shown in [IV.8]-[IV.13]. The voltage equations of a three-phase IPMSM can be expressed as:

$$[v_{abc}(t)] = R[i_{abc}] + \frac{d[\lambda_{abc}]}{dt} \tag{4.3}$$

where $[v_{abc}]$, $[i_{abc}]$, $[\lambda_{abc}]$ are the stator voltage vectors, the stator current vectors and the stator flux linkages vectors in the *abc*-reference frame, respectively. With the use of Park transformation, described in Chapter 1, it is possible to define the *dq*-axes voltage equations:

$$v_d = Ri_d + L_d \frac{d\lambda_d}{dt} - \omega_e \lambda_q \tag{4.4}$$

$$v_q = Ri_q + L_q \frac{d\lambda_q}{dt} + \omega_e \lambda_d \tag{4.5}$$

Furthermore, the *dq*-axis flux linkages can be described as follow:

$$\lambda_d(t) = \lambda_{di}(t) + \lambda_{dPM} \tag{4.6}$$

$$\lambda_q(t) = \lambda_{qi}(t) + \lambda_{qPM} \tag{4.7}$$

where λ_{di} and λ_{qi} are the *dq*-axes flux linkages produced by the stator currents excitation and λ_{dPM} and λ_{qPM} are *dq*-axes flux linkages produced by the permanent magnet (PMs), respectively. In the relationships (4.6) and (4.7), the flux linkages λ_d and λ_q are functions of time and, in an equivalent manner, they can be expressed as functions of the *dq*-axes currents i_d, i_q and rotor position θ_m. Therefore, as already mentioned, it is possible to define the *dq*-axes flux linkages with the following equations:

$$\lambda_d(t) = \lambda_d(i_d, i_q, \theta_m) = \lambda_{di}(i_d, i_q, \theta_m) + \lambda_{dPM} \tag{4.8}$$

$$\lambda_q(t) = \lambda_q(i_d, i_q, \theta_m) = \lambda_{qi}(i_d, i_q, \theta_m) + \lambda_{qPM} \tag{4.9}$$

Employing the total differential theorem to expand the derivative terms in relationships (4.4) and (4.5), the following equations can be derived:

$$\begin{aligned} \frac{d\lambda_d(t)}{dt} &= \frac{\partial \lambda_d(i_d, i_q, \theta_m)}{\partial i_d}\frac{di_d}{dt} + \frac{\partial \lambda_d(i_d, i_q, \theta_m)}{\partial i_q}\frac{di_q}{dt} + \frac{\partial \lambda_d(i_d, i_q, \theta_m)}{\partial \theta_m}\frac{d\theta_m}{dt} = \\ &= L_{dd}^{inc}(i_d, i_q, \theta_m)\frac{di_d}{dt} + L_{dq}^{inc}(i_d, i_q, \theta_m)\frac{di_q}{dt} + \omega_m \frac{\partial \lambda_d(i_d, i_q, \theta_m)}{\partial \theta_m} \end{aligned} \tag{4.10}$$

$$\begin{aligned} \frac{d\lambda_q(t)}{dt} &= \frac{\partial \lambda_q(i_d, i_q, \theta_m)}{\partial i_d}\frac{di_d}{dt} + \frac{\partial \lambda_q(i_d, i_q, \theta_m)}{\partial i_q}\frac{di_q}{dt} + \frac{\partial \lambda_q(i_d, i_q, \theta_m)}{\partial \theta_m}\frac{d\theta_m}{dt} = \\ &= L_{qd}^{inc}(i_d, i_q, \theta_m)\frac{di_d}{dt} + L_{qq}^{inc}(i_d, i_q, \theta_m)\frac{di_q}{dt} + \omega_m \frac{\partial \lambda_q(i_d, i_q, \theta_m)}{\partial \theta_m} \end{aligned} \tag{4.11}$$

where L_{dd}^{inc} and L_{qq}^{inc} are the self-incremental inductances, L_{dq}^{inc} and L_{qd}^{inc} are the mutual-incremental inductances between the *d*-axis and *q*-axis and ω_m is the mechanical

rotor angular speed ($\omega_e=p\omega_m$). Therefore, it is possible to define the matrix of incremental inductances as:

$$L_{dq}^{inc}(i_d,i_q,\theta_m)=\begin{bmatrix}L_{dd}^{inc}(i_d,i_q,\theta_m) & L_{dq}^{inc}(i_d,i_q,\theta_m)\\ L_{qd}^{inc}(i_d,i_q,\theta_m) & L_{qq}^{inc}(i_d,i_q,\theta_m)\end{bmatrix} \tag{4.12}$$

where each quantity of the incremental inductances matrix is:

$$L_{dd}^{inc}(i_d,i_q,\theta_m)=\frac{\partial\lambda_d(i_d,i_q,\theta_m)}{\partial i_d} \qquad L_{dq}^{inc}(i_d,i_q,\theta_m)=\frac{\partial\lambda_d(i_d,i_q,\theta_m)}{\partial i_q} \tag{4.13}$$

$$L_{qd}^{inc}(i_d,i_q,\theta_m)=\frac{\partial\lambda_q(i_d,i_q,\theta_m)}{\partial i_d} \qquad L_{qq}^{inc}(i_d,i_q,\theta_m)=\frac{\partial\lambda_q(i_d,i_q,\theta_m)}{\partial i_q} \tag{4.14}$$

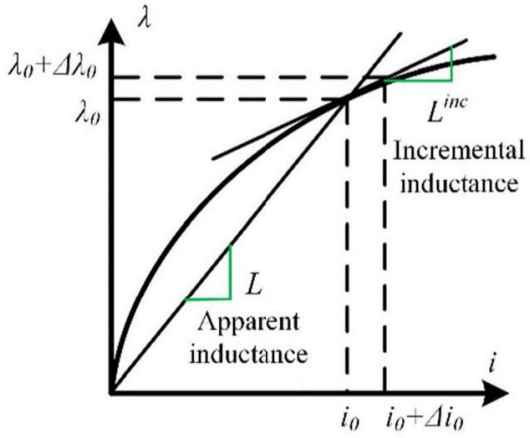

Fig. 121 Definition of the incremental and apparent inductances.

The incremental inductances can be defined as the slope of the tangent at the magnetization curve operating point, as shown in Fig. 121. In particular, the incremental inductance can be calculated by $L_{inc}=\partial\lambda/\partial i$, whereas the apparent inductances can be calculated by $L_{app}=\lambda/i$. In order to obtain the values of the apparent and incremental inductances, the IPMSM *dq*-axes flux linkages must be evaluated for several working conditions by fixing the current values. This requires a large number of experimental investigations on the IPMSM under test or a large number of finite-element analysis (FEA) simulations. Since the *dq*-axes flux linkages are nonlinear functions of *dq*-axes currents, consequently the apparent and incremental inductances are also nonlinear functions of *dq*-axes currents. Therefore, the apparent and incremental inductance values take into account the saturation and cross-coupling effects, as shown in [IV.8]-[IV.11] and [IV.21].

In detail, the *dq*-axes flux linkages equations (4.8) and (4.9) can be expanded in the following way:

$$\lambda_d(i_d, i_q, \theta_m) = \lambda_{di}(i_d, i_q, \theta_m) + \lambda_{dPM} = \lambda_{dd}(i_d, i_q, \theta_m) + \lambda_{dq}(i_d, i_q, \theta_m) + \lambda_{dPM} \quad (4.15)$$

$$\lambda_q(i_d, i_q, \theta_m) = \lambda_{qi}(i_d, i_q, \theta_m) + \lambda_{qPM} = \lambda_{qd}(i_d, i_q, \theta_m) + \lambda_{qq}(i_d, i_q, \theta_m) + \lambda_{dPM} \quad (4.16)$$

where λ_{dd} is the *d*-axis flux linkage produced by *d*-axis current, λ_{dq} is the *d*-axis flux linkage produced by *q*-axis current, the λ_{qq} is the *q*-axis flux linkage produced by *q*-axis current and the λ_{qd} is the *q*-axis flux linkage produced by *d*-axis current. The *dq*-axes flux linkages λ_d and λ_q can be expressed by the use of apparent inductances with the following relationships:

$$\lambda_d(i_d, i_q, \theta_m) = L_{dd}(i_d, i_q, \theta_m) i_d + L_{dq}(i_d, i_q, \theta_m) i_q + \lambda_{dPM} \quad (4.17)$$

$$\lambda_q(i_d, i_q, \theta_m) = L_{qd}(i_d, i_q, \theta_m) i_d + L_{qq}(i_d, i_q, \theta_m) i_q + \lambda_{dPM} \quad (4.18)$$

where L_{dd}^{app} and L_{qq}^{app} are the self-apparent inductances, L_{dq}^{app} and L_{qd}^{app} are the mutual-apparent inductances between the *d*-axis and *q*-axis. It is possible to define the apparent inductances matrix as:

$$L_{dq}^{app}(i_d, i_q, \theta_m) = \begin{bmatrix} L_{dd}^{app}(i_d, i_q, \theta_m) & L_{dq}^{app}(i_d, i_q, \theta_m) \\ L_{qd}^{app}(i_d, i_q, \theta_m) & L_{qq}^{app}(i_d, i_q, \theta_m) \end{bmatrix} \quad (4.19)$$

In detail, they can be calculated with the following relationships:

$$L_{dd}^{app}(i_d, i_q, \theta_m) = \frac{\lambda_{dd}(i_d, i_q, \theta_m)}{i_d} \qquad L_{dq}^{app}(i_d, i_q, \theta_m) = \frac{\lambda_{dq}(i_d, i_q, \theta_m)}{i_d} \quad (4.20)$$

$$L_{qd}^{app}(i_d, i_q, \theta_m) = \frac{\lambda_{qd}(i_d, i_q, \theta_m)}{i_q} \qquad L_{qq}^{app}(i_d, i_q, \theta_m) = \frac{\lambda_{qq}(i_d, i_q, \theta_m)}{i_q} \quad (4.21)$$

This matrix can be simplified with a mathematical adjustment and the following non-coupled apparent inductances are defined as:

$$L_d^{app}(i_d, i_q, \theta_m) = \frac{L_{dd}^{app}(i_d, i_q, \theta_m) i_d(t) + L_{dq}^{app}(i_d, i_q, \theta_m) i_q(t)}{i_d(t)} \quad (4.22)$$

$$L_q^{app}(i_d, i_q, \theta_m) = \frac{L_{qd}^{app}(i_d, i_q, \theta_m) i_d(t) + L_{qq}^{app}(i_d, i_q, \theta_m) i_q(t)}{i_q(t)} \quad (4.23)$$

$$L_{dq-adj}^{app}(i_d, i_q, \theta_m) = \begin{bmatrix} L_d^{app}(i_d, i_q, \theta_m) & 0 \\ 0 & L_q^{app}(i_d, i_q, \theta_m) \end{bmatrix} \quad (4.24)$$

where L_d^{app} and L_q^{app} are the *dq*-axis adjusted apparent inductances. The calculation of the *dq*-axes non-coupled apparent inductances are easier than of the apparent inductances quantity present in (4.19) because they require only the values of the *dq*-axis flux linkages produced by the stator currents excitation λ_{di} and λ_{qi} and not of each component of *dq*-axes flux linkages. In detail, the *dq*-axes non-coupled apparent inductances can be determined with the following relationships:

$$L_d^{app}(i_d, i_q, \theta_m) = \frac{\lambda_{di}(i_d, i_q, \theta_m)}{i_d} \tag{4.25}$$

$$L_q^{app}(i_d, i_q, \theta_m) = \frac{\lambda_{qi}(i_d, i_q, \theta_m)}{i_q} \tag{4.26}$$

The *dq*-axes flux linkages can be defined with the following relationships:

$$\lambda_d(i_d, i_q, \theta_m) = L_d^{app}(i_d, i_q, \theta_m) i_d + \lambda_{dPM} \tag{4.27}$$

$$\lambda_q(i_d, i_q, \theta_m) = L_q^{app}(i_d, i_q, \theta_m) i_q + \lambda_{qPM} \tag{4.28}$$

Therefore, the IPMSM voltage equations that take into account the saturation, cross-coupling and spatial harmonics effects are:

$$\begin{aligned} v_d = {} & R i_d(t) + L_{dd}^{inc}(i_d, i_q, \theta_m)\frac{di_d}{dt} + L_{dq}^{inc}(i_d, i_q, \theta_m)\frac{di_q}{dt} + \\ & + \omega_m \frac{\partial \lambda_d(i_d, i_q, \theta_m)}{\partial \theta_m} - \omega_e\left[L_q^{app}(i_d, i_q, \theta_m) i_q(t) + \lambda_{qPM}\right] \end{aligned} \tag{4.29}$$

$$\begin{aligned} v_q = {} & R i_q(t) + L_{qd}^{inc}(i_d, i_q, \theta_m)\frac{di_d}{dt} + L_{qq}^{inc}(i_d, i_q, \theta_m)\frac{di_q}{dt} + \\ & + \omega_m \frac{\partial \lambda_q(i_d, i_q, \theta_m)}{\partial \theta_m} + \omega_e\left[L_d^{app}(i_d, i_q, \theta_m) i_d(t) + \lambda_{dPM}\right] \end{aligned} \tag{4.30}$$

In detail, it is possible to see that incremental inductances define the dynamic behaviour of IPMSM. While the apparent inductances define the amount of the *dq*-axes flux linkages at specific *dq*-axes currents values and, consequently, the *dq*-axes motional induced voltages due to flux linkage moving at steady-state conditions. Generically the flux linkage λ_{qPM} presents a very low value and can be neglected. But for completeness, in this work, it will be taken into consideration.

The torque equation of IPMSM considering the saturation, cross-coupling, and spatial harmonics effects can be derived from the power relationships in *dq* reference frame. In detail, the following hypotheses are taken into account:

- No iron losses;

- No mechanical losses;
- Constant temperature;
- Energy stored in the permanent magnets is constant.

The input power in *dq* reference frame is:

$$P_{dq} = v_d i_d + v_q i_q = R\left[i_d^2 + i_q^2\right] + \left[L_{dd}^{inc}\frac{di_d}{dt}i_d + L_{dq}^{inc}\frac{di_q}{dt}i_d + L_{qd}^{inc}\frac{di_d}{dt}i_q + L_{qq}^{inc}\frac{di_q}{dt}i_q\right] + + \left[\omega_e\left(\lambda_d i_q - \lambda_q i_d\right) + \omega_m\frac{\partial\lambda_d\left(i_d, i_q, \theta_m\right)}{\partial\theta_m}i_d + \omega_m\frac{\partial\lambda_q\left(i_d, i_q, \theta_m\right)}{\partial\theta_m}i_q\right] = = P_{dq1} + P_{dq2} + P_{dq3} \quad (4.31)$$

where P_{dq1} is the copper power loss, P_{dq2} is the power associated with the stored energy in the magnetic field, and P_{dq3} is the mechanical power. The power in *abc*-reference frame can be calculated with the following relationship:

$$P_{abc} = \frac{3}{2}P_{dq} + 3P_o \quad (4.32)$$

where P_o is the zero sequence power and, since it is assumed that no zero sequence currents exist in the system, it is equal to zero. Therefore the mechanical power of the IPMSM is:

$$P_{em} = \left[\omega_e\left(\lambda_d i_q - \lambda_q i_d\right) + \omega_m\frac{\partial\lambda_d\left(i_d, i_q, \theta_m\right)}{\partial\theta_m}i_d + \omega_m\frac{\partial\lambda_q\left(i_d, i_q, \theta_m\right)}{\partial\theta_m}i_q\right] \quad (4.33)$$

The electromagnetic torque can be calculated with the following relationship:

$$T_{em} = \frac{P_{em}}{\omega_m} = \frac{3}{2}p\left[\lambda_d i_q - \lambda_q i_d\right] + \frac{3}{2}\left[\frac{\partial\lambda_d\left(i_d, i_q, \theta_m\right)}{\partial\theta_m}i_d + \frac{\partial\lambda_q\left(i_d, i_q, \theta_m\right)}{\partial\theta_m}i_q\right] \quad (4.34)$$

Replacing the flux linkage equations (4.27) and (4.28) in the torque equation, the derived torque equation is:

$$T_{em} = \frac{3}{2}p\left\{\lambda_{dPM} i_q - \lambda_{qPM} i_d + \left[L_d^{app}\left(i_d, i_q, \theta_m\right) - L_q^{app}\left(i_d, i_q, \theta_m\right)\right] i_d i_q\right\} + \frac{3}{2}\left[\frac{\partial\lambda_d\left(i_d, i_q, \theta_m\right)}{\partial\theta_m}i_d + \frac{\partial\lambda_q\left(i_d, i_q, \theta_m\right)}{\partial\theta_m}i_q\right] = = T_{em1} + T_{em2} \quad (4.35)$$

where the torque component T_{em1} is similar respect the torque equation of the conventional modelling approach (1.65). However the apparent inductance are functions of i_d, i_q and θ_m and, therefore, the torque component T_{em1} represents the mainly average

torque of IPMSM plus some ripple torque component. Instead, the torque component T_{em2} is an additional ripple torque component of IPMSM due by the variation of *dq*-axes flux linkages with the rotor position θ_m.

4.3 Characterization of IPMSM in Ansys Maxwell environment

In order to validate the effectiveness of the new proposed modelling approach, the IPMSM under test has been implemented and numerically simulated in *Ansys Maxwell* environment (FEA software). The cross-sectional view of the IPMSM is shown in Fig. 122. The IPMSM main electrical, mechanical and geometrical data are summarized in Table 35 and Table 36. The stator winding is a double layer fractional winding with slots per pole and per phase $q=1.5$ and its scheme is reported in Fig. 123 (a). The iron pack magnetic material is a 0.5 mm wide laminated sheet of type M330-50A while the PMs are made by SMCo-18 MGOe. The SMCo-18 MGOe magnets B-H curves are shown in Fig. 123 (b).

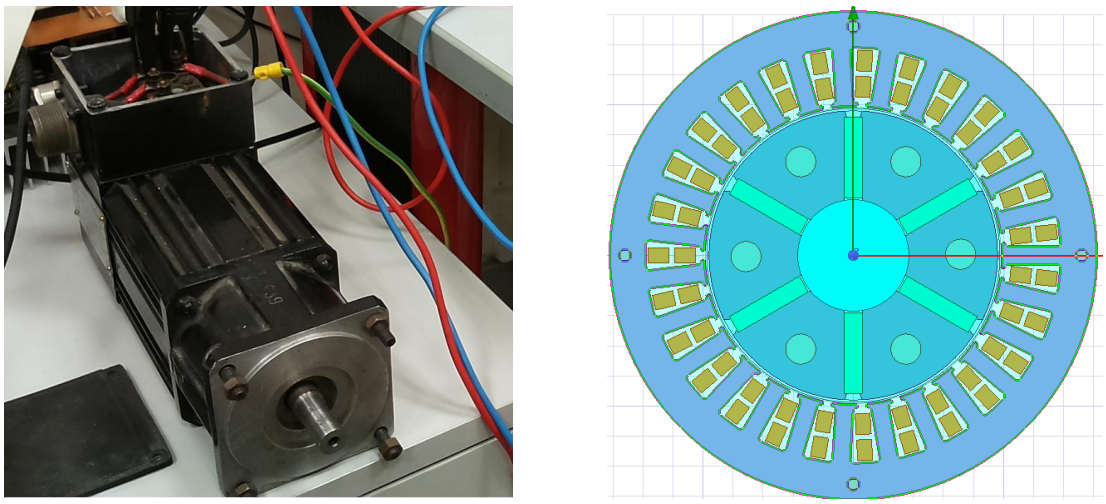

(a) (b)

Fig. 122 IPMSM under test (a) and its cross-section (b).

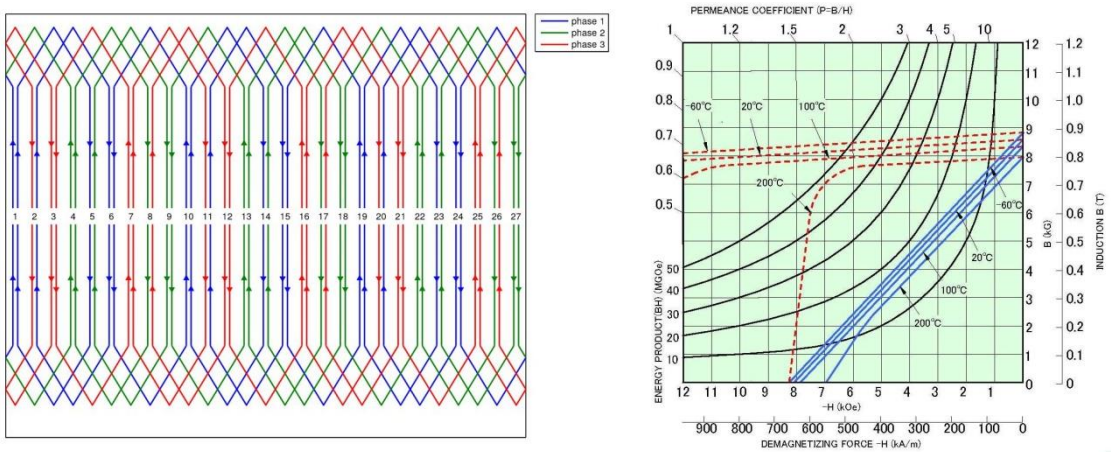

(a) (b)

Fig. 123 IPMSM winding scheme (a) and PMs B-H curves (b).

Table 35 Main electrical and mechanical data of the IPMSM under test.

Quantity	***Value***
Power [kW]	0.8
Rated current [A]	3,6
Nominal Speed [rpm]	4000
Maximum Speed [rpm]	6000
Nr. of pole pairs	3
Nr. of phases	3
Nominal torque [Nm]	1,8
Peak torque [Nm]	9.2

Table 36 Geometrical data of the IPMSM.

Geometrical data	***Value***
Nr. of stator slot	27
Axial stator length [mm]	59
External stator diameter [mm]	81
Inner stator diameter [mm]	49,6
External rotor diameter [mm]	48
Inner rotor diameter [mm]	19
Stator tooth length [mm]	9.7
Stator tooth width [mm]	3
Stator slot opening [mm]	1.6
PMs lenght [mm]	13,45
PMs thickness [mm]	3
Airgap [mm]	0,8
Iron pack laminations factor	0.95
Slot depth [mm]	9,2

The goal of the FEA investigations concerns the characterization of IPMSM under test. In order to take into account the magnetic self-saturation and cross-coupling effects, it is necessary to determinate the flux mapping or the variation of *dq*-axes flux linkage λ_d, λ_q, and the electromagnetic torque mapping T_{em} for several values of *dq*-axes currents i_d, i_q

and of rotor electrical angular position θ_e ($\theta_e=p\ \theta_m$). In particular, with FEA simulations it is possible to capture all torque components, including the cogging torque that is present even with currents equal to 0 A [IV.22]. Moreover, the apparent and incremental inductances components can be derived from the flux mapping data. Another goal of the FEA investigations is the evaluation of iron loss for several values of *dq*-axis currents i_d, i_q. In detail, this analysis has been used for the definition of mathematical model of iron loss and, consequently, their integration in the IPMSM modelling approach proposed. The FEA investigations are described in detail below.

4.3.1 Mapping of the flux linkages and of the torque

The *dq*-axis flux linkages λ_d, λ_q and electromagnetic torque T_{em} mapping are obtained by varying i_d, i_q and θ_e in the range [-7.5 A,7.5 A], [0 A,7.5 A] and [0°-360°] ([0°-120°] in mechanical degrees), respectively. Negative values of the *q*-xis current i_q are not taken into account because this IPMSM is used only for motor operation. The i_d, i_q and θ_e samples in the FE calculations are 30, 16 and 49, respectively, and the total number of FEA simulations carried out are 23250. The *dq*-axes flux linkages values, in each FEA simulations, are obtained from the flux linkage in *abc*-reference frame with the *dqo* Park transformation described in the section 1.32 of this work. By way of example, the *dq*-axes flux linkages and torque maps as functions of *dq*-axes currents at a 0° rotor electrical position are reported in Fig. 124-Fig. 126. In particular, from these figures, it is possible to evaluate the self-saturation and cross-coupling effects on each component of the flux linkage. The *dq*-axes flux linkages and electromagnetic torque trends as a function of the rotor electrical position for fixed values of *dq*-axes currents ($i_d=-5A$, $i_q=4.5A$) are reported in Fig. 127-Fig. 129, respectively. In these last figures, it is possible to see the spatial harmonics effects and, therefore, the presence of torque ripple even with constant *dq*-axes currents that is present in a real IPMSM but cannot be predicted with the use of conventional modelling approach.

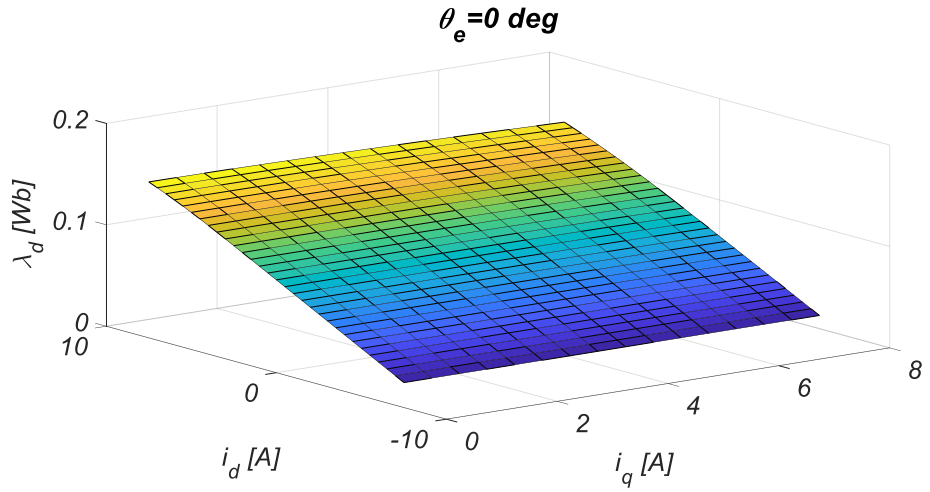

Fig. 124 *d*-axis flux linkage map at 0° rotor electrical position.

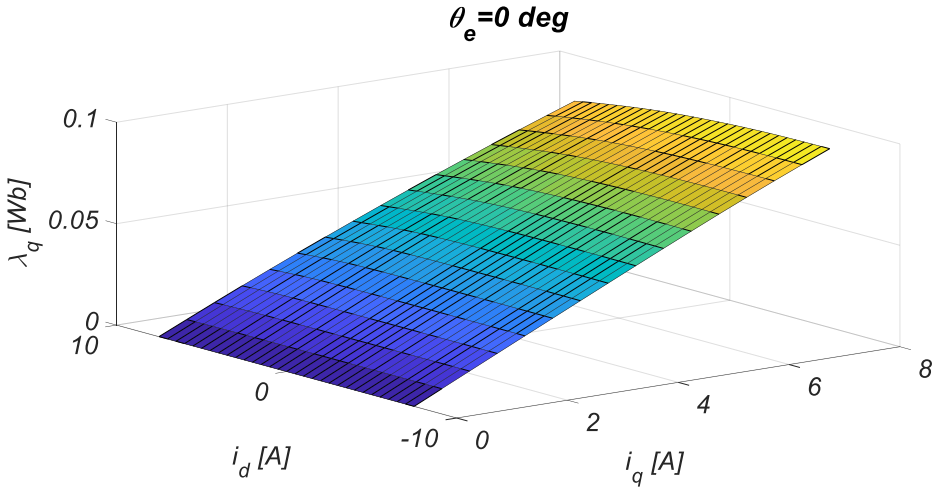

Fig. 125 *q*-axis flux linkage map at 0° rotor electrical position.

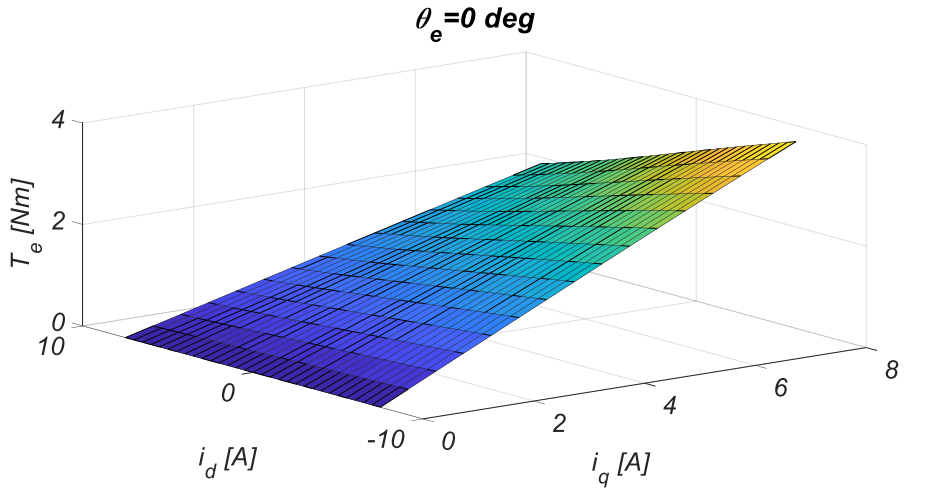

Fig. 126 Torque map at 0° rotor electrical position.

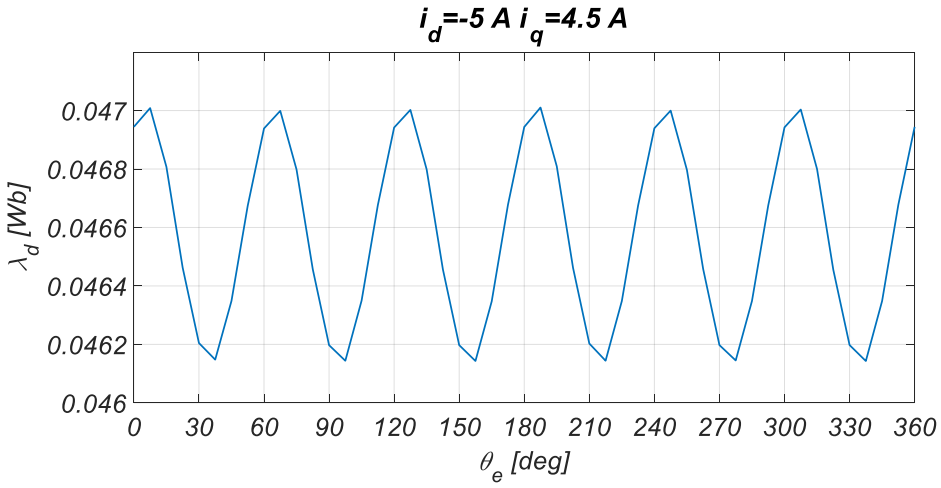

Fig. 127 *d*-axis flux linkage variation with rotor electrical position at i_d=-5A and i_q=4.5A.

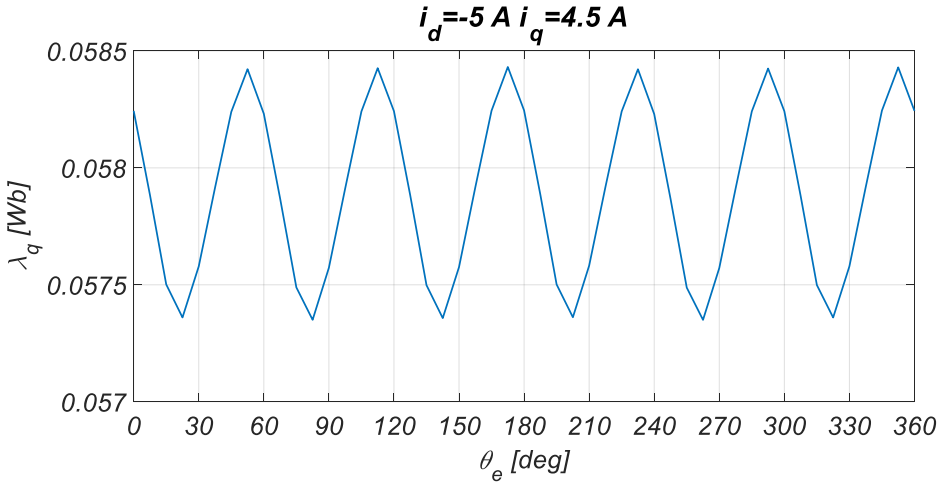

Fig. 128 *q*-axis flux linkage variation with rotor electrical position at i_d=-5A and i_q=4.5A.

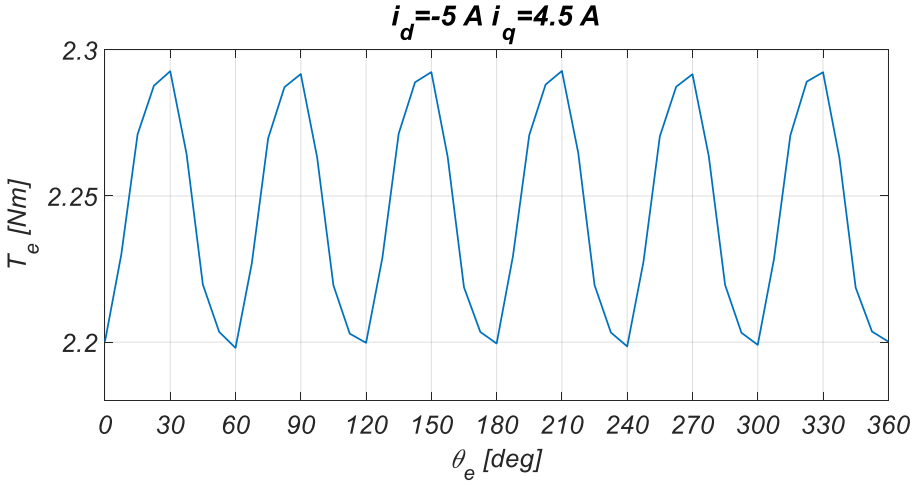

Fig. 129 Electromagnetic torque variation with rotor electrical position at i_d=-5A and i_q=4.5A.

The elaboration of the data acquired from FEA simulations and the determination of the quantities of interest, such as the *dq*-axes flux linkage components and apparent and

incremental inductances, have been carried out in the *Matlab* environment. The *dq*-axes non-coupled apparent inductances can be derived from the *dq*-axes flux linkages $\lambda_d(i_d, i_q, \theta_e)$, $\lambda_q(i_d, i_q, \theta_e)$ data acquired. For this purpose, it is necessary to obtain the *dq*-axes flux linkages components λ_{di}, λ_{qi} that are produced by the stator current excitation and the *dq*-axes flux linkages component produced by the PMs λ_{dPM}, λ_{qPM}. In this discussion, the *dq*-axes flux linkages $\lambda_d(i_d, i_q, \theta_e)$, $\lambda_q(i_d, i_q, \theta_e)$and their components are defined in the following way:

$$\lambda_d(i_d, i_q, \theta_e) = \lambda_{di}(i_d, i_q, \theta_e) + \lambda_{dPM}(0, i_q, \theta_e) \tag{4.36}$$

$$\lambda_q(i_d, i_q, \theta_e) = \lambda_{qi}(i_d, i_q, \theta_e) + \lambda_{qPM}(i_d, 0, \theta_e) \tag{4.37}$$

where the flux linkage quantities λ_{dPM}, λ_{qPM} are the *dq*-axes flux linkages component produced by the PMs that take into account the cross-coupling effects. These quantities are easy to determine because they are equal to the value of *dq*-axes flux linkage obtained in the absence of *dq*-axes currents excitation $\lambda_d(0, i_q, \theta_e)$, $\lambda_q(i_d, 0, \theta_e)$, respectively. Therefore, the *dq*-axes flux linkages components $\lambda_{di}(i_d, i_q, \theta_e)$, $\lambda_{qi}(i_d, i_q, \theta_e)$are obtained with the following relationships:

$$\lambda_{di}(i_d, i_q, \theta_e) = \lambda_d(i_d, i_q, \theta_e) - \lambda_{dPM}(0, i_q, \theta_e) \tag{4.38}$$

$$\lambda_{qi}(i_d, i_q, \theta_e) = \lambda_q(i_d, i_q, \theta_e) - \lambda_{qPM}(i_d, 0, \theta_e) \tag{4.39}$$

The *dq*-axes non-coupled apparent inductances have been determined with the following equations:

$$L_d^{app}(i_d, i_q, \theta_m) = \frac{\lambda_{di}(i_d, i_q, \theta_e)}{i_d} \tag{4.40}$$

$$L_q^{app}(i_d, i_q, \theta_m) = \frac{\lambda_{qi}(i_d, i_q, \theta_e)}{i_q} \tag{4.41}$$

By way of example, the *dq*-axes non-coupled apparent inductances L_d^{app} and L_q^{app} at a 90° rotor electrical position are reported in Fig. 130 and Fig. 131, respectively.

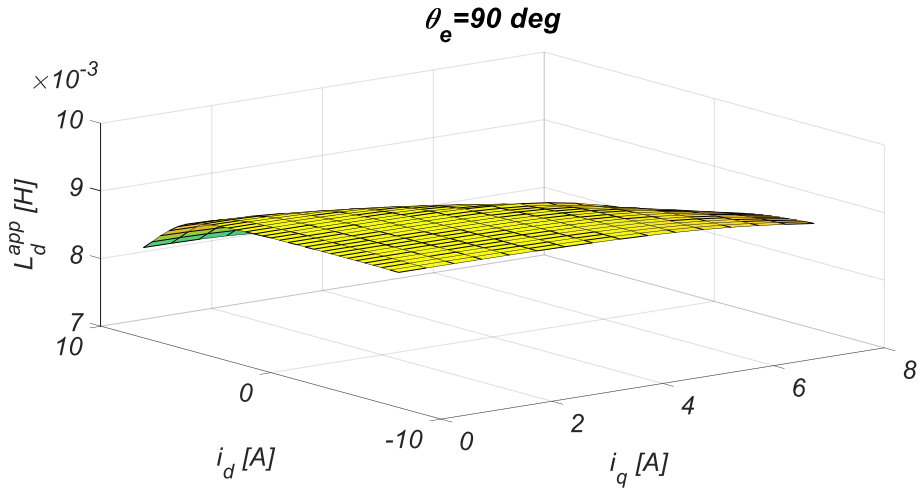

Fig. 130 *d*-axis non-coupled apparent inductance map at 90° rotor electrical position.

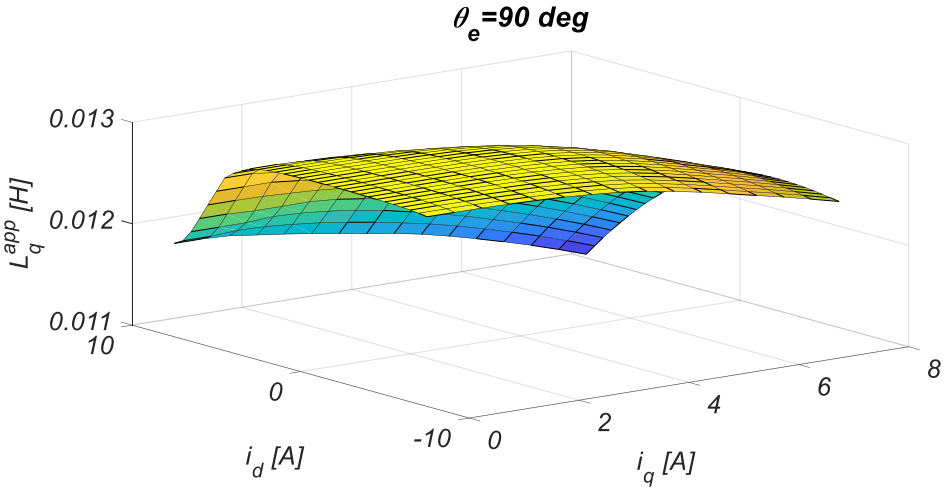

Fig. 131 *q*-axis non-coupled apparent inductance map at 90° rotor electrical position.

Instead, the values of *dq*-axes incremental inductances have been calculated with the equations (4.13) and (4.14). By way of example, the *dq*-axes incremental inductance L_{dd}^{incr}, L_{qq}^{incr}, L_{dq}^{incr} and L_{qd}^{incr} at a 90° rotor electrical position are reported in Fig. 132-Fig. 135, respectively.

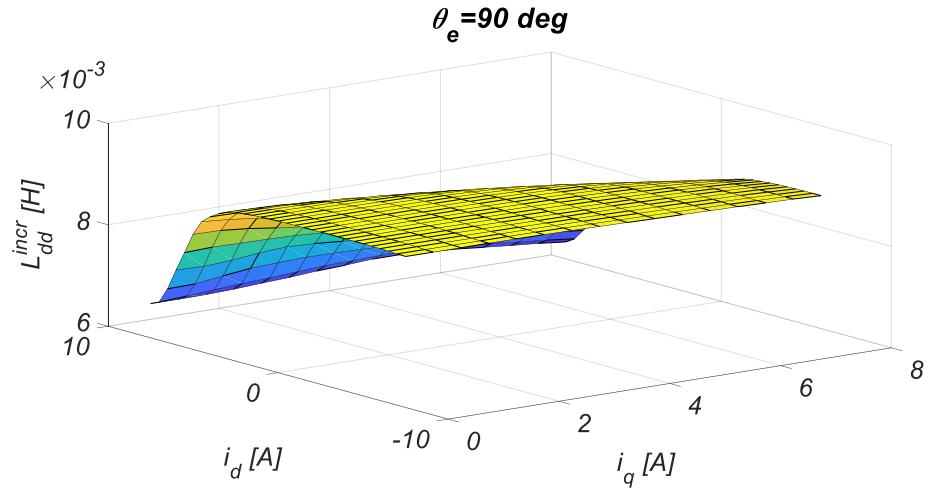

Fig. 132 Incremental inductance L_{dd} map at 90° rotor electrical position.

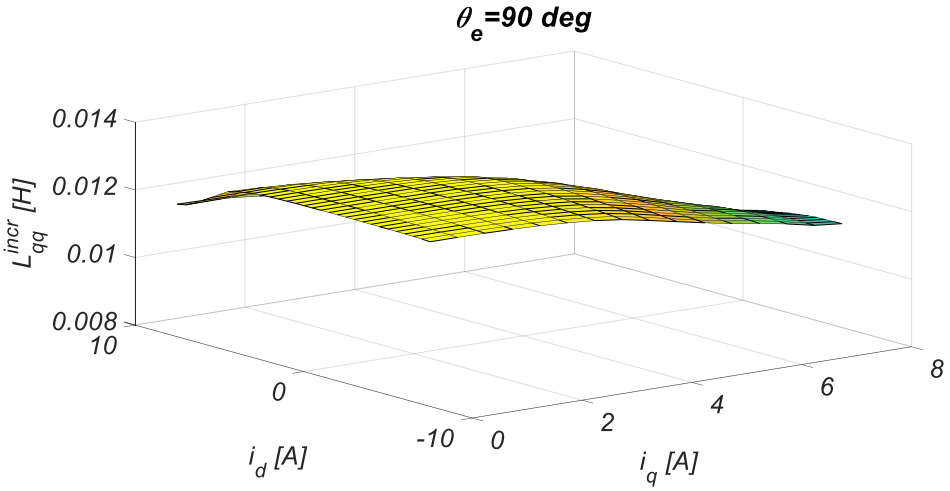

Fig. 133 Incremental inductance *Lqq* map at 90° rotor electrical position.

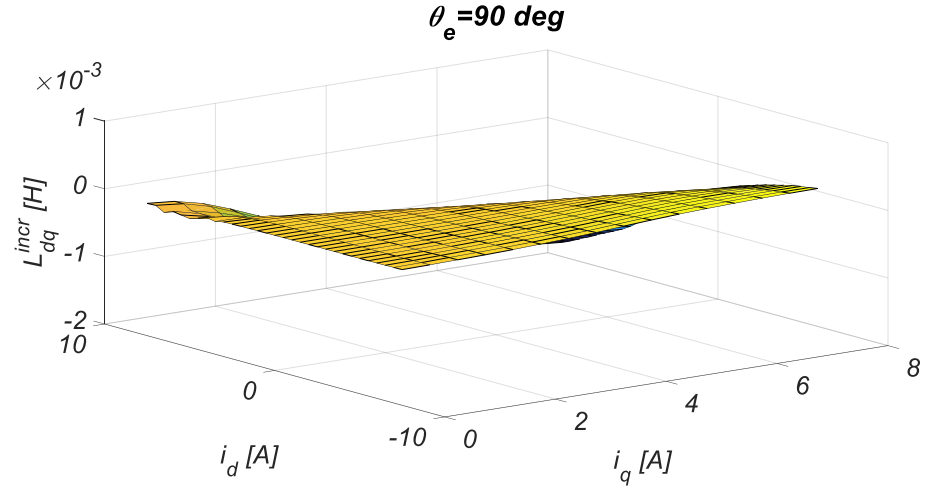

Fig. 134 Incremental inductance L_{dq} map at 90° rotor electrical position.

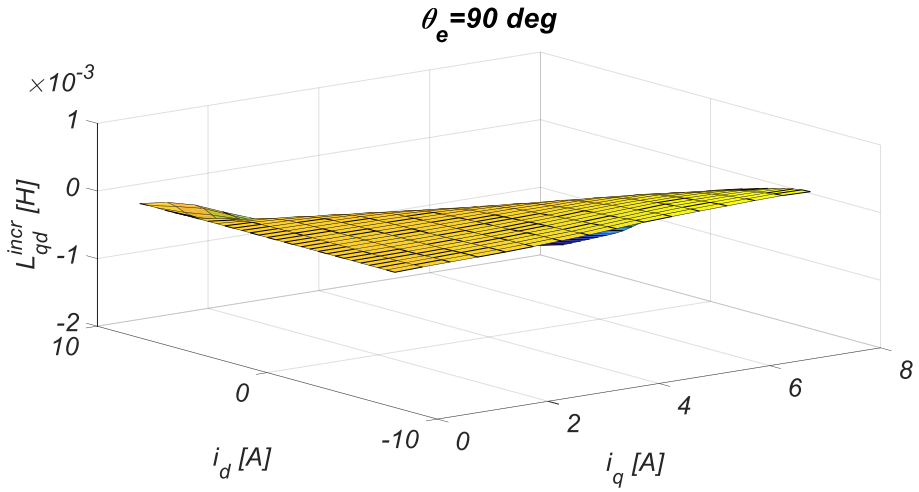

Fig. 135 Incremental inductance L_{qd} map at 90° rotor electrical position.

Furthermore, in order to show the influence of the spatial harmonics on each inductance components, the trends of *dq*-axes apparent and incremental inductances can be shown for each pair of *dq*-axes current values (i_d, i_q). For simplicity, only the *dq*-axes non-coupled apparent inductances L_d^{app} and L_q^{app} trends as a function of the rotor electrical position θ_e, for fixed values of *dq*-axes currents (i_d=-2A, i_q=3A), are reported in Fig. 136 and Fig. 137.

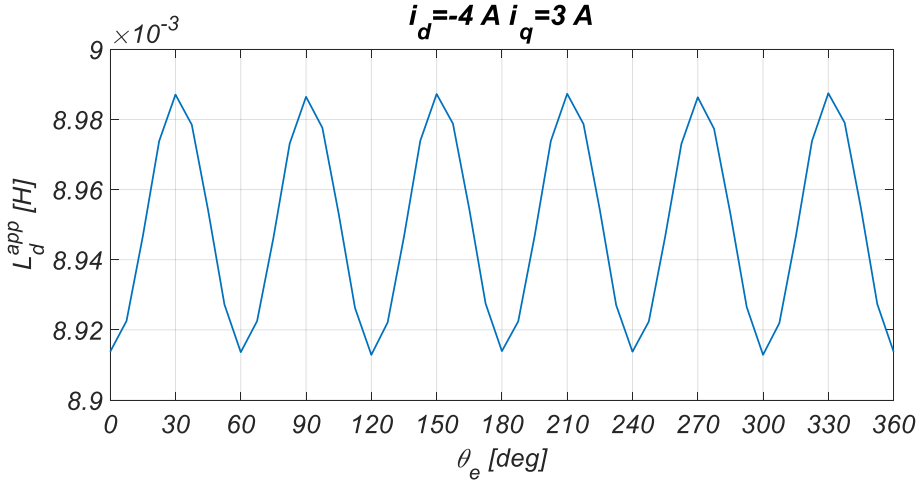

Fig. 136 *d*-axis non-coupled apparent inductance variation with rotor electrical position at i_d=-4A and i_q=3A.

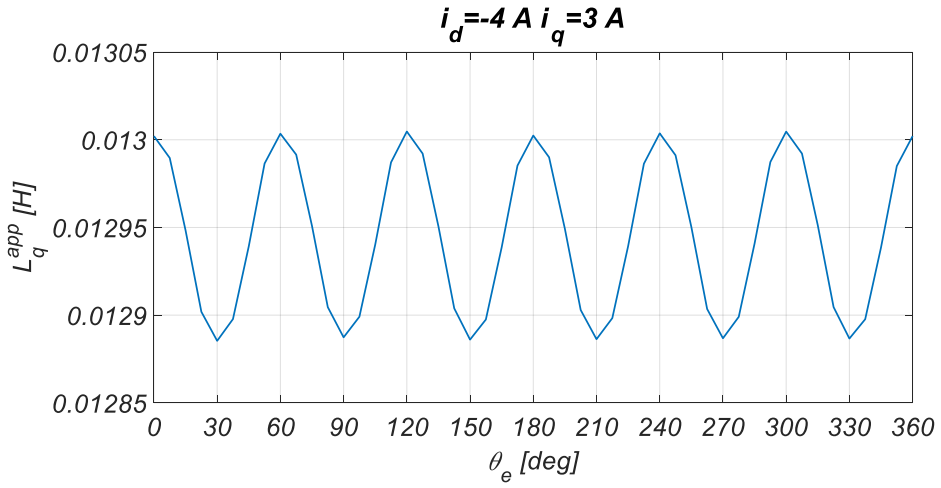

Fig. 137 *q*-axis non-coupled apparent inductance variation with rotor electrical position at i_d=-4A and i_q=3A.

In order to numerically validate the accuracy of the proposed *dq*-axes flux linkages modelling approach, the *dq*-axes flux linkages have been calculated starting from the values of non-coupled *dq*-axes apparent inductances and from the *dq*-axes flux linkage produced by the PMs with the following equations:

$$\lambda_{dcalc}(i_d, i_q, \theta_e) = L_d^{app}(i_d, i_q, \theta_e) i_d + \lambda_{dPM}(0, i_q, \theta_e) \tag{4.42}$$

$$\lambda_{qcalc}(i_d, i_q, \theta_e) = L_q^{app}(i_d, i_q, \theta_e) i_q + \lambda_{qPM}(i_d, 0, \theta_e) \tag{4.43}$$

The values of the calculated *dq*-axes flux linkages $\lambda_{dcalc}(i_d, i_q, \theta_e)$, $\lambda_{qcalc}(i_d, i_q, \theta_e)$ are compared with the original values of *dq*-axes flux linkages obtained from FEA simulations $\lambda_d(i_d, i_q, \theta_e)$, $\lambda_q(i_d, i_q, \theta_e)$ through the following error quantities:

$$err_{\lambda_d}\%(i_d, i_q, \theta_e) = \frac{\lambda_d(i_d, i_q, \theta_e) - \lambda_{dcalc}(i_d, i_q, \theta_e)}{\lambda_d(i_d, i_q, \theta_e)} 100 \tag{4.44}$$

$$err_{\lambda_q}\%(i_d, i_q, \theta_e) = \frac{\lambda_q(i_d, i_q, \theta_e) - \lambda_{qcalc}(i_d, i_q, \theta_e)}{\lambda_q(i_d, i_q, \theta_e)} 100 \tag{4.45}$$

The *dq*-axes flux linkages error maps are reported below in Fig. 138 and Fig. 139.

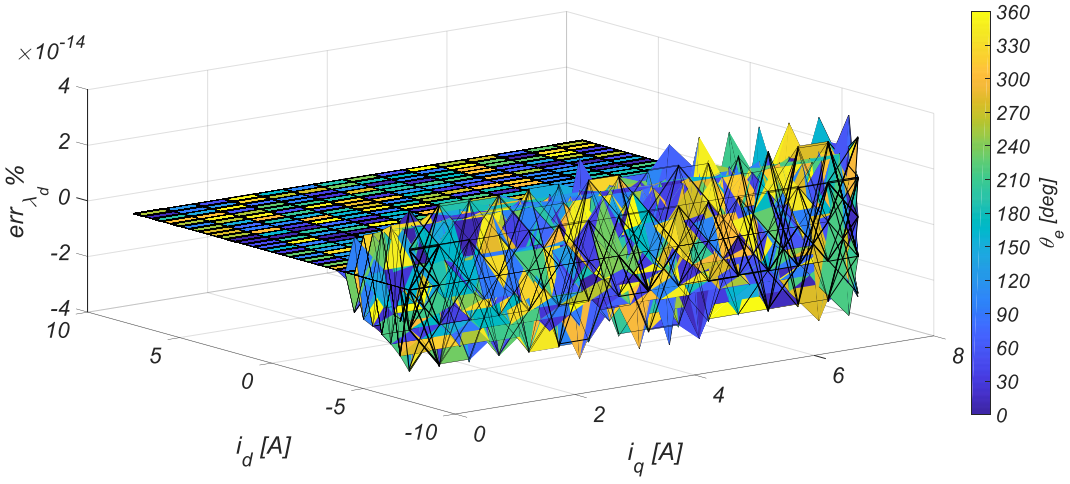

Fig. 138 *d*-axis flux linkage error map.

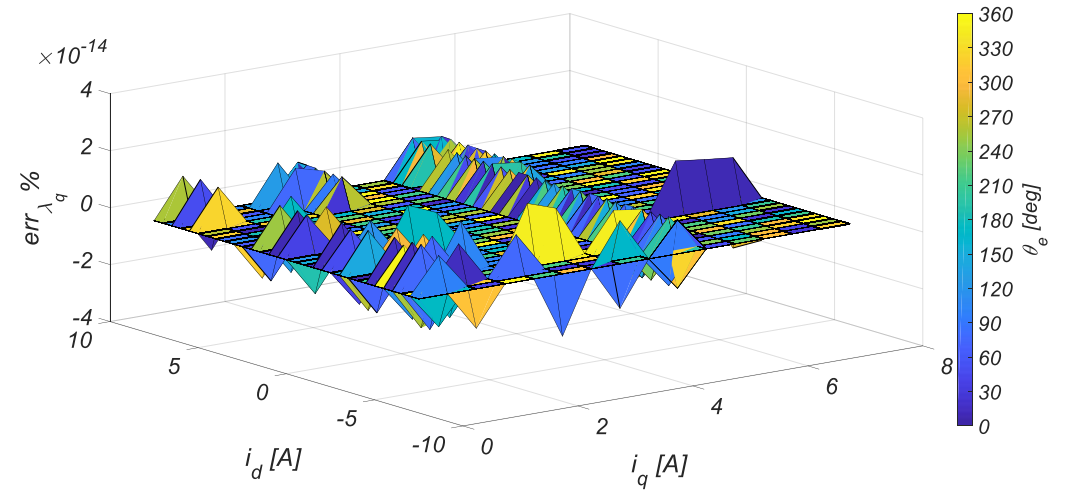

Fig. 139 *q*-axis flux linkage error map.

As can be noticed, the differences between the calculated *dq*-axes flux linkage values and the *dq*-axes flux linkages original values obtained from FEA simulations are so limited that they can be considered negligible. In particular, the limited amplitude of the error can be attributed to the accuracy of calculation algorithm or to the computational errors.

Further analysis has been performed by calculating the mean values of *dq*-axes flux linkages quantities in 360° electrical degree range:

$$\lambda_{dcalc_{mean}}(i_d, i_q) = \frac{\sum_{i=1}^{n} \lambda_{dcalci}(i_d, i_q, \theta_{ei})}{n} \tag{4.46}$$

$$\lambda_{qcalc}(i_d, i_q) = \frac{\sum_{i=1}^{n} \lambda_{qcalci}(i_d, i_q, \theta_{ei})}{n} \tag{4.47}$$

Consequently, these flux linkage quantities have been compared with the mean values of the *dq*-axes flux linkages obtained from FEA simulation by defining the following flux-linkage mean error quantities:

$$err_{\lambda_{dmean}}\%(i_d, i_q) = \frac{\lambda_{d_{mean}}(i_d, i_q) - \lambda_{dcalc_{mean}}(i_d, i_q)}{\lambda_d(i_d, i_q)} 100 \tag{4.48}$$

$$err_{\lambda_{qmean}}\%(i_d, i_q) = \frac{\lambda_{q_{mean}}(i_d, i_q) - \lambda_q(i_d, i_q)}{\lambda_q(i_d, i_q)} 100 \tag{4.49}$$

Also in this case, the differences between the calculated *dq*-axes flux linkage mean values and the *dq*-axes flux linkages mean values obtained from FE simulations are so limited that they can be considered negligible.

In order to numerically validate the accuracy of the electromagnetic torque modelling approach proposed, the electromagnetic torque $T_{em\text{-}calc}$ values have been calculated starting from the values of calculated *dq*-axes flux linkages $\lambda_{dcalc}(i_d, i_q, \theta_e)$, $\lambda_{qcalc}(i_d, i_q, \theta_e)$, with the help of equation (4.35). In detail, the mathematical equation of each torque components are summarized below:

$$T_{em-calc} = T_{em1_{calc}} + T_{em2_{calc}} \tag{4.50}$$

$$T_{em1_{calc}} = \frac{3}{2} p\left[\lambda_{dcalc}(i_d, i_q, \theta_e) i_q - \lambda_{qcalc}(i_d, i_q, \theta_e) i_d\right] \tag{4.51}$$

$$T_{em2_{calc}} = \frac{3}{2}\left[\frac{\partial \lambda_{dcalc}(i_d, i_q, \theta_e)}{\partial \theta_e} i_d + \frac{\partial \lambda_{qcalc}(i_d, i_q, \theta_e)}{\partial \theta_e} i_q\right] \tag{4.52}$$

The *dq*-axes flux linkages derivatives as a function of rotor electrical angular position are calculated with the function "gradient" in the *Matlab* environment. The calculated values of electromagnetic torque $T_{em\text{-}calc}$ are compared with those of electromagnetic torque obtained from FEA simulations T_{em} through the following error quantity:

$$err_{T_{em}}\%(i_d, i_q, \theta_e) = \frac{T_{em}(i_d, i_q, \theta_e) - T_{em-calc}(i_d, i_q, \theta_e)}{T_{em}(i_d, i_q, \theta_e)} 100 \tag{4.53}$$

The electromagnetic torque error map is reported below in Fig. 140.

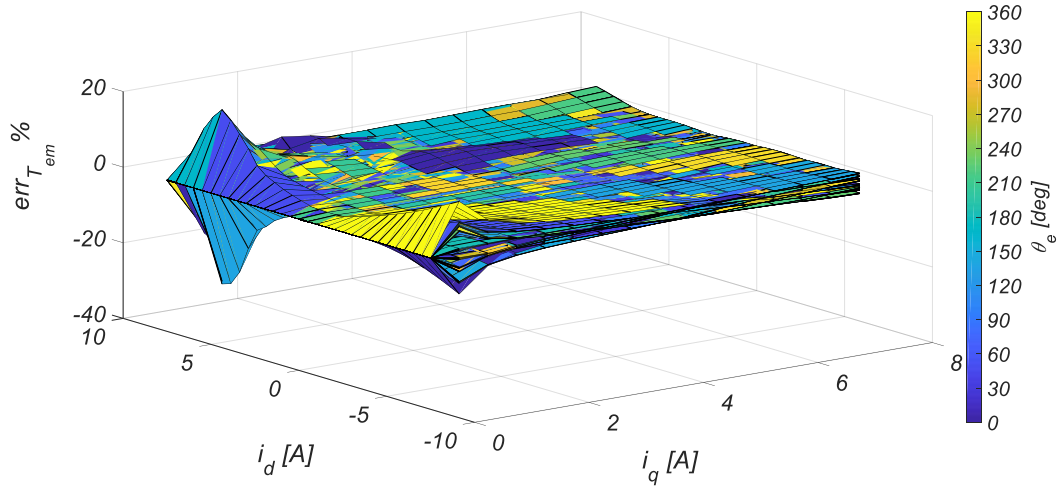

Fig. 140 Electromagnetic torque error map.

In this case, the difference between the calculated electromagnetic torque values and the electromagnetic torque values obtained from FEA simulations is not negligible and present high values especially at the ends of the rotor electrical angular position variation range (0° and 360°). This behaviour can be attributed to derived functions, that for rotor electrical angular position values near to zero, tend to diverge. Furthermore, it can also be observed that high electromagnetic torque error values occur when the *q*-axis current is equal to 0 A or presents very low value and, consequently, the electromagnetic torque presents very small values. In detail, it can be observed that the maximum and minimum the electromagnetic torque error values are *19.63%* and *-26.73%*, respectively.

Further analysis has been performed by comparing the mean values, calculated in 360° electrical degree range, of the proposed electromagnetic torque model and those of electromagnetic torque obtained from FE simulations through the following error quantity:

$$err_{T_{em\,mean}}\%(i_d, i_q) = \frac{T_{em\,mean}(i_d, i_q) - T_{em-calc\,mean}(i_d, i_q)}{T_{em\,mean}(i_d, i_q)} 100 \qquad (4.54)$$

The electromagnetic torque mean values error map is reported below in Fig. 141.

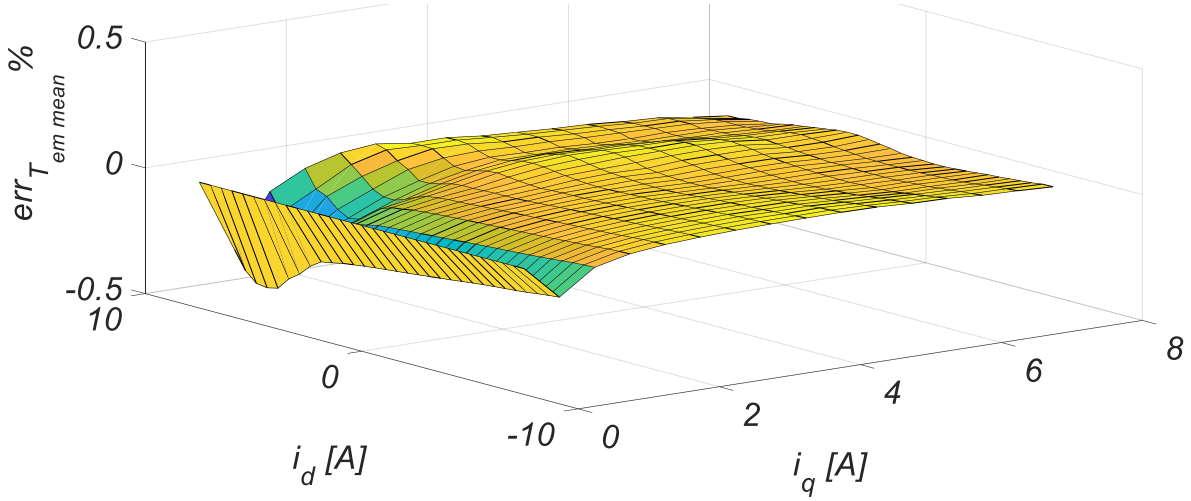

Fig. 141 Electromagnetic torque mean values error map.

As can be noticed, the differences between the calculated electromagnetic torque mean values and the electromagnetic torque mean values obtained from FE simulations are much more limited than the one found previously. In detail, it can be observed that the maximum and minimum the electromagnetic torque error mean values are *0.04%* and *-0.4%*, respectively.

4.3.2 Iron loss evaluation and their mathematical modelization

The accurate estimation of iron loss is a fundamental parameter not only for the design process of the electrical machines but also for the drive control purpose, especially when a control algorithm based on the knowledge of the mathematical model of the machine, such as the LMA, is used. In the variable speed drive applications, this is not easy due to the wide variation of the supply frequency and impact of the inverter switching harmonics on the machine flux linkages. In this work, in order to consider the iron loss effects on the IPMSM electromagnetic behaviour at different working conditions in a computationally efficient way, the iron loss model presented in [IV.23]and [IV.24] has been considered. The iron loss model is based on voltage-dependent loss functions. The iron losses are separated in two loss components, one associated with the main magnetizing flux linkage and another one associated with the demagnetizing flux linkage that occurs during field weakening operations. In detail, this iron loss model tries to take into account the field weakening current effects than involves a stator reaction field component which opposed with the main PM excitation field. Therefore, during the field weakening operations, the resultant flux linkage with

the stator winding is thus reduced. Consequently, iron losses in field weakening operations would be to be lower respect to the iron losses obtained at the same conditions without field weakening operations. The iron losses component associated with the main magnetizing flux linkage can be directly related to the induced stator voltage E_m:

$$P_{FE1} = f_1(E_m) \tag{4.55}$$

The second component of iron losses associated to the demagnetizing flux linkage can be related to the voltage due to the armature reaction of the *d*-axis current E_d:

$$P_{FE2} = f_1(E_d) \tag{4.56}$$

The expressions of the induced stator voltage E_m and of voltage due to the armature reaction of the *d*-axis current E_d can be derived from the IPMSM mathematical model in *dq*- reference frame:

$$E_m = 2\pi f \sqrt{\lambda_d^2(i_d, i_q) + \lambda_q^2(i_d, i_q)} \tag{4.57}$$

$$E_d = -2\pi f \left[\lambda_d(i_d, i_q) - \lambda_{dPM}(0, i_q)\right] \tag{4.58}$$

The iron loss function f_1 and f_2 are obtained with time-stepping FEA simulations. In detail, magnetostatic 2D FEA open circuit simulations are used to determinate loss function $f_1(E_m)$ and 2D FEA short circuit simulations are used to determinate loss function $f_2(E_d)$. The short circuit test is performed with i_d=-I_{sc} and i_q=*0 A* where the value of short circuit current I_{sc} is equal to the value of *d*-axis current that allows obtaining a *d*-axis flux linkage equal to zero and consequently induced voltage equal to zero at any supply frequency or speed. Based on the modified Steinmetz equation, each iron loss component can be expressed as the sum of hysteresis losses and eddy current losses with the following relationships:

$$P_{FE1}(E_m) = P_{FE}^{OC}(f) = a_h f + a_e f^2 \tag{4.59}$$

$$P_{FE2}(E_d) = P_{FE}^{SC}(f) = b_h f + b_e f^2 \tag{4.60}$$

where a_h, a_e, b_h. b_e are the hysteresis and eddy current coefficients of the iron loss estimated by FEA open circuit simulations and of the iron loss estimated by FEA short circuit simulation, respectively. In this way, the hysteresis losses and eddy current losses can be found from the FEA simulations at a single arbitrary frequency. The loss functions f_1 and f_2 can be found by substituting the frequency f with the following

relationships obtained by the expression of the induced voltage in open circuit and short circuit operations, respectively:

$$f = \frac{E_m}{2\pi\lambda_{dPM}(0, i_q)} \tag{4.61}$$

$$f = \frac{E_d}{2\pi\lambda_{dPM}(0, i_q)} \tag{4.62}$$

Replacing the equation (4.61) and (4.62) to the relationships (4.59) and (4.60), it is possible to obtain:

$$P_{FE1}(E_m) = P_{FE}^{OC}(f) = a_h \frac{E_m}{2\pi\lambda_{dPM}(0, i_q)} + a_e \left(\frac{E_m}{2\pi\lambda_{dPM}(0, i_q)}\right)^2 \tag{4.63}$$

$$P_{FE2}(E_d) = P_{FE}^{SC}(f) = b_h \frac{E_d}{2\pi\lambda_{dPM}(0, i_q)} + b_e \left(\frac{E_d}{2\pi\lambda_{dPM}(0, i_q)}\right)^2 \tag{4.64}$$

The total iron loss for a given IPMSM operating condition can be calculated as the sum of P_{FE1} and P_{FE2}:

$$P_{FEmodel} = P_{FE1}(E_m) + P_{FE2}(E_d) \tag{4.65}$$

For the purpose of hysteresis and eddy currents coefficient estimation, several no-load and short circuits FEA simulations have been performed by varying the rotor angular speed ω_m in the range [500 rpm, 6000 rpm] with speed step of 500 rpm or in frequency terms in the range [25 Hz, 300 Hz] with frequency step pf 25 Hz. Moreover, in order to numerically validate the iron model proposed, several FEA simulations of the IPMSM have been performed for several values od *d-q* axes currents i_d, i_q in the range [0A, 5A] and for several values of the mechanical speed in the range [0 rpm, 6000 rpm] and the values of iron losses $P_{FE}(i_d, i_q, \omega_m)$ have been determinate for each case of study. The iron losses, obtained from the aforementioned FEA simulation, are compared with the iron loss estimated only with the iron loss component of open circuit simulations that is the conventional iron loss modelling approach. In detail, for this comparison the following error quantity is defined:

$$err_{P_{FEOC}}\% = \frac{P_{FE}(i_d, i_q, \omega_m) - P_{FE}^{OC}(i_d, i_q, \omega_m)}{P_{FE}(i_d, i_q, \omega_m)} 100 \tag{4.66}$$

The iron losses model errors map, relating to the conventional iron loss modelling approach, is reported in Fig. 142.

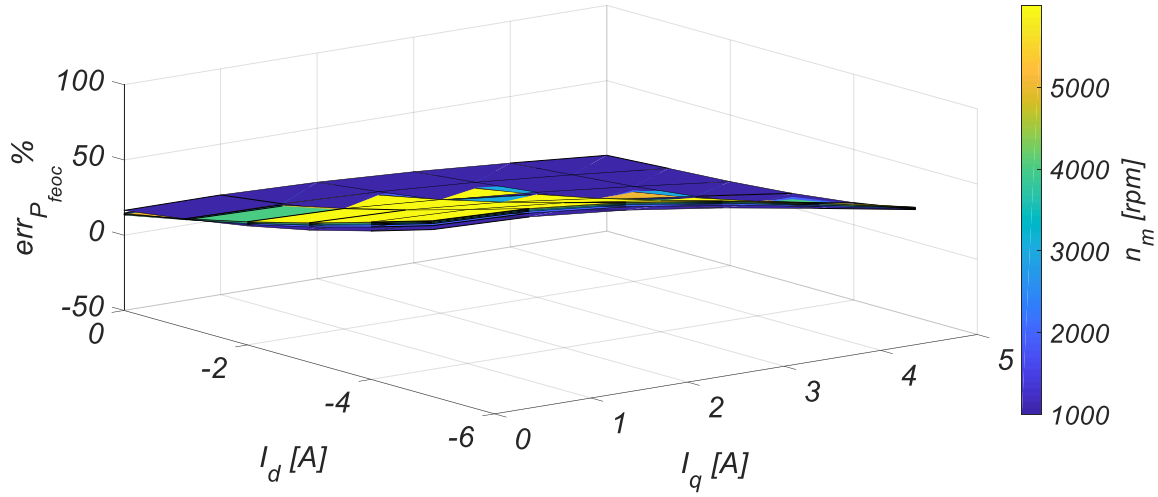

Fig. 142 Iron losses error map relating to the conventional iron loss modelling approach.

As can be noticed, the iron losses error, relating to the conventional iron losses modelling approach, presents considerable values for several working points. In detail, it can be observed that the maximum and minimum iron loss error values are *66.85%* and *-10.24%*, respectively. In a similar way, the differences between the values of iron losses of the aforementioned FEA simulation and the iron losses values estimated with the proposed iron losses modelling approach have been evaluated with the following error quantity:

$$err_{P_{FE}}\% = \frac{P_{FE}(i_d, i_q, \omega_m) - P_{FEmodel}(i_d, i_q, \omega_m)}{P_{FE}(i_d, i_q, \omega_m)} 100 \tag{4.67}$$

The iron losses model errors map, relating to the iron losses modelling approach proposed, is reported in Fig. 143.

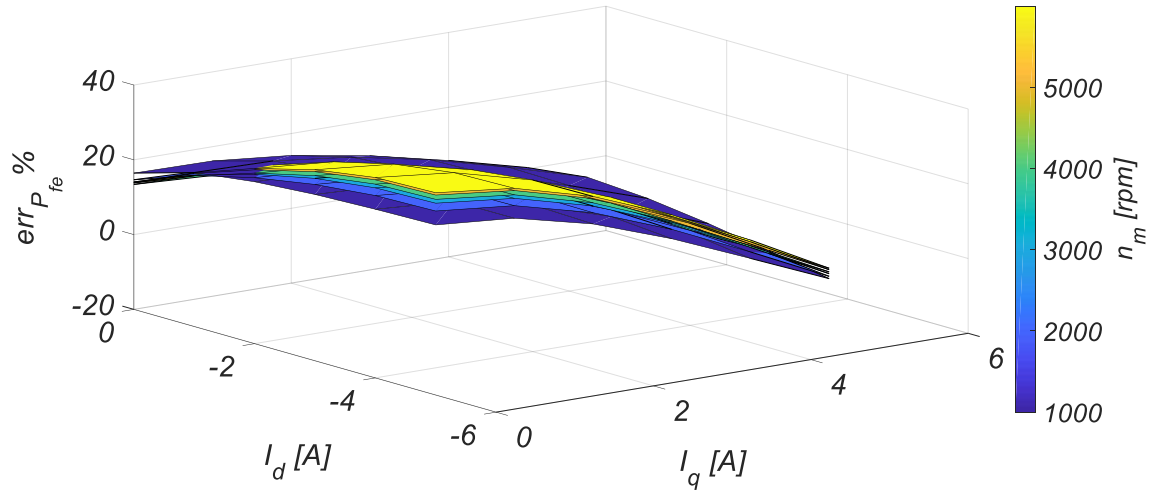

Fig. 143 Iron losses error map relating to the iron loss modelling approach proposed.

In this case, as can be noticed, the iron losses error presents lower values respect those obtained with the conventional iron losses model approach. In detail, it can be observed that the maximum and minimum iron losses error values are *24.65%* and *-10.24%*, respectively. This result allows to successfully validate the new iron losses modelling approach. The iron loss in the electrical machines increases the input active power when it works as a motor whereas decreases the output active power when they operate as a generator. In order to take into account the iron losses effects in the *dq*-axes modelling approach of IPMSM, it is possible consider an equivalent current the incur losses in the equivalent resistors across the *d*- and *q*-axis induced voltages as shown in Fig. 144.

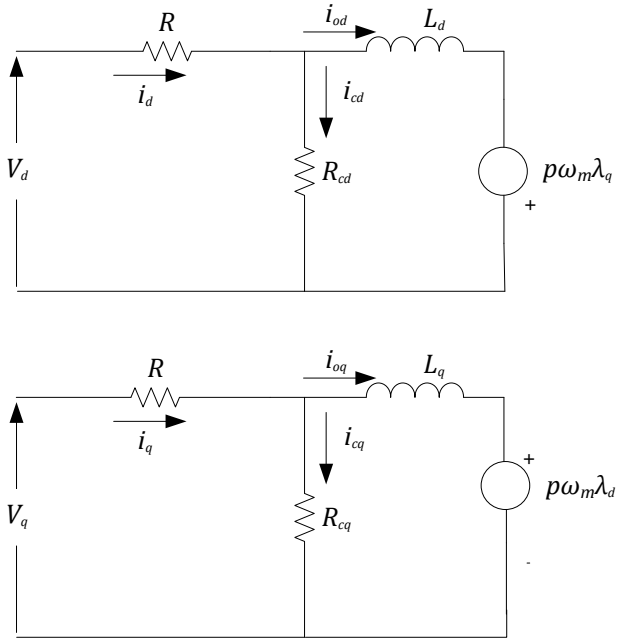

Fig. 144 Circuit model with equivalent iron losses components: (a) *d*-axis circuit model;(b) *q*-axis circuit model.

For this purpose, the iron loss can be decomposed in the components associated with the *dq*-axes flux linkage, as expressed by:

$$P_{FE\_d} = \frac{\lambda_q^2}{\lambda_d^2 + \lambda_q^2} P_{FE}^{OC} + P_{FE}^{SC} \tag{4.68}$$

$$P_{FE\_q} = \frac{\lambda_d^2}{\lambda_d^2 + \lambda_q^2} P_{FE}^{OC} \tag{4.69}$$

The corresponding iron loss *dq*-axes currents components can be derived through the following relationships:

$$i_{cd} = \frac{P_{FE\_d}}{V_d - Ri_d} \tag{4.70}$$

$$i_{cq} = \frac{P_{FE\_q}}{V_q - Ri_q} \tag{4.71}$$

The equivalent *d*-axis and *q*-axis iron loss resistances can be derived with the following relationships:

$$R_{cd} = \frac{(V_d - Ri_d)^2}{P_{FE\_d}} \tag{4.72}$$

$$R_{cq} = \frac{\left(V_q - Ri_q\right)^2}{P_{FE\_q}} \tag{4.73}$$

4.4 Implementation and validation of enhanced mathematical model of IPMSM in Matlab®/Simulink environment

The proposed enhanced mathematical model of the IPMSM has been implemented in *Matlab®/Simulink* environment and validated by means of several FEA simulations carried out in *Ansys Maxwell* environment. The implementation of the proposed mathematical model of the IPMSM in *Simulink* environment can be very useful as it allows to evaluate the electromagnetic behaviour of the IPMSM in various operating conditions with much smaller computational times than those required for simulations in the FEA environment. Moreover, a high fidelity model of the IPMSM implemented in Simulink environment is of considerable utility for a control purpose, since it allows in a simple way to evaluate the effectiveness of the control algorithms. In detail, firstly the validation of the IPMSM mathematical model that take into account the magnetic self-saturation, cross-coupling and spatial harmonics are described. Subsequently, the iron loss mathematical model is integrated into the previous mathematical model and the validation is carried out.

4.4.1 Validation of the IPMSM mathematical model that take into account magnetic self-saturation, cross-coupling and spatial harmonics effects

For the validation purpose, several IPMSM working points have been analyzed. In detail several FEA simulations have been performed and in each of them the *dq*-axes currents i_d, i_q and the mechanical angular speed ω_m are set as input quantities and the following output quantities have been evaluated:

- induced voltages in *abc*-reference frame E_{abc};
- induced voltages in *dqo*-referennce frame E_{dqo};
- input supply voltage in dqo-referennce frame V_{dqo};
- electromagnetic torque T_{em};

The input supply voltage in *dqo*-reference frame V_{dqo} are calculated as the sum of the value of the induced voltages in *dqo*-reference frame E_{dqo} and the voltage drop on the resistance that is set equal to 2.21 Ω, the same value employed in the Simulink simulations. In order to simulate the same IPMSM working points considered in FEA simulations, a *Field Oriented Control* (FOC) of IPMSM is implemented in *Matlab®/Simulink* environment. In detail, the Simulink block diagram of the implemented FOC is reported in Fig. 145.

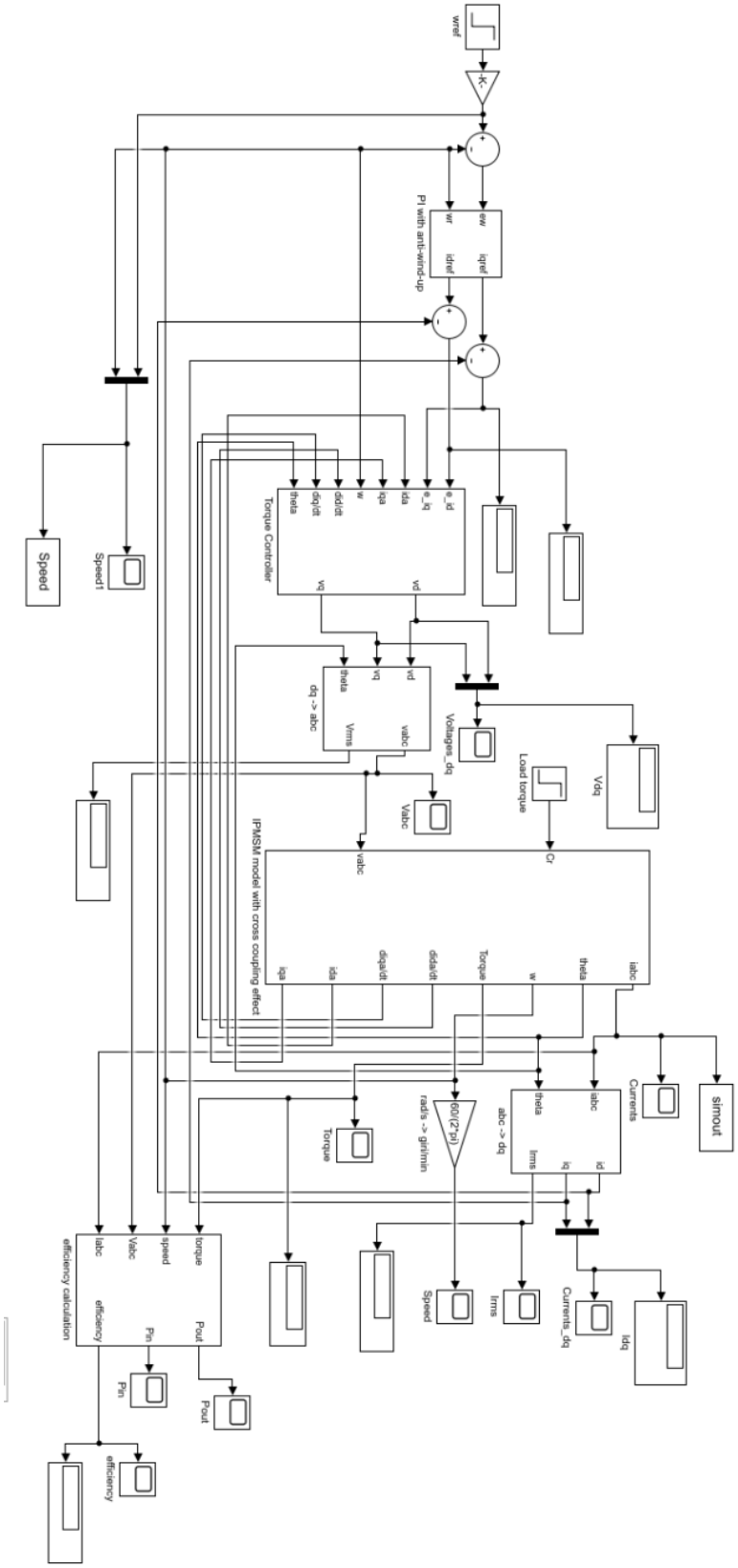

Fig. 145 Simulink schematic model.

The FOC input quantities are represented by the reference mechanical angular speed ω_m, by the value of the load torque T_L and the reference value of the *d*-axis current i_d. In order to compare the Simulink model results with those of the FEA simulations, the values of mechanical angular speed ω_m and of the *d*-axis current i_d have been set equal to those of each FEA simulation and the value of the load torque T_L has been set equal to the mean value obtained in each FEA simulations. The reference angular speed ω_m^* is compared with the actual value of the mechanical angular speed ω_m and the relative speed error is processed by the PI anti-windup block that returns the reference value of the *q*-axis current i_q. The reference values of *dq*-axes currents are compared with the actual values of the *dq*-axes currents and the respective error quantities processed in the torque controller that returns the reference value of *dq*-axis voltages. These latter represent the input quantities of the IPMSM mathematical model proposed. In detail, the IPMSM mathematical model equations, including the mechanical equations, are:

$$v_d = Ri_d(t) + L_{dd}^{inc}(i_d, i_q, \theta_m)\frac{di_d}{dt} + L_{dq}^{inc}(i_d, i_q, \theta_m)\frac{di_q}{dt} + \\ +\omega_m \frac{\partial \lambda_d(i_d, i_q, \theta_m)}{\partial \theta_m} - \omega_e\left[L_q^{app}(i_d, i_q, \theta_m) i_q(t) + \lambda_{qPM}\right] \tag{4.74}$$

$$v_q = Ri_q(t) + L_{qd}^{inc}(i_d, i_q, \theta_m)\frac{di_d}{dt} + L_{qq}^{inc}(i_d, i_q, \theta_m)\frac{di_q}{dt} + \\ +\omega_m \frac{\partial \lambda_q(i_d, i_q, \theta_m)}{\partial \theta_m} + \omega_e\left[L_d^{app}(i_d, i_q, \theta_m) i_d(t) + \lambda_{dPM}\right] \tag{4.75}$$

$$T_{em} = \frac{3}{2}p\{\lambda_{dPM} i_q - \lambda_{qPM} i_d + \left[L_d^{app}(i_d, i_q, \theta_m) - L_q^{app}(i_d, i_q, \theta_m)\right] i_d i_q\} \\ +\frac{3}{2}\left[\frac{\partial \lambda_d(i_d, i_q, \theta_m)}{\partial \theta_m} i_d + \frac{\partial \lambda_q(i_d, i_q, \theta_m)}{\partial \theta_m} i_q\right] \tag{4.76}$$

$$T_{em} = T_L + F\omega_r + J\frac{d\omega_m}{dt} \tag{4.64}$$

A schematic representation of the IPMSM mathematical model proposed, implemented in *Matlab®/Simulink* environment, are reported in Fig. 146.

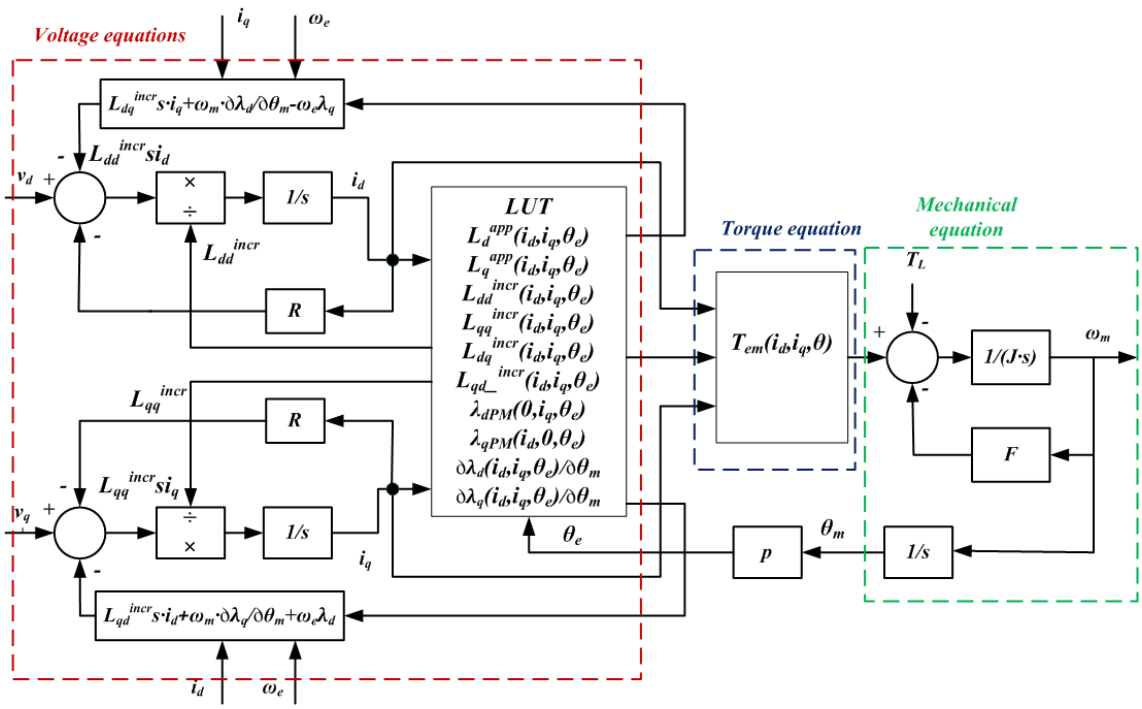

Fig. 146 Schematic representation of the IPMSM mathematical model proposed.

The values of the *dq*-axes non-coupled apparent inductances, of the *dq*-axes incremental inductances, of the *dq*-axes flux linkage produced by the PMs, derived by the characterization carried out in *Ansys Maxwell* environment, are implemented as lookup tables (LUT). The quantities taken into account for the validation of the IPMSM mathematical model proposed are:

- *dq*-axes currents i_d and i_q;
- induced voltages in *abc*-reference frame E_{abc};
- input supply voltages in dqo-reference frame V_{dqo};
- electromagnetic torque T_{em};

Several IPMSM working points are simulated and compared for validation purpose. Since the ripples on both the flux linkages and the electromagnetic torque are more significant at high speeds, the comparisons are illustrated at the rated mechanical angular speed of 4000 *rpm* and for several values of *dq*-axes currents i_d and i_q. By way of example, the comparisons between the trends of the *dq*-axes currents within 360 electrical degrees, evaluated in four cases of study, are reported in Fig. 147-Fig. 150, respectively.

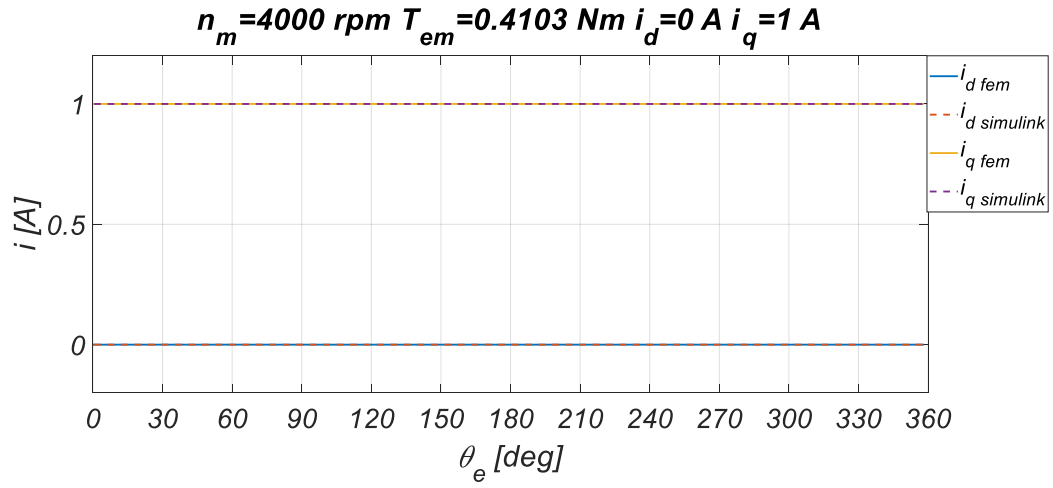

Fig. 147 *dq*-axes currents comparison at 4000 rpm, i_d=0 A, i_q=1 A.

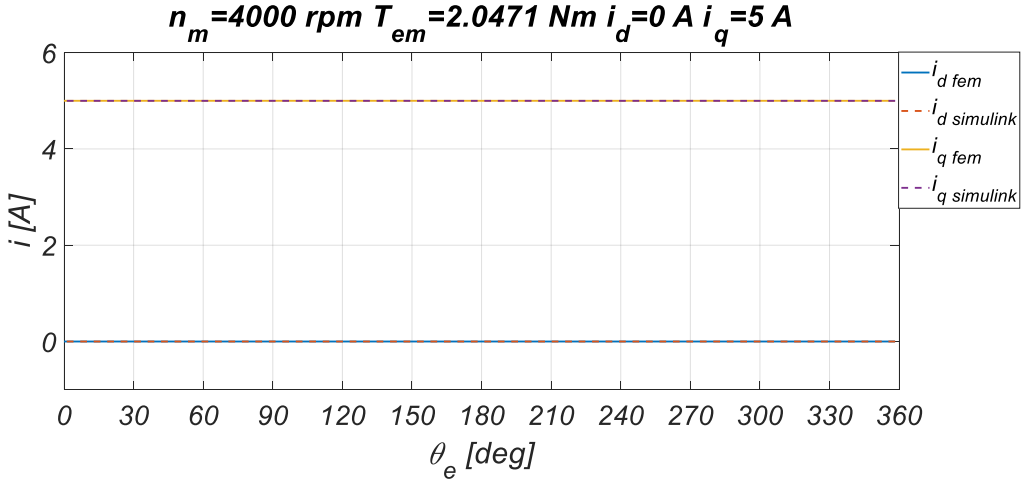

Fig. 148 *dq*-axes currents comparison at 4000 rpm, i_d=0 A, i_q=5 A.

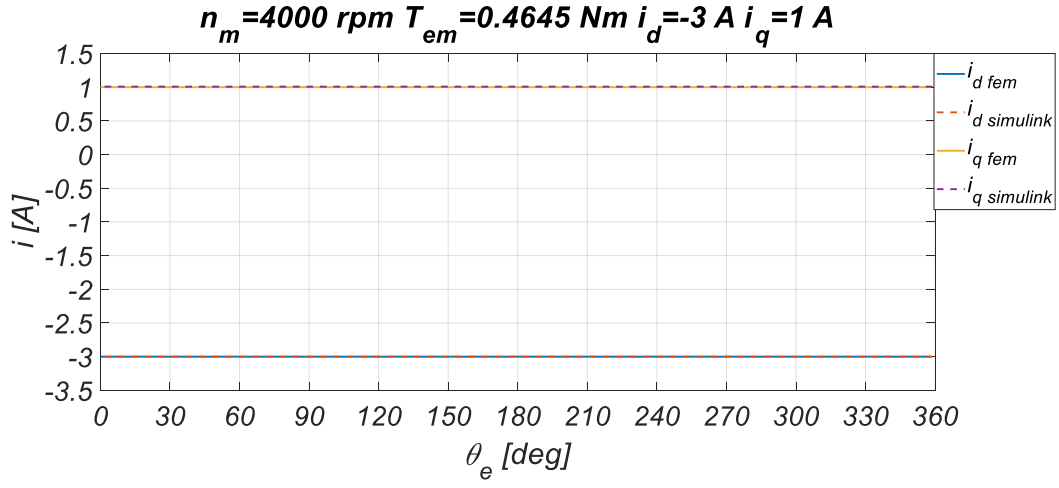

Fig. 149 *dq*-axes currents comparison at 4000 rpm, i_d=-3 A, i_q=1 A.

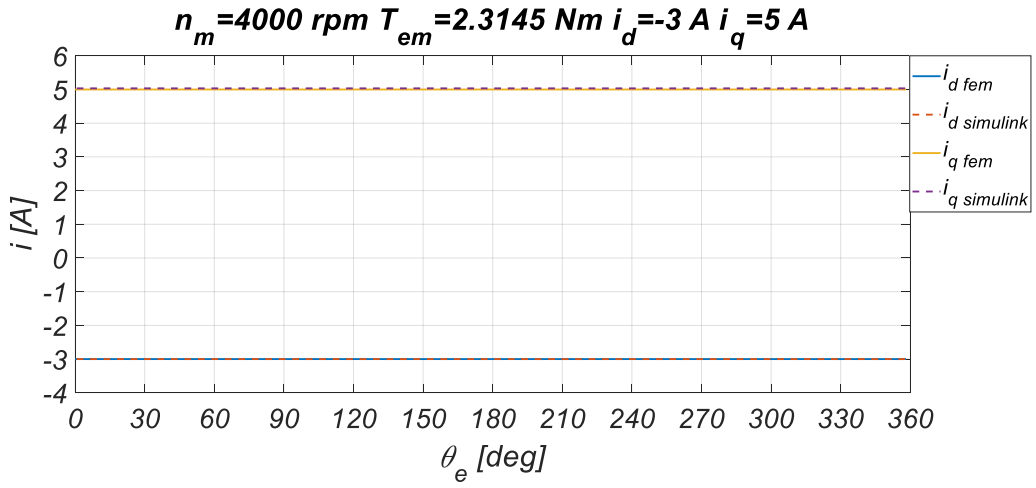

Fig. 150 *dq*-axes currents comparison at 4000 rpm, i_d=-3 A, i_q=5 A.

It can be observed that the current waveforms predicted by the FE and Simulink models almost coincide at the same load torque conditions. Particular attention must be paid to the comparison between the *q*-axis currents, since the *d*-axis current is an input quantity in both models. The comparison between the electromagnetic torque waveforms within 360 electrical degrees obtained with FE and Simulink models are reported in Fig. 151-Fig. 154.

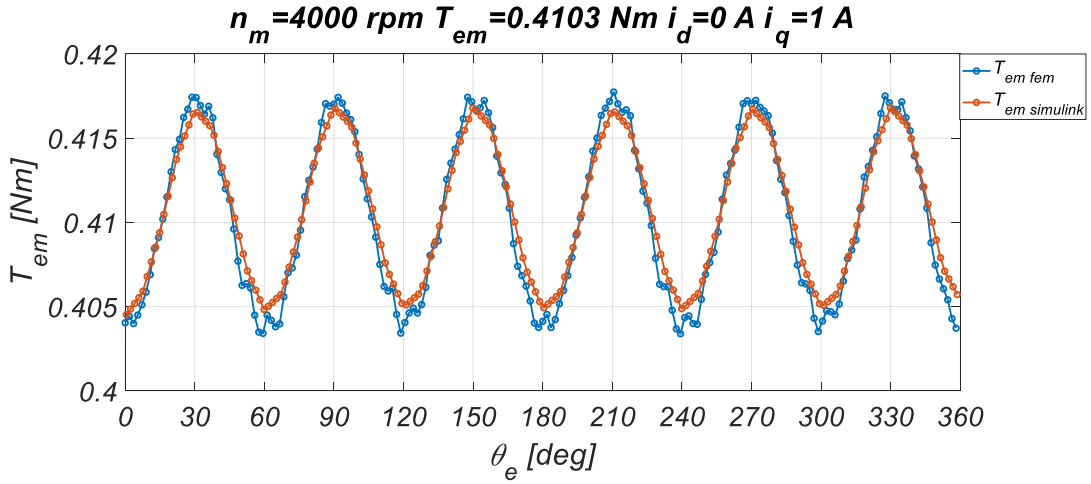

Fig. 151 Electromagnetic torques comparison at 4000 rpm, i_d=0 A, i_q=1 A.

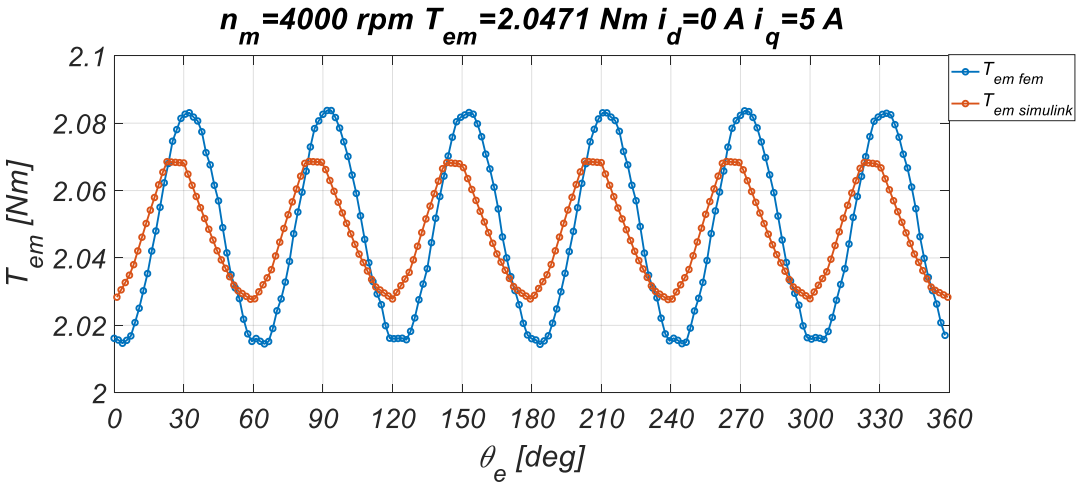

Fig. 152 Electromagnetic torques comparison at 4000 rpm, i_d=0 A, i_q=5 A.

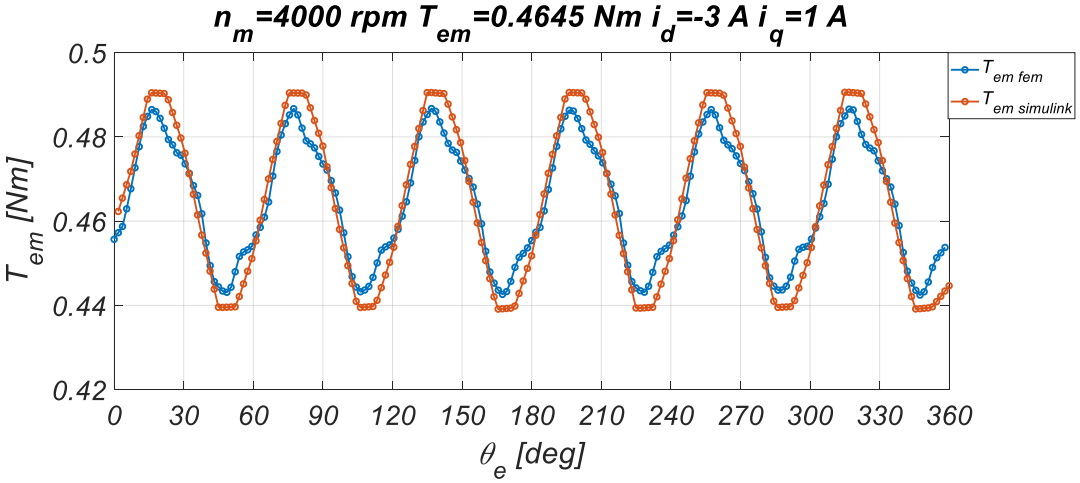

Fig. 153 Electromagnetic torques comparison at 4000 rpm, i_d=-3 A, i_q=1 A.

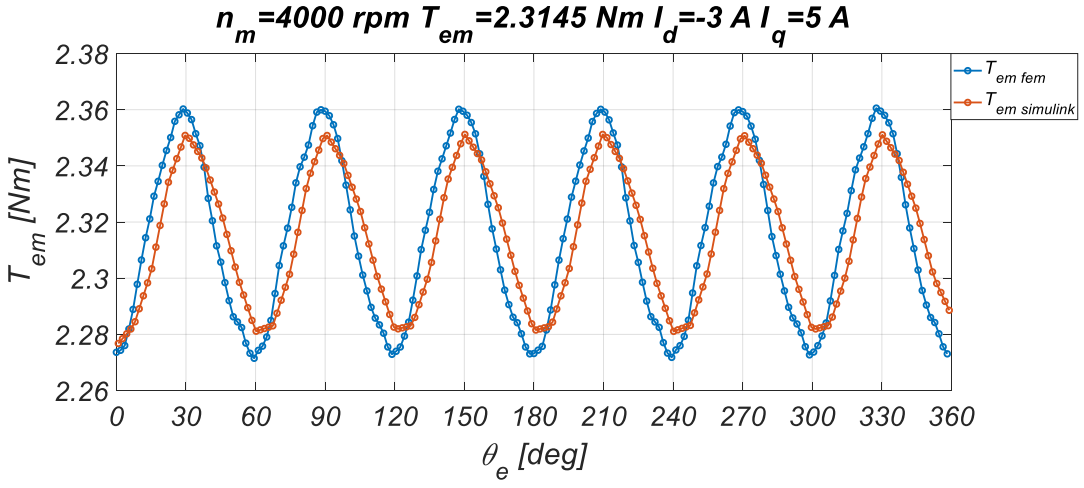

Fig. 154 Electromagnetic torques comparison at 4000 rpm, i_d=-3 A, i_q=5 A

It can be observed that the electromagnetic torque waveforms predicted by the FE and Simulink models almost coincide at low values of *q*-axis current. Instead, for high

values of *q*-axis currents, the electromagnetic torque waveforms predicted by the FE and Simulink models present the same mean value of electromagnetic torque but the torque ripple amplitudes are slightly different. The comparison between *dq*-axis voltage waveforms within 360 electrical degrees obtained with FE and Simulink models are reported in Fig. 155-Fig. 162.

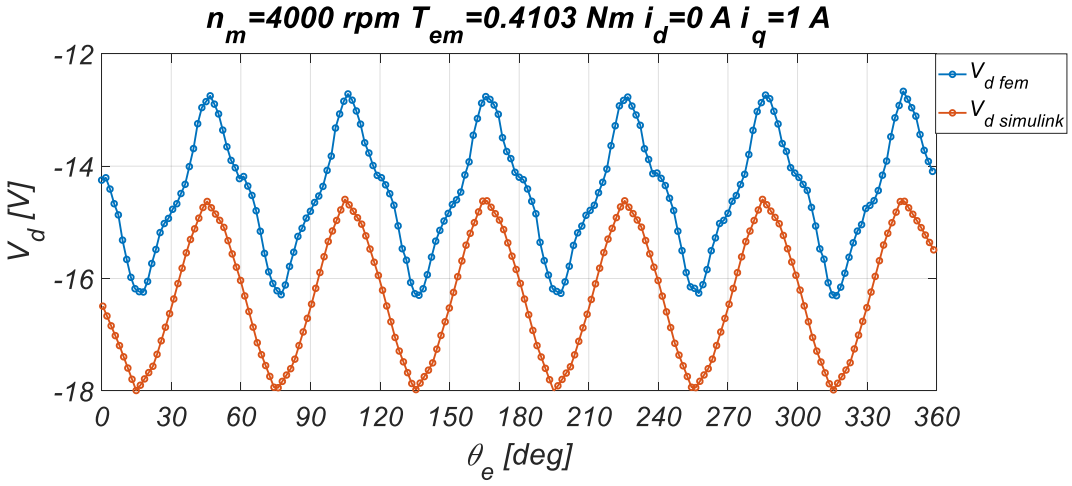

Fig. 155 *d*-axis voltages comparison at 4000 rpm, i_d=0 A, i_q=1 A.

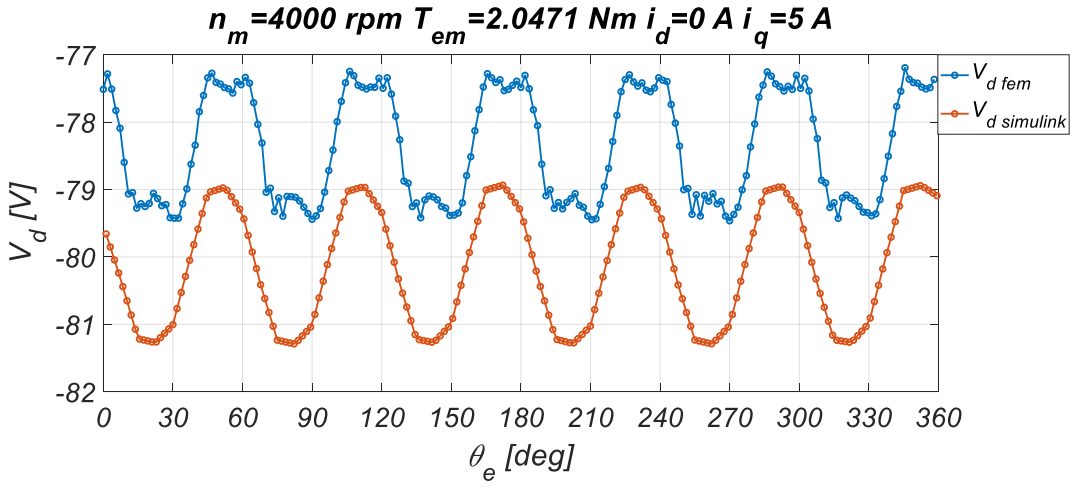

Fig. 156 *d*-axis voltages comparison at 4000 rpm, i_d=0 A, i_q=5 A.

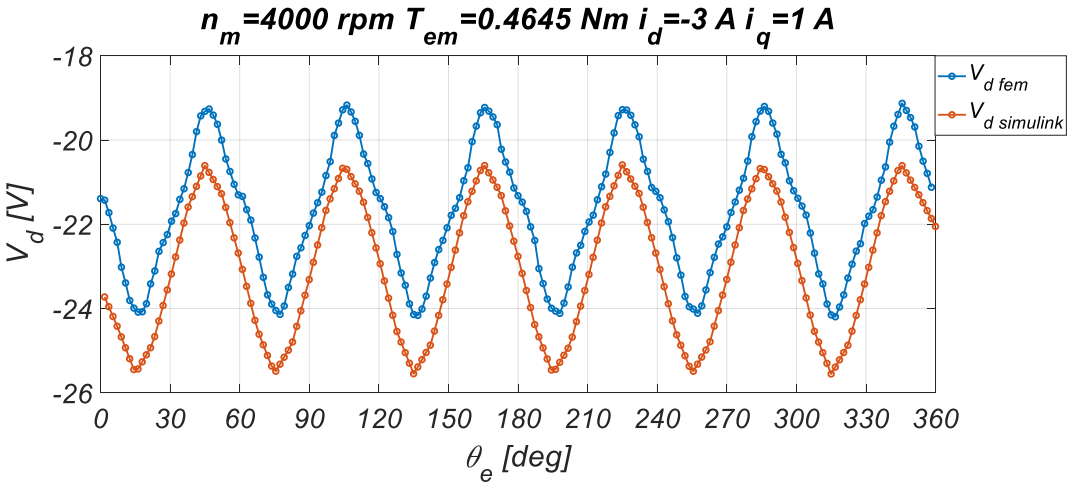

Fig. 157 *d*-axis voltages comparison at 4000 rpm, i_d=-3 A, i_q=1 A.

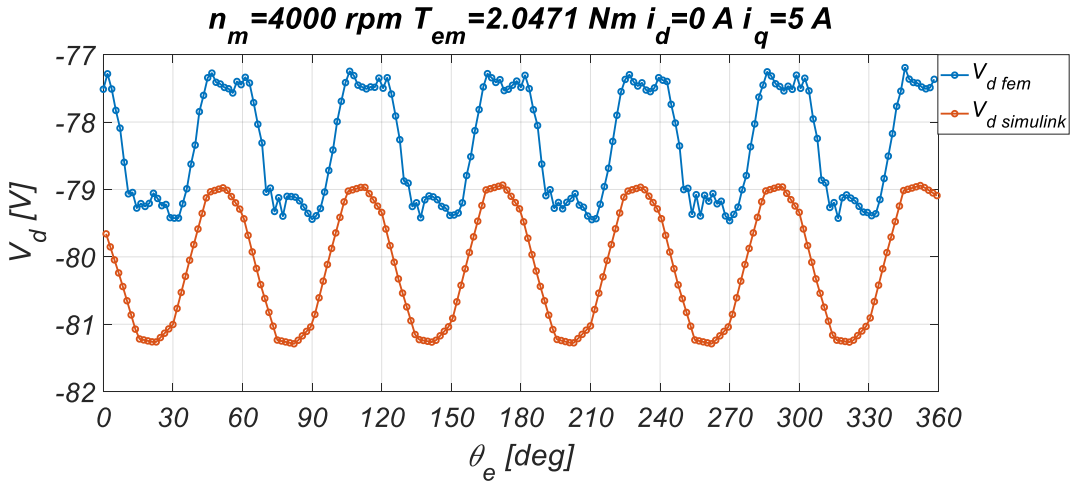

Fig. 158 *d*-axis voltages comparison at 4000 rpm, i_d=-3 A, i_q=5 A.

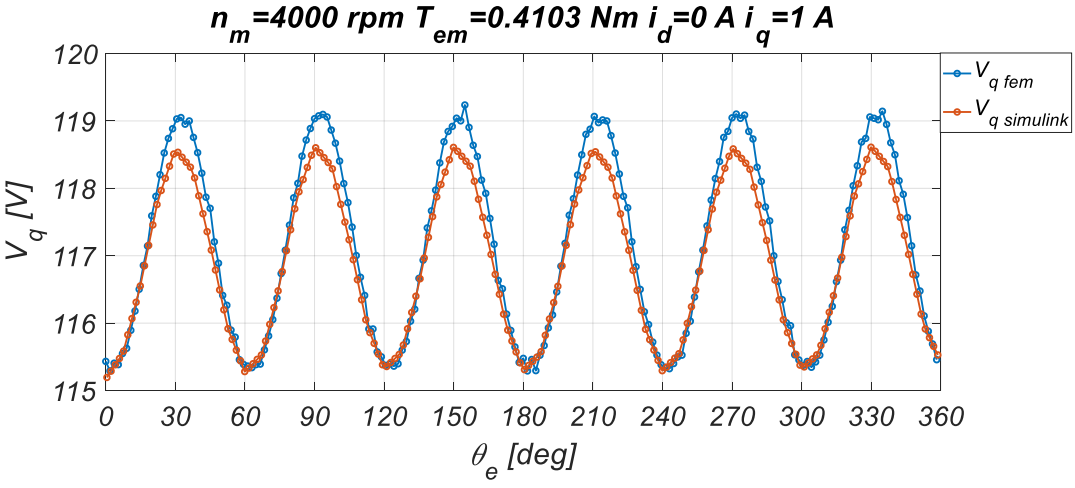

Fig. 159 *q*-axis voltages comparison at 4000 rpm, i_d=0 A, i_q=1 A.

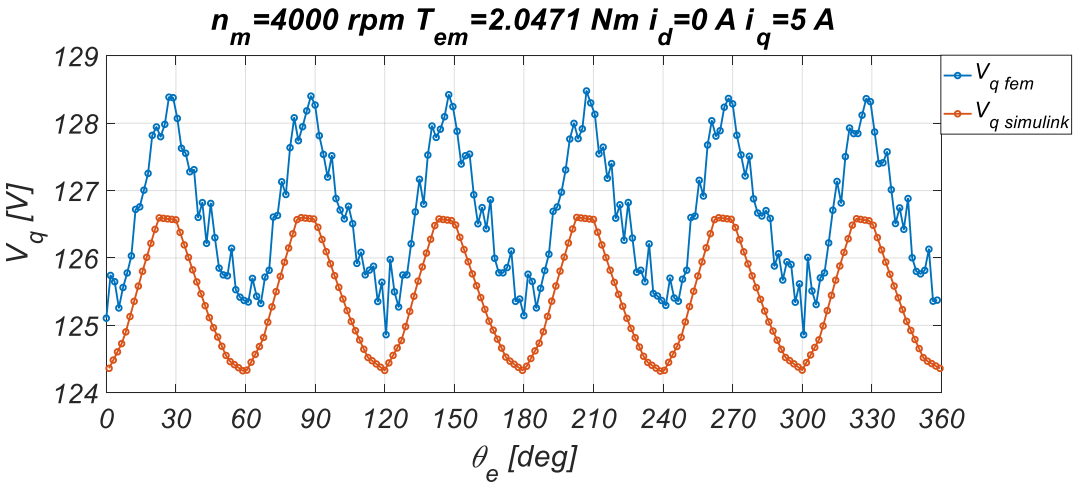

Fig. 160 *q*-axis voltages comparison at 4000 rpm, i_d=0 A, i_q=5 A

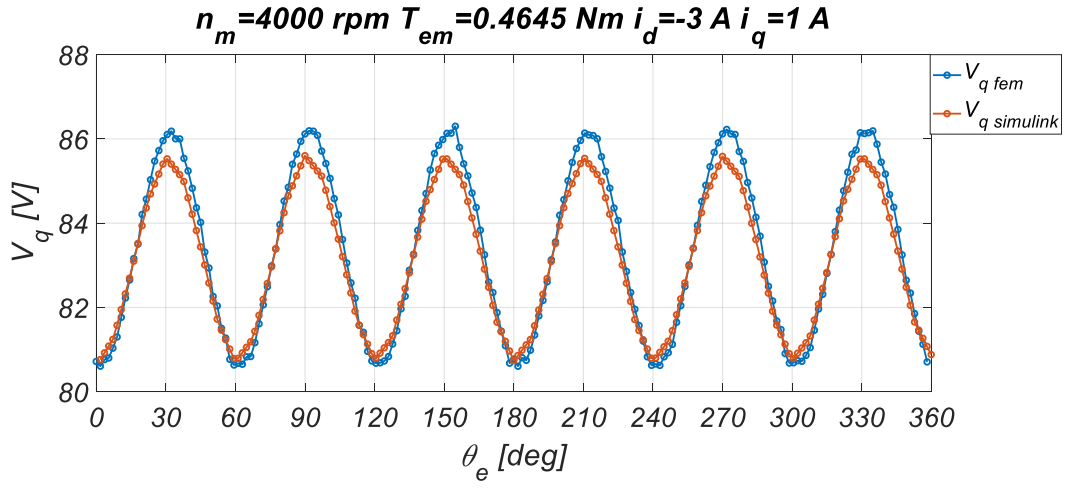

Fig. 161 *q*-axis voltages comparison at 4000 rpm, i_d=-3 A, i_q=1 A

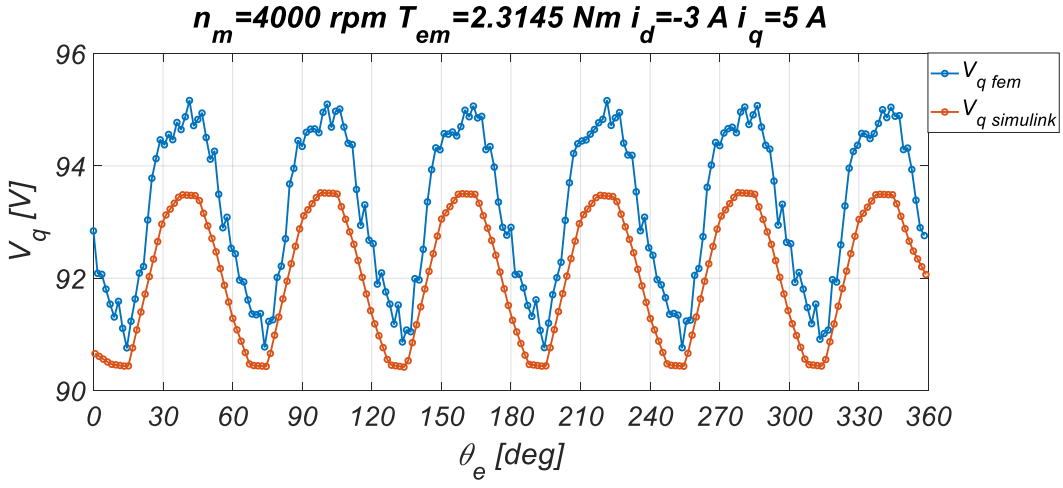

Fig. 162 *q*-axis voltages comparison at 4000 rpm, i_d=-3 A, i_q=5 A

It can be observed that *dq*-axes voltage waveforms predicted by the FE and Simulink models present the same trends but there small differences between the average values,

especially for *d*-axis voltages. This behaviour can be attributed to possible numerical errors carried out in the derivations of the IPMSM model parameters or to the accuracy of the *dq*-axes flux linkages derivatives $\partial\lambda_{dq}/\partial\theta_m$ that are present in the *dq*-axes voltage equations. A greater number of FE simulations in the characterization phase of the IPMSM could improve the accuracy of the *dq*-axes flux linkages derivatives and the other model parameters. However, these results can be considered satisfactory for the validation purpose. In this regard, a further comparison was made on the induced voltages in *abc*-reference frame. In detail, the induced voltage waveforms obtained in FE simulations present a distorted waveform due to the saturation effects or to the distorted airgap flux density, whereas the induced voltage waveforms obtained in Simulink simulations present sinusoidal waveforms as shown in Fig. 163 and Fig. 164, respectively.

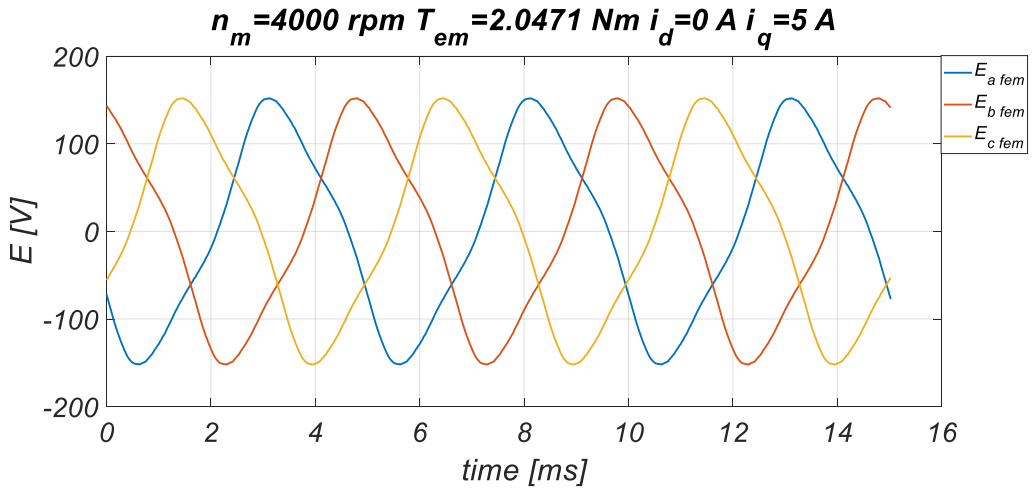

Fig. 163 Three phase induced voltage waveforms obtained in FE simulations.

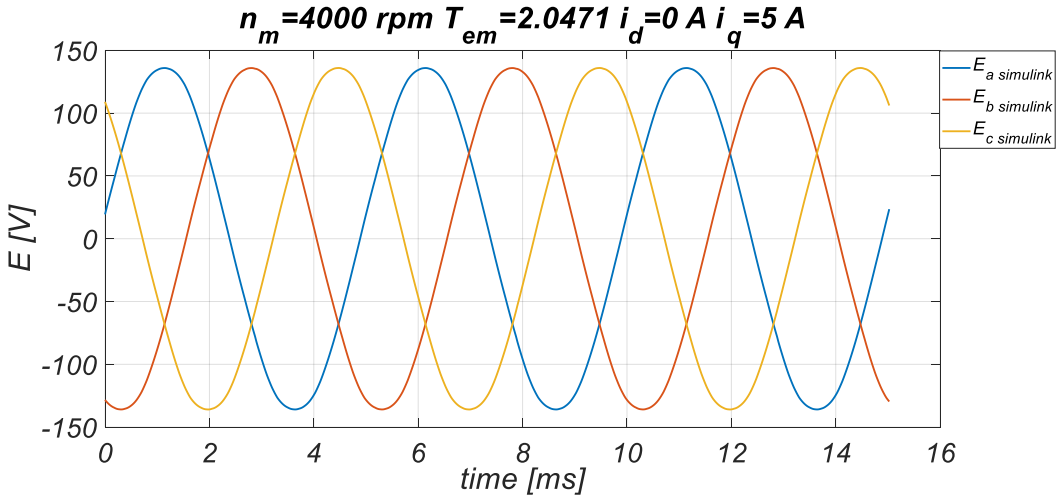

Fig. 164 Three phase induced voltage waveforms obtained in Simulink simulations.

Therefore, in order to perform a comparison between the induced voltages obtained in FE and Simulink simulations, a fast Fourier transform (FFT) of these quantities has been performed. The FFT of the induced voltages obtained with FE and Simulink models are reported in Fig. 165-Fig. 172.

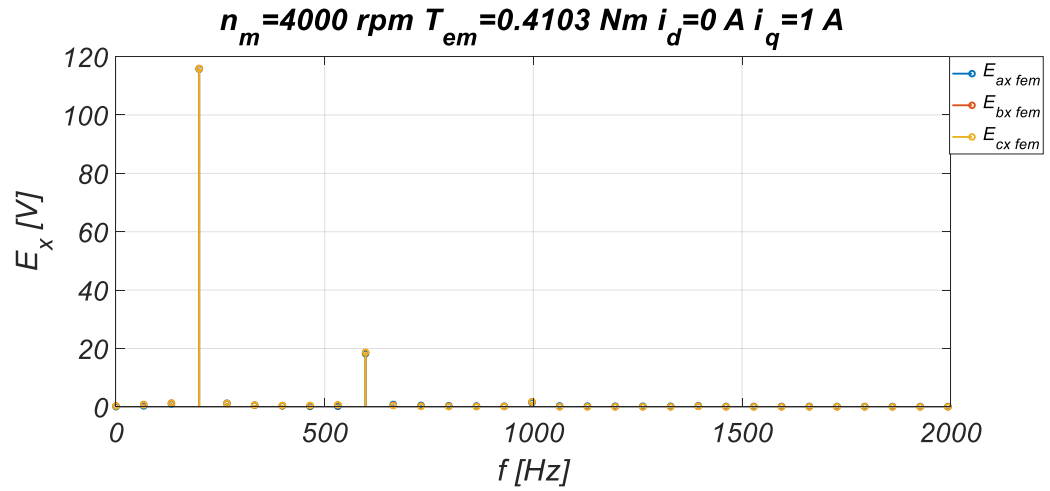

Fig. 165 FFT of the induced voltages obtained in FE simulation at 4000 rpm, i_d=0 A, i_q=1 A.

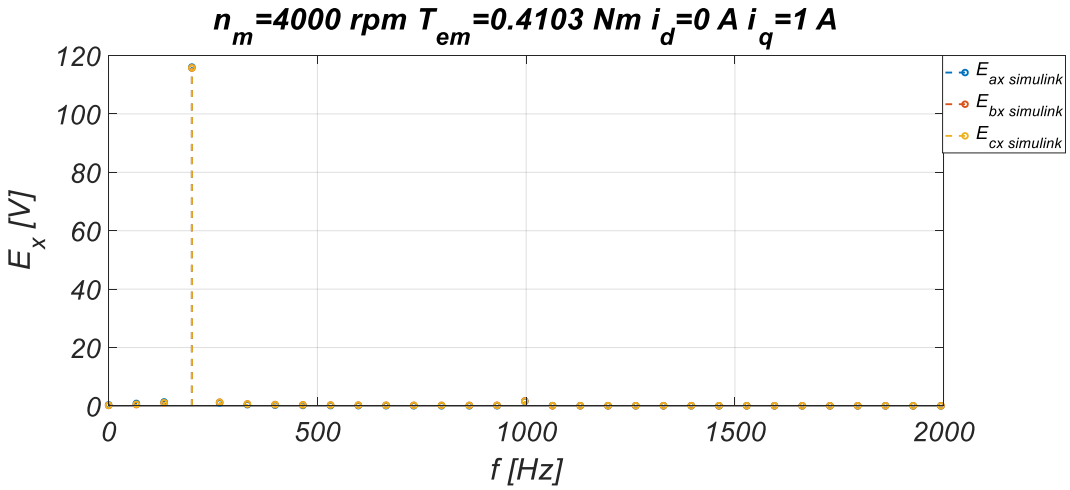

Fig. 166 FFT of the induced voltages obtained in Simulink simulation at 4000 rpm, i_d=0A, i_q=1A

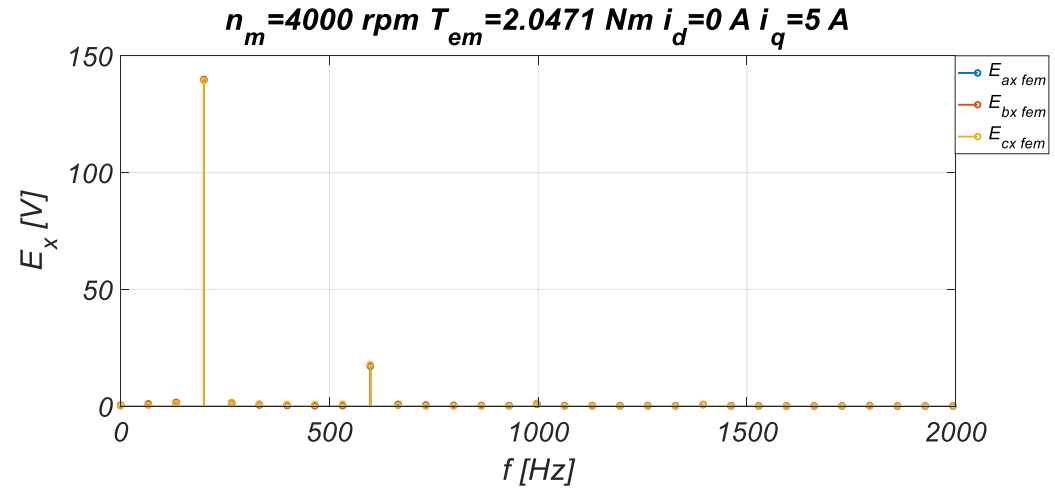

Fig. 167 FFT of the induced voltages obtained in FE simulation at 4000 rpm, i_d=0 A, i_q=5 A.

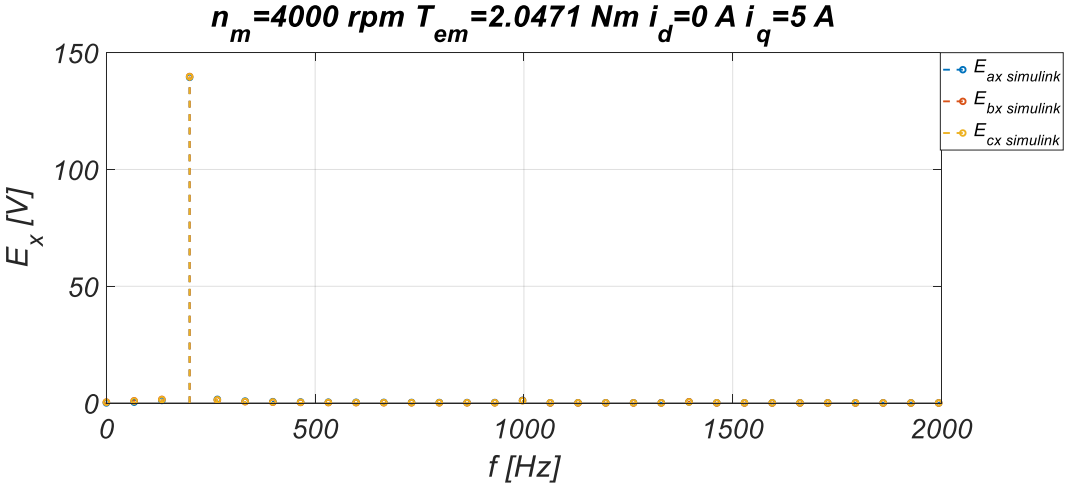

Fig. 168 FFT of the induced voltages obtained in Simulink simulation at 4000 rpm, i_d=0 A, i_q=5 A.

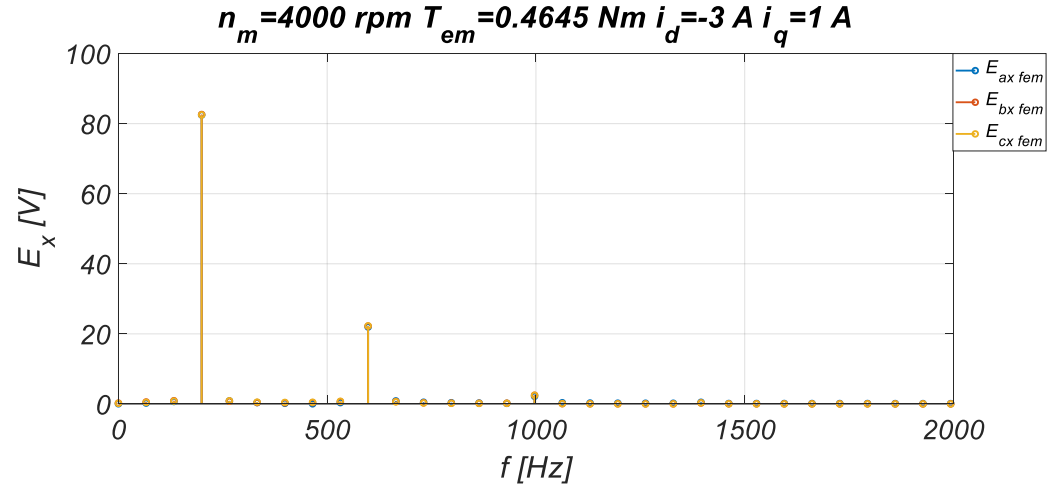

Fig. 169 FFT of the induced voltages obtained in FE simulation at 4000 rpm, i_d=-3 A, i_q=1 A.

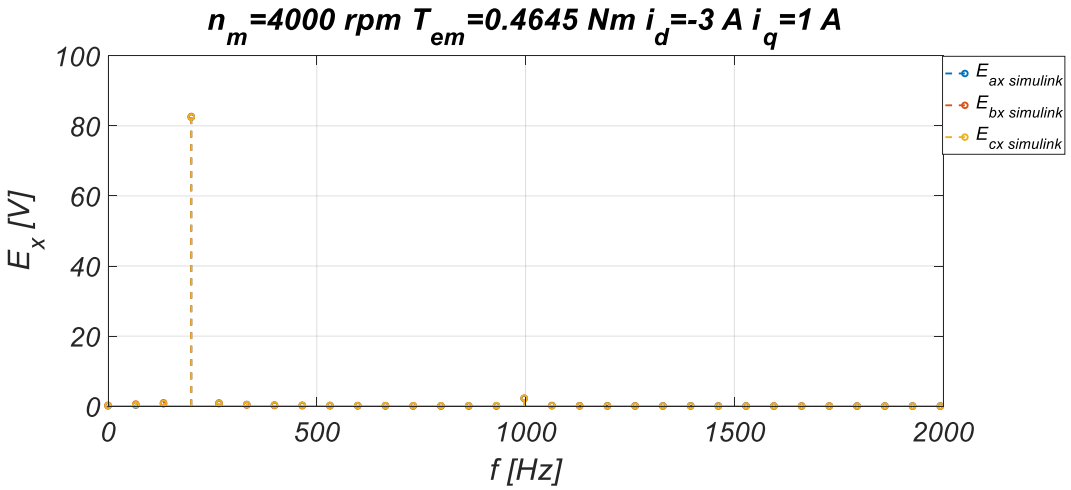

Fig. 170 FFT of the induced voltages obtained in Simulink simulation at 4000 rpm, i_d=-3 A, i_q=1 A.

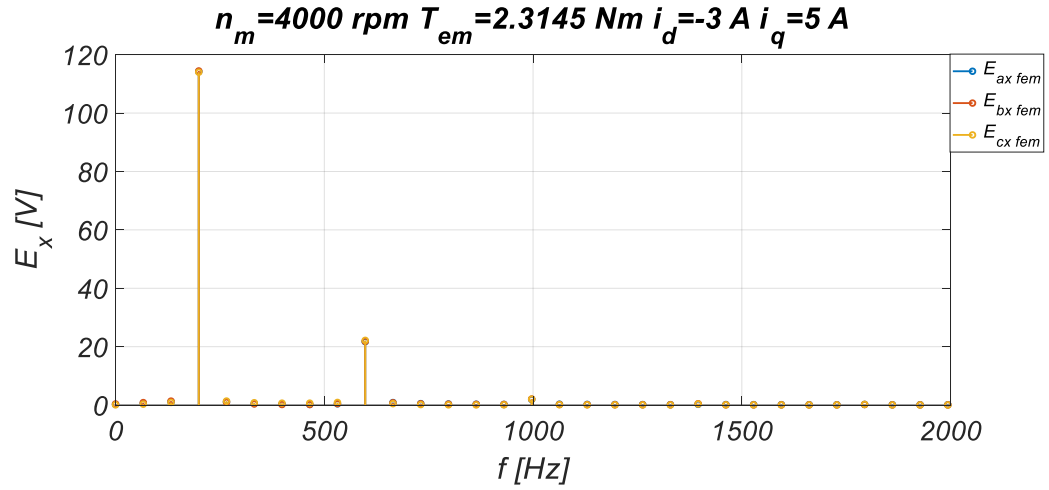

Fig. 171 FFT of the induced voltages obtained in FE simulation at 4000 rpm, i_d=-3 A, i_q=5 A.

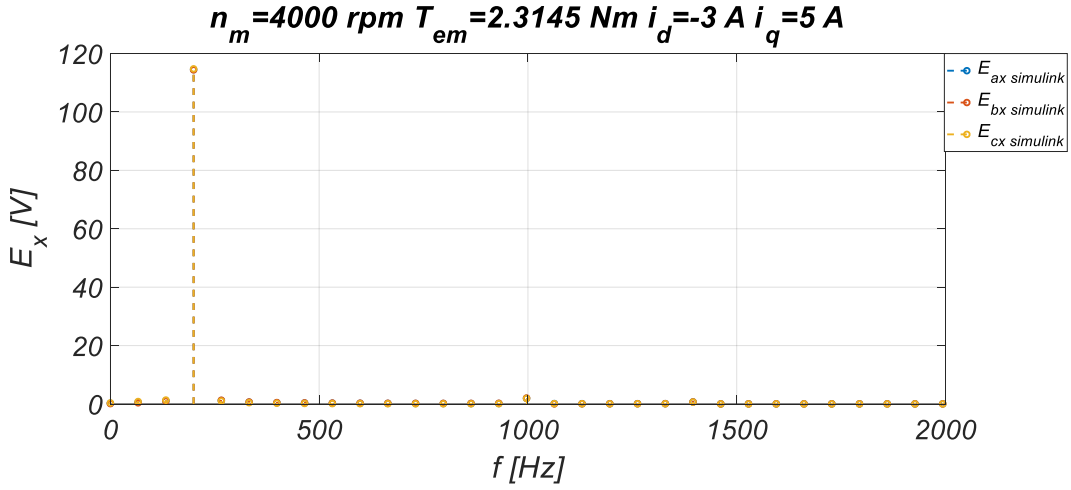

Fig. 172 FFT of the induced voltages obtained in Simulink simulation at 4000 rpm, i_d=-3 A, i_q=5 A.

It can be observed that the FFT of the induced voltages obtained in FE and Simulink simulations present the same amplitude of the fundamental harmonic and a third

harmonic component is present in the FFT of the induced voltages obtained in FE simulation. A third harmonic component is not present in the FFT of the induced voltages obtained in Simulink simulations because the zero sequence quantities are not useful for control purposes and in *dqo* modelling approach are set usually equal to zero.

4.4.2 Validation of IPMSM mathematical model that take into account magnetic self-saturation, cross-coupling, spatial harmonics and iron losses effects

The iron loss effects on the electromagnetic behaviour of the IPMSM have been studied and implemented in the proposed mathematical model. The IPMSM mathematical model that also includes the iron loss effects is represented by the following equations:

$$v_d = Ri_d(t) + L_{dd}^{inc}\left(i_d, i_q, \theta_m\right)\frac{di_{od}}{dt} + L_{dq}^{inc}\left(i_d, i_q, \theta_m\right)\frac{di_{oq}}{dt} + \\ +\omega_m \frac{\partial \lambda_d\left(i_d, i_q, \theta_m\right)}{\partial \theta_m} - \omega_e\left[L_q^{app}\left(i_d, i_q, \theta_m\right) i_{oq}(t) + \lambda_{qPM}\right] \tag{4.77}$$

$$v_q = Ri_q(t) + L_{qd}^{inc}\left(i_d, i_q, \theta_m\right)\frac{di_{od}}{dt} + L_{qq}^{inc}\left(i_d, i_q, \theta_m\right)\frac{di_{oq}}{dt} + \\ +\omega_m \frac{\partial \lambda_q\left(i_d, i_q, \theta_m\right)}{\partial \theta_m} + \omega_e\left[L_d^{app}\left(i_d, i_q, \theta_m\right) i_{od}(t) + \lambda_{dPM}\right] \tag{4.78}$$

$$T_{em} = \frac{3}{2}p\left\{\lambda_{dPM} i_{oq} - \lambda_{qPM} i_{od} + \left[L_d^{app}\left(i_d, i_q, \theta_m\right) - L_q^{app}\left(i_d, i_q, \theta_m\right)\right] i_{od} i_{oq}\right\} \\ +\frac{3}{2}\left[\frac{\partial \lambda_d\left(i_d, i_q, \theta_m\right)}{\partial \theta_m} i_{od} + \frac{\partial \lambda_q\left(i_d, i_q, \theta_m\right)}{\partial \theta_m} i_{oq}\right] \tag{4.79}$$

$$T_{em} = T_L + F\omega_r + J\frac{d\omega_m}{dt} \tag{4.65}$$

The schematic representation of the IPMSM mathematical model that accounts for the iron losses is shown in Fig. 173.

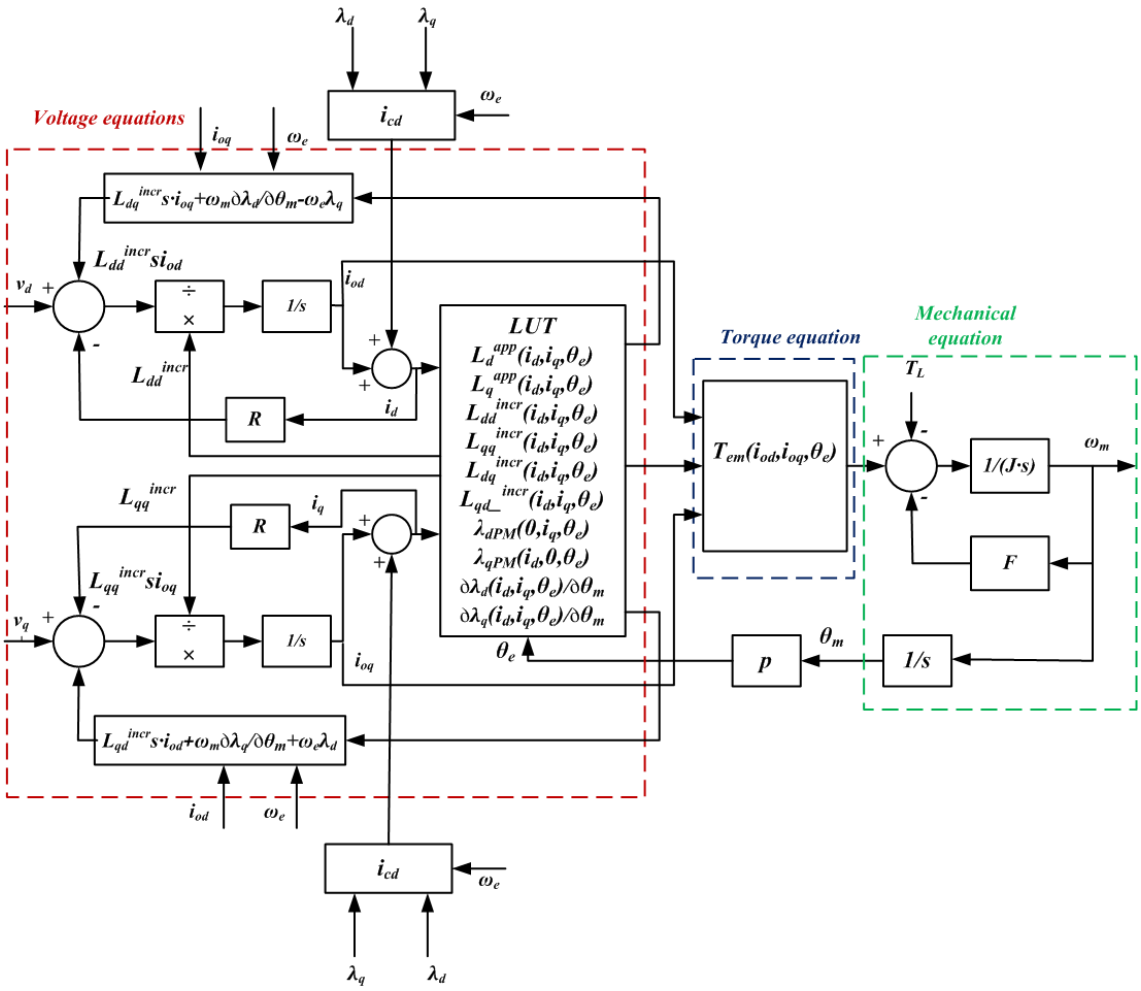

Fig. 173 Schematic representation of the IPMSM mathematical model proposed with the iron losses effect.

For the validation purpose, the same working point of the IPMSM, employed for the previous validation, are taken into account. The quantities taken into account for the validation of the proposed IPMSM mathematical model, are:

- *dq*-axes currents i_d and i_q;
- induced voltages in *abc*-reference frame E_{abc};
- input supply voltages in dqo-reference frame V_{dqo};
- electromagnetic torque T_{em};

In this case, since the modelization of the iron loss effects consists in the definition of the equivalent currents i_{cd}. i_{cq} that provide losses in the equivalent resistors across *dq*-axes induced voltages, the resultant *q*-axis current should be larger than that predicted with the IPMSM mathematical model described previously at the same IPMSM working conditions. In order to highlight the above-described behaviour, several cases of study with high values of the electromagnetic load torque or the *dq*-axes currents

have been considered. By way of example, three comparisons between the trends of the *dq*-axes currents within 360 electrical degrees, obtained with the FE and Simulink simulations, are reported in Fig. 174-Fig. 176.

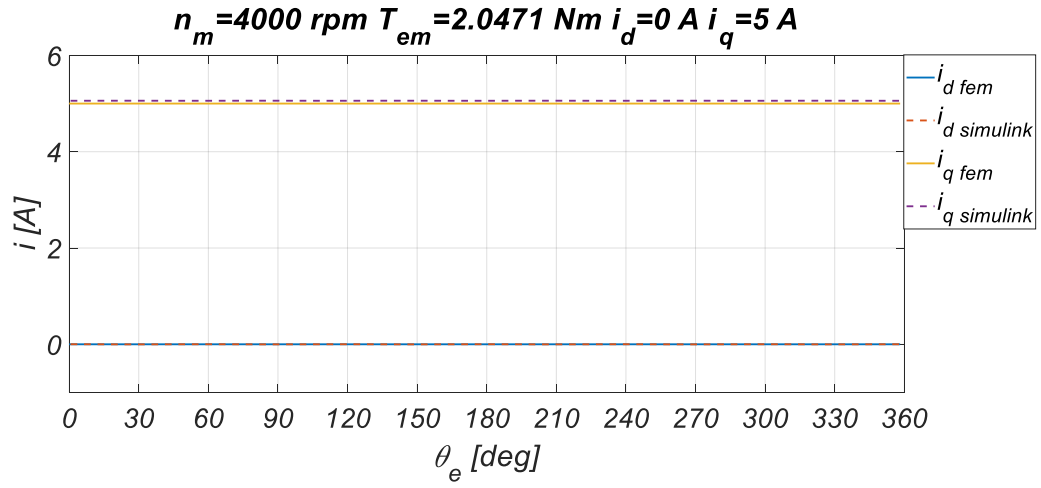

Fig. 174 *dq*-axes currents comparison at 4000 rpm, i_d=0 A, i_q=5 A.

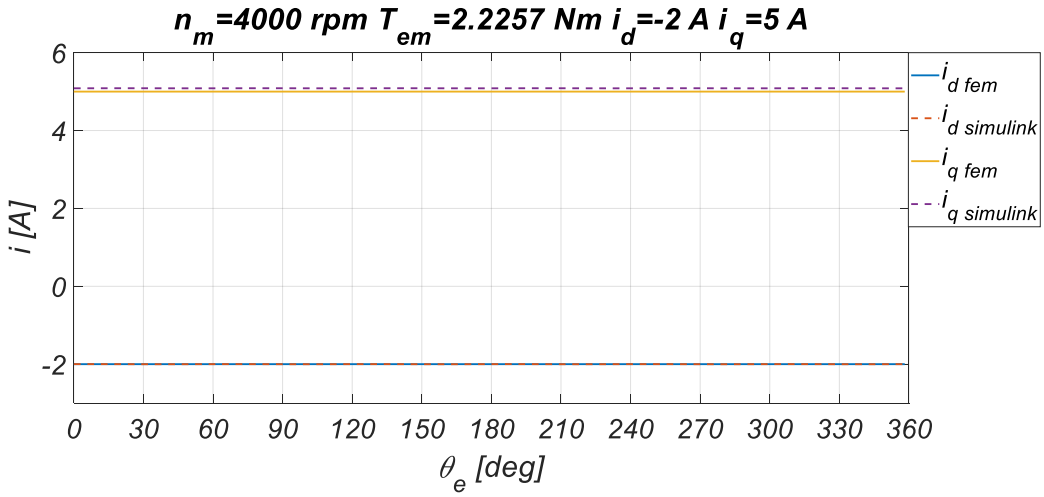

Fig. 175 *dq*-axes currents comparison at 4000 rpm, i_d=-2 A, i_q=5 A.

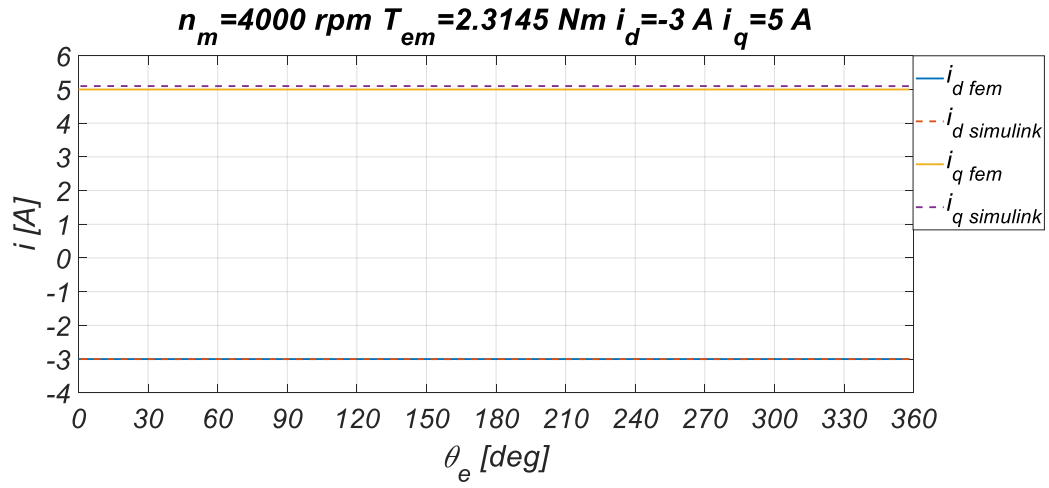

Fig. 176 *dq*-axes currents comparison at 4000 rpm, i_d=-3 A, i_q=5 A.

It can be observed that the current waveforms predicted by the FE and Simulink models almost coincide at the same load torque conditions. Particular attention must be paid to the comparison between the *q*-axis currents, where it is possible to appreciate a small difference between the predicted *q*-axis currents, as expected. The comparison between the electromagnetic torque waveforms within 360 electrical degrees obtained with FE and Simulink models are reported in Fig. 177-Fig. 179.

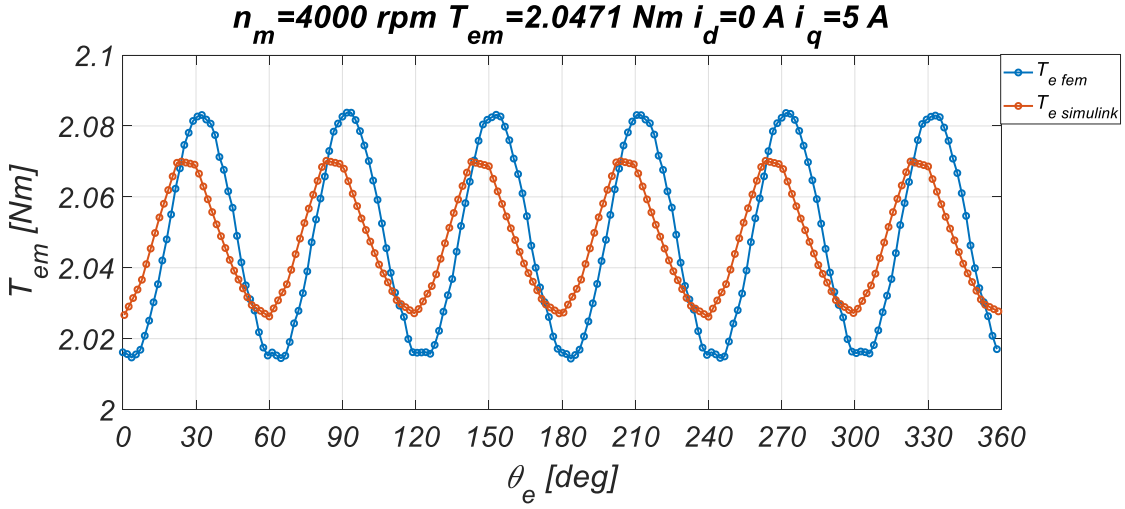

Fig. 177 Electromagnetic torques comparison at 4000 rpm, i_d=0 A, i_q=5 A.

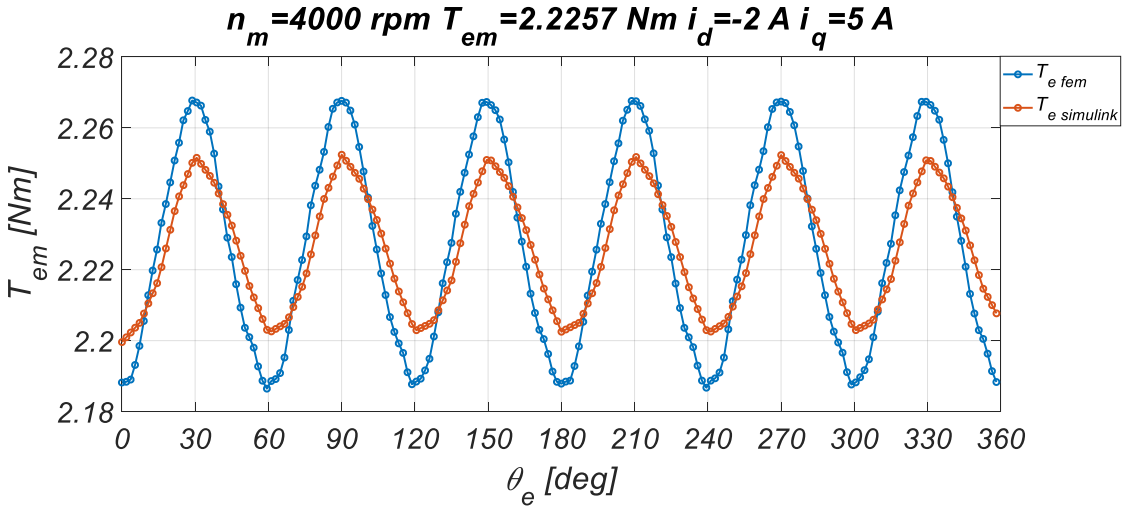

Fig. 178 Electromagnetic torques comparison at 4000 rpm, i_d=-2 A, i_q=5 A.

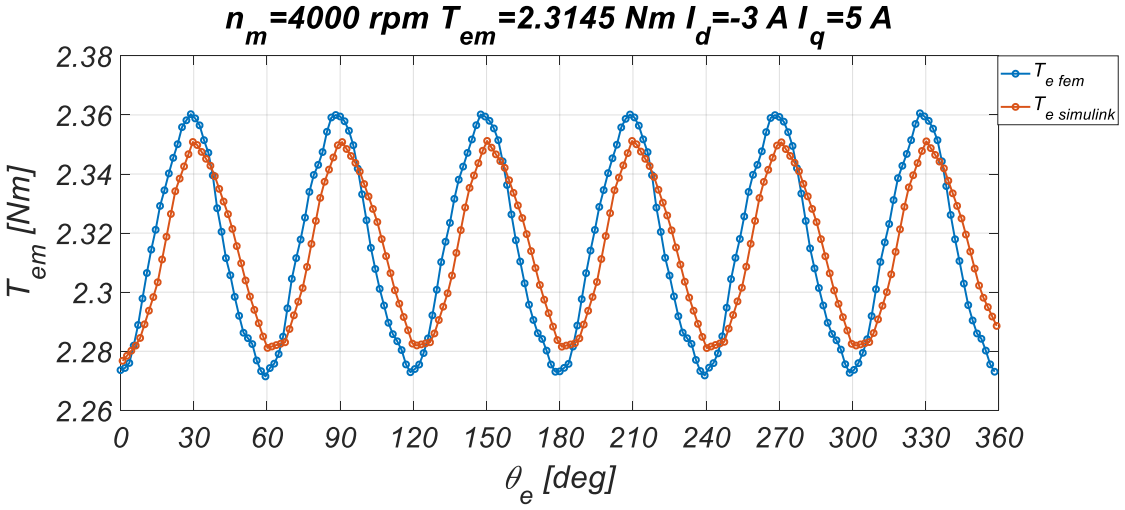

Fig. 179 Electromagnetic torques comparison at 4000 rpm, i_d=-3 A, i_q=5 A.

It can be observed that electromagnetic torque waveforms predicted by the FE and Simulink models present the same mean value of electromagnetic torque but the torque ripple amplitudes are slightly different. The comparison between *dq*-axes voltage waveforms in 360 electrical degrees obtained with FE and Simulink models are reported in Fig. 180-Fig. 185.

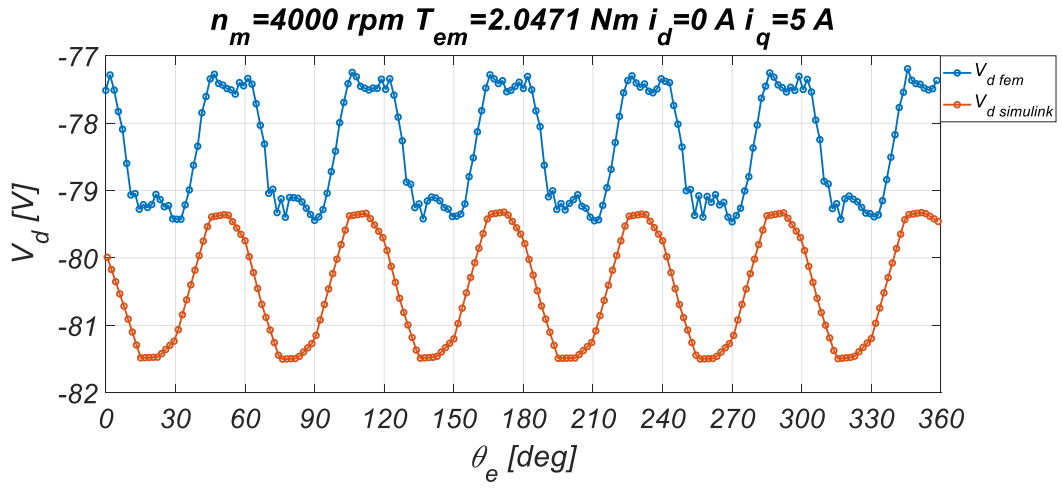

Fig. 180 *d*-axis voltages comparison at 4000 rpm, i_d=0 A, i_q=5 A.

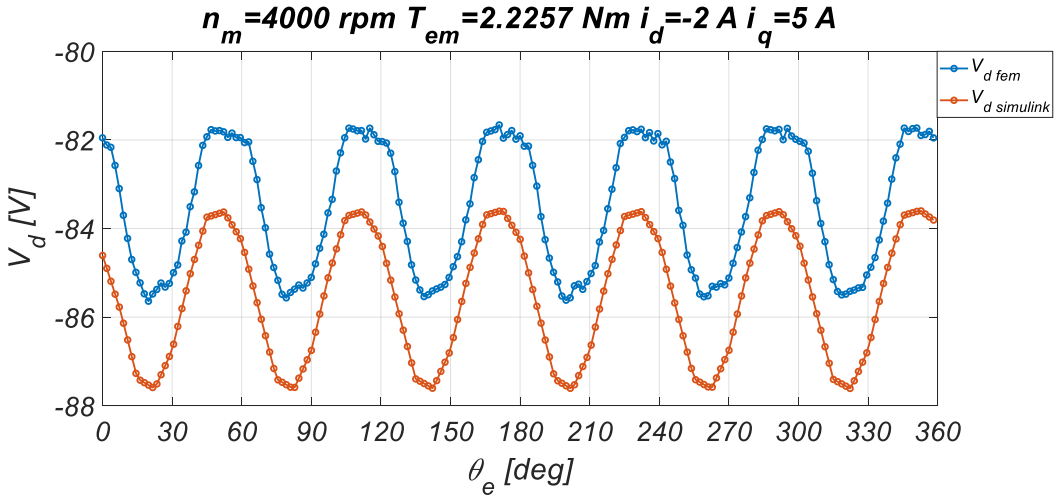

Fig. 181 *d*-axis voltages comparison at 4000 rpm, i_d=-2 A, i_q=5 A.

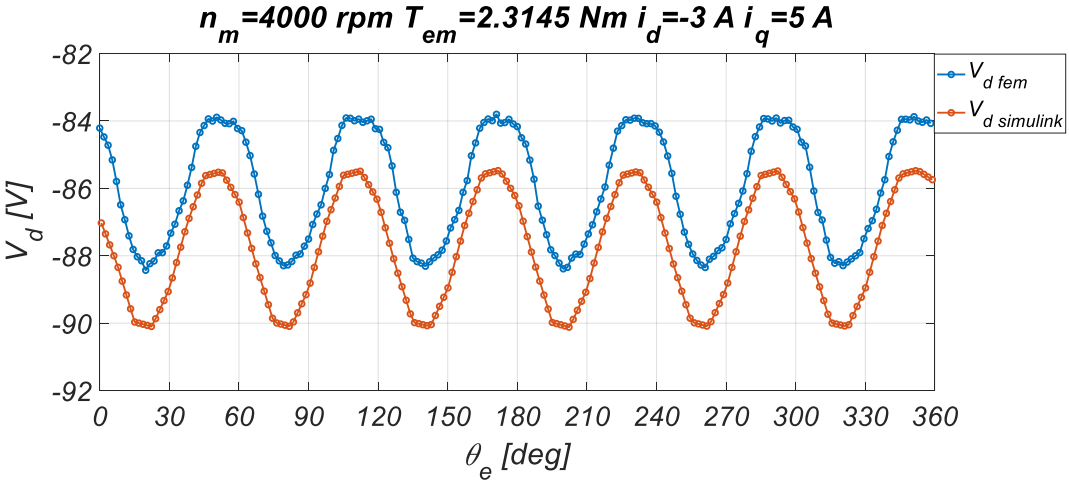

Fig. 182 *d*-axis voltages comparison at 4000 rpm, i_d=-2 A, i_q=5 A.

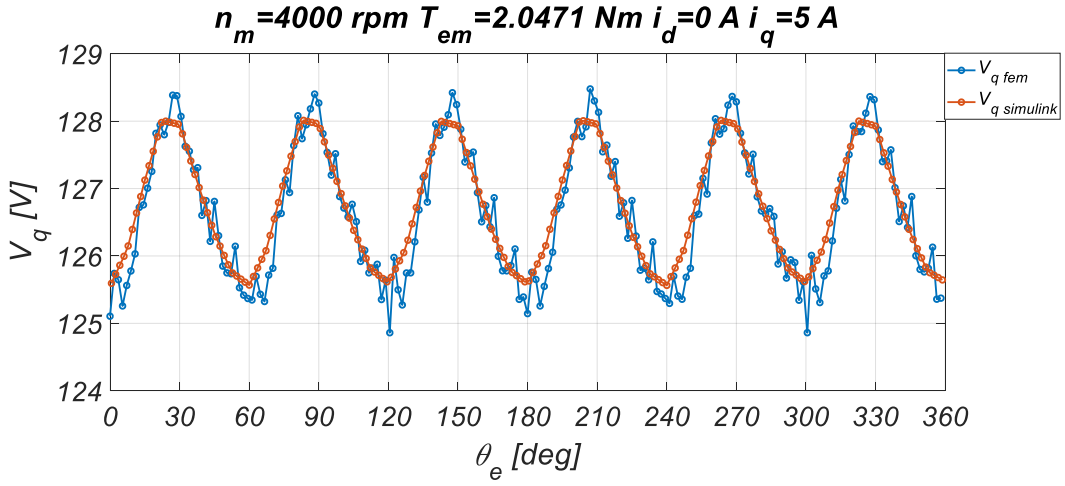

Fig. 183 *q*-axis voltages comparison at 4000 rpm, i_d=0 A, i_q=5 A.

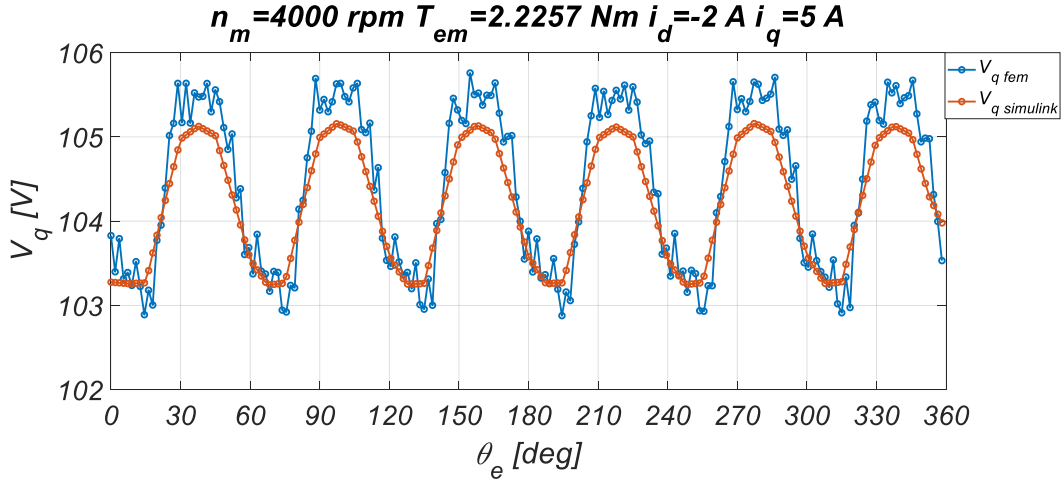

Fig. 184 *q*-axis voltages comparison at 4000 rpm, i_d=-2 A, i_q=5 A

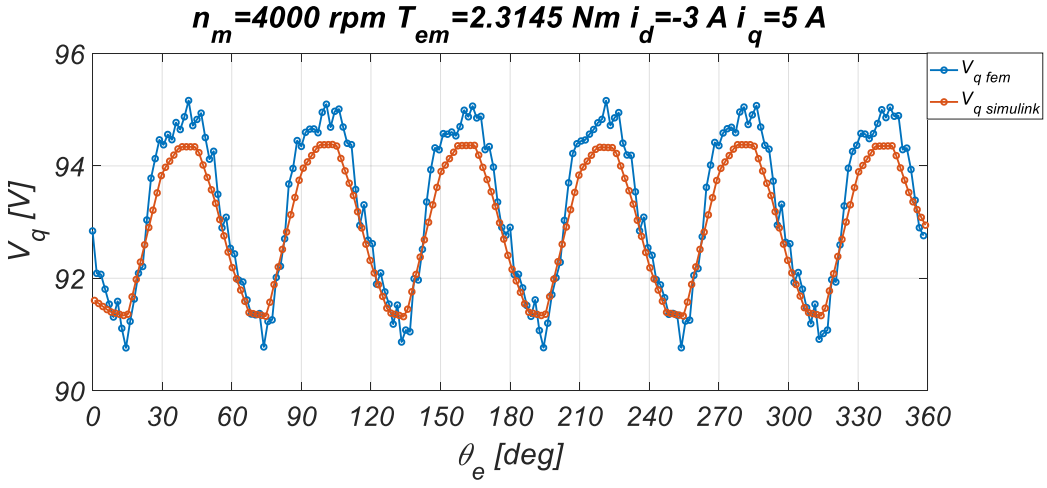

Fig. 185 *q*-axis voltages comparison at 4000 rpm, i_d=-3 A, i_q=5 A

It can be observed that *dq*-axes voltage waveforms predicted by the FE and Simulink models present the same trends. In detail, the *d*-axis voltage waveforms predicted present

small differences in the average values. Instead, the *q*-axis voltages waveforms predicted by the FE and Simulink models are very close. The differences found can be attributed to possible numerical errors carried out in the derivations of the IPMSM model parameters or the accuracy of the *dq*-axes flux linkages derivatives $\partial\lambda_{dq}/\partial\theta_m$ that are present in the *dq*-axes voltage equations. A greater number of FE simulations in the characterization phase of the IPMSM could improve the accuracy of the *dq*-axes flux linkages derivatives and the other model parameters. However, these results can be considered satisfactory for the validation purpose. In this regard, a further comparison was made on the induced voltages in *abc*-reference frame. The results obtained are quite similar to those obtained in the validation described previously. By way of example, the FFT of the induced voltages obtained with FE and Simulink models at 4000 *rpm*, i_d=-2 *A*, i_q=5 *A* are reported in Fig. 186 and Fig. 187, respectively.

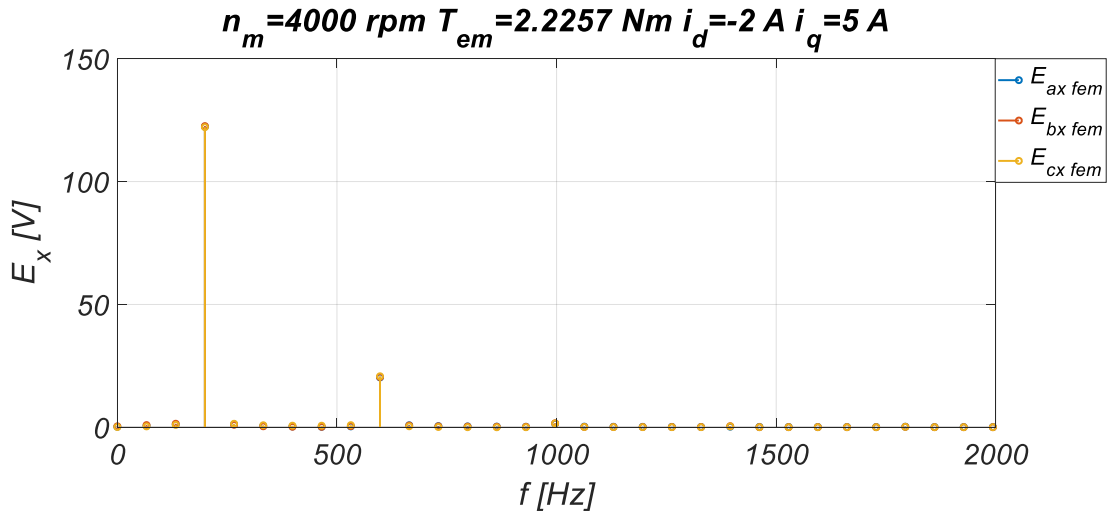

Fig. 186 FFT of the induced voltages obtained in FE simulation at 4000 rpm, i_d=-2 A, i_q=5 A.

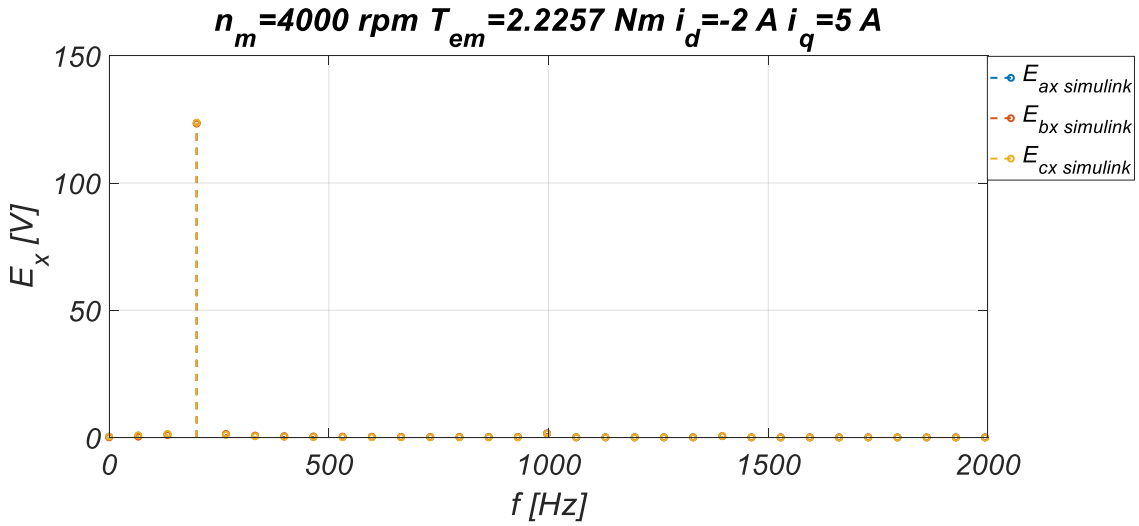

Fig. 187 FFT of the induced voltages obtained in Simulink simulation at 4000 rpm, i_d=-2 A, i_q=5 A.

Also in this case, it can be observed that the FFT of the induced voltages obtained in FE and Simulink simulations present the same amplitude of the fundamental harmonic and a third harmonic component is present in the FFT of the induced voltages obtained in FE simulation. Therefore, it is possible to state that the results obtained validate successfully the enhanced IPMSM mathematical model proposed.

References

[IV.1] I. Boldea, L. N. Tutelea, L. Parsa, and D. Dorrell, “Automotive electric propulsion systems with reduced or no permanent magnets: An overview,” IEEE Trans. Ind. Electron., vol. 61, no. 10, pp. 5696–5711, Oct. 2014.

[IV.2] D. Dorrell, L. Parsa, and I. Boldea, “Automotive electric motors, generators, and actuator drive systems with reduced or no permanent magnets and innovative design concepts,” IEEE Trans. Ind. Electron., vol. 61, no. 10, pp. 5693–5695, Oct. 2014.

[IV.3] Z. Yang, F. Shang, I. P. Brown, and M. Krishnamurthy, “Comparative study of interior permanent magnet, induction, and switched reluctance motor drives for EV and HEV applications,” IEEE Trans. Transport. Electrific., vol. 1, no. 3, pp. 245–254, Oct. 2015.

[IV.4] G. Pellegrino, A. Vagati, P. Guglielmi, and B. Boazzo, “Performance comparison between surface-mounted and interior PM motor drives for electric vehicle application,” IEEE Trans. Ind. Electron., vol. 59, no. 2, pp. 803–811, Feb. 2012.

[IV.5] H. Lin, H. Guo and H. Qian, "Design of High- Performance Permanent Magnet Synchronous Motor for Electric Aircraft Propulsion," 2018 21st International Conference on Electrical Machines and Systems (ICEMS), Jeju, 2018, pp. 174-179.

[IV.6] B. Sarlioglu and C. T. Morris, “More electric aircraft: Review, challenges, and opportunities for commercial transport aircraft,” IEEE Trans. Transport. Electrific., vol. 1, no. 1, pp. 54–64, Jun. 2015.

[IV.7] G. Sulligoi, A. Vicenzutti, and R. Menis, “All-electric ship design: From electrical propulsion to integrated electrical and electronic power systems,” IEEE Trans. Transport. Electrific., vol. 2, no. 4, pp. 507–521, Dec. 2016.

[IV.8] B. Stumberger, G. Stumberger, D. Dolinar, A. Hamler, and M. Trlep, “Evaluation of saturation and cross-magnetization effects in interior permanent-magnet synchronous motor,” IEEE Trans. Ind. Appl., vol. 39, no. 5, pp. 1264–1271, Sep. 2003.

[IV.9] N. Bianchi and S. Bolognani, "Magnetic models of saturated interior permanent magnet motors based on finite element analysis," *Conference Record*

of 1998 IEEE Industry Applications Conference. Thirty-Third IAS Annual Meeting (Cat. No.98CH36242), St. Louis, MO, USA, 1998, pp. 27-34 vol.1.

[IV.10] Z. Q. Zhu, Y. Li, D. Howe, C. M. Bingham and D. Stone, "Influence of Machine Topology and Cross-Coupling Magnetic Saturation on Rotor Position Estimation Accuracy in Extended Back-EMF Based Sensorless PM Brushless AC Drives," *2007 IEEE Industry Applications Annual Meeting*, New Orleans, LA, 2007, pp. 2378-2385.

[IV.11] A. Pouramin, R. Dutta, M. F. Rahman, J. E. Fletcher and D. Xiao, "A preliminary study of the effect of saturation and cross-magnetization on the inductances of a fractional-slot concentrated-wound interior PM synchronous machine," *2015 IEEE 11th International Conference on Power Electronics and Drive Systems*, Sydney, NSW, 2015, pp. 828-833.

[IV.12] X. Chen, J. Wang, B. Sen, P. Lazari and T. Sun, "A High-Fidelity and Computationally Efficient Model for Interior Permanent-Magnet Machines Considering the Magnetic Saturation, Spatial Harmonics, and Iron Loss Effect," in *IEEE Transactions on Industrial Electronics*, vol. 62, no. 7, pp. 4044-4055, July 2015.

[IV.13] X. Chen, J. Wang and A. Griffo, "A High-Fidelity and Computationally Efficient Electrothermally Coupled Model for Interior Permanent-Magnet Machines in Electric Vehicle Traction Applications," in *IEEE Transactions on Transportation Electrification*, vol. 1, no. 4, pp. 336-347, Dec. 2015.

[IV.14] L. Di Leonardo, F. Parasiliti, M. Tursini and M. Villani, "Transient analysis of PM synchronous motor drives by finite element model co-simulation," *IECON 2013 - 39th Annual Conference of the IEEE Industrial Electronics Society*, Vienna, 2013, pp. 6834-6840.

[IV.15] S. Vaez and V. I. John, "Minimum loss operation of PM motor drives," *Proceedings 1995 Canadian Conference on Electrical and Computer Engineering*, Montreal, Quebec, Canada, 1995, pp. 284-287 vol.1.

[IV.16] A. H. Wijenayake and P. B. Schmidt, "Modeling and analysis of permanent magnet synchronous motor by taking saturation and core loss into account," *Proceedings of Second International Conference on Power Electronics and Drive Systems*, Singapore, 1997, pp. 530-534 vol.2.

[IV.17] F. Fernandez-Bernal, A. Garcia-Cerrada and R. Faure, "Model-based loss minimization for DC and AC vector-controlled motors including core saturation," in *IEEE Transactions on Industry Applications*, vol. 36, no. 3, pp. 755-763, May-June 2000.

[IV.18] J. Lee, K. Nam, S. Choi and S. Kwon, "Loss-Minimizing Control of PMSM With the Use of Polynomial Approximations," in *IEEE Transactions on Power Electronics*, vol. 24, no. 4, pp. 1071-1082, April 2009.

[IV.19] J. G. Cintron-Rivera, A. S. Babel, E. E. Montalvo-Ortiz, S. N. Foster and E. G. Strangas, "A simplified characterization method including saturation effects for permanent magnet Machines," *2012 XXth International Conference on Electrical Machines*, Marseille, 2012, pp. 837-843.

[IV.20] S. A. Odhano *et al*., "Parameter extraction for three phase IPM machines through simple torque tests," *2015 IEEE Energy Conversion Congress and Exposition (ECCE)*, Montreal, QC, 2015, pp. 1892-1898.

[IV.21] S. Li, D. Han and B. Sarlioglu, "Modeling of Interior Permanent Magnet Machine Considering Saturation, Cross Coupling, Spatial Harmonics, and Temperature Effects," in *IEEE Transactions on Transportation Electrification*, vol. 3, no. 3, pp. 682-693, Sept. 2017.

[IV.22] N. Bianchi and L. Alberti, "MMF Harmonics Effect on the Embedded FE Analytical Computation of PM Motors," in *IEEE Transactions on Industry Applications*, vol. 46, no. 2, pp. 812-820, March-april 2010.

[IV.23] P. H. Mellor, R. Wrobel and D. Holliday, "A computationally efficient iron loss model for brushless AC machines that caters for rated flux and field weakened operation," *2009 IEEE International Electric Machines and Drives Conference*, Miami, FL, 2009, pp. 490-494.

[IV.24] J. Goss, P. H. Mellor, R. Wrobel, D. A. Staton and M. Popescu, "The design of AC permanent magnet motors for electric vehicles: A computationally efficient model of the operational envelope," *6th IET International Conference on Power Electronics, Machines and Drives (PEMD 2012)*, Bristol, 2012, pp. 1-6.

Conclusions

In this PhD thesis, several aspects of loss minimization control of interior permanent magnet synchronous machines have been discussed. In order to highlight the main features of loss minimization control algorithm, a description of the loss minimization control state of the art was performed. In detail, this work was focused on the loss model control algorithms (LMA) that are based on the knowledge of the IPMSM mathematical model. In this regard, in order to evaluate the possible performances of the LMA, two power loss models have been taken into account. The first is derived from the conventional IPMSM mathematical modelling approach, that presents constant values of the magnetic and electrical parameters. This IPMSM mathematical modelling approach doesn't take into account the non-linear magnetic behaviour of the machine and the variability of the iron losses with the supply frequency of the machine. The second is derived from an IPMSM mathematical model that take into account the self-saturation effects and the iron loss variations with the supply frequency. In order to estimate the electrical and magnetic parameters values and their variation with the working conditions, experimental characterization of the IPMSM under test has been performed. The data acquired was used to study and simulate the impact of the proposed IPMSM mathematical models on the performances of the electric drive under test controlled with a LMA. Furthermore, several experimental investigations are carried out for the estimation of the total controllable losses for several working conditions of the electric drive. Therefore, the controllable losses estimated in simulation with the IPMSM mathematical models are compared with those obtained from the experimental investigations. In particular, a first comparison analysis was performed on the controllable power losses referred to the supply voltage fundamental harmonic. In this case, the IPMSM mathematical model, that take into account the magnetic self-saturation effects and the iron loss variability with the supply frequency, allows estimating more accurately the motor controllable losses respect to the conventional IPMSM mathematical modelling approach. A second comparison analysis was performed on the controllable power losses referred to the supply voltage entire harmonic content. In this case, the analysis carried out has shown that the performances of the two loss models are comparable. This study highlights how the harmonics of electrical quantities, such as supply voltages and absorbed currents, generate a no-

negligible contribution of active power respect to that evaluated at the fundamental harmonic and such as to compromise the effectiveness of the LMAs based on IPMSM mathematical models defined at fundamental harmonic. This result may be characteristic of the electric drive under test, and different results can be obtained for other electric drives, especially for high power electrical drives where the additional harmonic power losses impact can present negligible amplitude respect the controllable losses amplitude evaluated respect to fundamental harmonic of the supply voltage.

Therefore, the evaluation of the LMA effectiveness on the electric drive performances requires an accurate estimation of the electric drive efficiency or its power losses. For this purpose, the efficiency measurement approaches for electrical drives equipped with IPMSMs proposed by the international standard have been discussed. For this purpose, the standard IEC61800-9 prescriptions have been taken into account for the measurement system design. In this regard, a measurement system able to estimate the active power in each section of the electric drive under test has been realized. Furthermore, in order to evaluate the impact of the measurement equipment accuracy on the efficiency measurement uncertainty, the power drive system (PDS) input active power was measured with the two current transducers. In detail, a non-inductive Fluke A40B shunt resistor and a Fluke i400 current probe have been employed. The first current transducer presents high accuracy and high cost whereas the second current transducer is less accurate but cheaper. In order to simulate the control action of three control algorithms, the PDS efficiency has been evaluated with the two measurement systems for three *d*-axis current values and for several load conditions. Therefore, it has been shown that the measurement system equipped with the shunt resistor is able to accurately measure the efficiency of the electric drive and can be used for its energy classification, whereas the measurement system equipped with the Fluke i400 current probe cannot be used for the accurate measurement of the electric drive efficiency. Finally, a new measurement approach for the comparison of electrical drive performances controlled by several control algorithms are designed and experimentally validate. This approach defines the $\Delta\Delta P_{PDS}$ quantity that represents an index of the power recovered passing from the first control algorithm to the second control algorithm. Since the measurement uncertainty is affected only by the uncertainty related to random errors, the measurement of the $\Delta\Delta P_{PDS}$ quantity can be carried out also with

low accurate measurement equipment. In this regards, the two measurement system described have been used to measure $\Delta\Delta P_{PDS}$ quantity for several load conditions. The analysis conducted showed that the difference between the $\Delta\Delta P_{PDS}$ quantity evaluated with the two measurement system is negligible. This result validates the proposed measurement method.

Finally, an enhanced mathematical modelling of IPMSM that take into account the magnetic saturation, cross-coupling, spatial harmonics and iron loss effects has been addressed. In particular, in order to take into account these phenomena , the electrical, magnetic and electromagnetic quantities are defined as functions of the *dq*-axes currents and rotor angular position. For this purpose, a finite element model of the IPMSM under test has been implemented and characterized in *Ansys Maxwell* simulation environment.

In particular, in order to define the non-linear relationships between the *dq*-axes flux linkages and the *dq*-axes currents and the rotor position, a large number of FEA simulations have been carried out. The proposed enhanced mathematical model of the IPMSM has been implemented in *Matlab®/Simulink* environment. In detail, this mathematical model captures all significant effects associated with the electromagnetic behaviour of the machines, including magnetic saturation, spatial harmonics, and the iron loss effect and it has been validated by means FEA investigations. The results obtained are of considerable importance since a high-fidelity mathematical model can be used both for the design of innovative LMAs and for the evaluation of the control algorithm effectiveness. Moreover, the simulation time can be greatly reduced compared with circuit-FEA cosimulation.

List of publications

[1] M. Caruso, A. O. Di Tommaso, R. Miceli, C. Nevoloso, C. Spataro and F. Viola, "Interior permanent magnet synchronous motors: Impact of the variability of the parameters on their efficiency," *2016 IEEE International Conference on Renewable Energy Research and Applications (ICRERA)*, Birmingham, 2016, pp. 1163-1167-.

[2] G. Agnello, M. Caruso, V. Di Dio, R. Miceli, C. Nevoloso and C. Spataro, "Speed control of tubular linear induction motors for industrial automated applications," 2016 IEEE International Conference on Renewable Energy Research and Applications (ICRERA), Birmingham, 2016, pp. 1196-1201.

[3] M. Caruso, A. O. Di Tommaso, R. Miceli, C. Nevoloso, C. Spataro, F. Viola, "Characterization of the parameters of interior permanent magnet synchronous motors for a loss model algorithm", in Measurement, Volume 106, August 2017,Pages196–202.

[4] Caruso, M., Di Tommaso, A.O., Miceli, R., Nevoloso, C., Spataro, C., Viola, F., " Comparison of three Control Drive Systems for Interior Permanent Magnet Synchronous Motors", (2017) 22nd IMEKO TC4 International Symposium & 20th International Workshop on ADC Modelling and Testing SUPPORTING WORLD DEVELOPMENT THROUGH ELECTRICAL&ELECTRONIC MEASUREMENTS IASI, ROMANIA, September 14-15, 2017.

[5] A. O. Di Tommaso, F. Genduso, R. Miceli and C. Nevoloso, "Fast procedure for the calculation of maximum slot filling factors in electrical machines," 2017 Twelfth International Conference on Ecological Vehicles and Renewable Energies (EVER), Monte Carlo, 2017, pp. 1-8.

[6] M. Caruso, A. O. Di Tommaso, R. Miceli, Member, IEEE, C. Nevoloso, C. Spataro and F. Viola, "Enhanced Loss Model Algorithm for Interior Permanent Magnet Synchronous Machines", 2017 AEIT International Annual Conference (AEIT), Cagliari, 2017.

[7] M. Caruso, A. O. Di Tommaso, M. Lombardo, R. Miceli, C. Nevoloso and C. Spataro, "Maximum Torque Per Ampere control algorithm for low saliency ratio interior permanent magnet synchronous motors," 2017 IEEE 6th International

Conference on Renewable Energy Research and Applications (ICRERA), San Diego, CA, 2017, pp. 1186-1191.

[8] M. Caruso, A. O. Di Tommaso, M. Lombardo, R. Miceli, C. Nevoloso and C. Spataro, "Experimental comparison of two control algorithms for low-saliency ratio interior permanent magnet synchronous motors," 2018 Thirteenth International Conference on Ecological Vehicles and Renewable Energies (EVER), Monte-Carlo, 2018, pp. 1-6.

[9] V. Castiglia et al., "An efficient wireless power transfer prototype for electrical vehicles," 2017 IEEE 6th International Conference on Renewable Energy Research and Applications (ICRERA), San Diego, CA, 2017, pp. 1215-1220.

[10] M. Caruso et al., "Nanostructured lead acid battery for electric vehicles applications," 2017 International Conference of Electrical and Electronic Technologies for Automotive, Torino, 2017, pp. 1-5.

[11] Caruso, M., Cipriani, G., Di Dio, V., Miceli, R. & Nevoloso, C. 2017, "Experimental characterization and comparison of TLIM performances with different primary winding connections", Electric Power Systems Research, vol. 146, pp. 198-205.

[12] V. Castiglia, P. Ciotta, A. O. Di Tommaso, R. Miceli and C. Nevoloso, "High Performance FOC for Induction Motors with Low Cost ATSAM3X8E Microcontroller," 2018 7th International Conference on Renewable Energy Research and Applications (ICRERA), Paris, 2018, pp. 1495-1500.

[13] M. Caruso, A. O. Di Tommaso, R. Miceli and C. Nevoloso, "Algorithmic Approach for Slot Filling Factors Determination in Electrical Machines," 2018 7th International Conference on Renewable Energy Research and Applications (ICRERA), Paris, 2018, pp. 1489-1494.

[14] R. Leuzzi et al., "High-Speed Machines: Typologies, Standards, and Operation Under PWM Supply," 2018 AEIT International Annual Conference, Bari, 2018, pp. 1-6.

[15] Caruso, M., Di Tommaso, A.O., Miceli, R., Nevoloso, C., Spataro, C. & Trapanese, M. 2019, "Maximum Torque per Ampere Control strategy for low-saliency ratio IPMSMs", International Journal of Renewable Energy Research, vol. 9, no. 1, pp. 374-383.

[16] A. Bruno, M. Caruso, A. O. D. Tommaso, C. Nevoloso and R. Miceli, "Experimental Comparison of Efficiency Enhancement Algorithms for Three-Phase Induction Motors," 2019 Fourteenth International Conference on Ecological Vehicles and Renewable Energies (EVER), Monte-Carlo, Monaco, 2019, pp. 1-6.

[17] M. Caruso, V. Cecconi, A. O. Di Tommaso, R. Miceli and C. Nevoloso, "Performance Comparison of Electrical Motors equipped with slightly Asymmetrical Windings," 2019 AEIT International Conference of Electrical and Electronic Technologies for Automotive (AEIT AUTOMOTIVE), Torino, Italy, 2019, pp. 1-6.

[18] Caruso, M., Di Tommaso, A.O., Miceli, R., Nevoloso, C., Spataro, C. & Trapanese, M. 2019, "Maximum Torque per Ampere Control strategy for low-saliency ratio IPMSMs", International Journal of Renewable Energy Research, vol. 9, no. 1, pp. 374-383.